Dissertation

submitted to the
Combined Faculty of Mathematics, Engineering and Natural Sciences

Heidelberg University, Germany

for the degree of
Doctor of Natural Sciences

Put forward by

Samuele Montefiori
born in Lugo,
Italy.

Oral examination: 7th May, 2025.

Analytical and Numerical Methods for High-Precision Studies in Ultrarelativistic Strong-Field Quantum Electrodynamics

Referee & Supervisor:	**Prof. Dr. Christoph H. Keitel**
Referee:	**apl. Prof. Dr. Sandra P. Klevansky**
Supervisor:	**Dr. Matteo Tamburini**

Zusammenfassung

Diese Dissertation bietet eine umfassende Untersuchung sowohl analytischer als auch numerischer Techniken zur Modellierung von Prozessen in der ultrarelativistischen Starkfeld Quanten-Elektrodynamik (SFQED). Wir haben SFQEDtoolkit entwickelt, eine Open-Source-Bibliothek, die fortschrittliche Funktionsnäherungsverfahren verwendet, um die nichtlineare Compton-Emission (NIC) und die nichtlineare Breit-Wheeler-Paarerzeugung (NBW) präzise zu modellieren. Simulationen, die Particle-in-Cell (PIC)-Codes mit SFQEDtoolkit kombinieren, wurden eingesetzt, um Kollisionen zwischen ultrarelativistischen dichten Elektronenstrahlen und Plasmazielen zu untersuchen. Dabei wurde gezeigt, dass sich Elektron-Positron-Jets mit Dichten oberhalb der von Festkörpern innerhalb selbstgenerierter Magnetfelder von bis zu 10 MT bilden können. Diese Ergebnisse offenbaren ein neuartiges Regime, in dem SFQED, Atom- und Plasmaphysik untrennbar miteinander verwoben sind, und eröffnen somit einen neuen Forschungsbereich in der SFQED. Darüber hinaus leiten wir analytische Ausdrücke für die differentiellen Verteilungen der NIC- und NBW-Prozesse her, die die Energie-, Winkel-, Spin- und Polarisationscharakteristika der erzeugten Teilchen beschreiben. Bemerkenswerterweise führt die Herleitung dieser Verteilungen unter Anwendung modernster Methoden zu Ergebnissen, die in bestimmten Parameterbereichen negative Werte annehmen können, was ihre probabilistische Interpretation untergräbt. Wir zeigen, dass eine Integration dieser Verteilungen über die „Formationszeit“ des Quantenprozesses ihre konventionelle physikalische Bedeutung wiederherstellt. Insgesamt tragen die in dieser Dissertation präsentierten Arbeiten zur Weiterentwicklung der analytischen und numerischen Modellierung von SFQED-Prozessen bei. Sie liefern ein solides Fundament für zukünftige experimentelle Studien zur SFQED, die für die extremfeld-Plasmaphysik sowie die Mikrophysik von Pulsaren und Magnetaren von entscheidender Bedeutung sind.

Abstract

This thesis presents a comprehensive exploration of both analytical and numerical techniques used to model processes in ultrarelativistic strong-field quantum electrodynamics (SFQED). We developed SFQEDtoolkit, an open-source library that employs advanced function approximation techniques to accurately model nonlinear Compton (NIC) emission and nonlinear Breit-Wheeler (NBW) pair creation processes. Simulations combining particle-in-cell (PIC) codes with SFQEDtoolkit have been used to investigate collisions between ultrarelativistic dense electron beams and plasma targets, demonstrating that electron-positron jets exceeding solid densities can be produced within self-generated magnetic fields up to 10 MT. These findings reveal a novel regime where SFQED, atomic, and plasma physics are intrinsically interwoven, opening a new avenue of research in SFQED. Furthermore, we derive analytical expressions for NIC and NBW differential distributions that describe the energy, angular, spin, and polarization characteristics of the produced particles. Notably, the derivation of these distributions, following state-of-the-art methodologies, yields results that can give negative values over certain parameter intervals, undermining their probabilistic interpretation. We demonstrate that integrating these distributions over the "formation time" of the quantum process restores their conventional physical meaning. Overall, the contributions of this thesis advance the analytical and numerical modeling of SFQED processes, providing a robust framework for forthcoming experimental studies of SFQED, which are critically relevant for extreme-field plasma physics and the microphysics of pulsars and magnetars.

Regarding the topic of this thesis, one article has been published by a peer reviewed journal:

- S. Montefiori and M. Tamburini
  SFQEDtoolkit: A high-performance library for the accurate modeling of strong-field QED processes in PIC and Monte Carlo codes
  Computer Physics Communications
  https://doi.org/10.1016/j.cpc.2023.108855

While other two articles related to this thesis are in preparation:

- S. Montefiori, C. H. Keitel, M. Tamburini, et al.
  Superdense gamma-electron-positron jets from beam-plasma interaction

- S. Montefiori, C. H. Keitel, A. Di Piazza and M. Tamburini
  Angular-spin and polarization resolved nonlinear Compton emission

Outside the scope of this thesis, the following article has been published by a peer reviewed journal:

- A. Matheron, P. Claveria San Miguel, R. Ariniello, H. Ekerfelt, F. Fiuza, S. Gessner, M. F. Gilljohann, M. J. Hogan, C. H. Keitel, A. Knetsch, M. Litos, Y. Mankovska, S. Montefiori, Z. Nie, B. O'Shea, J. R. Peterson, D. Storey, Y. Wu, X. Xu, V. Zakharova, X. Davoine, L. Gremillet, M. Tamburini and S. Corde
  Probing strong-field QED in beam-plasma collisions
  Communications Physics
  https://doi.org/10.1038/s42005-023-01263-4

Contents

1 Introduction **1**

1.1 This Thesis 5

1.2 The Maxwell-Vlasov model 7

1.3 Particle-in-Cell method 8

2 Chebyshev Polynomials and ChAppX **13**

2.1 Chebyshev polynomials 13

2.2 Clenshaw's recurrence formula 16

2.3 Generalization to multivariable functions 17

2.4 `ChAppX`: a code for Chebyshev approximations 19

2.4.1 One-variable function approximation 21

2.4.2 Two- and three-variables function approximation 24

2.4.3 Stopping strategy: how to stop the iterated version? 28

2.4.4 Implemented stopping strategy 31

2.5 Important notes 35

2.6 Conclusions 36

3 SFQEDtoolkit **37**

3.1 Strong-Field QED 37

3.1.1 The Furry picture 38

3.1.2 Volkov states 38

3.1.3 Locally-Constant-Field Approximation 40

3.2 Methodology of `SFQEDtoolkit`'s implementation 41

3.3 Photon emission and pair creation in the LCFA 42

3.3.1 Photon emission rate 43

3.3.2 Pair creation rate 46

3.3.3 Photon emission spectrum 48
3.3.4 Pair creation spectrum 51
3.3.5 Changing the number of coefficients used in a simulation . 53
3.4 Photon emission beyond the locally-constant-field approximation . 54
3.5 Conclusions 58

4 The "thick-target" simulation 59
4.1 The simulation set-up 60
4.1.1 Simulation specifics 60
4.2 Discussion and results 61
4.3 Conclusions 66

5 Fully resolved NIC and NBW processes 71
5.1 The Quasiclassical operator method 72
5.2 The full-resolution NIC and NBW distributions 75
5.2.1 The fully-resolved NIC differential distribution 75
5.2.2 The fully-resolved NBW differential distribution 81
5.3 The pure and mixed spin-states approach 86
5.4 Probabilities and energies 87
5.4.1 The initial spin-resolved NIC photon emission rate and energy distribution 88
5.4.2 The polarization-resolved NBW pair production rate and energy distribution 94
5.5 Angular distribution algorithms 98
5.5.1 NIC: Photons' angular distribution from spin resolved electrons 99
5.5.2 NBW: Angular distribution from polarization resolved photons 103
5.6 Determination of the final inner states 106
5.6.1 Internal states for particles without angular resolution . . . 106
5.6.2 Internal states for particles with angular resolution 120

5.7 An ill-defined differential probability 132
5.7.1 Analytical study 138
5.7.2 Recovering the probabilistic meaning behind the fully-resolved distribution 142
5.8 Conclusions 149

6 Conclusions and Outlook **151**
6.1 Outlook 152

A User guide **155**

B The Sokolov-Ternov effect **163**

C Bessel functions approximations **165**

Bibliography **169**

Acknowledgments **177**

Chapter 1

Introduction

Twenty years after the first laser was realized [1], the introduction of chirped pulse amplification (CPA) [2] enabled optical laser systems to reach intensities of $10^{14}-10^{15}$ W/cm^2, generating electric field amplitudes comparable to the Coulomb field in atoms. Continuous technological advancements further pushed this threshold to $10^{17}-10^{18}$ W/cm^2, entering the relativistic regime, where the laser's electromagnetic (EM) fields can accelerate electrons (e^-) to relativistic velocities within a single cycle. Today, the highest recorded laser intensity has been achieved using multi-PW laser systems at CoReLs [3], reaching 1.1×10^{23} W/cm^2 [4]. Meanwhile, 10-PW-class lasers are expected to become operational in several facilities worldwide, including Apollon [5], CoReLs [3], ELI [6], NIF [7] and ZEUS [8] for instance (see map in Fig. 1.1 and [9]). These systems are projected to achieve intensities approaching 10^{24} W/cm^2. This progress could soon enable experimental investigations into an unexplored regime of quantum electrodynamics (QED). QED remains the most precisely tested quantum field theory (QFT) and a cornerstone of the Standard Model (SM): the remarkable agreement between theoretical predictions and experimental results underscores its success.

In order to grasp the mysteries that QED still conceals, let us pause for a moment and consider the Heisenberg uncertainty principle in its time-energy form:

$$\Delta\epsilon\Delta t \geq \frac{\hbar}{2}.$$

This celebrated inequality, which from our human perspective represents one of the most counterintuitive aspects of quantum mechanics, implies that, for an extremely short duration Δt, nature can seemingly "violate" or temporarily "ignore" energy conservation. As a consequence, a *virtual* particle-antiparticle pair can momentarily emerge from the vacuum, only to annihilate shortly after. Specifically, an electron-positron (e^--e^+) pair with energy $\varepsilon \sim m_e c^2$ may appear for a time comparable to the Compton scale: $\tau_C = \frac{\hbar}{m_e c^2} \sim 1.3 \times 10^{-21}$ s. Here, c denotes the speed of light in vacuum, $\hbar$ is the reduced Planck constant, while m_e and e represent the electron mass and charge, respectively. These quantum fluctuations can be brought on-shell, transitioning from virtual to real particles, when subjected to a strong, uniform electric field capable of supplying energy on the order of the pair's rest energy ($2m_e c^2$) across a distance comparable to the reduced Compton wavelength $\lambda_C = \frac{\hbar}{m_e c} \sim 3.86 \times 10^{-13}$ m. The QED critical field, $E_{cr} = \frac{m_e^2 c^3}{|e|\hbar} \sim 1.3 \times 10^{16}$ V/cm,

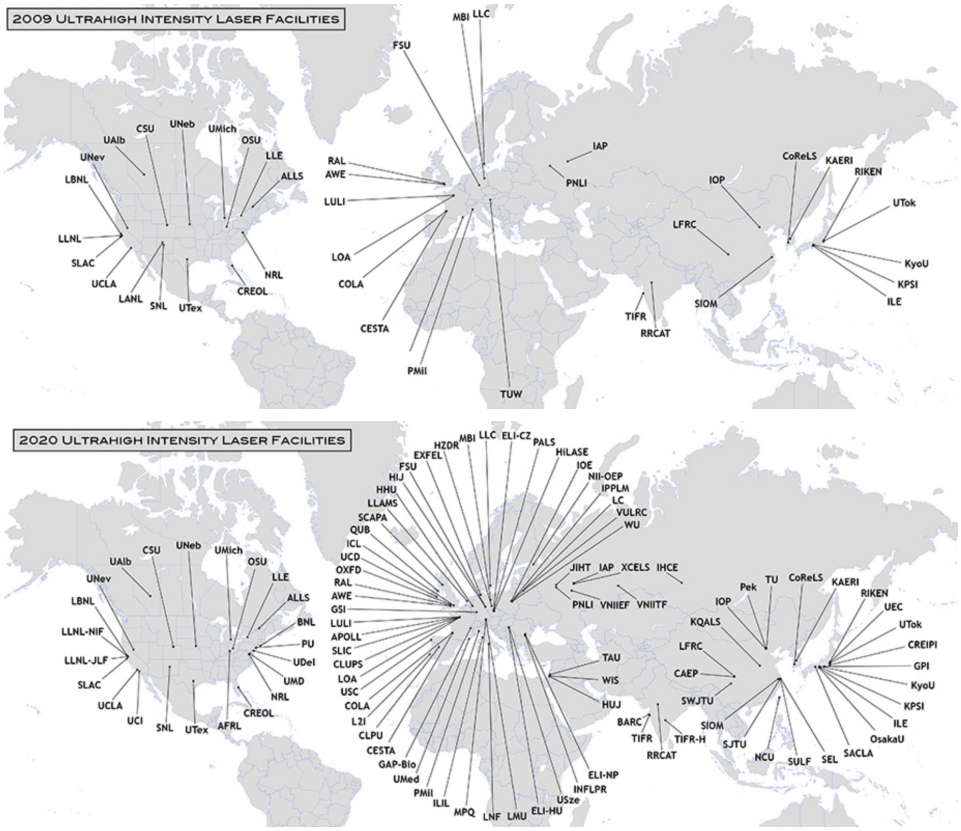

Figure 1.1: Location of the main ultrahigh intenisty laser facilities worldwide, in 2009 (top) and 2020 (bottom). The rapid growth of this research field is evident in the significant increase in the number of new laser facilities established within just a decade. See [9] for further details.

serves precisely this purpose, rendering the vacuum unstable with respect to spontaneous pair creation (Fig. 1.2). This process, first proposed by Sauter [10] and later formalized by Schwinger [11], became known as *Schwinger pair production*.

Despite the significant theoretical and experimental efforts driven by new experimental capabilities, achieving an electromagnetic field strength of E_{cr} in the laboratory remains far from feasible. Reaching this threshold would require a laser with a critical intensity of $I_{cr} = 4.6 \times 10^{29}$ W/cm^2. While this prevents direct investigation of exotic phenomena such as Schwinger pair production in vacuum, it is still possible to study the behavior of ultra-relativistic particles in strong electromagnetic fields. Indeed, according to classical electrodynamics, during a time interval t a constant electric field with peak strength E_0 can impart an energy of approximately $\varepsilon \sim |eE_0ct|$ to an electron [12]. For electrons interacting with a laser, the angular frequency ω sets the characteristic time scale, so that $t \sim \frac{1}{\omega}$. Thus, by introducing the gauge- and Lorentz-invariant *classical nonlinearity parameter*

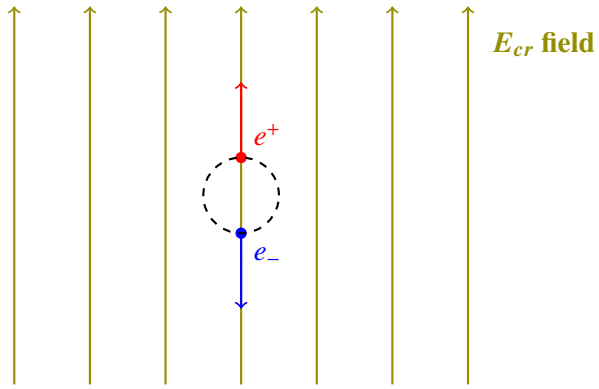

Figure 1.2: A virtual electron-positron pair emerges from the vacuum, momentarily violating energy conservation. The energy supplied by the critical field E_{cr} brings the pair on-shell. The region enclosed by the dashed circle corresponds to the Compton wavelength λ_C.

ξ (see Chap. 3)

$$\xi = \frac{|e|E_0}{m_e c\omega},$$

we observe that an electron initially at rest reaches relativistic speeds within a single laser cycle when $\xi \sim 1$. Modern petawatt-class lasers enable access to the *Strong-Field QED* (SFQED) regime, characterized by $\xi \gg 1$. In this regime, coupling such high-intensity optical systems with ultrarelativistic charged particle beams enables the particles to experience, in their instantaneous rest frame, an electric field E that exceeds E_{cr} ($E > E_{cr}$) and drives the emergence of novel quantum phenomena. In this thesis we will specifically focus on two key SFQED processes: the nonlinear inverse (or multiphoton) Compton scattering (NIC) and the nonlinear Breit-Wheeler pair production (NBW).

The first process occurs when a charged particle, such as an electron, moves through an intense electromagnetic field. In essence, the electron can absorb multiple photons from the field, along with their energy and momentum, and subsequently emit a high-energy photon, altering its trajectory (Fig. 1.3). Multiphoton Compton scattering was first observed in 1996 at the Stanford Linear Accelerator (SLAC) [13]. In this experiment, an ultra-relativistic electron beam with an energy of approximately 46.6 GeV collided with an intense laser pulse ($I \sim 10^{18}$ W/cm^2), leading to the detection of the scattering via a nonlinear energy shift in the outgoing electron spectrum (see Fig. 1.4). Another fundamental and perhaps even more intriguing QED prediction is the possibility of converting light into matter. If two photons collide with a total energy above the threshold $\varepsilon_{tot} \geq 2m_e c^2$, the creation of an e^+-e^- pair becomes kinematically allowed [14], defining the linear Breit-Wheeler pair production process. However, realizing an experimental setup where high-energy photon beams collide is an enormous challenge. The inherently small cross-section

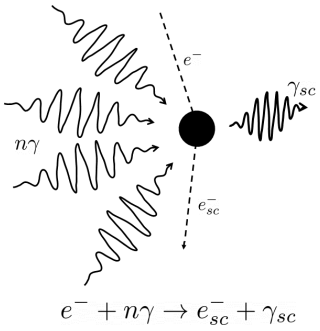

Figure 1.3: Sketch of the nonlinear inverse Compton scattering: an electron absorbs n photons γ from the field it moves within and then emits a hard, energetic, photon γ_{sc}. Source: Wikipedia.

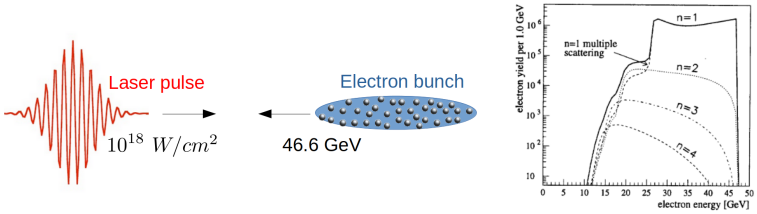

Figure 1.4: Illustration of the 1996 SLAC experiment that first revealed the NIC effect: a 10^{18} W/cm^2 intense laser pulse collides head-on with a 46.6 GeV electron bunch. The energy shift in the spectrum of the electrons produced in the interaction (inset from [13]) enabled the detection of four-photon nonlinear scattering.

of this process makes it exceedingly difficult to trigger and detect, and to date, linear Breit-Wheeler pair production remains unobserved. In contrast to the linear process, the nonlinear Breit-Wheeler mechanism, where a single high-energy photon interacts with multiple lower-energy photons (from an intense background field) to produce an electron-positron pair, was successfully detected in 1997 at SLAC [15]. In an experiment nearly identical to the one conducted a year earlier to observe NIC [13], the photons produced via NIC were themselves able to absorb additional photons from the laser field, ultimately decaying into electron-positron pairs.

The study of SFQED processes in plasmas−including the potential to generate extended dense electron-positron jets [16, 17]−offers unprecedented access to the microphysics governing both plasma dynamics and the intense emission processes observed around compact astrophysical objects such as pulsars and magnetars [18–21]. These unique opportunities have spurred growing interest and experimental effort in exploring SFQED effects in extreme-field plasma physics. A prominent example is provided by QED cascades, whose dynamics is governed by the interplay between SFQED processes and the collective plasma response [22–34].

Cascades are chain reactions occurring in intense EM fields where self-sustaining cycles of NIC and NBW processes alternate with each other, leading to the exponential multiplication of electrons, positrons, and photons. According to Bell and Kirk [22], even a single electron initially at rest in a standing wave formed by two identical counterpropagating, circularly polarized laser fields can trigger an avalanche process at field intensities on the order of 10^{24} W/cm^2.

It is clear that SFQED-dominated plasmas are complex, strongly nonlinear systems. Understanding and modeling the intrinsically multiscale dynamics of these plasmas in realistic conditions critically depend on the development of advanced numerical tools and codes that can run efficiently on high-performance computing (HPC) machines. These considerations have motivated the project presented in this thesis, which is thoroughly outlined in the following sections and chapters.

1.1 This Thesis

In recent decades, Monte-Carlo (MC) and Particle-in-Cell (PIC) codes have been developed to study beam physics and classical plasma dynamics [35]. Some of these codes have been further enhanced with specialized routines designed to simulate high-energy photon emission and electron-positron pair creation in strong electromagnetic fields [24, 32, 36–42]. Motivated by the computational challenges posed by SFQED distributions, which involve numerically expensive special functions and integrals, state-of-the-art codes model the NIC and NBW mechanisms by employing binary search and interpolation on pre-computed lookup tables. In these tables, the required distributions are sampled over a limited number of points[1] [36, 39, 41]. However, this approach presents two significant challenges: (i) it struggles to cover the entire range of parameters (for example, a cut-off in the photon spectrum is often introduced), and (ii) achieving high accuracy demands a very high number of sampling points, which substantially increases computational cost. Conversely, an insufficient resolution in the lookup tables can introduce substantial systematic errors and numerical artifacts (see Ref.[42] and section3.3), potentially compromising both the viability of simulations and the reliability of their results. For these reasons, after a concise overview of plasma physics and the PIC method is provided in chapter 1, the SFQED-oriented library `SFQEDtoolkit` is presented in chapter 3. Designed for the implementation into existing PIC and MC codes, `SFQEDtoolkit` is a suite of modules that leverages advanced function approximation techniques (detailed in Chapter 2) to overcome the aforementioned challenges while maintaining an impressive better then 0.1% accuracy.

Following the standard methodology for incorporating SFQED processes into a code, the library operates in two main steps: first, it determines whether a NIC or

[1] The sampling points are logarithmically distributed between a minimum and a maximum value to span several orders of magnitude.

NBW event occurs based on its probability per unit time; then, it samples the final state from the corresponding distribution. In Chapter 4, we present the results of several resource-demanding simulations performed using CALDER [43], a massively parallel PIC code equipped with the basic version of `SFQEDtoolkit`, available on GitHub[2]. These simulations involved a 9 GeV or 90 GeV electron beam colliding with a fixed plasma target composed of either lithium or gold. As the ultrarelativistic electrons traverse the plasma, the extremely intense self-generated electromagnetic fields trigger a cascade of photon generation and pair production processes. These effects are so pronounced, especially in the 90 GeV case, that they would be unmanageable without the assistance of `SFQEDtoolkit`. Remarkably, the intense magnetic fields generated within the target reach up to 10 MT, a magnitude comparable to those found near pulsars, suggesting a viable pathway for recreating the microphysics of these astrophysical entities in the laboratory. Finally, the large number of produced e^+-e^- pairs, combined with their high energy and tight collimation, indicates the potential for realizing an apparatus capable of delivering a multi-GeV, solid-density, plasma composed entirely of electrons and positrons.

Complying with standard practices in modern SFQED codes, the basic implementation of `SFQEDtoolkit` (introduced in chapter 3) employs the collinear emission approximation and averages the NIC and NBW distributions over the polarization states of the particles involved—thus neglecting photon polarization, lepton spin, and angular distributions. Motivated by the increasing need for a numerical tool that supports precision SFQED tests—one that is both accurate and efficient while fully resolving all particle degrees of freedom—we present in Chapter 5 *fully* resolved expressions for the NIC and NBW distributions. Derived via the quasi-classical operator approach developed by Baier and Katkov [44], these expressions explicitly depend on energy, emission angle, and spin/polarization. Remarkably, and quite unexpectedly, these fully resolved distributions prove to be *improper*, as they can become negative over certain parameter intervals, rendering a direct probabilistic interpretation untenable. This critical issue, previously unaddressed in the literature, must be resolved to restore their conventional stochastic meaning. By incorporating the concept of formation time[3] τ_f (or equivalently, formation length λ_f), we show that the fully resolved NIC distribution[4] regains its standard probabilistic interpretation only when integrated over the time interval of the order of its formation time. In this context, τ_f is confirmed to be the minimal time required for the conversion of the initial field excitations (ingoing particles) into the final ones (outgoing particles), i.e., for a particle to transition from a state with momentum $\vec{p}$ and spin $\vec{\zeta}$, to one with momentum $\vec{p}\,'$ and $\vec{\zeta}\,'$.

The following sections introduce the basics of plasma physics and the fundamental

[2] https://github.com/QuantumPlasma/SFQEDtoolkit

[3] In our case, the formation time corresponds to either the time taken by an electron to emit a NIC photon or the time needed by a photon to decay into a NBW pair.

[4] An analogous argument holds for the NBW distributions.

equations that describe its dynamics. In particular, we present the Maxwell-Vlasov model, a system of coupled equations governing the evolution of charged particles within the self-consistent electromagnetic fields they generate, and the PIC method, the numerical tool used to solve these equations.

1.2 The Maxwell-Vlasov model

Plasma, often referred to as the fourth state of matter, is an ionized gas composed of charged particles, such as free electrons, positrons, and ions, that exhibit distinctive properties. Due to their charged nature, plasma constituents interact strongly with electric and magnetic fields, leading to *collective behaviors* where long-range electromagnetic forces dominate over short-range collisions. Additionally, plasmas are typically *quasineutral*, meaning that the densities of positive and negative charges are nearly equal on macroscopic scales, and they exhibit high electrical conductivity. Together, these characteristics facilitate the formation of complex structures and phenomena, such as waves, instabilities, and turbulence.

Plasmas are typically characterized by two fundamental length scales: (i) the distance over which EM radiation propagates in the plasma, and (ii) the characteristic separation over which electrons redistribute to effectively screen internal electric fields. By classical electrodynamics, the first length scale is related to the oscillation frequency of electrons around their equilibrium positions, given by

$$\omega_e = \Big(\frac{4\pi n_e e^2}{m_e}\Big)^{\frac{1}{2}}, \tag{1.1}$$

where n_e is the electron density. The associated distance, known as the skin depth, is then defined as

$$l_e = \frac{c}{\omega_e}. \tag{1.2}$$

In contrast, the characteristic length scale for electron redistribution, the Debye length, is given by

$$\lambda_D = \Big(\frac{k_B T_e}{4\pi n_e e^2}\Big)^{\frac{1}{2}}, \tag{1.3}$$

where k_B is the Boltzmann constant and T_e is the electron temperature. Modeling the dynamics of charged particles requires a framework that self-consistently couples the motion of the particles with the electromagnetic fields they generate. For collisionless plasmas, where collective EM interactions dominate over binary collisions, kinetic theory provides the Vlasov equation

$$\frac{\partial}{\partial t}[f(\vec{x},\vec{v},t)] + \vec{v}(\vec{p})\cdot\vec{\nabla}_x[f(\vec{x},\vec{v},t)] + \vec{F}_L\cdot\vec{\nabla}_p[f(\vec{x},\vec{v},t)] = 0. \tag{1.4}$$

which expresses the conservation of the particle distribution function $f(\vec{x},\vec{v},t)$ in six-dimensional phase space. Here, the particles, with momentum $\vec{p}$ (or equiva-

lently velocity $\vec{v}$) and charge q, evolve under the influence of the Lorentz force

$$\vec{F}_L = q(\vec{E} + \frac{\vec{v}}{c} \times \vec{B}), \tag{1.5}$$

where $\vec{E}$ and $\vec{B}$ denote the electric and magnetic fields, respectively. If the plasma consists of N_s distinct charged species, each with distribution function f_i, the total charge density is given by

$$\rho(\vec{x}, t) = \sum_i^{N_s} q_i \int f_i(\vec{x}, \vec{p}, t) d\vec{p} \tag{1.6}$$

and the current density is

$$\vec{j}(\vec{x}, t) = \sum_i^{N_s} q_i \int f_i(\vec{x}, \vec{p}, t) \vec{v}_i(\vec{p}) d\vec{p}. \tag{1.7}$$

These quantities serve as sources for the electromagnetic fields, which are governed by Maxwell's equations:

$$\begin{aligned}
\vec{\nabla} \cdot \vec{B} &= 0, \\
\vec{\nabla} \cdot \vec{E} &= 4\pi\rho, \\
\vec{\nabla} \times \vec{B} &= \frac{1}{c}\frac{\partial \vec{E}}{\partial t} + \frac{4\pi}{c}\vec{j}, \\
\vec{\nabla} \times \vec{E} &= -\frac{1}{c}\frac{\partial \vec{B}}{\partial t}.
\end{aligned} \tag{1.8}$$

Equations (1.5)–(1.8) constitute the Maxwell-Vlasov system, a set of coupled equations that describe the interaction between charged particles and electromagnetic fields. In realistic scenarios, finding an analytic solution to these partial differential equations is nearly impossible, necessitating numerical methods. Among these, the PIC method is one of the most effective and well-validated approaches. The next section discusses the PIC technique in detail.

1.3 Particle-in-Cell method

The PIC method leverages the collective nature of plasmas by solving the Maxwell-Vlasov equations (1.5)–(1.8) through the discrete evolution of representative particles over a computational grid (see Fig. 1.5). This grid's spatial dimensions are tailored to the specific problem at hand, while the total simulation time is divided into smaller intervals known as timesteps. In this framework, the concept of a particle is redefined, giving rise to the numerical construct of a macro-particle. In addition to its physical mass m and charge q, each macro-particle is assigned a

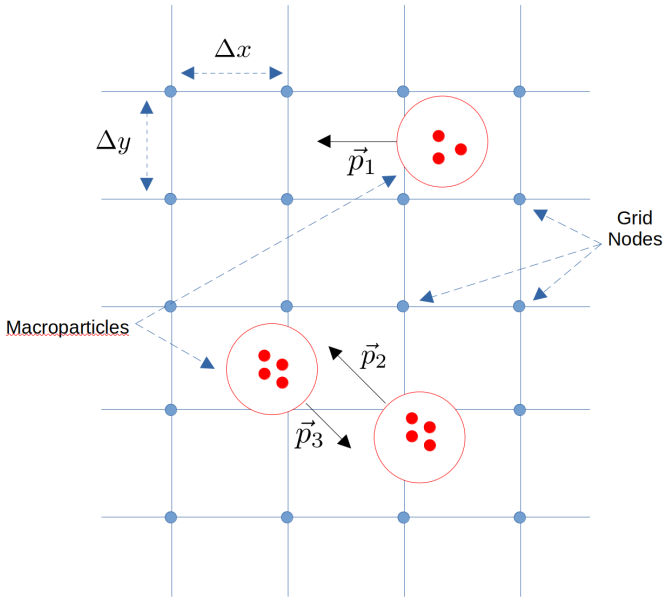

Figure 1.5: Schematic of a two-dimensional Particle-In-Cell computational grid: three macro-particles (large red circles), representing four and three real particles (small red dots within), move with momenta $\vec{p}_i$ ($i = 1, 2, 3$) over a grid with resolution $\Delta x \times \Delta y$. The charge current carried by the particles is deposited at the mesh nodes, where Maxwell's equations are solved.

weight w, allowing it to represent multiple real plasma particles. This approach effectively reinstates the collective and stochastic properties of a physical plasma. Once the macro-particles are initialized[5] and the initial electromagnetic fields are determined[6], the core PIC algorithm proceeds in a loop where four fundamental operations are repeated at each timestep Δt:

1. Particle push: Macro-particles' positions and velocities are updated on the grid using a standard function integrator method[7], based on their equations of motion. These equations can be directly derived from (1.5)-(1.8), assuming the phase space distribution function $f(\vec{x}, \vec{p}, t)$ takes the form

$$f(\vec{x}, \vec{p}, t) = \sum_{i}^{N_p} w_i \, S\,(\vec{x} - \vec{x}_i(t)) \, \delta(\vec{p} - \vec{p}_i(t)), \tag{1.9}$$

   where $S\,(\vec{x})$ defines the spatial shape of each macro-particle and is normal-

[5]The initialization follows spatial and/or momentum distributions characteristic of the plasma, ensuring that each macro-particle has well-defined mass, charge, weight, position, and momentum.

[6]Typically, charge and current densities are interpolated onto the grid nodes, from which the electric and magnetic fields are computed by solving the relativistic Poisson equation. A detailed explanation of these numerical techniques is beyond the scope of this manuscript, but interested readers may refer to [45].

[7]See Boris pusher [35] or Runge-Kutta method [46].

ized to 1, while the Dirac delta selects its momentum. Substituting (1.9) into the Vlasov equation (1.4) simplifies it to

$$\sum_{i=1}^{N_p} \{\vec{\nabla}_x \cdot [(\vec{v}(\vec{p}) - \dot{\vec{x}}_i(t))\, S(\vec{x} - \vec{x}_i(t))\, \delta(\vec{p} - \vec{p}_i(t))] + \\ + \vec{\nabla}_p \cdot [(\vec{F}_L - \dot{\vec{p}}_i(t))\, S(\vec{x} - \vec{x}_i(t))\, \delta(\vec{p} - \vec{p}_i(t))]\} = 0. \tag{1.10}$$

By integrating over $\vec{p}$ or $\vec{x}$, and considering that boundary terms vanish[8], one recovers the Newton-Lorentz equations:

$$\dot{\vec{x}}_i(t) = \vec{v}(\vec{p}_i), \tag{1.11}$$

$$\dot{\vec{p}}_i(t) = \vec{F}_L = q_i\Big(\vec{E}(\vec{x}_i, t) + \frac{\vec{v}(\vec{p}_i)}{c} \times \vec{B}(\vec{x}_i, t)\Big). \tag{1.12}$$

This confirms that macro-particles follow the expected trajectories dictated by classical electrodynamics.

2. Charge and current deposition: The charge and current densities are computed based on the macro-particle distribution and assigned to the grid nodes using interpolation techniques [47].

3. Field evolution: Maxwell's equations (1.8) are solved using a finite-difference scheme [48] to evolve the electric and magnetic fields by a timestep Δt.

4. Field interpolation: The updated electromagnetic fields are interpolated back to the positions of the macro-particles, providing the force $\vec{F}_L$ required for step 1.

In essence, this method transforms the problem of solving a coupled system of partial differential equations into a fully self-consistent simulation, where numerical particles and fields evolve together. The spatial resolution of the simulation is dictated by the grid cell size Δx, which must be sufficiently small to capture essential plasma dynamics. In particular, Δx must be smaller than both the skin depth (1.2) and the Debye length (1.3) to resolve the collective effects characteristic of plasmas. Similarly, the timestep Δt is chosen based on the physical phenomena of interest, often corresponding to a fraction of the laser period in laser-plasma simulations or another characteristic timescale of the system.

Beyond the core algorithm, PIC codes can incorporate additional physical processes, such as Coulomb collisions, ionization, and radiation emission. In particular, several research groups worldwide have developed stochastic SFQED modules capable of simulating NIC and NBW via Monte Carlo methods, although later studies revealed that some of these implementations exhibit numerical issues [42]. From the next chapter onward, this thesis focuses on the numerical implementation

[8] This follows from the properties of $\delta(\vec{p} - \vec{p}_i(t)) = 0$ and $S(\vec{x})$, which decay at large distances.

of such SFQED effects, identifying limitations in existing approaches and introducing a novel technique based on Chebyshev polynomial expansions in chapter 2. As will become clear, these expansions form the foundation of `SFQEDtoolkit`, the library developed as part of this PhD project.

Chapter 2

Chebyshev Polynomials and ChAppX

The continuous advancement of PIC codes, along with the growing need to incorporate SFQED effects, has driven us to develop and release the open-source suite of modules `SFQEDtoolkit`, presented in chapter 3, that integrate NIC and NBW high-accuracy computations into plasma simulations. This chapter introduces the multi-variable Chebyshev expansion method and `ChAppX`, a stand-alone software we developed for computing Chebyshev coefficients of generic functions. Designed for flexibility and ease of use, `ChAppX` serves as both a precursor to and a complement of `SFQEDtoolkit`. We begin with a brief introduction to Chebyshev polynomials and the properties that make them an ideal basis for approximating smooth functions.

2.1 Chebyshev polynomials

Chebyshev polynomials form an infinite-dimensional basis of piecewise continuous functions on the interval $-1 \leq x \leq 1$, where they are defined via the recurrence relation

$$T_{n+1}(x) = 2xT_n(x) - T_{n-1}(x), \quad \text{with} \quad T_0(x) = 1, \quad T_1(x) = x \tag{2.1}$$

and are orthogonal with respect to the weight $1/\sqrt{1-x^2}$

$$\int_{-1}^{+1} \frac{T_i(x)T_j(x)}{\sqrt{1-x^2}} = \pi\delta_{\frac{ij}{2}0}, \tag{2.2}$$

$\delta_{\frac{ij}{2}0}$ being the altered Kronecker delta symbol[1]

$$\delta_{\frac{ij}{2}0} = \begin{cases} 0, & i \neq j \\ \frac{1}{2}, & i = j \neq 0 \\ 1, & i = j = 0 \end{cases} . \tag{2.4}$$

[1] A more compact and useful expression for $\delta_{\frac{ij}{2}0}$, which will be used throughout the following chapter, is

$$\delta_{\frac{ij}{2}0} = \delta_{ij}\left(\frac{1}{2} + \frac{1}{2}\delta_{j0}\right), \tag{2.3}$$

δ_{ij} being the standard Kronecker delta. Summations involving the altered Kronecker delta should always be made explicit.

The recurrence relation (2.1) has the following solution:

$$T_n(x) = \cos(n \arccos(x)) \tag{2.5}$$

which highlights the relationship between the expansion in Chebyshev polynomials and the discrete Fourier transform. A continuous function $f(x)$ can therefore be approximated as

$$f(x) \approx \sum_{i=0}^{N} c_i T_i(x), \tag{2.6}$$

where c_i are the coefficients and N represents the order (i.e., the highest polynomial degree) of the expansion. The Chebyshev polynomials satisfy a set of discrete orthogonality relations, making the evaluation of the coefficients c_i in Eq. (2.6) numerically efficient, which is a key advantage of approximation theory:

- the N zeros of the $N-$th Chebyshev polynomial $T_N(x)$ are given by

$$\bar{x}_k = \cos\Big(\frac{\pi(2k-1)}{2N}\Big), \qquad k = 1, ..., N. \tag{2.7}$$

  For these zeros, the orthogonality relation is

$$\sum_{k=1}^{N} T_i(\bar{x}_k) T_j(\bar{x}_k) = N\delta_{\frac{ij}{2}0}, \tag{2.8}$$

  where $i, j < N$;

- the $N + 1$ extrema of the $N-$th Chebyshev polynomial $T_N(x)$ are given by

$$\hat{x}_k = \cos\Big(\frac{k\pi}{N}\Big), \qquad k = 0, ..., N. \tag{2.9}$$

  For these extrema, the orthogonality relation is:

$$\sum_{k=0}^{N}{}'' T_i(\hat{x}_k) T_j(\hat{x}_k) = N\delta_{\frac{ij}{2}0}, \tag{2.10}$$

  in which $i, j < N$. The *altered sum* $\sum''$ indicates that the first and last terms in the summation are halved.

Assume we now evaluate equation (2.6) at the generic k-th extreme $\hat{x}_k$ of $T_{N+1}(x)$:

$$f(\hat{x}_k) = \sum_{i=0}^{N} c_i T_i(\hat{x}_k), \tag{2.11}$$

where the approximation "≈" symbol has been replaced by equality "=" for convenience. Multiplying equation (2.11) by $T_r(\hat{x}_k)$ and carrying out an altered sum over all the extrema of T_{N+1}, we obtain:

$$\sum_{k=0}^{N+1}{}'' f(\hat{x}_k)T_r(\hat{x}_k) = \sum_{i=0}^{N} c_i \sum_{k=0}^{N+1}{}'' T_i(\hat{x}_k)T_r(\hat{x}_k) \overset{(2.10)}{=} \sum_{i=0}^{N} c_i(N+1)\delta_{\frac{ir}{2}0} \overset{(2.3)}{=} (N+1)c_r(\frac{1}{2}+\frac{1}{2}\delta_{r0}). \tag{2.12}$$

This formula can be easily inverted to give the coefficients [49]:

$$c_i = \frac{2}{(N+1)(1+\delta_{i0})} \sum_{k=0}^{N+1}{}'' f(\hat{x}_k)T_i(\hat{x}_k). \tag{2.13}$$

The same argument holds for the zeros of T_{N+1} as well (in which case relation (2.8) would have been used), leading to an alternative expression for the Chebyshev coefficients

$$c_i = \frac{2}{(N+1)(1+\delta_{i0})} \sum_{k=1}^{N+1} f(\bar{x}_k)T_i(\bar{x}_k). \tag{2.14}$$

Alternatively, one can resort to the inner product (2.2) and find the i-th coefficient c_i through the projection of f onto the i-th Chebyshev basis element $T_i(x)$:

$$c_i = \frac{2}{\pi(1+\delta_{i0})} \int_{-1}^{+1} \frac{f(x)T_i(x)}{\sqrt{1-x^2}} dx. \tag{2.15}$$

While equation (2.15) gives the coefficients exactly, the coefficients obtained from equations (2.13) and (2.14) are exact only if f has a *finite* Chebyshev expansion. For example, this holds for N-th degree polynomials, where $c_i = 0$ for $i > N$. Consider the simple quadratic function $g(x) = x^2 + 2x + 1$. Assuming a second-order Chebyshev expansion

$$g(x) = \sum_{i=0}^{2} c_i T_i(x), \tag{2.16}$$

the coefficients can be found exactly using any method, resulting in:

$$c_0 = 1.5, \quad c_1 = 2, \quad c_2 = 0.5. \tag{2.17}$$

In contrast, if we assume an approximation with any order ($N \neq 2$), methods (2.13) and (2.14) will fail, yielding nonzero (but small) coefficients $c_j \neq 0$ for $j > 2$.

Once we get hold of the set of coefficients, a mechanism to evaluate the sum (2.6) at any point x_P is necessary: the Clenshaw recurrence algorithm (see next section) is designed to address this objective.

2.2 Clenshaw's recurrence formula

Whenever the Chebyshev expansion coefficients c_i are known, one can compute the function

$$f(x) = \sum_{i=0}^{N} c_i T_i(x) = c_0 T_0(x) + c_1 T_1(x) + ... + c_N T_N(x), \tag{2.18}$$

by directly evaluating the Chebyshev polynomials (for instance, via their defining recurrence relation in Eq. (2.1)) and summing the contributions. However, because of delicate cancellations among terms, proceeding in this way may lead to significant round-off errors. In contrast, Clenshaw's recurrence offers a numerically stable and efficient alternative for evaluating (2.18). Starting from the Chebyshev coefficients c_i, Clenshaw's recurrence exploits the recurrence relation

$$T_n(x) - 2xT_{n+1}(x) + T_{n+2}(x) = 0, \tag{2.19}$$

to define a new set of auxiliary coefficients b_i via

$$b_n - 2xb_{n+1} + b_{n+2} = c_n, \qquad b_{N+1} = b_{N+2} = 0. \tag{2.20}$$

(Note that the b_i generally depend on x; i.e., $b_i \equiv b_i(x)$.) Substituting Eq.(2.20) into Eq.(2.18) yields

$$\begin{aligned} f(x) = {} & (b_0 - 2xb_1 + b_2)T_0(x) + \\ & + (b_1 - 2xb_2 + b_3)T_1(x) + \\ & + (b_2 - 2xb_3 + b_4)T_2(x) + \\ & + ... + \\ & + (b_{N-3} - 2xb_{N-2} + b_{N-1})T_{N-3}(x) + \\ & + (b_{N-2} - 2xb_{N-1} + b_N)T_{N-2}(x) + \\ & + (b_{N-1} - 2xb_N)T_{N-1}(x) + \\ & + b_N T_N(x). \end{aligned} \tag{2.21}$$

In this sum, the "diagonal" (same colored) terms cancel as a consequence of Eq. (2.19): if one collects the terms corresponding to $T_0(x)$ and $T_1(x)$ and recalls that $T_0(x) = 1$ and $T_1(x) = x$, one finds

$$\begin{aligned} f(x) = \sum_{i=0}^{N} c_i T_i(x) = & \\ = b_0 T_0(x) - 2xb_1 T_0(x) + b_1 T_1(x) = & \\ = b_0 - 2xb_1 + b_1 x = & \\ = b_0 - xb_1. & \end{aligned} \tag{2.22}$$

Thus, there is no need to compute the Chebyshev polynomials $T_i(x)$ explicitly. Elegant, computationally efficient, and stable against round-off errors, Clenshaw's recurrence is a robust method for evaluating Chebyshev series, as stated in Ref. [50]:

> You need to be aware that recurrence relations are not necessarily stable against roundoff error in the direction that you propose to go (either increasing n or decreasing n). [...] Clenshaw's recurrence is always stable, independent of whether the recurrence for the functions F_k [the functions appearing in the series] is stable in the upward or downward direction.

2.3 Generalization to multivariable functions

As long as a function is piecewise continuous in all its arguments, it is eligible for expansion in terms of Chebyshev polynomials. For functions of two (2V) and three (3V) variables, the expansions take the forms

$$f(x,y) = \sum_{i=0}^{\infty}\sum_{j=0}^{\infty} c_{ij}T_i(x)T_j(y) \tag{2.23}$$

and

$$f(x,y,z) = \sum_{i=0}^{\infty}\sum_{j=0}^{\infty}\sum_{k=0}^{\infty} c_{ijk}T_i(x)T_j(y)T_k(z) \tag{2.24}$$

respectively. Moreover, the coefficients in Eqs. (2.23) and (2.24) can be derived following procedures analogous to those described in Section 2.1.

- *2V*: consider a $[(N-1)\times(M-1)]$-th order expansion for $f(x,y)$

$$f(x,y) = \sum_{i=0}^{N-1}\sum_{j=0}^{M-1} c_{ij}T_i(x)T_j(y), \tag{2.25}$$

and, without loss of generality, evaluate f at the points $(\hat{x}_k, \hat{y}_l)$:

$$f(\hat{x}_k,\hat{y}_l) = \sum_{i=0}^{N-1}\sum_{j=0}^{M-1} c_{ij}T_i(\hat{x}_k)T_j(\hat{y}_l), \tag{2.26}$$

where $\hat{x}_k$ ($\hat{y}_l$) is the k-th (l-th) extremum of the N-th (M-th) order Chebyshev polynomial $T_N(x)$ ($T_M(y)$). Multiplying both sides of Eq. (2.26) by $T_r(\hat{x}_k)T_q(\hat{y}_l)$ and performing the altered sum over the indices k and l, we obtain

$$\begin{aligned}\sum_{k=0}^{N}{}'' \sum_{l=0}^{M}{}'' f(\hat{x}_k,\hat{y}_l)T_r(\hat{x}_k)T_q(\hat{y}_l) &= \sum_{i=0}^{N-1}\sum_{j=0}^{M-1} c_{ij}\sum_{k=0}^{N}{}''T_i(\hat{x}_k)T_r(\hat{x}_k)\sum_{l=0}^{M}{}''T_j(\hat{y}_l)T_q(\hat{y}_l) = \\ &\overset{(2.10)}{=} \sum_{i=0}^{N-1}\sum_{j=0}^{M-1} c_{ij}N\delta_{\frac{ir}{2}0}M\delta_{\frac{jq}{2}0} = \\ &\overset{(2.3)}{=} NMc_{rq}(\frac{1}{2}+\frac{1}{2}\delta_{r0})(\frac{1}{2}+\frac{1}{2}\delta_{q0}).\end{aligned} \tag{2.27}$$

From this, the coefficients are given by

$$c_{ij} = \frac{4}{NM(1+\delta_{i0})(1+\delta_{j0})} \sum_{k=0}^{N}{}'' \sum_{l=0}^{M}{}'' f(\hat{x}_k, \hat{y}_l) T_i(\hat{x}_k) T_j(\hat{y}_l). \tag{2.28}$$

Similarly, if we evaluate Eq. (2.26) at the zeros $\bar{x}_a$ and $\bar{y}_b$ of $T_N(x)$ and $T_M(y)$, we obtain

$$c_{ij} = A_{ij}(N,M) \sum_{k=1}^{N} \sum_{l=1}^{M} f(\bar{x}_k, \bar{y}_l) T_i(\bar{x}_k) T_j(\bar{y}_l), \tag{2.29}$$

with

$$A_{ij}(N,M) = \frac{4}{NM(1+\delta_{i0})(1+\delta_{j0})}. \tag{2.30}$$

For reasons that will be disclosed later in this manuscript, the more general integral projection method will not be discussed here.

- *3V*: in an analogous manner, approximating Eq. (2.24) with

$$f(x,y,z) = \sum_{i=0}^{N-1} \sum_{j=0}^{M-1} \sum_{k=0}^{L-1} c_{ijk} T_i(x) T_j(y) T_k(z), \tag{2.31}$$

and using the discrete orthogonality relations from Eq. (2.10), one finds

$$\sum_{a=0}^{N}{}'' \sum_{b=0}^{M}{}'' \sum_{c=0}^{L}{}'' f(\hat{x}_a, \hat{y}_b, \hat{z}_c) T_i(\hat{x}_a) T_j(\hat{y}_b) T_k(\hat{z}_c) = NMLc_{ijk}(\frac{1}{2}+\frac{1}{2}\delta_{i0})(\frac{1}{2}+\frac{1}{2}\delta_{j0})(\frac{1}{2}+\frac{1}{2}\delta_{k0}), \tag{2.32}$$

where $\hat{x}_a$, $\hat{y}_b$ and $\hat{z}_c$ are the extrema of $T_N(x)$, $T_M(y)$ and $T_L(z)$. Hence

$$c_{ijk} = A_{ijk}(N,M,L) \sum_{a=0}^{N}{}'' \sum_{b=0}^{M}{}'' \sum_{c=0}^{L}{}'' f(\hat{x}_a, \hat{y}_b, \hat{z}_c) T_i(\hat{x}_a) T_j(\hat{y}_b) T_k(\hat{z}_c), \tag{2.33}$$

with

$$A_{ijk}(N,M,L) = \frac{8}{NML(1+\delta_{i0})(1+\delta_{j0})(1+\delta_{k0})}. \tag{2.34}$$

An analogous expression can be derived using the zeros $\bar{x}_a$, $\bar{y}_b$ and $\bar{z}_c$ of $T_N(x)$, $T_M(y)$ and $T_L(z)$:

$$c_{ijk} = A_{ijk}(N,M,L) \sum_{a=1}^{N} \sum_{b=1}^{M} \sum_{c=1}^{L} f(\bar{x}_a, \bar{y}_b, \bar{z}_c) T_i(\bar{x}_a) T_j(\bar{y}_b) T_k(\bar{z}_c). \tag{2.35}$$

In summary, Chebyshev expansions are not limited to univariate (1V) functions; Clenshaw's recurrence can be generalized and applied to multivariate functions as well. For instance, if

$$f(x,y) = \sum_{i=0}^{N} \Big[\sum_{j=0}^{M} c_{ij} T_j(y) \Big] T_i(x) \tag{2.36}$$

is the Chebyshev approximation of a two-variable function, one can first apply Clenshaw's recurrence to the expression within the square brackets to compute a new set of coefficients $b_{i,(m)}$ from the c_{ij} (with i held fixed):

$$\forall i, \qquad b_{i,(m)} - 2yb_{i,(m+1)} + b_{i,(m+2)} = c_{im}, \qquad b_{i,(M+1)} = b_{i,(M+2)} = 0. \tag{2.37}$$

This yields $N + 1$ coefficients $g_i(y) = b_{i,(0)} - yb_{i,(1)}$, and Eq. (2.36) becomes

$$f(x, y) = \sum_{i=0}^{N} \Big[b_{i,(0)} - yb_{i,(1)} \Big] T_i(x) \equiv \sum_{i=0}^{N} g_i(y) T_i(x). \tag{2.38}$$

Finally, applying Clenshaw's recurrence to the coefficients $g_i(y)$ gives $f(x, y)$ evaluated at the desired x, y. From a numerical standpoint, if $f(x, y)$ must be evaluated multiple times at fixed values of y, the $N + 1$ coefficients $g_i(y)$ remain constant, thereby significantly reducing the computational cost. This iterative procedure can be naturally extended to functions of an arbitrary number of variables.

2.4 ChAppX: a code for Chebyshev approximations

Chebyshev polynomials are a powerful and flexible tool for approximating even complex and computationally demanding functions. Their advantages can be summarized as follows:

1. The coefficients c_i can be easily computed by exploiting the orthogonality relations of Chebyshev polynomials (see Sec. 2.1 or [49]).

2. A Chebyshev approximation closely resembles the minimax polynomial, that is, the polynomial with the smallest maximum deviation from the true function $f(x)$ among all polynomials of the same degree. However, unlike the exact minimax polynomial, its coefficients are readily computed.

3. The approximation error is distributed almost uniformly over the entire interval.

4. The magnitude of the first neglected Chebyshev coefficient provides a good estimate of the error. This follows from the property $T_n(x) = \cos(n \arccos x) \leq 1$.

5. For smooth functions, the Chebyshev expansion converges rapidly. This rapid convergence allows most of the function's information to be compressed in relatively few coefficients that can easily fit within a modern CPU cache. Indeed, as stated in Ref. [50]:

   > Any function that is bounded on the interval [of the Chebyshev polynomials] will have a convergent Chebyshev approximation as

> [the order] $N \to \infty$, even if there are nearby poles in the complex plane. For functions that are not infinitely smooth, the actual rate of convergence depends on the smoothness of the function: the more derivatives that are bounded, the greater the convergence rate. For the special case of a C^∞ function, the convergence is exponential.

6. Thanks to the recurrence relation in Eq.(2.1), a Chebyshev expansion can be efficiently evaluated using Clenshaw's recurrence formula [51]. This method computes the expanded function using only the coefficients c_i, without explicitly evaluating the Chebyshev polynomials $T_i(x)$. Moreover, Clenshaw's recurrence guarantees both computational efficiency and numerical stability against roundoff errors (see Sec.2.2).

7. A generic multivariable function $f(x, y)$ can be expanded as

$$f(x,y) \approx \sum_{i=0}^{N}\sum_{j=0}^{M} c_{ij}T_i(x)T_j(y). \tag{2.39}$$

   If $f(x, y)$ is to be evaluated repeatedly, for example, at several different x values while y remains fixed, the computational cost can be significantly reduced. In fact, Eq. (2.39) can be rewritten as

$$f(x,y) \approx \sum_{i=0}^{N}\left[\sum_{j=0}^{M} c_{ij}T_j(y)\right]T_i(x) = \sum_{i=0}^{N} d_i(y)T_i(x). \tag{2.40}$$

   Here, Clenshaw's recurrence is first used to compute the $N + 1$ coefficients $d_i(y)$. Then it is applied again to evaluate the function in x using these coefficients. After this initial computation, evaluating the function for any x with the same y is reduced to that of a single-variable function with $N + 1$ coefficients (instead of a two-variable function with $(N+1)\times(M+1)$ coefficients). This is especially beneficial when using root-finding routines.

All these features form the foundation of the independent software `ChAppX`, which is described in detail in the remainder of this chapter. Instrumental to the realization of `SFQEDtoolkit`, `ChAppX` not only identifies the Chebyshev coefficients for generic functions of one, two, or three variables, but it is also equipped with a heuristic "stopping" algorithm that guarantees the resulting approximation meets a user-specified accuracy. This section is divided into three parts, each outlining a different set of coefficient-finding routines based on the number of arguments required to evaluate the function. The discussion on "stopping strategies" is deferred until the end of the chapter. As mentioned earlier, `ChAppX` is limited to functions with up to three variables, since generalizations of Clenshaw's recurrence formula for functions with more than three variables tend to be highly inefficient. Moreover, a large number of coefficients is required to approximate multivariate functions.

2.4.1 One-variable function approximation

In ChAppX, the extraction of the c_i coefficients in Eq. (2.6) is implemented in two distinct modes: *direct* and *iterated*.

Direct mode

In direct mode, the user must specify an integer N, representing the approximation order plus one. This tells the software to compute all corresponding coefficients from c_0 to c_{N-1}. Direct mode supports three routines for calculating the c_i sequence, mirroring the methods discussed in Section 2.1: the *extrema* approach (Eq.(2.13)), the *zeroes* approach (Eq.(2.14)), and the *projections* approach (Eq. (2.15)).

- In the *extrema* method, the coefficients c_i are obtained using a slightly modified version of formula (2.13). Here, expression (2.9) is employed within (2.5) to accelerate the computation and then substituted into (2.13), yielding

$$c_i = \frac{2}{N(1+\delta_{i0})} \sum_{k=0}^{N}{}'' f\Big(\cos\Big(\frac{k\pi}{N}\Big)\Big) \cos\Big(\frac{ik\pi}{N}\Big). \tag{2.41}$$

  This formula can be easily translated into code, enabling efficient computation of the coefficients.

- The same technique is applied to Eq. (2.14) for the *zeroes* case, which then becomes

$$c_i = \frac{2}{N(1+\delta_{i0})} \sum_{k=1}^{N} f\Big(\cos\Big(\frac{\pi(2k-1)}{2N}\Big)\Big) \cos\Big(\frac{i\pi(2k-1)}{2N}\Big). \tag{2.42}$$

- Similarly, by substituting the integration variable with $x = \cos(\theta)$ in Eq. (2.15), the coefficients for the *projections* method are given by

$$c_i = \frac{2}{\pi(1+\delta_{i0})} \int_0^{\pi} f(\cos(\theta)) \cos(i\theta) d\theta. \tag{2.43}$$

Numerically, Eqs.(2.41) and (2.42) compute the coefficients using a finite number of function evaluations, specifically at the extrema or zeroes, whereas Eq.(2.43) (the projection method) depends heavily on the chosen quadrature scheme for evaluating the integrals. It is worth noting that when the coefficients corresponding to a specific approximation order are computed as sums of products, as in Eqs. (2.41) and (2.42), the attainable accuracy[2] is limited by the machine epsilon, given by

[2] In our computational context, "accuracy" refers to the relative difference between the numerical and the exact value of a quantity.

$\varepsilon = 2^{n-52}$, where 2^n is the binary order of magnitude of the largest term in the sum, and 52 is the number of bits in the mantissa for double-precision numbers. This results in very small uncertainties[3]. In contrast, to ensure the convergence of the integral in the projection method (2.43)−which, by its nature, always yields the "exact" coefficients−the absolute and relative error tolerances must be set several orders of magnitude above the machine epsilon. These considerations led us to favor the extrema and zeroes methods over the projection method.

Iterated mode

The iterated version operates using two integers, N and `max_iterations`, along with a double-precision floating-point number, `threshold`. In this mode, `ChAppX` begins by sequentially invoking the direct method described earlier, first with 2^N and then with 2^{N+1} as its argument. This yields the coefficients corresponding to the $(2^N - 1)$-th and $(2^{N+1} - 1)$-th order approximations, respectively. These two sets of coefficients are then compared according to the stopping strategy (see Sec. 2.4.3), producing the quantity `difference`. If `difference` < `threshold`, the process terminates. Otherwise, it continues: the coefficients for the $(2^{N+2} - 1)$-th order are computed and new `difference` is obtained by comparing the $(2^{N+1} - 1)$-th and $(2^{N+2} - 1)$-th order coefficients. This loop repeats for up to `max_iterations` times[4].

The procedure used to compute the coefficients in each new iteration depends on whether the extrema, zeroes, or projection approach is employed.

- The 1V iterated mode proves to be exceptionally intriguing when employed alongside the extrema method, where eq. (2.13)

$$c_{i,(n-1)} = \frac{2}{n(1+\delta_{i0})} \sum_{k=0}^{n}{}'' f(\hat{x}_{k,n}) T_i(\hat{x}_{k,n}) \tag{2.44}$$

  determines the $(n-1)$−th order coefficients. For clarity of notation, a second subscript index has been introduced to indicate the approximation order of the coefficient set. Similarly, $\hat{x}_{k,n}$ will denote one of the $n+1$ extrema, given by

$$\hat{x}_{k,n} = \cos\Big(\frac{k\pi}{n}\Big), \qquad k = 0, ..., n, \tag{2.45}$$

  of the n-th Chebyshev polynomial $T_n(x)$.

  Let us consider the extrema corresponding to the 2^s-th

$$\hat{x}_{l,2^s} = \cos\Big(\frac{l\pi}{2^s}\Big), \qquad l = 0, ..., 2^s \tag{2.46}$$

[3]Here, we refer to the uncertainties associated with calculating a function's Chebyshev coefficients for a finite-order polynomial expansion, rather than those inherent to the "exact" order expansion.

[4]The default value is 2, and it cannot be set lower.

and 2^{s+1}-th Chebyshev polynomial

$$\hat{x}_{k,2^{s+1}} = \cos\Big(\frac{k\pi}{2^{s+1}}\Big), \qquad k = 0, ..., 2^{s+1}. \tag{2.47}$$

By splitting the latter into two subgroups: one for the *even* values of the index k

$$\hat{x}_{2l,2^{s+1}} = \cos\Big(\frac{2l\pi}{2^{s+1}}\Big) = \cos\Big(\frac{l\pi}{2^{s}}\Big) \equiv \hat{x}_{l,2^{s}}, \tag{2.48}$$

where we set $k = 2l$ (with $l = 0, ..., 2^s$), and one for the *odd* values of k

$$\hat{x}_{2l+1,2^{s+1}} = \cos\Big(\frac{(2l+1)\pi}{2^{s+1}}\Big), \tag{2.49}$$

this time with $k = 2l + 1$ ($l = 0, ..., 2^s - 1$), we notice that the even subset in Eq. (2.48) matches the entire set of extrema in Eq. (2.46). This in turn means that the $2^s + 1$ extrema used in the computation of the Chebyshev coefficients, corresponding to the $(2^s - 1)$-th order approximation, can be entirely reused for calculating the coefficients of the $(2^{s+1} - 1)$-th. By writing the expressions for the coefficients $c_{i,2^s-1}$

$$c_{i,2^s-1} = \frac{2}{2^s(1+\delta_{i0})} \sum_{k=0}^{2^s}{}'' f(\hat{x}_{k,2^s}) T_i(\hat{x}_{k,2^s}), \quad i = 0, ..., 2^s - 1 \tag{2.50}$$

and $c_{j,2^{s+1}-1}$

$$c_{j,2^{s+1}-1} = \frac{2}{2^{s+1}(1+\delta_{i0})} \sum_{k=0}^{2^{s+1}}{}'' f(\hat{x}_{k,2^{s+1}}) T_j(\hat{x}_{k,2^{s+1}}), \quad j = 0, ..., 2^{s+1} - 1, \tag{2.51}$$

we could split the altered summation in (2.51) into its even/odd parts[5], as we did before, yielding

$$\begin{aligned} c_{j,2^{s+1}-1} &= \frac{2}{2^{s+1}(1+\delta_{j0})} \sum_{k=0}^{2^{s+1}}{}'' f(\hat{x}_{k,2^{s+1}}) T_j(\hat{x}_{k,2^{s+1}}) = \\ &= \frac{2}{2^{s+1}(1+\delta_{j0})} \Bigg[\sum_{l=0}^{2^s}{}'' f(\hat{x}_{2l,2^{s+1}}) T_j(\hat{x}_{2l,2^{s+1}}) + \sum_{l=0}^{2^s-1} f(\hat{x}_{2l+1,2^{s+1}}) T_j(\hat{x}_{2l+1,2^{s+1}}) \Bigg] = \\ &\overset{(2.48)}{=} \frac{2}{2^{s+1}(1+\delta_{j0})} \Bigg[\sum_{l=0}^{2^s}{}'' f(\hat{x}_{l,2^{s}}) T_j(\hat{x}_{l,2^{s}}) + \sum_{l=0}^{2^s-1} f(\hat{x}_{2l+1,2^{s+1}}) T_j(\hat{x}_{2l+1,2^{s+1}}) \Bigg] = \\ &\overset{(2.50)}{=} \frac{1}{2} c_{j,2^s-1} + \frac{2}{2^{s+1}(1+\delta_{j0})} \sum_{l=0}^{2^s-1} f(\hat{x}_{2l+1,2^{s+1}}) T_j(\hat{x}_{2l+1,2^{s+1}}) \end{aligned} \tag{2.52}$$

[5]Since the altered sum requires only the first ($k = 0$) and last ($k = 2^{s+1}$) index terms to be halved, the *alteration* will exclusively be inherited by the even part after the splitting.

for $j = 0, ..., 2^s - 1$. This means that all the coefficients belonging to the $(2^s - 1)$-th order Chebyshev approximation can be reused to compute the first 2^s coefficients associated to the new $(2^{s+1}-1)$-th order, thus substantially affecting the time complexity of our algorithm.

- Unfortunately, a similar trick does not work for the zeros and projection approaches. In these methods, every iteration forces the direct routine to be called with an increasingly larger argument. Moreover, as noted earlier, the projection method consistently returns the exact coefficients (aside from minor numerical deviations): the i-th iteration does not add any new information to the coefficients computed in the $(i-1)$-th, and hence no corrections are needed. Each new step simply computes the missing coefficients, leaving those computed before unaltered. The projection method will not be discussed any further.

The identity derived in Eq. (2.52) is not unexpected: when transitioning from one approximation order (2^N) to the next (2^{N+1}), some extrema remain unchanged. As a result, a subset of the new coefficients can be directly obtained from the previous ones, requiring only minor corrections. This property, which we will refer to as the *extrema trick*, extends naturally to two-, three-, and even multi-variable cases, proving useful in section 2.4.2.

Finally, the precise method for computing the variable `difference` mentioned earlier remains to be defined, a discussion we defer to section 2.4.4.

2.4.2 Two- and three-variables function approximation

The coefficient-finding routines in `ChAppX` for 2V and 3V functions closely mirror their 1V counterparts. Not only are they implemented in the same direct and iterated modes described in Sec. 2.4.1, but they also operate in an almost identical manner, with the only distinction arising from the increased "dimensionality" of the problem. In these cases, the array of Chebyshev coefficients c_i extends to a two- or three-dimensional matrix, c_{ij} for 2V functions and c_{ijk} for 3V functions. Accordingly, the code replaces the 1V formulas (2.41) and (2.42) with their higher-dimensional counterparts:

$$c_{ij} = A_{ij}(N, M) \sum_{k=0}^{N}{}'' \sum_{l=0}^{M}{}'' f\Big(\cos\Big(\frac{k\pi}{N}\Big), \cos\Big(\frac{l\pi}{M}\Big)\Big) \cos\Big(\frac{ik\pi}{N}\Big) \cos\Big(\frac{jl\pi}{M}\Big) \tag{2.53}$$

and

$$c_{ij} = A_{ij}(N, M) \sum_{k=1}^{N} \sum_{l=1}^{M} f\Big(\cos\Big(\frac{\pi(2k-1)}{2N}\Big), \cos\Big(\frac{\pi(2l-1)}{2M}\Big)\Big) \cos\Big(\frac{i\pi(2k-1)}{2N}\Big) \cos\Big(\frac{j\pi(2l-1)}{2M}\Big) \tag{2.54}$$

for 2V functions, while uses

$$c_{ijk} = A_{ijk}(N, M, L) \sum_{n=0}^{N}{}'' \sum_{m=0}^{M}{}'' \sum_{l=0}^{L}{}'' f\Big(\cos\Big(\frac{n\pi}{N}\Big), \cos\Big(\frac{n\pi}{M}\Big), \cos\Big(\frac{l\pi}{L}\Big)\Big) \cos\Big(\frac{in\pi}{N}\Big) \cos\Big(\frac{jm\pi}{M}\Big) \cos\Big(\frac{kl\pi}{L}\Big) \tag{2.55}$$

and

$$c_{ijk} = A_{ijk}(N, M, L) \sum_{n=1}^{N} \sum_{m=1}^{M} \sum_{l=1}^{L} f\Big(\cos\Big(\frac{\pi(2n-1)}{2N}\Big), \cos\Big(\frac{\pi(2m-1)}{2M}\Big), \cos\Big(\frac{\pi(2l-1)}{2L}\Big)\Big) \times \\ \times \cos\Big(\frac{i\pi(2n-1)}{2N}\Big) \cos\Big(\frac{j\pi(2m-1)}{2M}\Big) \cos\Big(\frac{k\pi(2l-1)}{2L}\Big) \tag{2.56}$$

when dealing with 3V functions. As mentioned at the end of Sec. 2.4.1, an analogue of Eq. (2.43) is not available here. In addition to the reasons stated earlier, the projection method becomes computationally impractical when multiple numerical integrations are required. As a result, it has not been implemented in either the 2V or 3V Chebyshev approximators.

The 2V and 3V coefficient-finding algorithms incorporate the extrema trick as well, just as in the 1V case, allowing the 2V and 3V code to run in iterated mode. The extension of this trick to functions of two and three variables is discussed in the following sections.

The extrema trick for 2V functions

We begin by rewriting Eq. (2.28) as

$$c_{ij,(N-1,M-1)} = A_{ij}(N, M) \sum_{k=0}^{N}{}'' \sum_{l=0}^{M}{}'' f(\hat{x}_{k,N}, \hat{y}_{l,M}) T_i(\hat{x}_{k,N}) T_j(\hat{y}_{l,M}), \tag{2.57}$$

explicitly showing the dependence on the two approximation orders, $(N-1)$ and $(M-1)$, in both the coefficients ($c_{ij,(N-1,M-1)}$) and the extrema ($\hat{x}_{k,N}, \hat{y}_{l,M}$). This effectively reinstates the same notation introduced in Sec. 2.4.1. As in the 1V case, we assume $N = 2^s$ and $M = 2^t$ to be powers of two. By leveraging the properties of the extrema given in Eqs. (2.48) and (2.49), we can express $c_{ij,(2^{s+1}-1,2^{t+1}-1)}$ in terms of $c_{ij,(2^s-1,2^t-1)}$. However, unlike the 1V case, increasing the approximation order in 2V can be done in three distinct ways, each of which must be considered separately.

- $N = 2^s \to N' = 2^{s+1}$ but same M:

  $c_{ij,(2^{s+1}-1,M-1)} =$

$$
\begin{aligned}
&= A_{ij}(2^{s+1}, M) \sum_{k=0}^{2^{s+1}}{}'' \sum_{l=0}^{M}{}'' f(\hat{x}_{k,2^{s+1}}, \hat{y}_{l,M}) T_i(\hat{x}_{k,2^{s+1}}) T_j(\hat{y}_{l,M}) = \\
&\overset{split}{=} A_{ij}(2^{s+1}, M) \Bigg[\sum_{k'=0}^{2^s}{}'' \sum_{l=0}^{M}{}'' f(\hat{x}_{2k',2^{s+1}}, \hat{y}_{l,M}) T_i(\hat{x}_{2k',2^{s+1}}) T_j(\hat{y}_{l,M}) + \\
&\qquad + \sum_{k'=0}^{2^s-1} \sum_{l=0}^{M}{}'' f(\hat{x}_{2k'+1,2^{s+1}}, \hat{y}_{l,M}) T_i(\hat{x}_{2k'+1,2^{s+1}}) T_j(\hat{y}_{l,M}) \Bigg] = \\
&\overset{(2.48)}{=} \frac{1}{2} c_{ij,2^s-1,M-1} + \\
&\qquad + A_{ij}(2^{s+1}, M) \sum_{k'=0}^{2^s-1} \sum_{l=0}^{M}{}'' f(\hat{x}_{2k'+1,2^{s+1}}, \hat{y}_{l,M}) T_i(\hat{x}_{2k'+1,2^{s+1}}) T_j(\hat{y}_{l,M})
\end{aligned}
\tag{2.58}
$$

- same N but $M = 2^t \to M' = 2^{t+1}$: the derivation is symmetric to the one right above, so that we end up with

$$
\begin{aligned}
&c_{ij,(N-1,2^{t+1}-1)} = \\
&\quad = \frac{1}{2} c_{ij,(N-1,2^t-1)} + \\
&\qquad + A_{ij}(N, 2^{t+1}) \sum_{k=0}^{N}{}'' \sum_{l'=0}^{2^t-1} f(\hat{x}_{k,N}, \hat{y}_{2l'+1,2^{s+1}}) T_i(\hat{x}_{k,N}) T_j(\hat{y}_{2l'+1,2^{t+1}}).
\end{aligned}
\tag{2.59}
$$

- $N = 2^s \to N' = 2^{s+1}$ and $M = 2^t \to M' = 2^{t+1}$:

$$
\begin{aligned}
&c_{ij,(2^{s+1}-1,2^{t+1}-1)} = \\
&\quad = A_{ij}(2^{s+1}, 2^{t+1}) \sum_{k=0}^{2^{s+1}}{}'' \sum_{l=0}^{2^{t+1}}{}'' f(\hat{x}_{k,2^{s+1}}, \hat{y}_{l,2^{t+1}}) T_i(\hat{x}_{k,2^{s+1}}) T_j(\hat{y}_{l,2^{t+1}}) = \\
&\overset{split(k)}{=} A_{ij}(2^{s+1}, 2^{t+1}) \Bigg[\sum_{k'=0}^{2^s}{}'' \sum_{l=0}^{2^{t+1}}{}'' f(\hat{x}_{2k',2^{s+1}}, \hat{y}_{l,2^{t+1}}) T_i(\hat{x}_{2k',2^{s+1}})] T_j(\hat{y}_{l,2^{t+1}}) + \\
&\qquad + \sum_{k'=0}^{2^s-1} \sum_{l=0}^{2^{t+1}}{}'' f[\hat{x}_{2k'+1,2^{s+1}}, \hat{y}_{l,2^{t+1}}) T_i(\hat{x}_{2k'+1,2^{s+1}}) T_j(\hat{y}_{l,2^{t+1}}) \Bigg] = \\
&\overset{split(l)}{=} A_{ij}(2^{s+1}, 2^{t+1}) \Bigg[\sum_{k'=0}^{2^s}{}'' \sum_{l'=0}^{2^t}{}'' f[\hat{x}_{2k',2^{s+1}}, \hat{y}_{2l',2^{t+1}}) T_i(\hat{x}_{2k',2^{s+1}}) T_j(\hat{y}_{2l',2^{t+1}}) + \\
&\qquad + \sum_{k'=0}^{2^s}{}'' \sum_{l'=0}^{2^t-1} f(\hat{x}_{2k',2^{s+1}}, \hat{y}_{2l'+1,2^{t+1}}) T_i(\hat{x}_{2k',2^{s+1}}) T_j(\hat{y}_{2l'+1,2^{t+1}}) +
\end{aligned}
$$

$$+\sum_{k'=0}^{2^s-1}\sum_{l'=0}^{2^t}{}''f(\hat{x}_{2k'+1,2^{s+1}},\hat{y}_{2l',2^{t+1}})T_i(\hat{x}_{2k'+1,2^{s+1}})T_j(\hat{y}_{2l',2^{t+1}})+$$
$$+\sum_{k'=0}^{2^s-1}\sum_{l'=0}^{2^t-1}f(\hat{x}_{2k'+1,2^{s+1}},\hat{y}_{2l'+1,2^{t+1}})T_i(\hat{x}_{2k'+1,2^{s+1}})T_j(\hat{y}_{2l'+1,2^{t+1}})\Bigg] =$$
$$\overset{(2.48)}{=}\frac{1}{4}c_{ij,(2^s-1,2^t-1)}+A_{ij}(2^{s+1},2^{t+1})\times$$
$$\times\Bigg[\sum_{k'=0}^{2^s}{}''\sum_{l'=0}^{2^t-1}f(\hat{x}_{k',2^s},\hat{y}_{2l'+1,2^{t+1}})T_i(\hat{x}_{k',2^s})T_j(\hat{y}_{2l'+1,2^{t+1}})+$$
$$+\sum_{k'=0}^{2^s-1}\sum_{l'=0}^{2^t}{}''f(\hat{x}_{2k'+1,2^{s+1}},\hat{y}_{l',2^t})T_i(\hat{x}_{2k'+1,2^{s+1}})T_j(\hat{y}_{l',2^t})+$$
$$+\sum_{k'=0}^{2^s-1}\sum_{l'=0}^{2^t-1}f(\hat{x}_{2k'+1,2^{s+1}},\hat{y}_{2l'+1,2^{t+1}})T_i(\hat{x}_{2k'+1,2^{s+1}})T_j(\hat{y}_{2l'+1,2^{t+1}})\Bigg]. \tag{2.60}$$

Eq.s (2.58), (2.59) and (2.60) could be condensed into the more general form

$$c_{ij,(N'-1,M'-1)}=\frac{1}{(2-\delta_{N'N})(2-\delta_{M'M})}c_{ij,(N-1,M-1)}+A_{ij}(N',M')\times$$
$$\times\Bigg[(1-\delta_{M'M})\sum_{k'=0}^{N}{}''\sum_{l'=0}^{M-1}f(\hat{x}_{k',N},\hat{y}_{2l'+1,M'})T_i(\hat{x}_{k',N})T_j(\hat{y}_{2l'+1,M'})+$$
$$+(1-\delta_{N'N})\sum_{k'=0}^{N-1}\sum_{l'=0}^{M}{}''f(\hat{x}_{2k'+1,N'},\hat{y}_{l',M})T_i(\hat{x}_{2k'+1,N'})T_j(\hat{y}_{l',M})+$$
$$+(1-\delta_{N'N})(1-\delta_{M'M})\sum_{k'=0}^{N-1}\sum_{l'=0}^{M-1}f(\hat{x}_{2k'+1,N'},\hat{y}_{2l'+1,M'})T_i(\hat{x}_{2k'+1,N'})T_j(\hat{y}_{2l'+1,M'})\Bigg]. \tag{2.61}$$

Here, N and N' are powers of 2 such that either $N'=N$ or $N'=2N$; the same relationship holds for M and M'. As in the 1V case, the trick only applies to the indices $i=0,...,2^s-1$ and $j=0,...,2^t-1$, meaning that i and j must lie within the range of the previous order.

The extrema trick for 3V functions

In the 3V iterated mode implemented in `ChAppX`, the extrema trick is used to express the 3V Chebyshev coefficients $c_{ijk,(N'-1,M'-1,L'-1)}$ in terms of $c_{ijk,(N-1,M-1,L-1)}$. This trick is based on arguments similar to those leading to Eq. (2.61), also the notation employed here is the natural extension of that used to write Eq. (2.61), and holds when the primed and unprimed orders are related by $(N',M',L')=$

$(2^a N, 2^b M, 2^c L)$, with $a, b, c \in (0, 1)$. Without delving into the (excessively cumbersome) details, the final algorithm is as follows:

$$
\begin{aligned}
c_{ijk,(N'-1,M'-1,L'-1)} = {} & \frac{1}{(2-\delta_{N'N})(2-\delta_{M'M})(2-\delta_{L'L})} c_{ijk,(N-1,M-1,L-1)} + \\
& + A_{ijk}(N', M', L') \times \\
& \times \Bigg[H_{M'M} \sum_{a'=0}^{N}{}'' \sum_{b'=0}^{M-1} \sum_{c'=0}^{L}{}'' f(\hat{x}_{a',N}, \hat{y}_{2b'+1,M'}, \hat{z}_{c',L}) T_i(\hat{x}_{a',N}) T_j(\hat{y}_{2b'+1,M'}) T_k(\hat{z}_{c',L}) + \\
& \quad + H_{N'N} \sum_{a'=0}^{N-1} \sum_{b'=0}^{M}{}'' \sum_{c'=0}^{L}{}'' f(\hat{x}_{2a'+1,N'}, \hat{y}_{b',M}, \hat{z}_{c',L}) T_i(\hat{x}_{2a'+1,N'}) T_j(\hat{y}_{b',M}) T_k(\hat{z}_{c',L}) + \\
& \quad + H_{L'L} \sum_{a'=0}^{N}{}'' \sum_{b'=0}^{M}{}'' \sum_{c'=0}^{L-1} f(\hat{x}_{a',N}, \hat{y}_{b',M}, \hat{z}_{2c'+1,L'}) T_i(\hat{x}_{a',N}) T_j(\hat{y}_{b',M}) T_k(\hat{z}_{2c'+1,L'}) + \\
& + H_{N'N} H_{M'M} \sum_{a'=0}^{N-1} \sum_{b'=0}^{M-1} \sum_{c'=0}^{L}{}'' f(\hat{x}_{2a'+1,N'}, \hat{y}_{2b'+1,M'}, \hat{z}_{c',L}) T_i(\hat{x}_{2a'+1,N'}) T_j(\hat{y}_{2b'+1,M'}) T_k(\hat{z}_{c',L}) + \\
& + H_{N'N} H_{L'L} \sum_{a'=0}^{N-1} \sum_{b'=0}^{M}{}'' \sum_{c'=0}^{L-1} f(\hat{x}_{2a'+1,N'}, \hat{y}_{b',M}, \hat{z}_{2c'+1,L'}) T_i(\hat{x}_{2a'+1,N'}) T_j(\hat{y}_{b',M}) T_k(\hat{z}_{2c'+1,L'}) + \\
& + H_{M'M} H_{L'L} \sum_{a'=0}^{N}{}'' \sum_{b'=0}^{M-1} \sum_{c'=0}^{L-1} f(\hat{x}_{a',N}, \hat{y}_{2b'+1,M'}, \hat{z}_{2c'+1,L'}) T_i(\hat{x}_{a',N}) T_j(\hat{y}_{2b'+1,M'}) T_k(\hat{z}_{2c'+1,L'}) + \\
& + H_{N'N} H_{M'M} H_{L'L} \sum_{a'=0}^{N-1} \sum_{b'=0}^{M-1} \sum_{c'=0}^{L-1} f(\hat{x}_{2a'+1,N'}, \hat{y}_{2b'+1,M'}, \hat{z}_{2c'+1,L'}) T_i(\hat{x}_{2a'+1,N'}) T_j(\hat{y}_{2b'+1,M'}) T_k(\hat{z}_{2c'+1,L'}) \Bigg],
\end{aligned}
\tag{2.62}
$$

where

$$
H_{ij} = (1 - \delta_{ij}). \tag{2.63}
$$

2.4.3 Stopping strategy: how to stop the iterated version?

The following sections are devoted to describing the *stopping strategy* (StSt) currently implemented in the code. As an auxiliary component of `ChAppX`, the StSt adaptively compares two consecutive sets of coefficients generated by the iterated modes (see Secs. 2.4.1 and 2.4.2) to determine when to halt the calculation. This approach guarantees that the code achieves high accuracies, with errors ranging between $10^{-3}\%$ and $10^{-13}\%$. While various algorithms could be devised for this comparison, we focus on schemes that yield a parameter, already denoted as `difference` in sec. 2.4.1, which quantifies the improvement in accuracy obtained by increasing the approximation order.

Below, we present three preliminary considerations that will be useful before outlining the actual StSt implemented in the code. In the following discussion, the

iteration I that a given set of coefficients corresponds to will be indicated in square brackets. For example, for one-variable functions we denote the coefficients as $c_i[I]$ and $c_i[I+1]$; for two-variable functions, we use $c_{ij}[I]$ and $c_{ij}[I+1]$[6]. Designing an effective stopping strategy is not as straightforward as it might seem; ultimately, selecting the optimal approach involves both mathematical considerations and numerical performance issues.

1^{st} consideration

Suppose we have computed the approximation order $\bar{O} = 2^{\bar{N}} - 1$, and obtained all its corresponding coefficients. If we set $\bar{N}$ to be the largest representable integer, our approximation cannot be improved further, litterally: our coefficients would be determined with the maximum precision allowed by the machine. At this point, by predicting the behavior of the target function, we could disregard all Chebyshev coefficients beyond the point where they become "sufficiently small". For example, consider the Taylor expansion of the sine function,

$$\sin(x) = \sum_{i=0}^{\infty} \frac{(-1)^i}{(2i+1)!} x^{2i+1}. \tag{2.64}$$

Notice that the coefficients drop below the $(n = 0)$-th order machine epsilon (i.e., 2^{0-52}) after only 9 terms (since $\frac{1}{(2\cdot 9+1)!} < 2^{-52}$), meaning that the contribution of terms beyond the ninth becomes negligible. Therefore, instead of iteratively computing successive approximation orders until the desired accuracy is reached, we could, in principle, compute the optimal approximation in one step, using for example the projection method (despite all its drawbacks), and store only the necessary coefficients. This approach would reduce both time and space complexity.

2^{nd} consideration

In Section 2.4.1 we introduced the parameter `difference` and its underlying concept. But what if we prescribe an entire array of such values? Denoting this array by $\texttt{difference}_i$, a naive definition for its i-th component is

$$\texttt{difference}_i = c_i[I+1] - c_i[I], \tag{2.65}$$

which represents the difference between the i-th coefficients of two successive approximations. However, Eq. (2.65) is sensitive to the machine epsilon discussed

[6]For simplicity, we have abandoned the notation previously used, which explicitly specified the approximation orders in the coefficients, in favor of a more compact representation that emphasizes the iteration steps. Nonetheless, note that in iterated mode, the approximation orders for successive iterations are related by: iteration : $I \to$ order : $2^N - 1$ and iteration : $I+1 \to$ order : $2^{N+1} - 1$.

earlier, as it strongly depends on the magnitude of the coefficients. To mitigate this sensitivity, one might instead use a normalized difference:

$$\texttt{difference}_i = \frac{c_i[I+1] - c_i[I]}{c_i[I+1]}. \tag{2.66}$$

Yet, if a coefficient (say, the n-th) is expected to be zero, then (due to numerical precision) it might end up being on the same order of the machine epsilon (e.g. $c_n[I] \approx 2^{-52}$). In such cases, Eq. (2.66) could yield an artificially large value (e.g. $\texttt{difference}_n \approx 1$), and if $c_n[I+1] = 0$, it would result in a division by zero.

For the time being, let us set aside these complications. Regardless of the specific method used to compute $\texttt{difference}_i$, we can compare each element of this array to a predefined threshold, denoted by `threshold` (also mentioned in Section 2.4.1), and decide to stop the iterated algorithm when

$$\texttt{difference}_i < \texttt{threshold} \quad \forall\ i. \tag{2.67}$$

At that point, one might retain only those coefficients $c_i[I+1]$ that satisfy

$$c_i[I+1] > \texttt{threshold}, \tag{2.68}$$

discarding all coefficients beyond the first index $\bar{i}$ (in ascending order) for which $c_{\bar{i}}[I+1] < \texttt{threshold}$. If condition (2.67) is not met, the algorithm computes the next iteration $I+2$ and the process repeats.

3rd consideration

Suppose our 2V iterated mode is approximating a function $f(x, y)$, so that at each iteration I we obtain a two-dimensional matrix of coefficients $c_{ij}[I]$. It is natural to generalize the 1V definitions of $\texttt{difference}_i$ (Eqs. (2.65) and (2.66)) to two dimensions:

$$\texttt{difference}_{ij} = \begin{cases} c_{ij}[I+1] - c_{ij}[I] \\ \\ \frac{c_{ij}[I+1] - c_{ij}[I]}{c_{ij}[I+1]} \end{cases}. \tag{2.69}$$

One might then evaluate the condition $\texttt{difference}_{ij} < \texttt{threshold}$ for all i and j. However, it is not immediately clear how to determine which coefficients to retain. In the 1V case, we processed the coefficients by ascending index order, but this time we have both a row- and column-order (or equivalently an i- or j-direction). One option is to apply the 1V procedure separately to each of the N rows and M columns. We could then form a *row-ensemble* and a *column-ensemble* from the resulting subsets, and finally construct a submatrix $c_{\bar{i}\bar{j}}[I+1]$ (where $\bar{i} < N$ and $\bar{j} < M$) by selecting the coefficients that belong to both ensembles.

Alternatively, we could view the matrix in Eq. (2.69) as a discrete surface and use methods from multivariate calculus to assess its flatness. If the surface exhibits a particularly steep slope along one direction (either i or j), we would then increase the corresponding approximation order in the next iteration. Recall that 2V coefficient-finding routines require two approximation orders, N and M, one for each variable. These orders correspond directly to the number of rows and columns in the coefficient matrix c_{ij}. In any case, this idea can be reduced to the 1V case, where Eqs. (2.65) or (2.66) describe a curve whose behavior can be analyzed by computing discrete derivatives. Specifically, we can outline the following StSt: after computing $\texttt{difference}_i$ using either Eq. (2.65) or Eq. (2.66), we calculate the discrete derivative

$$d_i = \frac{\texttt{difference}_{i+1} - \texttt{difference}_i}{(i+1) - i}, \tag{2.70}$$

and use `threshold` as an upper bound on the slope of this curve. Proceeding in ascending order, if there exists an index $i = \bar{i}$ such that $d_{\bar{i}} > \texttt{threshold}$ and $c_{\bar{i}}[I+1] < \texttt{threshold}$, then the process stops and only the first $\bar{i}$ coefficients are retained; otherwise, the iteration continues.

However, one can readily imagine a scenario where this approach fails. For instance, if all the c_i change by the same amount between iterations, the $\texttt{difference}_i$ curve would appear perfectly flat, even though every coefficients have changed significantly: if the coefficients change too much in a single iteration, it clearly indicates that there is still room for improvement and that the algorithm must continue. This suggests that further examination of the coefficients and their relative differences is needed.

2.4.4 Implemented stopping strategy

In light of the previous discussion, we now present the definitive version of the StSts implemented in `ChAppX`. What follows is a list of variables that the 1V and 2V algorithms either expect as input arguments or define internally.

- `thr_num` and `thr_qual` are both double-precision numbers representing two distinct thresholds. The first, `thr_num`, defines the value below which computed Chebyshev coefficients are considered negligible. The second, `thr_qual`, determines whether the relative change in a coefficient from one iteration to the next is small enough to halt the algorithm. Both thresholds must be positive; otherwise, an error is raised.[7]

- $\texttt{i}_{start}$, $\bar{i}$, and $i^\star$ are local integer variables initialized as $\texttt{i}_{start} = 0$, $\bar{i} = -1$, and $i^\star = -1$. These serve as checkpoints or temporary buffers, marking key indices where constraints begin to be checked.

[7] For added flexibility, if $\texttt{thr\_num} < 0$, the algorithm automatically sets $\texttt{thr\_num} = \texttt{thr\_qual}$.

- N, frequently encountered throughout, is an integer defining the approximation order $O = 2^N$. Initially, it is set to $N = 3$.
- $\texttt{EPS}_0$ represents the standard zero-order `machine_epsilon`, given by $\texttt{EPS}_0 = 2^{-52} \approx 10^{-16}$.
- To clarify which iteration a given coefficient set belongs to, we adopt the notation $c_i[last]$ for the most recently computed set and $c_i[prev]$ for the one immediately before it.
- If the iterated mode fails to converge, the keyword *FAIL* is used: this triggers N to increase by 1 ($N = N + 1$) and the process to restart from step 1.
- Lastly, `ChAppX` requires the user to specify the domain over which a 1V or 2V function should be approximated.

The flowcharts for the complete 1V and 2V iterated modes, including their StSts, are provided below. As the reader might soon notice, no StSt is available for the 3V iterated mode, which will never be used. As it will become clear in Chapter 3, handling 3V approximations is not only impractical but also severely impacts the performances.

1V version

0. As a preliminary step, the function is first approximated to order $O = 2^N$

$$f(x) = \sum_{a=0}^{2^N-1} c_a T_a(x).$$

   For the sake of clarity, note that the polynomial order of the approximation is actually $2^N - 1 = O - 1$. Once this initial approximation is obtained, N is incremented by 1 ($N = N + 1$), and the iterated mode loop begins.

1. The 2^N-order approximation is computed (again, its polynomial order is $2^N - 1$).

2. The first four coefficients from the latest iteration are combined into the variable

$$\texttt{f\_order} = \frac{|c_0[last]| + |c_1[last]| + |c_2[last]| + |c_3[last]|}{2}. \tag{2.71}$$

   This "staggered average" provides a reasonable estimate of the function's order of magnitude. The division by 2 (rather than 4) accounts for the expected oscillatory behavior of the coefficients when approximating periodic

functions, where a division by 4 would likely underestimate (2.71). Expression (2.71) is then used to compute the inner threshold:

$$\texttt{thr\_inn} = \texttt{f\_order} \cdot 250 \cdot \texttt{EPS}_0, \tag{2.72}$$

which will later help determine whether a coefficient is small enough to be considered negligible. The factor 250 is chosen ad hoc to accelerate the algorithm's convergence.

3. The coefficients $c_i[last]$, with indices in the range $\texttt{i}_{start} \leq i < \frac{2^N}{2}$, form what we define as *ARRAY* ($ARRAY_i = c_i[last], \forall\ i : \texttt{i}_{start} \leq i < \frac{2^N}{2}$)[8]. Next, the following quantitative condition is evaluated for all elements in *ARRAY*

$$|c_i[last]| < \texttt{thr\_num} : \tag{2.73}$$

the index of the *last ARRAY* component violating (2.73) is stored in $\bar{i}$. To ensure proper convergence, we require $\bar{i} \leq \frac{2^N}{2} - 2$; otherwise, the process *FAIL*s. If no such $\bar{i}$ is found, we distinguish between two cases: either every element in *ARRAY* satisfies (2.73), in which case we set $\bar{i} = \frac{2^N}{2} - 1$ and proceed to the next step, or the process *FAIL*s.

4. The *qualitative* conditions

$$\begin{cases} |c_i[last]| < \texttt{thr\_inn} \\ |c_i[last] - c_i[prev]| < \texttt{thr\_inn} \\ |\frac{c_i[last]-c_i[prev]}{c_i[last]}| < \texttt{thr\_qual} \end{cases} \tag{2.74}$$

are evaluated for $i : \texttt{i}_{start} \leq i \leq \bar{i}$. We define $i^\star$ as the smallest index among the coefficients that fail to meet any of the three conditions specified in (2.74). If no such $i^\star$ is found, then every coefficient is deemed valid, and the algorithm is considered a *SUCCESS*: it terminates, retaining the first $\bar{i}$ coefficients for the approximation. Otherwise, if $i^\star$ exists, we set $\texttt{i}_{start} = i^\star$ and the process *FAIL*s.

The current StSt operates under two key assumptions: the Chebyshev coefficients *i*) are monotonically decreasing, and *ii*) they reflect the approximated function's order of magnitude (as discussed above eq. (2.71)). Consequently, the absolute error ϵ_f of a Chebyshev approximation should correspond precisely to the magnitude of the first coefficient omitted from the expansion (2.6). Based on these assumptions, a user seeking an approximation for a function $f(x)$ should run `ChAppX`'s iterated mechanism with $\texttt{thr\_qual} = \epsilon_{\%}$ and $\texttt{thr\_num} = \epsilon_f \equiv \texttt{thr\_qual} \cdot \texttt{ORD}$, where `ORD` represents the average order of magnitude of $f(x)$ and $\epsilon_{\%}$ is the user-specified percentage error between $f(x)$ and its approximation.

[8] This ensures that *ARRAY* contains only those coefficients $c_i[last]$ that have a corresponding index in the previous iteration's set $c_i[prev]$.

2V version

Similarly to the 1V version, the 2V iterated mode introduces additional variables for the column direction. Specifically,

- a new set of variables, $\mathtt{j}_{start}$, $\bar{j}$, $j^\star$ and M, serve in the column direction the same roles that $\mathtt{i}_{start}$, $\bar{i}$, $i^\star$ and N play in the row direction. Their functions will be clarified in point 3 of the flowchart below;
- in addition, two Boolean flags, `increase_N` and `increase_M`, are introduced and are initially set to *true* (`increase_N` = *true*, `increase_M` = *true*).

The 2V algorithm proceeds through the following steps:

0. The function of interest is initially approximated to the order $O = O_N \times O_M = 2^N \times 2^M$ with $O_N = 2^N$ in x and $O_M = 2^M$ in y. Note that these values don't refer to the actual polynomial orders in x and y, which instead are $2^N - 1$ and $2^M - 1$, respectively.

1. New approximation orders are computed as follows:[9]

$$\begin{aligned} O_N &= O_N \times (1 + \mathtt{increase\_N}) \\ O_M &= O_M \times (1 + \mathtt{increase\_M}). \end{aligned} \tag{2.75}$$

   After these new orders are determined, the $O_N \times O_M$-th order approximation is extracted using the approach described in Section 2.4.2. Finally, both `increase_N` and `increase_M` are reset to *false* (`increase_N` = $false$, `increase_M` = $false$).

2. The `thr_inn` and `f_order` variables are extracted according to

$$\begin{aligned} \mathtt{f\_order\_1} &= \frac{|c_{00}[last]| + |c_{01}[last]| + |c_{02}[last]| + |c_{03}[last]|}{4} \\ \mathtt{f\_order\_2} &= \frac{|c_{00}[last]| + |c_{10}[last]| + |c_{20}[last]| + |c_{30}[last]|}{4} \\ \mathtt{thr\_inn} &= \frac{\mathtt{f\_order\_1} + \mathtt{f\_order\_2}}{2} \cdot 250 \cdot \mathtt{EPS}_0 \\ \mathtt{f\_order} &= min[\mathtt{f\_order\_1}, \mathtt{f\_order\_2}]. \end{aligned} \tag{2.76}$$

3. Points 3 and 4 of the 1V procedure are applied independently to the first row $c_{0j}[last]$ (from $\mathtt{j}_{start} \leq j < \frac{2^M}{2}$) and the first column $c_{i0}[last]$ (from $\mathtt{i}_{start} \leq i < \frac{2^N}{2}$) of the latest iteration's coefficient matrix. At this stage, if processing

[9] In Eq. (2.75), the Boolean values *true* and *false* are cast to the integers 1 and 0, respectively.

either the row or the column results in a failure, a corresponding*FAIL_M* and/or a *FAIL_N* is triggered. Any *FAIL_N* sets `increase_N`=*true* (and similarly, a *FAIL_M* sets `increase_M`=*true*), causing the 2V algorithm to restart from point 1. Note that $\mathtt{i}_{start}$ and $\mathtt{j}_{start}$ are updated in point 3, as specified in Section 2.4.4. Conversely, if everything proceeds correctly, both a $\bar{i}$ and a $\bar{j}$ are determined.

4. The set of conditions

$$\begin{cases} |c_{ij}[last]| < \mathtt{thr\_inn} \\ |c_{ij}[last] - c_{ij}[prev]| < \mathtt{thr\_inn} \\ |\frac{c_{ij}[last]-c_{ij}[prev]}{c_{ij}[last]}| < \mathtt{thr\_qual} \end{cases} \tag{2.77}$$

is evaluated for those coefficients whose pair of indices ij ranges within the interval $1 \leq i \leq \bar{i}$, $1 \leq j \leq \bar{j}$. If even a single c_{ij} fails to satisfy all the conditions in (2.77), we *FAIL*: both `increase_N` and `increase_M` are reset to *true*, and the algorithm restarts from point 1. Otherwise, the algorithm terminates, and the submatrix $c_{ij}[last]$ (with $0 \leq i \leq \bar{i}$, $0 \leq j \leq \bar{j}$) is retained for use in the 2D Clenshaw evaluation algorithm.

2.5 Important notes

We conclude our discussion of the Chebyshev approximator algorithms available in `ChAppX`. In the preceding sections, we detailed the mathematical framework for iteratively computing Chebyshev coefficients for successive approximation orders, and outlined the corresponding stopping strategies. Before closing this chapter, we wish to highlight several key points regarding the Chebyshev expansion of a function $f(x)$, which will be denoted henceforth as $C[f(x)]$. First, note that the convergence rate of $C[f(x)]$ depends critically on the smoothness of $f(x)$. Therefore, before computing the expansion, it is advisable to analyze $f(x)$ and consider whether its smoothness can be improved, for example, by applying a suitable change of variables. Moreover, partitioning the domain of definition for one- or two-variable functions into smaller intervals can substantially reduce the number of coefficients needed to achieve a desired accuracy. At runtime, the microprocessor selects the appropriate subinterval based on the actual values of the variables[10].

In some cases, it is both simpler and more computationally efficient to employ asymptotic expansions in regions where $f(x)$ or its derivatives increase rapidly, or when the domain is unbounded. Asymptotic expansions are also preferable when

[10]This process, known as branching, can create bottlenecks in modern pipelined microprocessors, which execute multiple instructions per cycle. To mitigate this, processors are equipped with branch predictors that select the most likely subinterval; accurate predictions can significantly enhance performance. By carefully choosing the subintervals for approximation, one can ensure that a single subinterval is used most frequently, further improving efficiency.

$f(x)$ is exponentially small or decays much faster than any polynomial; under these conditions, $f(x)$ and $C[f(x)]$ may approach zero at different rates, reducing the accuracy of the approximation. Alternatively, it may be advantageous to compute the Chebyshev expansion of a function derived from $f(x)$. In this approach, one first expands a transformed or derived function and then recovers $f(x)$ from that expansion. For instance, if $f(x)$ or its derivatives diverge, expanding $1/f(x)$ or $f(x)/g(x)$, where $g(x)$ is an easily computable asymptotic function that renders $f(x)/g(x)$ smooth, may yield a more rapidly convergent Chebyshev series than expanding $f(x)$ directly. The original function can then be recovered as $(C[1/f(x)])^{-1}$ or $g(x)C[f(x)/g(x)]$, respectively.

2.6 Conclusions

This concludes our overview of `ChAppX`, the code used to systematically generate Chebyshev approximations within `SFQEDtoolkit`. Designed to be both flexible and intuitive, `ChAppX` is optimized for parallel execution across multiple CPUs and can compute Chebyshev approximations for any function with arbitrarily high accuracy. At present, the code is not publicly available, but access can be granted upon request[11]. In the next chapter, we will introduce `SFQEDtoolkit`, a library that integrates Chebyshev, asymptotic, and exponential expansions to achieve the most efficient approximations of NIC and NBW distributions.

[11] For more details, please contact `samuele.montefiori@mpi-hd.mpg.de`.

Chapter 3

SFQEDtoolkit

`SFQEDtoolkit` [52] is an open-source library designed to integrate NIC photon emission and NBW pair production processes into existing codes. It works by computing and returning the probability rates and energies of particles generated by these phenomena. Leveraging the Chebyshev approximator `ChAppX` and the methods outlined in Chapter 2, the toolkit is optimized for both accuracy and efficiency. Its accuracy target is set above 99.9%, ensuring a relative error below 0.1%.

This chapter focuses on describing the implementation of `SFQEDtoolkit`, along with its advantages and limitations. We begin with a brief introduction to the theoretical framework underlying NIC and NBW distributions, deferring a detailed derivation of their expressions to Chapter 5.

3.1 Strong-Field QED

The dynamics of spin-$\frac{1}{2}$ particles (e^- and e^+) in an electromagnetic background field are governed by Quantum Electrodynamics (QED), described by the Lagrangian

$$\mathcal{L}_{QED} = -\frac{1}{4}F^{\mu\nu}F_{\mu\nu} + \bar{\psi}(i\gamma^\mu\partial_\mu - m)\psi - e\bar{\psi}\gamma^\mu A_\mu\psi, \tag{3.1}$$

where ψ and A_μ denote the fermion and photon fields, respectively, and $F_{\mu\nu} = \partial_\mu A_\nu - \partial_\nu A_\mu$ is the electromagnetic field-strength tensor. The adjoint spinor is given by $\bar{\psi} = \psi^\dagger\gamma^0$. Varying (3.1) with respect to A_μ yields the Maxwell equations in the presence of a source:

$$\partial_\mu F^{\mu\nu} = e\bar{\psi}\gamma^\nu\psi. \tag{3.2}$$

Similarly, variation with respect to $\bar{\psi}$ and ψ produces the equations of motion for the fermion field:

$$i\gamma^\mu(\partial_\mu + ieA_\mu)\psi = m\psi \tag{3.3}$$

$$-i(\partial_\mu - ieA_\mu)\bar{\psi}\gamma^\mu = m\bar{\psi}. \tag{3.4}$$

To enforce a specific gauge condition, such as the Lorenz gauge ($\partial_\mu A^\mu = 0$), a gauge-fixing term $-\frac{\rho}{2}(\partial_\mu A^\mu)^2$ can be added to (3.1), where ρ is the gauge-fixing parameter.

In modern experiments, the electromagnetic tensor field $F^{\mu\nu}$ is often realized through intense laser pulses [53], whose strength is typically characterized by the *classical nonlinearity parameter* (already introduced in chapter 1)

$$\xi \equiv a_0 = \frac{|e|E}{m_e \bar{\omega} c}, \tag{3.5}$$

which is Lorentz- and gauge-invariant. This parameter depends on the laser field amplitude E and its angular frequency $\bar{\omega}$, and represents the work (in units of $m_e c^2$) done by the laser on an electron over a single optical cycle. When $\xi \sim 1$, the electron becomes relativistic ($\varepsilon_e \sim m_e c^2$) within one laser cycle, and the fermion-photon interaction can no longer be treated perturbatively. This interaction, represented by the last term in the Lagrangian (3.1), typically scales with the fine-structure constant $\alpha = e^2/\hbar c \approx 1/137.036$. However, in the presence of strong electromagnetic fields, it reaches ~ 1 , indicating a breakdown of standard perturbation theory [54].

3.1.1 The Furry picture

The need to account for the fermion-field interaction exactly when computing quantum amplitudes does not preclude analytical solutions. In fact, by adopting the so-called Furry picture [55], we can decompose the photon field as

$$A_\mu = A_\mu^{rad} + A_\mu^{BG}. \tag{3.6}$$

Here, A_μ^{rad} represents radiation field components, describing virtual, incoming, and outgoing photons, while A_μ^{BG} models the background laser field. In essence, the first term in (3.6) accounts for quantum fluctuations around the classical background (second term). Given the high intensity of the laser field when $\xi \sim 1$, it is customary to assume that A_μ^{BG} remains largely unaffected by the interaction between fermions and the quantum radiation field A_μ^{rad}. Consequently, the background field satisfies the free-field equation of motion, $\partial^\mu F_{\mu\nu}^{BG} = 0$, and its vacuum expectation value coincides with that of the total field A_μ. The Furry picture enables us to treat the background potential classically while incorporating its interaction with the fermion field at the quantization level. As a result, the Dirac equation takes the form

$$i\gamma^\mu(\partial_\mu + ieA_\mu^{BG})\psi = m\psi, \tag{3.7}$$

and, when the background is a plane-wave laser field, its solutions are known as Volkov states (see section 3.1.2).

3.1.2 Volkov states

In 1935, Volkov [56] derived the first analytic solution of Eq. (3.7) in a plane-wave background, thereby revealing the exact dynamics of electrons and positrons

in such an electromagnetic field. Denoting the plane wave's four-momentum as $k \equiv k^\mu = (\omega, \vec{k})$, and the particle's space-time position as $x \equiv x^\mu = (t, \vec{x})$, Volkov assumed the wave to be switched off in both the remote past and far future. This ensures that the solutions to Eq. (3.7) reduce to free fermion states as $t \to \pm\infty$

$$\begin{aligned}\psi^{e^-}_{p,s}(x) &\xrightarrow[t\to\pm\infty]{} \frac{u_s(p)}{\sqrt{2\varepsilon V}} \exp\Big(-ix_\mu p^\mu\Big) \\ \psi^{e^+}_{p,s}(x) &\xrightarrow[t\to\pm\infty]{} \frac{v_s(p)}{\sqrt{2\varepsilon V}} \exp\Big(ix_\mu p^\mu\Big),\end{aligned} \tag{3.8}$$

where $p \equiv p^\mu = (\varepsilon, \vec{p})$ is the particle's four-momentum, s represents its spin, and V the quantization volume. The spinors $u_s(p)$ and $v_s(p)$ satisfy the free positive- and negative-frequencies Dirac equations

$$(\gamma^\mu p_\mu - m)u_s(p) = 0 \tag{3.9}$$

$$(\gamma^\mu p_\mu + m)v_s(p) = 0, \tag{3.10}$$

with the normalization conditions

$$\begin{aligned}\bar{u}_s(p)u_{s'}(p) = 2\delta_{ss'} &= -\bar{v}_s(p)v_{s'}(p) \\ \bar{u}_s(p)\gamma^\mu u_{s'}(p) = 2p^\mu\delta_{ss'} &= \bar{v}_s(p)\gamma^\mu v_{s'}(p).\end{aligned} \tag{3.11}$$

Without delving into the details of Volkov's derivation, the exact solutions to Eq. (3.7) for incoming and outgoing electron and positron states are [57]

$$\begin{aligned}\psi^{e^-}_{p,s}(x) &= \frac{u_s(p)}{\sqrt{2\varepsilon V}}\Big(1 + e\gamma^\mu\gamma^\nu\frac{n_\mu A_\nu}{2n_\rho p^\rho}\Big)\exp\Big(-ix_\mu p^\mu - i\int_0^{x_\mu n^\mu} d\phi'\Big[e\frac{p_\mu A^\mu(\phi')}{n_\nu p^\nu} - \frac{e^2}{2}\frac{A_\nu(\phi')A^\nu(\phi')}{n_\nu p^\nu}\Big]\Big) \\ \psi^{e^+}_{p,s}(x) &= \frac{v_s(p)}{\sqrt{2\varepsilon V}}\Big(1 - e\gamma^\mu\gamma^\nu\frac{n_\mu A_\nu}{2n_\rho p^\rho}\Big)\exp\Big(+ix_\mu p^\mu - i\int_0^{x_\mu n^\mu} d\phi'\Big[e\frac{p_\mu A^\mu(\phi')}{n_\nu p^\nu} + \frac{e^2}{2}\frac{A_\nu(\phi')A^\nu(\phi')}{n_\nu p^\nu}\Big]\Big),\end{aligned} \tag{3.12}$$

where $n^\mu = (1, \vec{n}) = \frac{k^\mu}{k^0}$, with $\vec{n}$ indicating the wave's propagation direction, and the four-potential $A_\mu(x')$ is expressed in terms of the phase $\phi' = x'_\mu n^\mu = t' - \vec{x}'$. To ensure consistency with the free states in Eq. (3.8), the incoming and outgoing Volkov states (3.12) must be multiplied by the additional phase factors:

$$\begin{aligned}\varphi^{e^-}_{in} &= \exp\Big(-i\int_{-\infty}^{0} d\phi'\Big[e\frac{p_\mu A^\mu(\phi')}{n_\nu p^\nu} - \frac{e^2}{2}\frac{A_\nu(\phi')A^\nu(\phi')}{n_\nu p^\nu}\Big]\Big) \\ \varphi^{e^-}_{out} &= \exp\Big(i\int_{0}^{\infty} d\phi'\Big[e\frac{p_\mu A^\mu(\phi')}{n_\nu p^\nu} - \frac{e^2}{2}\frac{A_\nu(\phi')A^\nu(\phi')}{n_\nu p^\nu}\Big]\Big)\end{aligned} \tag{3.13}$$

for electrons, or

$$\varphi^{e^+}_{in} = \exp\Big(-i\int_{-\infty}^{0} d\phi'\Big[e\frac{p_\mu A^\mu(\phi')}{n_\nu p^\nu} + \frac{e^2}{2}\frac{A_\nu(\phi')A^\nu(\phi')}{n_\nu p^\nu}\Big]\Big)$$

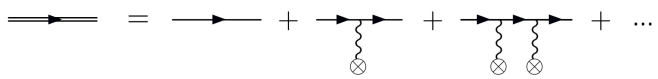

Figure 3.1: Fermion line in the Furry picture. Largely employed in SFQED Feynman diagrams, it denotes the dressed electron/positron propagator with respect to the external background field A_μ^{BG}.

$$\varphi_{out}^{e^+} = \exp\Big(i\int_0^\infty d\phi'\Big[e\frac{p_\mu A^\mu(\phi')}{n_\nu p^\nu} + \frac{e^2}{2}\frac{A_\nu(\phi')A^\nu(\phi')}{n_\nu p^\nu}\Big]\Big) \tag{3.14}$$

for positrons.

Volkov states (3.12) are used in Feynman diagrams to represent incoming and outgoing fermions quantized in the presence of a strong plane wave background. Similarly, virtual off-shell fermions propagating in the same field are described by the Volkov propagator [58]:

$$I(x,y) = \lim_{a\to 0}\int \frac{d^4p}{(2\pi)^4}\Big[R(p,x)\frac{\gamma^\mu p_\mu + m}{p^\nu p_\nu - m^2 + ia}\bar{R}(p,y)\Big], \tag{3.15}$$

where we introduce, for convenience, the operator

$$R(p,x) = \Big(1+e\gamma^\mu\gamma^\nu\frac{n_\mu A_\nu}{2n_\rho p^\rho}\Big)\exp\Big(-ix_\mu p^\mu - i\int_0^{x_\mu n^\mu} d\phi'\Big[e\frac{p_\mu A^\mu(\phi')}{n_\nu p^\nu} - \frac{e^2}{2}\frac{A_\nu(\phi')A^\nu(\phi')}{n_\nu p^\nu}\Big]\Big). \tag{3.16}$$

Expression (3.15) corresponds to the Green's function of the Dirac equation (3.7), satisfying

$$[i\gamma^\mu(\partial_\mu + ieA_\mu^{BG}) - m]I(x,y) = \delta^4(x-y). \tag{3.17}$$

Both Volkov *in*/*out*-states and the Volkov propagator are represented by double fermion lines in Feynman diagrams (see Fig. 3.1), to denote all the possible interactions between the fermion state and the background EM field. As we will see in Chapter 5, they play a fundamental role in the computation of all distributions employed in `SFQEDtoolkit`.

3.1.3 Locally-Constant-Field Approximation

The calculation of differential probabilities that `SFQEDtoolkit` can reproduce is carried out within the S-matrix formalism of SFQED, specifically using the quasi-classical operator method developed by Baier and Katkov (see Chapter 5 and [59]). This method involves complex time integrals over the entire time range, from $-\infty$ to $+\infty$, and in principle one must consider the asymptotic states in both the past and the future. However, when the temporal scale of the process is much smaller than the variation scale of the electromagnetic fields, it becomes possible to use rates that depend only on the instantaneous values of the particle parameters (see Refs. [54, 59] for further details). This assumption forms the basis of the widely

used locally-constant-field approximation (LCFA), which consists in treating the background fields as locally constant crossed fields (CCF).

In the case of photon emission by an electron or positron interacting with a laser pulse, the LCFA requires that:

$$\xi \gg 1 \quad \text{and} \quad \xi^3 \gg \chi_e, \tag{3.18}$$

where χ_e is the quantum nonlinearity parameter[1]. Physically, the conditions in (3.18) imply that:

- SFQED probabilities are dominated by a small region of the particle's trajectory, which is much smaller than the scale of variation of the background electromagnetic fields (referred to as the *formation length* of the physical process);
- The majority of the radiated photon spectrum is well approximated by the LCFA photon spectrum [61, 62], i.e., the spectrum produced by applying the LCFA at each photon emission from the electron.

3.2 Methodology of `SFQEDtoolkit`'s implementation

As stated at the beginning of this chapter, `SFQEDtoolkit` is designed to compute rates and probability distributions for NIC and NBW processes with better than 0.1% accuracy, while achieving performance that is comparable to or exceeds that of current state-of-the-art SFQED codes. Conventionally, these distributions are computed using coarse lookup tables, where the relevant functions are sampled at a finite number of points. In what follows, we use the precomputed tables from the open-source PIC code Smilei as a benchmark [63]. Specifically we will consider

[1] This dimensionless, Lorentz- and gauge-invariant quantity is defined as

$$\chi_e = \frac{e\hbar}{m_e^3 c^4}\sqrt{-(F^{\mu\nu}p_\nu)^2} \quad \text{and} \quad \chi_\gamma = \frac{e\hbar}{m_e^3 c^4}\sqrt{-(F^{\mu\nu}k_\nu)^2} \tag{3.19}$$

for electrons (or equivalently positrons) and photons, respectively. It characterizes the strength of the interaction between the field and a relativistic electron. For massive particles like electrons and positrons, it is more conveniently expressed as:

$$\chi_{e^\pm} = E^*/E_{cr}, \tag{3.20}$$

where E^* is the electromagnetic field amplitude in the fermion's instantaneous rest frame [54, 59, 60]. In addition to the covariant expression (3.19), χ can be explicitly written as:

$$\chi_{e/\gamma} = \frac{\varepsilon_{e/\gamma}}{m_e c^2 F_{cr}}\sqrt{\left(\vec{E} + \frac{\vec{p}_{e/\gamma}c}{\varepsilon_{e/\gamma}} \times \vec{B}\right)^2 - \left(\frac{\vec{p}_{e/\gamma}c}{\varepsilon_{e/\gamma}} \cdot \vec{E}\right)^2}, \tag{3.21}$$

which applies to electrons, positrons, and photons with momentum $\vec{p}e/\gamma$ and energy $\varepsilon e/\gamma$ in a background electric field $\vec{E}$ and magnetic field $\vec{B}$.

two default resolutions: 256 and 1024 points in 1D (or 256×256 and 1024×1024 in 2D).

The methodology employed to implement SFQED processes in `SFQEDtoolkit` chiefly resorts to a combination of: (i) function approximation with Chebyshev polynomials; (ii) asymptotic expansions; (iii) variable and function transformation. Although the LCFA dramatically simplifies the calculation of probabilities, the NIC photon spectrum computed within the LCFA framework differs both quantitatively and qualitatively from the exact spectrum at relatively low photon energies, i.e., when $\varepsilon_\gamma \lesssim (\chi_e/\xi^3)\varepsilon_e$, where ε_γ and ε_e denote the photon and electron energies, respectively [61].

To properly model this low-energy region one has to resort to more advanced techniques [62, 64–67]: while some of these accurately reproduce the interference features of the emitted photon spectrum predicted by SFQED, most of them are only suitable for specific cases (such as the interaction of particles with a plane-wave pulse or with a crystal). In `SFQEDtoolkit` the technique described in Ref. [62] is implemented (section 3.4), effectively allowing the library to reach *beyond* the LCFA (BLCFA). Albeit this approach cannot exactly reproduce the SFQED spectrum for all photon energies, it provides a several orders of magnitude better approximation than the LCFA in the low energy part of the photon spectrum, while retaining the advantages of the LCFA (the high energy part of the photon spectrum corresponds to the SFQED one, it depends only on the local instantaneous value of a particle's parameters, and it's suitable for background electromagnetic fields with *arbitrary* spacetime structure such as those occurring in PIC simulations).

`SFQEDtoolkit` can be used as a black box, in which case the user can directly refer to sec A, which summarizes the currently available routines and the essential steps for a straightforward implementation of `SFQEDtoolkit` in a code. More detailed instructions, updates and neat examples of its usage are provided in `C++` and `Fortran` in the "example_cpp" and "example_fortran" folders in the GitHub repository at `https://github.com/QuantumPlasma/SFQEDtoolkit`.

3.3 Photon emission and pair creation in the LCFA

Throughout the rest of the coming sections we will formally discuss the integration into `SFQEDtoolkit` of the NIC and NBW distributions. As discussed above, a detailed derivation of these complex functions is beyond the scope of this chapter and will be presented in Chapter 5.

We begin this section by introducing two key differential probabilities from SFQED. First, the differential probability per unit time t and per unit photon energy ε_γ for

photon emission by an electron (or positron) with energy ε_e [44] is given by

$$\frac{d^2W_{pe}}{dtd\varepsilon_\gamma}(\varepsilon_\gamma,\varepsilon_e,\chi_e)=\frac{\alpha m_e^2c^4}{\sqrt{3}\pi\hbar\varepsilon_e^2}\frac{1}{(1+u)}\left[[1+(1+u)^2]\mathrm{K}_{\frac{2}{3}}\left(\frac{2u}{3\chi_e}\right)-(1+u)\int_{\frac{2u}{3\chi_e}}^{\infty}\mathrm{K}_{\frac{1}{3}}(y)dy\right], \tag{3.22}$$

where $u=\varepsilon_\gamma/(\varepsilon_e-\varepsilon_\gamma)$ and $\mathrm{K}_\nu(x)$ denotes the modified Bessel functions of the second kind. Next, the differential probability per unit time and per unit electron energy for electron-positron pair creation by a photon of energy ε_γ is given by [44]:

$$\frac{d^2W_{pp}}{dtd\varepsilon_e}(\varepsilon_e,\varepsilon_\gamma,\chi_\gamma)=\frac{\alpha m_e^2c^4}{\sqrt{3}\pi\hbar\varepsilon_\gamma^2}\left[\frac{\varepsilon_e^2+\varepsilon_p^2}{\varepsilon_e\varepsilon_p}\mathrm{K}_{\frac{2}{3}}(\eta)+\int_\eta^\infty\mathrm{K}_{\frac{1}{3}}(y)dy\right]. \tag{3.23}$$

where $\eta=2\varepsilon_\gamma^2/(3\varepsilon_e\varepsilon_p\chi_\gamma)$, and $\varepsilon_p=\varepsilon_\gamma-\varepsilon_e$ is the energy of the produced positron. These expressions serve as the foundation for the differential probability distributions implemented in `SFQEDtoolkit`.

Equations (3.22)-(3.23) are valid provided that the two field invariants, $|\vec{E}^2-\vec{B}^2|/F_{\mathrm{cr}}^2$ and $|\vec{E}\cdot\vec{B}|/F_{\mathrm{cr}}^2$ are much smaller than $\min(1,\chi_{e/\gamma}^2)$, , and that both the initial and final electrons (or positrons) are ultrarelativistic, i.e., $\varepsilon_{e/p}/(m_ec^2)\gg 1$ (see Ref. [44]). In this limit, the discrete nature of energy levels and the contributions from spin degrees of freedom can be neglected, permitting a quasiclassical treatment. Furthermore, if the background fields remain nearly constant and uniform over the process's formation length, these equations can also be applied to time- and space-dependent electromagnetic fields [44, 54, 61, 62].

It is important to note that all current SFQED calculations assume that perturbation theory in the Furry picture is applicable[2]. Moreover, the ultrarelativistic assumption justifies the use of the collinear approximation, whereby the momenta of the initial and produced particles are assumed to be aligned immediately after the NIC or NBW event. In Eqs. (3.22)–(3.23), the initial (final) spin and polarization degrees of freedom are averaged (summed). The implementation of the angular distribution of the generated particles beyond the collinear approximation, as well as the inclusion of spin-dependent SFQED effects, will be presented in Chapter 5.

3.3.1 Photon emission rate

As briefly discussed, each computational cycle involving SFQED processes first consists in determining whether an event occurs according to its rate. From Eq. (3.22),

[2]However, according to the Ritus-Narozny conjecture, this assumption breaks down in the regime $\alpha\chi^{2/3}\gtrsim 1$ (i.e., for $\chi\gtrsim 1600$), where higher-order loop corrections become significant and the theory enters a non-perturbative phase (see, e.g., Ref. [68] and references therein). Recent studies have indicated that this breakdown is not universal; its onset depends on both the structure of the electromagnetic fields and the energy of the incoming particles [69, 70].

SFQED_INV_COMPTON_rate		SFQED_LCFA_INV_COMPTON_PHOTON_energy			
χ_e	Method	$r \le r_{min}$	$r_{min} < r < r_{inv}$	$r_{inv} \le r < r_{max}$	$r \ge r_{max}$
$0 \le \chi_e < 2$	C (12)	A. (3.39)	C (17×35)	C (17×84)	E. (3.41)
$2 \le \chi_e < 20$	C (11)	A. (3.39)	C (12×37)	C (10×84)	E. (3.41)
$20 \le \chi_e < 80$	C (8)	A. (3.39)	C (8×40)	C (7×49)	E. (3.41)
$80 \le \chi_e < 600$	C (10)	A. (3.39)	C (12×42)	C (9×53)	E. (3.41)
$600 \le \chi_e \le 2000$	C (7)	A. (3.39)	C (8×45)	C (7×60)	E. (3.41)

Table 3.1: Summary of the methods employed by the functions `SFQED_INV_COMPTON_rate` and `SFQED_LCFA_INV_COMPTON_PHOTON_energy` in each region of their domain. "C" denotes Clenshaw's recurrence applied to a Chebyshev expansion, with the number inside the round brackets reporting the available number of Chebyshev coefficients. The value of the Chebyshev coefficients is available in the "coefficients" folder of `SFQEDtoolkit`, see, e.g., https://github.com/QuantumPlasma/SFQEDtoolkit. "A." denotes the asymptotic approximation in Eq. (3.39), while "E." denotes the exponential approximation in Eq. (3.41).

the rate of photon emission is [44]

$$R_{pe}(\varepsilon_e,\chi_e) = \int_0^{\varepsilon_e} \frac{d^2W_{pe}}{dtd\varepsilon_\gamma}(\varepsilon_\gamma,\varepsilon_e,\chi_e)d\varepsilon_\gamma = \frac{\alpha m_e^2c^4}{3\sqrt{3}\pi\hbar\varepsilon_e}\int_0^\infty \frac{5u^2+7u+5}{(1+u)^3}\mathrm{K}_{\frac{2}{3}}\left(\frac{2u}{3\chi_e}\right)du. \tag{3.24}$$

For its implementation in `SFQEDtoolkit`, it is convenient to change the dummy variable of integration from u to $v = 2u/3\chi_e$ and express all quantities in normalized units. Namely, we use an angular frequency ω_r as a reference[3], and consequently obtain a reference time $T_r = 1/\omega_r$, a reference length $\lambda_r = c/\omega_r$ and a reference field $E_r = m_e c\omega_r/|e|$, while electron and photon energies are normalized as $\gamma_{e/\gamma} = \varepsilon_{e/\gamma}/m_e c^2$. Alternatively, one could express all the above reference quantities in units of the laser wavelength λ, defining $\lambda_r = \lambda/2\pi$ (from which $\omega_r = c/\lambda_r$). The use of normalized quantities exhibits the scale invariance of the Lorentz equation, and avoids to incur in possible numerical issues related to the use of numbers that are too big or too small for floating-point arithmetic. After the above transformations, Eq. (3.24) becomes

$$W_{\mathrm{rad}}(\gamma_e,\chi_e) = \frac{R_{pe}(\gamma_e,\chi_e)}{\omega_r} = \frac{\alpha}{\sqrt{3}\pi}\frac{\lambda_r}{\lambda_C}\frac{\chi_e}{\gamma_e}\tilde{W}_{\mathrm{rad}}(\chi_e), \tag{3.25}$$

where $\lambda_C = \hbar/m_e c$ is the reduced Compton length and[4]

$$\tilde{W}_{\mathrm{rad}}(\chi_e) = \int_0^\infty \frac{45(v\chi_e)^2+42v\chi_e+20}{(2+3v\chi_e)^3}\mathrm{K}_{\frac{2}{3}}(v)dv. \tag{3.26}$$

In order to implement Eq. (3.25), we only need to compute $C[\tilde{W}_{\mathrm{rad}}(\chi_e)]$ to the desired accuracy $\Delta_{pe} = \left|\left\{\tilde{W}_{\mathrm{rad}}(\chi_e) - C[\tilde{W}_{\mathrm{rad}}(\chi_e)\right\}/\tilde{W}_{\mathrm{rad}}(\chi_e)\right|$, notice that the notation

[3] Notice that in practice, for instance in PIC simulations, ω_r should correspond to an important frequency that we want to resolve, like that associated to the process being simulated.

[4] In practice, the upper bound of integration is 700 as the integrand becomes so small that the whole integral from 700 to infinity is $\lesssim 10^{-305}$, leading to underflow even with double precision accuracy.

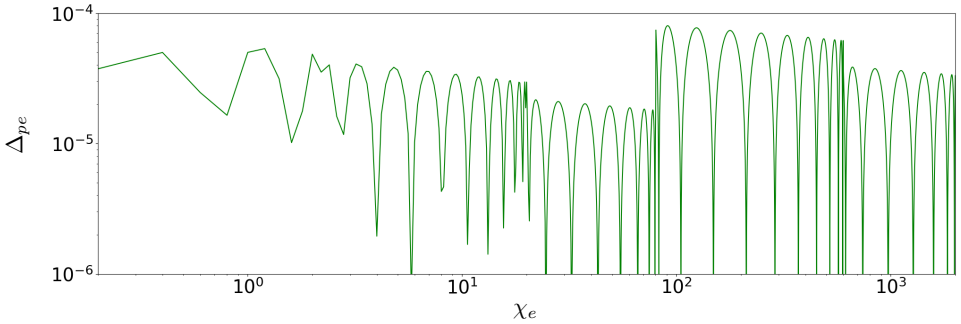

Figure 3.2: Relative accuracy $\Delta_{pe}(\chi_e) = \left|\left\{\tilde{W}_{\rm rad}(\chi_e) - C[\tilde{W}_{\rm rad}(\chi_e)\right\} / \tilde{W}_{\rm rad}(\chi_e)\right|$ between the analytical and the numerical `SFQEDtoolkit` photon emission rate (see function `SFQED_INV_COMPTON_rate` in A). Here $\Delta_{pe}(\chi_e)$ is evaluated at 10^4 evenly spaced points in the interval $0 \leq \chi_e \leq 2000$.

introduced at the end of chapter 2 to designate the Chebyshev expansion $C[f(x)]$ of a function $f(x)$ has been employed. Figure 3.2 displays Δ_{pe} over the considered interval $0 \leq \chi_e \leq 2000$ clearly showing `SFQEDtoolkit`'s better than 0.1% accuracy throughout its domain. In `SFQEDtoolkit`, the Chebyshev coefficients of $C[\tilde{W}_{\rm rad}(\chi_e)]$ are precomputed and stored into five separate text files according to the following ranges: $0 \leq \chi_e < 2$, $2 \leq \chi_e < 20$, $20 \leq \chi_e < 80$, $80 \leq \chi_e < 600$, and $600 \leq \chi_e \leq 2000$ (see the summary in Tab. 3.1). At runtime, coefficients are loaded once when the simulation is initialized. When the rate is calculated by calling the function `SFQED_INV_COMPTON_rate`, the relevant interval is selected depending on χ_e, and Clenshaw's recurrence formula is applied to the corresponding coefficients (see 2.2). Approximately, ten coefficients per interval are needed to compute $C[\tilde{W}_{\rm rad}(\chi_e)]$ with the desired accuracy (see Tab. 3.1). Such a small number of coefficients can fit in a modern CPU L1 cache greatly speeding up the simulation. Given the smoothness of $C[\tilde{W}_{\rm rad}(\chi_e)]$, no asymptotic expansion is used.

We stress that the fast and accurate calculation of SFQED rates has major implications on the simulation results. On the one hand, insufficient accuracy may result into a significant error in the predicted number of events, which systematically accumulates during the simulation. On the other hand, low performances may noticeably slow down the simulation given that SFQED rates are evaluated at each timestep and for each particle. For example, we implemented `SFQEDtoolkit` in Smilei and simulated the evolution of an ultralow-density bunch of $N_e = 10^{10}$ electrons with 10 GeV energy in a constant and uniform magnetic field. Parameters were chosen such that $\chi_e = 1$, initially, and the duration of the simulation was $T_{sim} = 1.3$ fs, i.e., approximately half of the mean time required for an electron to emit once. By comparing the number of photons produced in the Smilei simulation with `SFQEDtoolkit` $N_{tk} = 4.834 \times 10^9$, as well as in the Smilei simulation with its default 256 points table $N_S = 5.111 \times 10^9$, with the expected number of photons $N_a = N_e T_{sim} R_{pe}(\varepsilon_e, \chi_e = 1) \approx 4.835 \times 10^9$, we observe that even after such a short amount of time Smilei's 256 points table value N_S differs by 5.70% from the

analytical prediction, while `SFQEDtoolkit`'s value N_{tk} differs by 0.04%.

3.3.2 Pair creation rate

The treatment of the pair creation rate follows similar steps as those of the photon emission rate. By using the symmetry with respect to the $\varepsilon_\gamma/2$-axis of the integrand in Eq. (3.23) and changing the variable of integration to v with $0 < v < 1$ and $\varepsilon_e = \varepsilon_\gamma(1+v)/2$, the rate of photon conversion into an electron positron pair is [44]

$$R_{pp}(\varepsilon_\gamma,\chi_\gamma) = \int_0^{\varepsilon_\gamma} \frac{d^2W_{pp}}{dtd\varepsilon_e}(\varepsilon_e,\varepsilon_\gamma,\chi_\gamma)d\varepsilon_e = \frac{\alpha m_e^2c^4}{3\sqrt{3}\pi\hbar\epsilon_\gamma}\int_0^1 dv \frac{9-v^2}{1-v^2}\mathrm{K}_{\frac{2}{3}}\Big(\frac{8}{3\chi_\gamma(1-v^2)}\Big). \tag{3.27}$$

Notice that in Eq. (3.27) the ultrarelativistic assumption $\varepsilon_\gamma \gg m_ec^2$ and $\varepsilon_e \gg m_ec^2$ allowed us to approximate the upper and lower limits of integration to ε_γ and zero, respectively. By converting to normalized units, we get

$$W_{\mathrm{pair}}(\gamma_\gamma,\chi_\gamma) = \frac{R_{pp}(\varepsilon_\gamma,\chi_\gamma)}{\omega_r} = \frac{\alpha}{\sqrt{3}\pi}\frac{\lambda_r}{\lambda_C}\frac{1}{\gamma_\gamma}\tilde{W}_{\mathrm{pair}}(\chi_\gamma), \tag{3.28}$$

where

$$\tilde{W}_{\mathrm{pair}}(\chi_\gamma) = \int_0^1 dv \frac{9-v^2}{3(1-v^2)}\mathrm{K}_{\frac{2}{3}}\Big(\frac{8}{3\chi_\gamma(1-v^2)}\Big). \tag{3.29}$$

Thus, we only need to approximate $\tilde{W}_{\mathrm{pair}}(\chi_\gamma)$ to the desired accuracy Δ_{pp} defined, as in the photon case, as the relative error between the exact and the approximate function. This time the considered quantum nonlinearity range $0.01 \le \chi_\gamma \le 2000$ was divided into seven intervals: $0.01 \le \chi_\gamma < 0.24$, $0.24 \le \chi_\gamma < 0.4$, $0.4 \le \chi_\gamma < 2$, $2 \le \chi_\gamma < 20$, $20 \le \chi_\gamma < 80$, $80 \le \chi_\gamma < 600$ and $600 \le \chi_\gamma \le 2000$. While for each interval in $0.24 \le \chi_\gamma \le 2000$ the coefficients of $C[\tilde{W}_{\mathrm{pair}}(\chi_\gamma)]$ were computed, for $\chi_\gamma < 0.24$ the pair creation rate is exponentially small and a Chebyshev expansion is no longer suited to accurately calculate $\tilde{W}_{\mathrm{pair}}(\chi_\gamma)$. In this range `SFQEDtoolkit` uses the asymptotic expansion [44]

$$W_{\mathrm{pair}}(\gamma_\gamma,\chi_\gamma) \approx \frac{3\sqrt{3}\alpha}{16\sqrt{2}}\frac{\lambda_r}{\lambda_C}\frac{\chi_\gamma}{\gamma_\gamma}e^{-\frac{8}{3\chi_\gamma}}\Big(1-\frac{11}{64}\chi_\gamma+\frac{7585}{73728}\chi_\gamma^2\Big) \quad \text{for } \chi_\gamma < 0.24. \tag{3.30}$$

Note that the pair creation rate becomes negligibly small $W_{\mathrm{pair}} \lesssim 3.5{\times}10^{-119}\alpha\lambda_r/\lambda_C\gamma_\gamma$ for $\chi_\gamma < 0.01$. Hence, the contribution of the regions where $\chi_\gamma < 0.01$ is neglected in `SFQEDtoolkit`.

It is worth noticing that, when using simulations to model realistic scenarios, the value of χ_γ is necessarily affected by an experimental or observational uncertainty $\Delta\chi_\gamma$, e.g., because of the limited knowledge of physical parameters such as the electromagnetic field or the particle's energy, and the simulation itself is affected by numerical and round-off effects. This uncertainty $\Delta\chi_\gamma$ propagates to W_{pair} as

SFQED_BREIT_WHEELER_rate	
χ_γ	Method
$0.01 \le \chi_\gamma < 0.24$	A. (3.30)
$0.24 \le \chi_\gamma < 0.4$	C (7)
$0.4 \le \chi_\gamma < 2$	C (11)
$2 \le \chi_\gamma < 20$	C (12)
$20 \le \chi_\gamma < 80$	C (7)
$80 \le \chi_\gamma < 600$	C (10)
$600 \le \chi_\gamma \le 2000$	C (7)

SFQED_BREIT_WHEELER_ELECTRON_energy			
χ_γ	$0 \le \lvert r'\rvert < 0.9$	$0.9 \le \lvert r'\rvert \le 0.9999$	$\lvert r'\rvert > 0.9999$
$0.01 \le \chi_\gamma \le 0.3$	C (15×12)	C (15×63)	E. (3.49)
$0.3 \le \chi_\gamma \le 2$	C (9×11)	C (9×54)	E. (3.49)
$2 \le \chi_\gamma \le 20$	C (11×9)	C (12×37)	E. (3.49)
$20 \le \chi_\gamma \le 80$	C (7×8)	C (7×23)	E. (3.49)
$80 \le \chi_\gamma \le 600$	C (9×9)	C (8×14)	E. (3.49)
$600 \le \chi_\gamma \le 2000$	C (5×9)	C (5×8)	E. (3.49)

Table 3.2: Summary of the methods employed by the functions `SFQED_BREIT_WHEELER_rate` and `SFQED_BREIT_WHEELER_ELECTRON_energy` in each region of the computational domain. "C" denotes Clenshaw's recurrence applied to a Chebyshev expansion, with the number inside the round brackets reporting the available number of Chebyshev coefficients. The value of the Chebyshev coefficients is available in the "coefficients" folder of `SFQEDtoolkit`, see, e.g., https://github.com/QuantumPlasma/SFQEDtoolkit. "A." denotes the asymptotic approximation in Eq. (3.30), while "E." denotes the exponential approximation in Eq. (3.49).

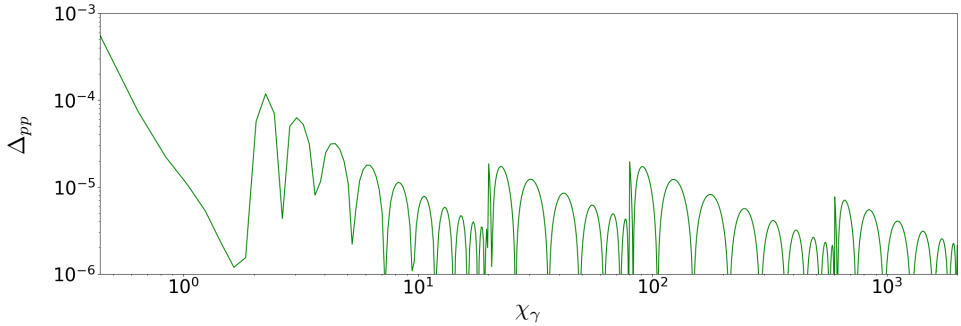

Figure 3.3: Relative accuracy $\Delta_{pp}(\chi_\gamma) = \left|\left\{\tilde{W}_{\text{pair}}(\chi_\gamma) - C[\tilde{W}_{\text{pair}}(\chi_\gamma)\right\} / \tilde{W}_{\text{pair}}(\chi_\gamma)\right|$ between the analytical and the numerical `SFQEDtoolkit` photon-to-electron-positron pair conversion rate (see function `SFQED_BREIT_WHEELER_rate` in A). Here $\Delta_{pp}(\chi_\gamma)$ is evaluated at 10^4 evenly spaced points in the interval $0.01 \le \chi_e \le 2000$.

$\Delta W_{\text{pair}} \approx (dW_{\text{pair}}/d\chi_\gamma)\Delta\chi_\gamma$. Since the relative error $d\ln\left(W_{\text{pair}}\right)/d\chi_\gamma$ rapidly diverges for $\chi_\gamma \to 0$, not only W_{pair} is tiny for small χ_γ, but also its relative error necessarily becomes large. For this reason it is often of limited significance to consider SFQED pair production in regions where $\chi_\gamma \ll 1$, and in addition to the function `SFQED_BREIT_WHEELER_rate` which returns $W_{\text{pair}}(\gamma_\gamma, \chi_\gamma)$ for $0.01 \le \chi_\gamma \le 2000$, `SFQEDtoolkit` also provides a function `SFQED_BREIT_WHEELER_rate_fast` which returns zero for $\chi_\gamma < 0.3$. Since $W_{\text{pair}} \lesssim 9.1 \times 10^{-6} \alpha \lambda_r / \lambda_C \gamma_\gamma$ for $\chi_\gamma < 0.3$, the computationally cheaper `SFQED_BREIT_WHEELER_rate_fast` is expected to provide essentially the same results as `SFQED_BREIT_WHEELER_rate` in many relevant cases while possibly improving the performance of the simulation.

Figure 3.3 displays Δ_{pp} over the considered domain $0.01 \le \chi_\gamma \le 2000$. Similarly to the photon emission rate, approximately ten coefficients per interval are needed to compute $C[\tilde{W}_{\text{pair}}(\chi_\gamma)]$ with the desired accuracy. Table 3.2 summarizes the strategies of the pair creation routines reported in sections 3.3.2-3.3.4.

3.3.3 Photon emission spectrum

Once an event is deemed to occur, the particles of the final state need to be generated according to the probability distribution of the process. By averaging (summing) over the initial (final) spin and polarization degrees of freedom, and by assuming that the momentum of the generated particles is aligned to the momentum of the incoming particle, only the energy of the outgoing particles needs to be computed in order to determine their state after the event. Now, let us assume that we want to sample a particle with energy $\bar{\varepsilon}$ in the range $0 < \bar{\varepsilon} < \varepsilon_{tot}$ according to an arbitrary distribution $f(x, \varepsilon)$. In this case one can resort to the inverse transform sampling (ITS) method. Namely, given an $f(x, \varepsilon)$, one needs to solve the equation

$$\int_0^{\bar{\varepsilon}} f(x, \varepsilon) d\varepsilon - r \int_0^{\varepsilon_{tot}} f(x, \varepsilon) d\varepsilon = 0 \tag{3.31}$$

in the unknown $\bar{\varepsilon}$. Here x represents generic constant parameters and $0 < r < 1$ is a uniformly distributed random number. For photon emission by an electron, this implies that one needs to solve

$$\int_0^{\bar{\varepsilon}} \frac{d^2 W_{pe}}{dt d\varepsilon_\gamma}(\varepsilon_\gamma, \varepsilon_e, \chi_e) d\varepsilon_\gamma - r \int_0^{\varepsilon_e} \frac{d^2 W_{pe}}{dt d\varepsilon_\gamma}(\varepsilon_\gamma, \varepsilon_e, \chi_e) d\varepsilon_\gamma = I_{pe}(\bar{\varepsilon}, \varepsilon_e, \chi_e) - r R_{pe}(\varepsilon_e, \chi_e) = 0, \tag{3.32}$$

where the cumulative distribution function $I_{pe}(\bar{\varepsilon}, \varepsilon_e, \chi_e)$ is obtained by integrating Eq. (3.22) up to an arbitrary energy value $\bar{\varepsilon}$

$$I_{pe}(\bar{\varepsilon}, \varepsilon_e, \chi_e) = \int_0^{\bar{\varepsilon}} \frac{d^2 W_{pe}}{dt d\varepsilon_\gamma}(\varepsilon_e, \varepsilon_\gamma, \chi_e) d\varepsilon_\gamma. \tag{3.33}$$

Equation (3.32) defines an implicit function $\bar{\varepsilon} = G_{pe}(r, \varepsilon_e, \chi_e)$, which can be calculated up to arbitrary accuracy by numerically solving Eq. (3.32) with a suitable root-finding algorithm, such as the Brent-Dekker method [71, 72]. However, direct application of the above recipe at runtime in a PIC code would be prohibitively expensive[5].

In `SFQEDtoolkit`, the function `SFQED_LCFA_INV_COMPTON_PHOTON_energy` provides users with a fast and accurate approximation of $G_{pe}(r, \varepsilon_e, \chi_e)$. The accuracy of the approximation Δ_r is given by $\Delta_r = |\bar{\varepsilon}_{ITS} - \bar{\varepsilon}_{tk}| / \bar{\varepsilon}_{ITS}$, where $\bar{\varepsilon}_{ITS}$ is the value obtained via the ITS method computed with more than ten significant digits accuracy, and $\bar{\varepsilon}_{tk}$ is the value returned by `SFQEDtoolkit`. It is worth noting that although the functions I_{pe} and R_{pe} in Eqs. (3.32)-(3.33) depend on two- and three-variables, respectively, the total energy of the parent particle ε_e can be easily factored out, and one is required to approximate functions of only one and two variables, in practice.

[5]The application of a root-finding routine to (3.32) requires several computational cycles to obtain $\bar{\varepsilon}$, in which modified Bessel functions of the second kind (e.g. $\mathrm{K}_{2/3}(x)$) and their integrals ($\int_\eta^\infty dy \mathrm{K}_{1/3}(y)$) are calculated multiple times.

χ_e	r_{min}	r_{inv}	r_{max}
$0 \leq \chi_e < 2$	0.028	0.986	0.99999
$2 \leq \chi_e < 20$	0.041	0.987	0.99999
$20 \leq \chi_e < 80$	0.045	0.987	0.99996
$80 \leq \chi_e < 600$	0.040	0.987	0.99997
$600 \leq \chi_e \leq 2000$	0.050	0.987	0.99998

Table 3.3: The numerical values of r_{min}, r_{inv} and r_{max} for each of the five intervals of χ_e.

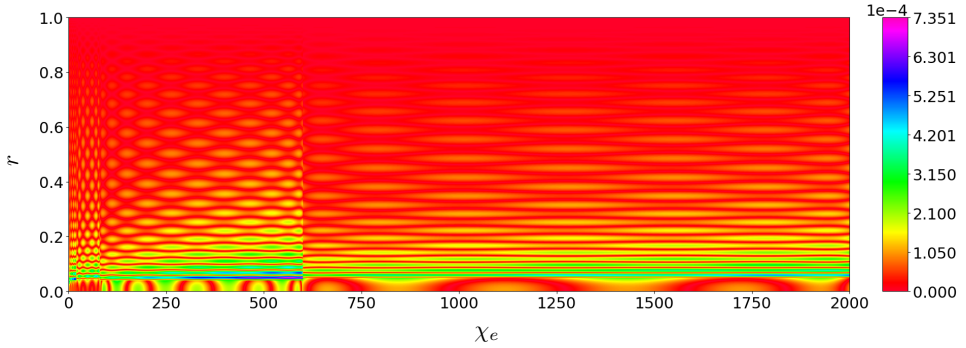

Figure 3.4: Relative difference $\Delta_r(\chi_e, r)$ between the exact and the `SFQEDtoolkit` computed photon emission energies (see `SFQED_LCFA_INV_COMPTON_PHOTON_energy` in A). The contour plot is obtained by evenly evaluating $\Delta_r(\chi_e, r)$ at $10^4(\chi_e) \times 10^3(r)$ points in the domain $0 \leq \chi_e \leq 2000$, $0 \leq r \leq 1$. The colorbar ranges from the lowest to the highest recorded Δ_r.

Similarly to the photon emission rate, the domain of χ_e and r was divided into smaller intervals either to reduce the required number of Chebyshev coefficients or to use a different approximation method. The same intervals as for the photon emission rate were used for χ_e, while r was divided into four intervals: $0 < r \leq r_{min}$, $r_{min} < r \leq r_{inv}$, $r_{inv} < r \leq r_{max}$, and $r_{max} < r < 1$. The value of r_{min}, r_{inv} and r_{max} depends on χ_e, and is reported in Tab. 3.3. Table 3.1 summarizes the decomposition of the domain, the method used in each interval and, when the function is approximated with Chebyshev polynomials, the number of employed Chebyshev coefficients. Figure 3.4 plots the value of Δ_r for the whole range of $0 \leq \chi_e \leq 2000$ and $0 < r < 1$, which shows that $\Delta_r < 10^{-4}$ throughout the whole considered domain.

For its implementation in `SFQEDtoolkit`, the function I_{pe} in eq. (3.33) was converted to normalized units, and the dummy variable of integration was changed from ε_γ to

$$w = \sqrt[3]{\frac{2\varepsilon_\gamma}{3(\varepsilon_e - \varepsilon_\gamma)\chi_e}}; \qquad \varepsilon_\gamma = \frac{3\varepsilon_e \chi_e w^3}{2 + 3\chi_e w^3}, \tag{3.34}$$

which gives

$$I_{pe}(\bar{w}, \varepsilon_e, \chi_e) = \frac{\alpha}{\sqrt{3}\pi} \frac{\lambda_r}{\lambda_C} \frac{\chi_e}{\gamma_e} \omega_r \tilde{I}_{pe}(\bar{w}, \chi_e), \tag{3.35}$$

where

$$\tilde{I}_{pe}(\bar{w},\chi_e) = \int_0^{\bar{w}} \frac{9w^2 dw}{2(1+s)^3}\left\{\left[1+(1+s)^2\right]\mathrm{K}_{\frac{2}{3}}(w^3) - (1+s)\int_{w^3}^{\infty}\mathrm{K}_{\frac{1}{3}}(y)dy\right\}, \quad (3.36)$$

and $s = 3\chi_e w^3/2$. By comparing eq.s (3.25) and (3.35), one finds that the ITS equation (3.32) simplifies to

$$\tilde{I}_{pe}(\bar{w},\chi_e) - r\tilde{W}_{\mathrm{rad}}(\chi_e) = 0. \quad (3.37)$$

From $\bar{w}$, the photon energy ε_γ is easily obtained via Eq. (3.34). The change of variable defined in Eq. (3.34) improves the smoothness of I_{pe} by removing the $\varepsilon_\gamma^{-2/3}$ singularity of the integrand for $\varepsilon_\gamma \to 0$, thereby reducing the required number of Chebyshev coefficients.

We begin describing how `SFQEDtoolkit` implements the two-variable function $\bar{w} = \tilde{G}_{pe}(r,\chi_e)$, implicitly defined by eq. (3.37) in the interval $r_{min} < r < r_{max}$. A natural choice is to approximate $\tilde{G}_{pe}(r,\chi_e)$ with Chebyshev polynomials. In practice, despite this approach performs extremely well almost everywhere, $\tilde{G}_{pe}(r,\chi_e)$ and its derivatives rapidly grow for $r \to r_{max}$ such that the number of Chebyshev coefficients needed to accurately approximate the region around r_{max} becomes large. To reduce the number of required coefficients while retaining high accuracy, in the interval $r_{min} < r < r_{inv}$ and $r_{inv} < r < r_{max}$ the Chebyshev expansion of $\tilde{G}_{pe}(r,\chi_e)$ and of $1/\tilde{G}_{pe}(r,\chi_e)$ is respectively employed. In the latter case, $\tilde{G}_{pe}(r,\chi_e)$ is then readily obtained from $[1/\tilde{G}_{pe}(r,\chi_e)]^{-1}$.

By contrast, `SFQEDtoolkit` solves eq. (3.37) in the limit $r \to 0$ and $r \to 1$, i.e., when the lower and the higher energy tail of the photon spectrum are approached, by resorting to asymptotic expansions and exponential approximations. For $r \to 0$, one can expand eq. (3.36) as

$$\tilde{I}_{pe}(\bar{w},\chi_e) \xrightarrow{\bar{w}\to 0} \frac{9}{2^{1/3}}\Gamma\left(\frac{2}{3}\right)\bar{w}, \quad (3.38)$$

which is a better than 0.1% approximation of $\tilde{I}_{pe}(\bar{w},\chi_e)$ for $r \leq r_{min}$. Then by substituting eq. (3.38) in eq. (3.37), one immediately obtains

$$\bar{w} = r\tilde{W}_{\mathrm{rad}}(\chi_e)\left[\frac{9}{2^{1/3}}\Gamma\left(\frac{2}{3}\right)\right]^{-1}. \quad (3.39)$$

Regarding $r \to 1$, i.e., $\bar{w} \to \infty$, we leverage on the fact that for $\bar{w}$ above a certain threshold w_0, the function $\tilde{I}_{pe}(\bar{w},\chi_e)$ saturates to $\tilde{W}_{\mathrm{rad}}(\chi_e) = \tilde{I}_{pe}(\infty,\chi_e)$ and the following exponential approximation holds

$$\tilde{I}_{pe}(\bar{w},\chi_e) \approx \tilde{W}_{\mathrm{rad}}(\chi_e)(1 - e^{-(\bar{w}^3 - w_0^3)}) + \tilde{I}_{pe}(w_0,\chi_e)e^{-(\bar{w}^3 - w_0^3)}. \quad (3.40)$$

By substituting eq. (3.40) in eq. (3.37) one obtains

$$\bar{w} = \sqrt[3]{w_0^3 - \log\left[\frac{C[\tilde{W}_{\mathrm{rad}}(\chi_e)](1-r)}{C[\tilde{W}_{\mathrm{rad}}(\chi_e)] - C[\tilde{I}_{pe}(w_0,\chi_e)]}\right]}. \quad (3.41)$$

Note that: (i) there is no need to calculate the cubic root in eq. (3.41) since ε_γ depends on $\bar{w}^3$; (ii) in eq. (3.41) we have explicitly indicated that in `SFQEDtoolkit` the Chebyshev expansions of $\tilde{W}_{\rm rad}(\chi_e)$ and $\tilde{I}_{pe}(w_0,\chi_e)$ have been used; (iii) this approximation is used for $r \geq r_{max}$, and the corresponding χ_e-dependent threshold w_0 is obtained from $w_0 = C[\tilde{G}_{pe}(r_{max},\chi_e)]$, where $C[\tilde{G}_{pe}(r_{max},\chi_e)]$ is the Chebyshev approximation of the function obtained by setting $r = r_{max}$ in eq. (3.37).

We implemented `SFQEDtoolkit` in the open source PIC code Smilei [63, 73] version 4.7 and simulated the evolution of an ensemble of 10^{10} electrons. The charge density was kept very low to suppress self-fields−i.e., the fields generated by the ensemble of charges and their motion−and particles were placed in a constant and uniform external magnetic field with 10 GeV energy. Simulation parameters were chosen such that $\chi_e = 1$, initially. The total simulation time was set to one tenth of the time expected for an electron to emit once. We then repeated the same simulation using the original version of Smilei, which makes use of 256-points pre-computed lookup tables and compared the results with those obtained with `SFQEDtoolkit`. Figure 3.5(a) displays the photon spectrum obtained from the original version of Smilei (red line), with `SFQEDtoolkit` (blue line), and the analytical prediction (dashed green line). While Smilei with its default 256-points tables shows a marked stairlike pattern at high photon energies and a significant deviation from the analytic spectrum also for photon energies around $0.2\,\varepsilon_e$, `SFQEDtoolkit` nearly perfectly matches the analytic spectrum throughout the whole domain. Note that such discrepancies of Smilei with its 256-points tables with respect to the analytic spectrum originate from the coarse tabulation. By employing Smilei with 1024-points tables the agreement with the analytic spectrum significantly improves with respect to the 256-points tables, particularly in the region $\varepsilon_\gamma/\varepsilon_e \sim 0.2$, while the stairlike pattern is much milder but remains visible also with 1024-points tables. Regarding performance, a direct comparison of the execution time of the default version of Smilei and of the `SFQEDtoolkit` implementation does not directly reflect the improvement, because the total simulation time is strongly determined by the other operations of the PIC loop. Nevertheless, in our tests the implementation with `SFQEDtoolkit` outperformed the 256 points default Smilei by up to 12%.

3.3.4 Pair creation spectrum

The same methodology employed to sample the energy of emitted photons applies in the case of photon conversion into an electron-positron pair. One needs to solve the equation

$$\int_0^{\bar{\varepsilon}} \frac{d^2W_{pp}}{dtd\varepsilon_e}(\varepsilon_e,\varepsilon_\gamma,\chi_\gamma)d\varepsilon_e - r\int_0^{\varepsilon_\gamma} \frac{d^2W_{pp}}{dtd\varepsilon_e}(\varepsilon_e,\varepsilon_\gamma,\chi_\gamma)d\varepsilon_e = I_{pp}(\bar{\varepsilon},\varepsilon_\gamma,\chi_\gamma) - rR_{pp}(\varepsilon_\gamma,\chi_\gamma) = 0, \tag{3.42}$$

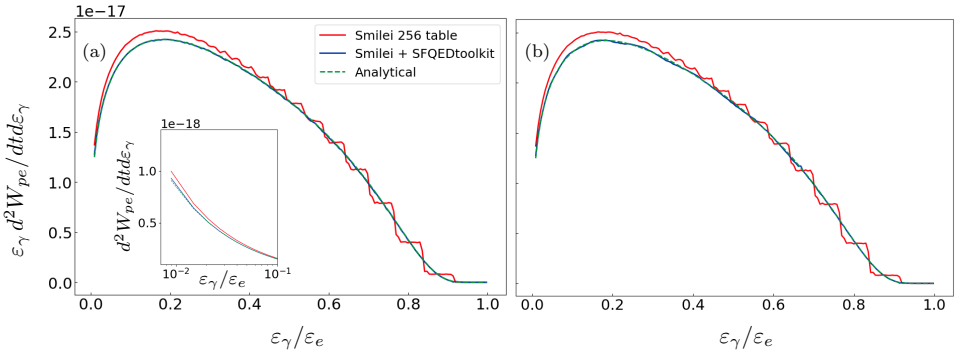

Figure 3.5: Synchrotron emission spectrum (main panel) and the low-energy region of the differential distribution (inset) obtained from the evolution of 10^{10} electrons with 10 GeV energy located in a constant and uniform magnetic field (such that $\chi_e = 1$). The results of the simulation performed using the default 256×256 points table of Smilei (red solid line), the results of the same simulation with the `SFQEDtoolkit` implementation (blue solid line) and the analytical spectrum (green dashed line) are showcased. The solid blue line in panels (a) and (b) displays the results obtained from the `SFQEDtoolkit` implementation where the provided 17×35 Chebyshev coefficient's matrix and the reduced 15×25 sub-matrix are used, respectively. See Sec. 3.3.5 for details.

where $I_{pp}(\bar{\varepsilon}, \varepsilon_\gamma, \chi_\gamma)$ is obtained by integrating Eq. (3.23) up to $\bar{\varepsilon}$

$$I_{pp}(\bar{\varepsilon}, \varepsilon_\gamma, \chi_\gamma) = \int_0^{\bar{\varepsilon}} \frac{d^2W_{pp}}{dtd\varepsilon_e}(\varepsilon_e, \varepsilon_\gamma, \chi_\gamma)d\varepsilon_e. \tag{3.43}$$

In `SFQEDtoolkit`, we exploited the symmetry of Eq. (3.43) with respect to $\varepsilon_\gamma/2$ to halve the domain of integration to $\varepsilon_\gamma/2 < \varepsilon_e < \varepsilon_\gamma$, converted to normalized units, and changed the dummy variable of integration to

$$v = \frac{2\varepsilon_e - \varepsilon_\gamma}{\varepsilon_\gamma}; \qquad \varepsilon_e = \frac{\varepsilon_\gamma(1+v)}{2}. \tag{3.44}$$

Thus, the equation that needs to be solved simplifies to

$$\tilde{I}_{pp}(\bar{v}, \chi_\gamma) - |r'|\tilde{W}_{\text{pair}}(\chi_\gamma) = 0 \tag{3.45}$$

where

$$\tilde{I}_{pp}(\bar{v}, \chi_\gamma) = \int_0^{\bar{v}} \left[\frac{2(1+v^2)}{1-v^2}\mathrm{K}_{\frac{2}{3}}(\eta_v) + \int_{\eta_v}^{\infty} \mathrm{K}_{\frac{1}{3}}(y)\, dy\right] dv, \tag{3.46}$$

$\eta_v = 8/[3\chi_\gamma(1-v^2)]$, and $r' = 2r - 1$ is a random number uniformly distributed in $-1 < r' < 1$ obtained from a random number r defined in $0 < r < 1$. Equation (3.45) defines an implicit function $\bar{v} = \tilde{G}_{pp}(|r'|, \chi_\gamma)$. Once $\bar{v}$ has been determined, the relation

$$\varepsilon_e = \frac{\varepsilon_\gamma[1 + \mathrm{sgn}(r')v]}{2} \tag{3.47}$$

allows us to obtain the electron ε_e and positron $\varepsilon_p = \varepsilon_\gamma - \varepsilon_e$ energy in their full $(0, \varepsilon_\gamma)$ domain. For χ_γ the domain of the function $\tilde{G}_{pp}(|r'|, \chi_\gamma)$ is divided into six intervals (see Tab. 3.2), while for $|r'|$ it is divided into three intervals: $0 \leq |r'| < 0.9$, $0.9 \leq |r'| \leq 0.9999$, and $|r'| > 0.9999$. In $0 \leq |r'| \leq 0.9999$, Chebyshev polynomials are used to approximate $\tilde{G}_{pp}(|r'|, \chi_\gamma)$ to the desired accuracy. The division into two intervals, i.e., in two distinct set of Chebyshev coefficients, is made only to reduce the number of required coefficients in the more probable region $0 \leq |r'| < 0.9$. In fact, when $|r'| \to 1$ the number of coefficients necessary to accurately approximate $\tilde{G}_{pp}(|r'|, \chi_\gamma)$ increases dramatically, and to preserve the computational speed granted by working with a restricted set of coefficients, we have chosen to separate the smaller interval requiring a larger number of coefficients $|r'| > 0.9$ from the more probable range $0 \leq |r'| < 0.9$. Finally, for $|r'| > 0.9999$ an exponential approximation similar to eq. (3.40) is used to approximate the cumulative function

$$\tilde{I}_{pp}(\bar{\nu}, \chi_\gamma) \approx \tilde{W}_{\text{pair}}(\chi_\gamma) \left[1 - e^{-\left(\frac{8}{3\chi_\gamma (1-\nu^2)} - \frac{8}{3\chi_\gamma (1-\nu_0^2)} \right)} \right] + \tilde{I}_{pp}(\bar{\nu}_0, \chi_\gamma) e^{-\left(\frac{8}{3\chi_\gamma (1-\nu^2)} - \frac{8}{3\chi_\gamma (1-\nu_0^2)} \right)}. \tag{3.48}$$

By substituting eq. (3.48) in eq. (3.45) one obtains

$$\bar{\nu} = \sqrt{1 - \left(\frac{1}{1-\nu_0^2} - \frac{3\chi_\gamma}{8} \log \left[\frac{C[\tilde{W}_{\text{pair}}(\chi_\gamma)](1-r)}{C[\tilde{W}_{\text{pair}}(\chi_\gamma)] - C[\tilde{I}_{pp}(\bar{\nu}_0, \chi_\gamma)]} \right] \right)^{-1}}, \tag{3.49}$$

where we have indicated that in `SFQEDtoolkit` a Chebyshev expansion is used to compute $\tilde{W}_{\text{pair}}(\chi_\gamma)$ as well as $\tilde{I}_{pp}(\bar{\nu}_0, \chi_\gamma)$, and $\nu_0 = C[\tilde{G}_{pp}(0.9999, \chi_\gamma)]$.

The function `SFQED_BREIT_WHEELER_ELECTRON_energy` returns the energy of the created electron once the normalized photon energy γ_γ, quantum parameter χ_γ and a random number r uniformly distributed in $(0, 1)$ are provided as input parameters. Figure 3.6 displays the accuracy of the approximation $\Delta_r = |\bar{\varepsilon}_{ITS} - \bar{\varepsilon}_{tk}| / \bar{\varepsilon}_{ITS}$ in the domain $0.3 < \chi_\gamma < 2000$ and $0 < r < 1$. Symbols have the same meaning as in the photon emission case.

3.3.5 Changing the number of coefficients used in a simulation

`SFQEDtoolkit` allows users to reduce the number of Chebyshev coefficients to be employed at runtime, therefore reducing the accuracy but possibly enhancing the performance of the library. For instance, the Chebyshev coefficients c_i of a one-variable function $f(x)$ are stored in text files where the first row is an integer reporting the total number n of coefficients stored in the file, the second and third row contain floating point numbers that report the minimum and the maximum of the interval where the function is approximated with Chebyshev polynomials, respectively, while from the fourth row on the coefficients c_i are written row by row. By adding a colon followed by an integer $k < n$, i.e., by replacing n with $n : k$, only the leading k coefficients out of the n total are employed at runtime.

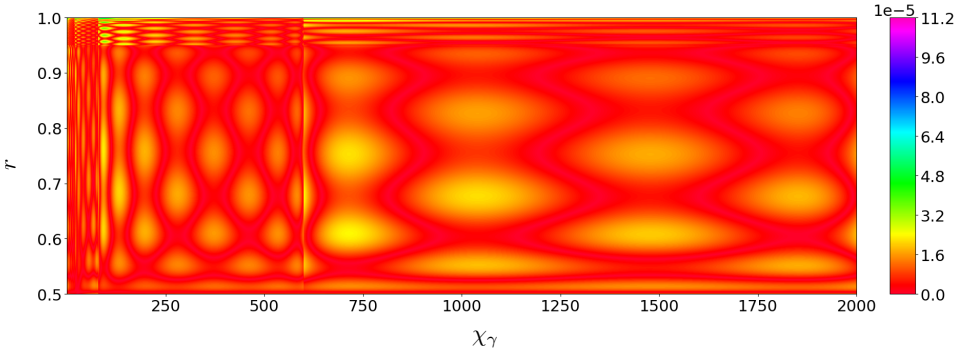

Figure 3.6: Relative difference $\Delta_r(\chi_\gamma, r)$ between the exact and the `SFQEDtoolkit` computed lepton energy in the nonlinear Breit-Wheeler conversion of an energetic photon in an electron-positron pair (see `SFQED_BREIT_WHEELER_ELECTRON_energy` in A). The contour plot is obtained by evenly evaluating $\Delta_r(\chi_\gamma, r)$ at $10^4(\chi_\gamma) \times 10^3(r)$ points in the domain $0.3 \leq \chi_e \leq 2000$, $0.5 \leq r \leq 1$. The colorbar ranges from the lowest to the highest recorded Δ_r.

Similarly, the Chebyshev coefficients c_{ij} of a two-variable function $f(x, y)$ are stored in text files where the first and fourth row report the number of columns n and of rows m of c_{ij}, respectively. The second and third (fifth and sixth) row of the file report the minimum and the maximum of first x (second y) variable of $f(x, y)$, respectively. Finally, starting from the seventh row of the file the coefficients c_{ij} are written row by row following a row-major order. Also in this case, one can reduce the number of used coefficients by editing the first (fourth) row of the file, i.e, replacing n (m) with $n : k$ ($m : l$) where k (l) is an integer smaller than n (m). Unless otherwise specified, `SFQEDtoolkit` uses all the coefficients available in a file.

For example, by repeating the simulation reported in Fig. 3.5(a) with a set of 15×25 coefficients (instead of the 17×35 provided with `SFQEDtoolkit`), the relative error rises up to 0.7% while the time to execute the specific task of calculating the photon spectrum reduces by approximately 30%. Figure 3.5(b) displays the photon spectrum obtained with the above-mentioned reduced set of coefficients. Even with the reduced set of coefficients, `SFQEDtoolkit` provides a photon spectrum in manifestly much better agreement with the analytical prediction than Smilei's default algorithm and 256×256 points table [see Fig. 3.5(b)].

3.4 Photon emission beyond the locally-constant-field approximation

In the following we detail how the method of photon emission beyond LCFA developed in Ref. [62] is implemented in `SFQEDtoolkit`. In order to retain flexibility and allow users to better adapt and customize functionality to their codes,

`SFQEDtoolkit` provides a set of independent functions, each carrying out a specific task of the algorithm.

We begin by briefly reviewing the rationale of the algorithm. As detailed in Ref. [62], the differential probability of photon emission $d^2W_{pe}/dtd\gamma_\gamma$ becomes almost flat for a broad range of photon energies below a threshold $\gamma_{\gamma,\mathrm{LCFA}}$, here normalized to m_ec^2, while it nearly coincides with the LCFA distribution above this threshold. Before proceeding, it must be mentioned that from this point onward the just described differential probability, and the photon emission rate related to it, will be referred to as the *improved* (or BLCFA) differential probability, and the *improved* rate. This implies that the use of the standard LCFA rate systematically results in an orders of magnitude overestimated number of emitted photons for $\varepsilon_\gamma \lesssim (\chi_e/\xi^3)\varepsilon_e$. Notice that $\gamma_{\gamma,\mathrm{LCFA}}$ depends on a characteristic local time of variation τ of the transverse Lorentz force $\vec{F}_{L,\perp}$ experienced by the emitting particle. This characteristic time τ is obtained from the first $\dot{\vec{F}}_{L,\perp}$ and second $\ddot{\vec{F}}_{L,\perp}$ time derivative of $\vec{F}_{L,\perp}$ calculated along the emitting particle's trajectory [62].

We stress that the calculation of the improved rate of photon emission for each particle and at each timestep now becomes relatively complex and computationally expensive. A simpler and more efficient option is to use the LCFA usual rate of photon emission to determine whether a photon emission event occurs. Only if the event is deemed to occur according to the LCFA model, then the expected photon energy is sampled from the LCFA differential probability of photon emission. If the sampled photon energy $\bar{\gamma}_\gamma$ exceeds the threshold $\gamma_{\gamma,\mathrm{LCFA}}$, a photon with energy $\bar{\gamma}_\gamma$ is generated and the emitting particle recoils. Otherwise, the photon emission event is either accepted or rejected by comparing an independent uniformly distributed random number in $(0, 1)$ with the ratio between the LCFA and the improved differential probability of photon emission calculated at $\bar{\gamma}_\gamma$ (see below). This greatly improves the performance of the code, given that most of the above-mentioned extra computational steps are performed rarely and only when needed.

`SFQEDtoolkit` provides a `C++` object named `BLCFA_Object` which contains (i) a three-element double precision array to store the transverse Lorentz force at the penultimate timestep, (ii) a three-element double precision array to store the difference between the Lorentz force at the penultimate and the antipenultimate timestep, and (iii) a boolean signaling whether the particle was created at the penultimate timestep. This boolean is needed because for a new particle the transverse Lorentz force at the penultimate and antipenultimate timestep is not available, and it thus serves to establish whether the algorithm we are going to illustrate is eligible to be employed or not (see Ref. [62] and below). These quantities, together with the simulation timestep Δt, the emitting particle energy γ_e and quantum parameter χ_e, are used by the routine `SFQED_BLCFA_INV_COMPTON_PHOTON_threshold` to calculate the threshold $\gamma_{\gamma,\mathrm{LCFA}}$ (see below and A)[6].

[6]In addition, the class `BLCFA_Object` has been conceived to derive, through inheritance, an

For clarity and completeness, we summarize below the steps needed to calculate $\gamma^{(n)}_{\gamma,\mathrm{LCFA}}$ at the (n)-th timestep, as well as the acceptance-rejection method. Following Ref. [62], by starting from $\vec{x}^{(n)}$ and $\vec{p}^{(n-1/2)}$ advance the momentum to $\vec{p}^{(n+1/2)}_L$ with the Lorentz force integrator existing in the code[7]. If the particle was created at the penultimate timestep, which is signaled by the boolean of the `BLCFA_Object`, set $\boldsymbol{F}^{(n-2)}_{L,\perp} = \boldsymbol{F}^{(n-1)}_{L,\perp} = \boldsymbol{F}^{(n)}_{L,\perp}$, then update the boolean describing its status, and continue to the next particle. Otherwise, calculate

$$\boldsymbol{F}^{(n)}_L = \frac{\boldsymbol{p}^{(n+1/2)}_L - \boldsymbol{p}^{(n-1/2)}}{\Delta t}, \tag{3.50}$$

$$\boldsymbol{p}^{(n)}_L = \frac{\boldsymbol{p}^{(n+1/2)}_L + \boldsymbol{p}^{(n-1/2)}}{2}, \tag{3.51}$$

$$\gamma^{(n)}_e = \sqrt{1 + [\boldsymbol{p}^{(n)}_L]^2}, \tag{3.52}$$

$$\boldsymbol{F}^{(n)}_{L,\perp} = \boldsymbol{F}^{(n)}_L - \frac{\boldsymbol{F}^{(n)}_L \cdot \boldsymbol{p}^{(n)}_L}{[\gamma^{(n)}]^2}\boldsymbol{p}^{(n)}_L, \tag{3.53}$$

$$\chi^{(n)}_e = \tau_C \gamma^{(n)} \sqrt{\left[\boldsymbol{F}^{(n)}_{L,\perp}\right]^2}, \tag{3.54}$$

where τ_C is the Compton time and normalized units are employed. Note that the ultrarelativistic approximation $\boldsymbol{p}^{(n)}_L/|\boldsymbol{p}^{(n)}_L| \approx \boldsymbol{p}^{(n)}_L/\gamma^{(n)}$ is used in Eq. (3.53). Compute

$$\dot{\boldsymbol{F}}^{(n)}_{L,\perp} = \frac{\boldsymbol{F}^{(n)}_{L,\perp} - \boldsymbol{F}^{(n-1)}_{L,\perp}}{\Delta t}, \tag{3.55}$$

$$\ddot{\boldsymbol{F}}^{(n)}_{L,\perp} = \frac{(\boldsymbol{F}^{(n)}_{L,\perp} - \boldsymbol{F}^{(n-1)}_{L,\perp}) - (\boldsymbol{F}^{(n-1)}_{L,\perp} - \boldsymbol{F}^{(n-2)}_{L,\perp})}{(\Delta t)^2}, \tag{3.56}$$

$$\delta^{(n)} = \tau_C^2 \left[(\dot{\boldsymbol{F}}^{(n)}_{L,\perp})^2 + |\boldsymbol{F}^{(n)}_{L,\perp} \cdot \ddot{\boldsymbol{F}}^{(n)}_{L,\perp}|\right]. \tag{3.57}$$

If $(\gamma^{(n)})^2\delta^{(n)}/\zeta^2 > (\chi^{(n)})^2(\boldsymbol{F}^{(n)}_{L,\perp})^2$ and $\chi^{(n)} > \zeta$, where ζ is a nearly negligible number relative to unity[8], then calculate $\tau^{(n)}/\tau_C = 2\pi\sqrt{[\boldsymbol{F}^{(n)}_{L,\perp}]^2/\delta^{(n)}}$. Otherwise the background fields are either basically constant, and the LCFA applies throughout the photon spectrum, or the quantum parameter $\chi^{(n)}$ is negligibly small. This condition is introduced to avoid numerical issues for constant background fields, where

extended C++ object, which can be used to include all needed information on the state of a computational particle. In the given PIC or Monte Carlo code where the user wants to implement `SFQEDtoolkit`, a linked list, or possibly better for memory locality, an array or a C++ vector class of particle objects derived from `BLCFA_Object` can be used to describe the state of an arbitrary number of computational particles. Each `BLCFA_Object` is created by calling the routine `SFQED_CREATE_BLCFA_OBJECT`, and its content is updated at each timestep and for each particle via the routine `SFQED_BLCFA_OBJECT_update` (see A for details).

[7] Here we consider a leapfrog integrator, i.e., position and momentum are shifted by half step. There is however no conceptual difference in the method if position and momentum are given at the same timestep, such as in a Runge-Kutta method.

[8] Assuming double precision arithmetic $\zeta \approx 2.22 \times 10^{-16}$.

the LCFA holds and $\tau^{(n)}/\tau_C$ diverges. Finally, following Ref. [62]

$$\gamma^{(n)}_{\gamma,\mathrm{LCFA}} = \frac{0.7\gamma_e^{(n)}}{1+\frac{4}{3\pi\chi_e^{(n)}}\sinh\left[3\sinh^{-1}\left(\frac{\chi_e^{(n)}}{8\gamma_e^{(n)}}\frac{\tau^{(n)}}{\tau_C}\right)\right]}, \tag{3.58}$$

and the condition $\gamma^{(n)}_{\gamma,\mathrm{LCFA}} < 0.75\gamma_e^{(n)}$ is evaluated. If this latter condition is violated, most of the spectrum is not approximated by the LCFA model, and the formation of the emission probability becomes an intrinsically nonlocal process. In this case we assume that no emission is deemed for the considered particle at this timestep.

Once $\gamma^{(n)}_{\gamma,\mathrm{LCFA}}$ is known, the routine `SFQED_BLCFA_INV_COMPTON_PHOTON_energy` samples the photon energy according the beyond (improved) LCFA differential probability of photon emission. Its input arguments are $\gamma_e^{(n)}, \chi_e^{(n)}, \gamma^{(n)}_{\gamma,\mathrm{LCFA}}$ as well as two independent uniformly distributed random numbers $0 < r_1 < 1$ and $0 < r_2 < 1$. This routine first calls `SFQED_LCFA_INV_COMPTON_PHOTON_energy`, by giving r_1 as input parameter, to sample the LCFA-predicted emitted photon energy $\bar{\gamma}_\gamma$. If $\bar{\gamma}_\gamma > \gamma^{(n)}_{\gamma,\mathrm{LCFA}}$, the routine simply returns $\bar{\gamma}_\gamma$. Otherwise, `SFQED_BLCFA_INV_-COMPTON_PHOTON_energy` uses the second random number r_2 to evaluate the condition

$$r_2\left[\frac{d^2W_{pe}}{dtd\gamma_\gamma}(\bar{\gamma}_\gamma,\gamma_e,\chi_e)\right] \leq \frac{d^2W_{pe}}{dtd\gamma_\gamma}(\gamma^{(n)}_{\gamma,\mathrm{LCFA}},\gamma_e,\chi_e). \tag{3.59}$$

If eq. (3.59) is fulfilled, then the routine returns $\bar{\gamma}_\gamma$. Otherwise, it returns zero, which implies that no photon emission occurs. Note that in eq. (3.59) γ_e has been written for clarity but is a global constant factor which multiplies both sides therefore canceling out. Hence, it is not used for evaluating eq. (3.59) in the code. In addition, for its implementation the change of variable $\gamma_\gamma = (3\gamma_e\chi_e w^3)/(2+3\chi_e w^3)$ was performed, which gives

$$\frac{d^2W_{pe}}{dtd\gamma_\gamma} = \frac{d^2W_{pe}}{dtdw}\left(\frac{d\gamma_\gamma}{dw}\right)^{-1} = \frac{d^2W_{pe}}{dtdw}\frac{(2+3w^3\chi_e)^2}{18\gamma_e w^2\chi_e}. \tag{3.60}$$

The above change of variable is motivated by the fact that the function $d^2W_{pe}/dtdw$ is efficiently approximated with Chebyshev polynomials in `SFQEDtoolkit`. By contrast, $d^2W_{pe}/dtd\gamma_\gamma$ exhibits a $\gamma_\gamma^{-2/3}$ divergence when γ_γ tends to zero, which makes it unsuitable for being expanded with Chebyshev polynomials, directly (see discussion in sec. 2.6).

Figure 3.7 displays the results obtained after implementing `SFQEDtoolkit` routines into a fourth-order Runge-Kutta pusher, and by repeating the electron beam-laser pulse simulations with the same choice of electron and laser parameters as in Ref. [62]. By comparing the results in Fig. 3.7 with the corresponding results in Ref. [62], it is apparent that the improved beyond LCFA spectrum is recovered.

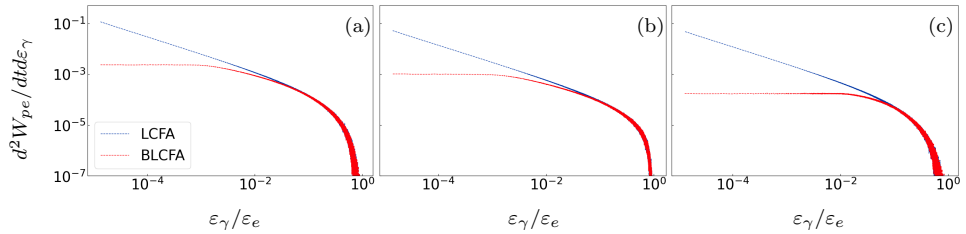

Figure 3.7: The LCFA vs the beyond LCFA (see Ref. [62]) differential photon emission probability for an electron colliding head-on with a plane-wave pulse for the following parameters: (a) 5 GeV electron initial energy, 5 fs (FWHM of the intensity) pulse duration, and $a_0 = 8$ normalized field amplitude; (b) 10 GeV electron initial energy, 5 fs pulse duration, and $a_0 = 10$ normalized field amplitude; (c) 10 GeV electron initial energy, 10 fs pulse duration, and $a_0 = 3$ normalized field amplitude.

3.5 Conclusions

In this chapter we have presented a novel approach that allows an efficient implementation of the complex and computationally expensive functions needed to model strong-field QED processes into codes. This approach leverages on a combination of advanced function approximation techniques, and its key concepts can be naturally used in other areas of research. The method resorts to a combination of: (i) function approximation with Chebyshev polynomials; (ii) asymptotic expansions; (iii) variable and function transformation (see the end of sec. 2.6). We have applied this method to create an open source library named `SFQEDtoolkit`, which is designed to allow users for a straightforward implementation of SFQED processes, namely nonlinear Compton emission and nonlinear Breit-Wheeler pair creation, in existing particle-in-cell and Monte Carlo codes.

`SFQEDtoolkit` provides users with an efficient and better than 0.1% accuracy implementation of SFQED processes throughout the whole particles' spectrum. Benchmarks performed with the PIC code Smilei version 4.7 have shown that `SFQEDtoolkit` outperforms the default 256-points tables and achieves an accuracy better than that of 1024-points lookup-tables. Currently, photon emission and pair creation with $\chi_{e/\gamma} \leq 2000$ are implemented by assuming the locally-constant-field approximation and collinear emission of the generated particles. For photon emission, the more advanced method beyond the locally-constant-field approximation presented in Ref. [62] (and section 3.4) is also included. The implementation of the angular distribution of generated particles, as well as of the spin and polarization-dependent SFQED processes will be presented in chapter 5.

Chapter 4

The "thick-target" simulation: production of solid-density e^+-e^- jets in beam-plasma collision

Electron-positron ($e^\pm$) pairs are believed to be essential components of the plasma in the vicinity of pulsars and magnetars, within the accretion disks surrounding black holes, and in the jet plasma of quasars [74–78]. In these extreme environments, $e^\pm$ pairs are often immersed in intense electromagnetic fields and exposed to a bath of radiation containing photons spanning a wide range of energies [75]. While our knowledge of $e^\pm$ plasmas is still speculative, the mass symmetry of positrons and electrons is believed to result in unique behaviors that differ qualitatively from those of conventional ion-electron plasmas [79–81]. Open questions include the study of the spatiotemporal dynamics of $e^\pm$ beams, as well as the transition between the linear and nonlinear stage of ultrarelativistic pair-plasma instabilities, of which little is currently known [82]. However, due to the formidable technical challenges in producing and maintaining a large number of e^+, the creation of quasi-neutral $e^\pm$ plasmas, particularly under highly magnetized conditions, remains a critical step toward probing the microphysics governing extreme astrophysical environments in the laboratory [83, 84].

Methods for generating $e^\pm$ beams include pair production from high-energy protons [85], electrons [86], or photon beams. In the latter method, high-energy photons are typically produced via bremsstrahlung when energetic particles collide with the nuclei of a target. These photons subsequently interact with the target nuclei, converting into $e^\pm$ pairs via the Breit-Wheeler process [17, 87]. Despite recent experimental advancements using these methods, the resulting pair plasmas have not yet exhibited collective features [17, 85]. High-energy electron beam collisions with intense laser pulses have also been proposed as a high-yield source of particle-antiparticle pairs, potentially suitable for probing collective pair plasma effects [88]. In this scheme, $e^\pm$ pair generation occurs through strong-field quantum electrodynamics (QED) cascades. Initially, high-energy photons are produced through the interaction of an intense optical laser pulse with an electron beam via NIC. Subsequently, $e^\pm$ pairs are generated from photon decay in the intense laser field, a process known as NBW pair production [44, 54, 89]. However, probing the interplay between SFQED and plasma dynamics via electron beam-laser pulse collisions requires the simultaneous availability of tens-of-GeV electron beams and multipetawatt laser pulses, a combination that is not currently present at any facil-

ity worldwide. Furthermore, this approach is hampered by significant shot-to-shot fluctuations as well as the stringent alignment and synchronization requirements between the electron beam and the laser pulse, which have thus far hindered substantial experimental progress.

In this work we present a laserless, single-electron-beam approach for producing low-emittance, collimated gamma-ray and $e^{\pm}$ pair jets with densities up to three orders of magnitude higher than that of a solid.

4.1 The simulation set-up

We have conducted fully three-dimensional (3D) particle-in-cell (PIC) simulations to study the interaction of an electron beam with a stack of thin aluminum foil [90], followed by its interaction with a thick target conductor (see Fig. 4.1). The initial electron beam has a charge of 2 nC and features Gaussian spatial and momentum distributions with a spherical shape and a full width at half maximum (FWHM) of 1.3 μm. It has a mean energy of 10 GeV, an energy spread of 212 MeV FWHM, and a normalized emittance of 3 mm-mrad. The beam collides with six consecutive aluminum foils, each with a thickness of 0.5 μm, an interfoil distance of 10 μm, and an initial electron density of 1.8×10^{29} m^{-3}. After interacting with the six thin foils, the mean beam energy is approximately 8.9 GeV. Notably, the simulation up to this stage was previously performed by our group in [90].

The electron beam generated from this "multifoil interaction" is then extracted, while high-energy photons and $e^{\pm}$ pairs produced in the process are neglected. The electron beam is subsequently used as input for three separate simulations, which are the focus of this chapter. In the first and second simulations, the 8.9 GeV electron beam collides with thick targets made of lithium and gold, respectively. The third simulation closely follows the second, but instead uses an 89 GeV electron beam, which is initialized by scaling up the momenta of all particles in the 8.9 GeV beam by a factor of ten.

4.1.1 Simulation specifics

At the start of the simulations, the center of the electron beam is approximately 5 μm from the surface of the foil, and particles' momentum is not updated for the first 3.42 μm to allow for the beam's self-field creation before the beam interacts with the target. Simulations were independently conducted using CALDER [43] and the open-source PIC code Smilei [63], showing very good agreement. The initial self-consistent beam fields, the effects of field [91] and collisional [92] ionization, and binary Coulomb collisions were included [92]. Bremsstrahlung emission and Bethe-Heitler pair production were implemented using state-of-the-art Monte-Carlo methods [93]. Nonlinear inverse Compton scattering (NIC) and nonlinear

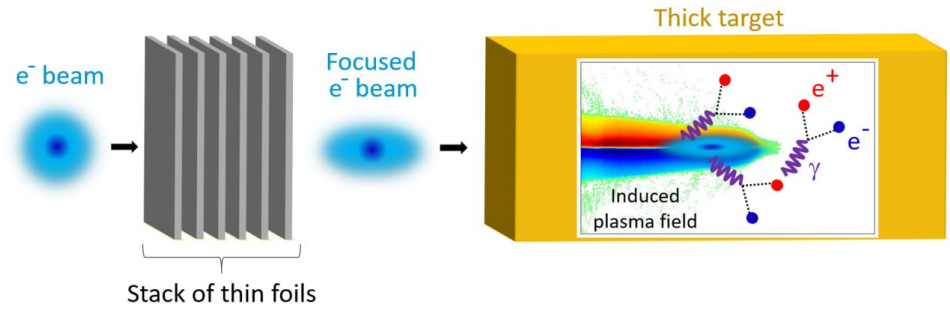

Figure 4.1: A dense, high-energy electron beam is directed at a stack of thin Al foils, where it is focused by the strong coherent transition radiation generated at the surface of each foil. The focused beam then collides with a thick target conductor (Li and Au are considered here), generating a plasma channel with ultra-strong electromagnetic fields, which field-ionize the conductor atoms. The interaction of the beam with the self-generated plasma channel fields results in copious gamma-ray emission and photon decay into $e^{\pm}$ pairs via the NIC and NBW processes, respectively.

Breit-Wheeler pair production (NBW) were implemented using the open-source strong-field QED library `SFQEDtoolkit` [52]. The computational box size is 5 μm $\times$ 2.7 μm $\times$ 2.7 μm, with grid points distributed as 800 $\times$ 864 $\times$ 864 in the x, y, and z directions, respectively. The simulations use a timestep of 4×10^{-18} s. To track the beam evolution, the moving window technique was employed. The target plasma consists of either gold or lithium, with electron number densities of $n_{Au} \approx 5.90 \times 10^{28}$ m^{-3} and $n_{Li} \approx 4.64 \times 10^{28}$ m^{-3}, respectively. At initialization, 2 particles per cell (ppc) are used for both electrons and ions in the target.

4.2 Discussion and results

A schematic of the setup is shown in Fig. 4.1. A dense, high-energy electron beam collides with a series of thin aluminum foils. During each beam-foil collision, the electron beam interacts with the strong coherent transition radiation (CTR) generated at the surface of the foils. This process has recently been demonstrated to both induce intense photon emission and focus the electron beam to densities approaching those of a solid [90]. The CTR-focused electron beam then collides with a thick gold target, with lithium also considered to highlight the critical role of the target material.

Within the target, the unipolar space-charge field of the beam transversely displaces plasma electrons, creating a plasma channel where the beam's electric field can be partially neutralized by the plasma. This leaves the magnetic self-pinching force of the beam partially uncompensated, resulting in a further increase of the beam density. This blowout mechanism is similar to that observed in plasma wakefield accelerators operating in gaseous media [94, 95]. Since the electromagnetic field of

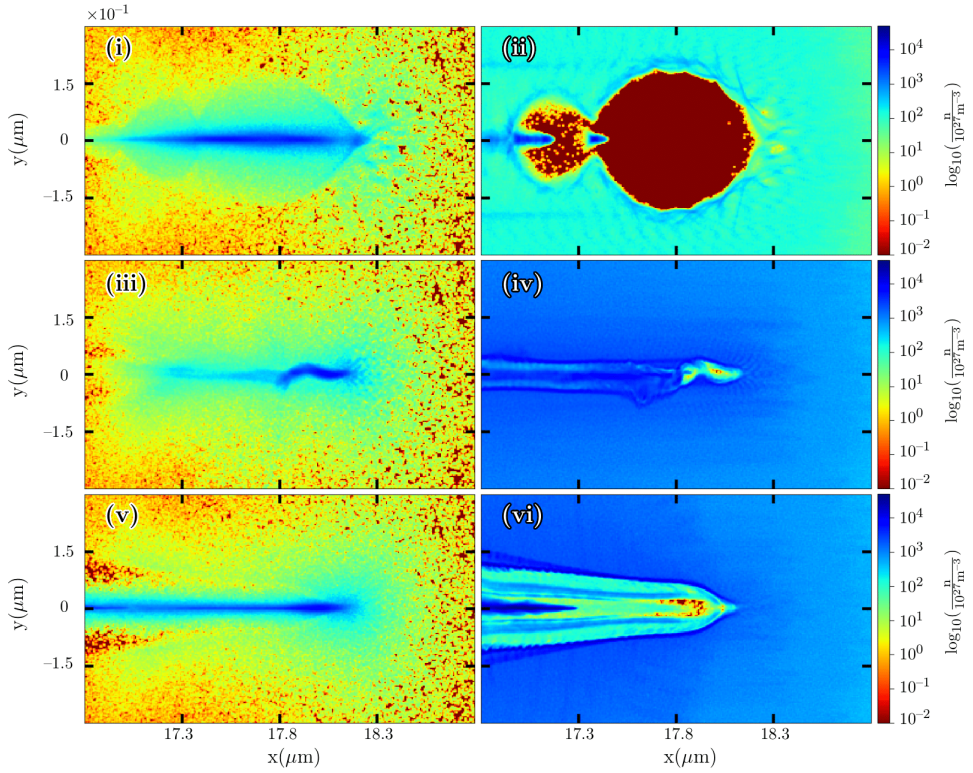

Figure 4.2: Densities (Log scale) of the plasma electrons (panels ii, iv and vi) and electron beam (panels i, iii and v), in units of 10^{27} m^{-3}, after the latter has propagated 10 μm inside the target. Panels i-ii correspond to the collision between the 8.9 GeV beam and the Li target, panels iii-iv to that between the 8.9 GeV beam and the Au target, and panels v-vi correspond to the interaction between the 89 GeV beam and Au target. Note the different scales on the x and y axis.

the beam exceeds the field ionization threshold [96], the target undergoes ionization within a narrow region surrounding the beam. The level of ionization depends on the atomic number Z of the target and the strength of the beam field. Ionization provides free electrons to the plasma, thus enhancing the screening of the beam electric field and increasing the pinching force of the magnetic field.

This mechanism is illustrated in Figs. 4.2 and 4.3, where the electron beam density (left column, panels i, iii, and v) and plasma electron density (right column, panels ii, iv, and vi) are shown for the three simulations. The figures compare results obtained with (Fig. 4.2) and without (Fig. 4.3) the activation of field ionization and pair production (check figures' captions for additional details), after the beam has propagated 10 μm into the target. The more electrons available to the plasma, either due to activated field ionization or the material's high atomic number (Z), the more easily it can shield the field induced by the beam and reduce the size of the plasma channel (see panels ii, iv, and vi in Figs. 4.2-4.3). At the same time, this process tightly focuses the electron beam to densities three orders of magnitude

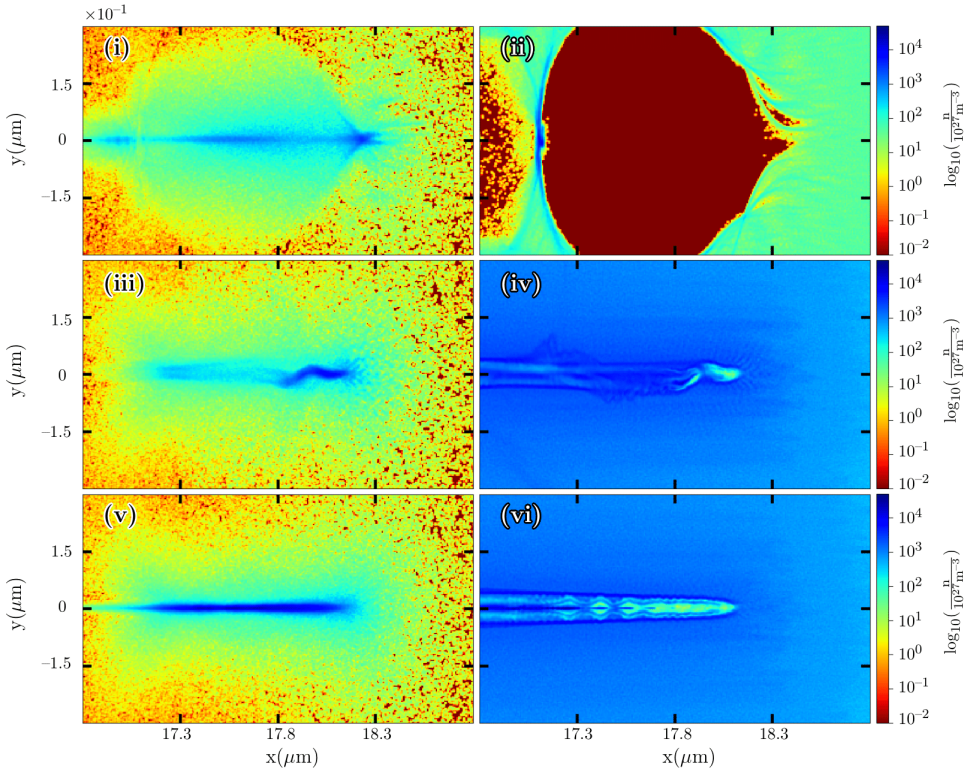

Figure 4.3: Identical to Fig. 4.2, except that the simulation for panels i–ii was performed without field ionization, while those for panels iii–vi exclude any $e^{\pm}$ pair creation modules.

higher than those of electrons in solids (panels i, iii, and v in Figs. 4.2-4.3), thereby amplifying the beam field amplitude and enhancing its capacity to further ionize the target atoms in a self-reinforcing cycle. The cycle continues until either the target becomes fully ionized or the beam field falls below the ionization threshold of the inner-shell electrons of the target material.

As shown in Fig. 4.4, the beam's self-generated magnetic field (panels ii, iv, and vi) reaches an intensity of approximately 10^7 T, while the corresponding electric field (panels i, iii, and v) exhibits a comparable magnitude. This field strength lies within the 10^7 – 10^9 T range typical of canonical radio pulsars, and is orders of magnitude higher than the 10^4 – 10^5 T characteristic of millisecond pulsars [97]. Achieving a field of similar strength would require a laser system capable of delivering an intensity of 10^{24} W/cm^2, which is an order of magnitude higher than the current world record [4]. Additionally, the beam parameters required for probing this regime are within reach of the Facility for Advanced Accelerator Experimental Tests (FACET-II) at the SLAC National Accelerator Laboratory once its advanced beam compression capabilities are fully realized [98].

For the high-energy electron beam considered here, and given the strong self-generated field within the target, the beam particles achieve a quantum parameter

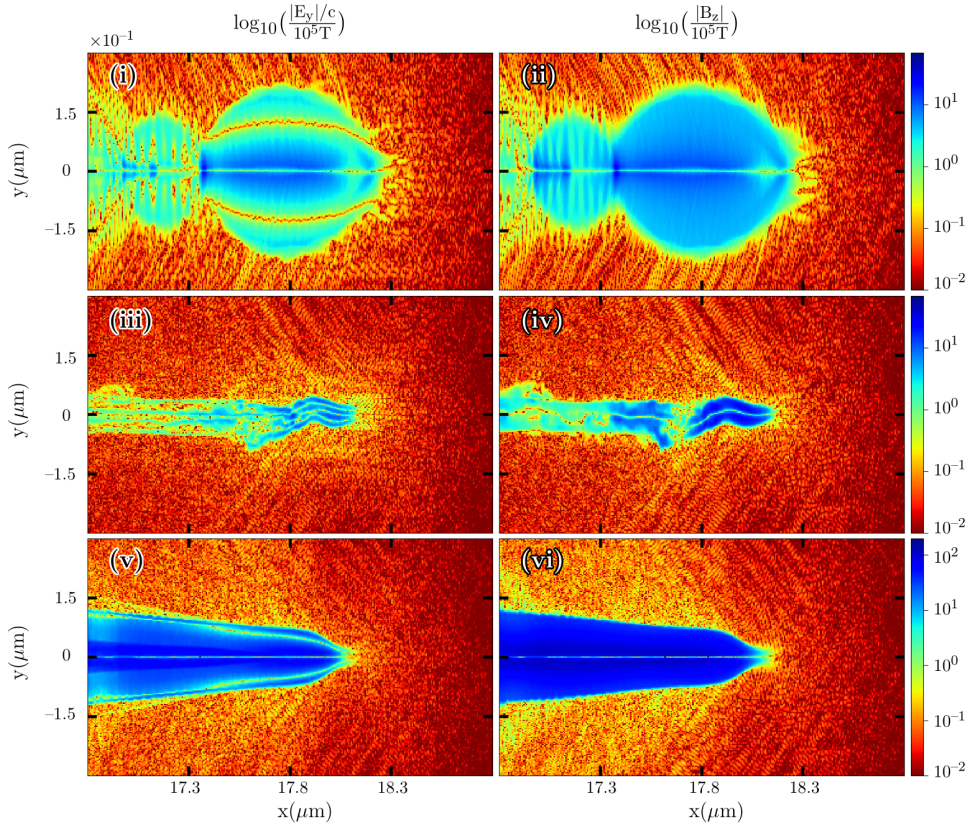

Figure 4.4: Absolute value (Log scale) of the y-component of the electric field $|E_y|$, in unit of $c \cdot 10^5$ T (panels i, iii and v), and z-component of the magnetic field $|B_z|$, in unit of 10^5 T (panels ii, iv and vi), after approximately 10 μm of beam propagation through the target. As in fig. 4.2, panels i-ii correspond to the collision between the 8.9 GeV beam and the Li target, panels iii-iv to that between the 8.9 GeV beam and the Au target, and panels v-vi correspond to the interaction between the 89 GeV beam and Au target. Note the different scales on the x and y axis.

$\chi = E^*/E_{cr}$ that significantly exceeds unity, thus entering the supercritical regime of strong-field QED [44, 54, 89]. Here, $E^* \sim \gamma|\vec{E}_\perp + \vec{v} \wedge \vec{B}|$ is the electric field experienced by a e^- in its instantaneous rest frame, and $E_{cr} \approx 1.3 \times 10^{18}$ V / m ($B_{cr} \approx 4.4 \times 10^9$ T) is the critical, or Schwinger, electric (magnetic) field of QED. The electric field component perpendicular to the particle velocity $\vec{v}$ is denoted by $\vec{E}_\perp$, and $\vec{B}$ represents the magnetic field. $\gamma = (1 - \frac{v^2}{c^2})^{\frac{1}{2}}$ is the relativistic Lorentz factor. As shown in Fig. 4.5, the beam's quantum nonlinearity parameter, χ, begins to increase immediately after it crosses the thick target interface at $x \approx 5\mu$m. Once inside the target, χ rapidly rises into the supercritical regime and then saturates at its maximum value between 8 and 10 μm of propagation. Moreover, a higher beam energy or a larger atomic number Z of the target enhances this effect: in panel iii

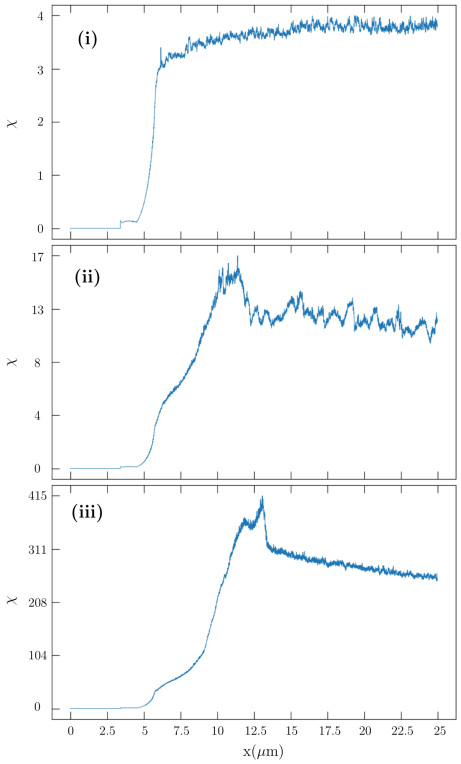

Figure 4.5: Evolution of the maximum quantum nonlinearity parameter (χ) of the electron beam during its collision with a thick solid metal target. The beam energies are 8.9 GeV (panels i–ii) and 89 GeV (panel iii), and the target materials are Lithium (panel i) and Gold (panels ii–iii).

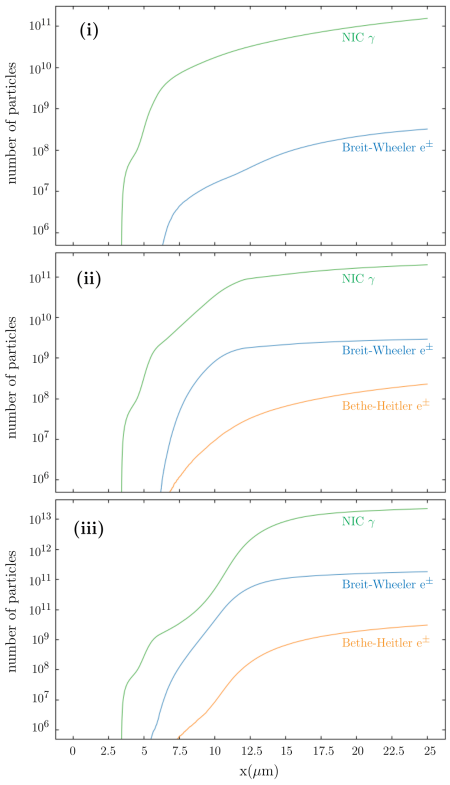

Figure 4.6: Evolution of the number of produced particles as the beam propagates through the target. The green line represents NIC photons, the blue line denotes NBW $e^{\pm}$ pairs, and the orange line shows Bethe–Heitler $e^{\pm}$ pairs. In panels i and ii, the beam energy is 8.9 GeV, while panel iii features a beam energy of 89 GeV. The target material is Lithium in panel i and Gold in panels ii and iii.

of Fig. 4.5, χ reaches values up to[1] 400!

At values of $\chi \gg 1$, electrons and positrons are highly likely to emit individual photons via NIC, with each photon carrying away a significant fraction of the emitter's kinetic energy. These energetic photons can subsequently convert into $e^{\pm}$ pairs through the NBW process [44, 54, 89]. As these newly created pairs can also emit photons, an exponentially growing strong-field QED cascade rapidly enriches the plasma surrounding the beam with additional pairs—often within just a few tens of femtoseconds. Figure 4.6 summarizes this exponential particle production process. In the figure, NIC photons (green line) are abundantly produced as the primary electrons of the beam interact with the self-induced electromagnetic field inside the target. These photons can then decay into electron–positron pairs either by colliding with the Coulomb field of the target nuclei via the Bethe–Heitler mechanism (yellow line) or by interacting with the strong electromagnetic fields inside the solid via the NBW process (blue line), with the latter channel being preferred.

As shown in fig. 4.7, the generated e^- (panels i, iii and v) are focused by the magnetic field around the beam axis, reaching densities up to four orders of magnitude higher than those typically found in solids. In contrast, e^+ (panels ii, iv and vi) are defocused, resulting in a substantial local increase in the electron current density, the associated magnetic field, and the χ experienced by the beam's particles. This, in turn, increases the probability of high-energy photon emission and their conversion into pairs, creating a positive feedback cycle. This cycle is ultimately limited by energy losses, as the generation of new $e^{\pm}$ pairs is strongly suppressed when χ drops below unity due to the rapid decrease in γ.

Finally, Figs. 4.7, 4.8, and 4.9 reveal something intriguing: the formation of "short jet" structures, consisting of highly collimated and ultrarelativistic NBW $e^{\pm}$ pairs, with average divergence and energy of $\langle\theta\rangle \approx 0.1$ rad and $\langle\varepsilon\rangle \approx 1$ GeV. These findings support the setup shown in Fig. 4.1 as a promising mechanism for pair plasma production.

4.3 Conclusions

Here we demonstrated that above-solid-density electron-positron jets, embedded in self-generated magnetic fields reaching up to ten megatesla, can be produced by colliding a dense, high-energy electron beam with a high-Z conductor such as gold. Remarkably, this occurs in a new regime in which the plasma response, atomic field ionization, high-energy photon emission, and photon decay into electron-positron pairs mutually reinforce one another through positive feedback cycles. Our results

[1] Simulating SFQED processes for particles in the supercritical regime is challenging without the `SFQEDtoolkit`, as state-of-the-art methods lose accuracy at such high χ values.

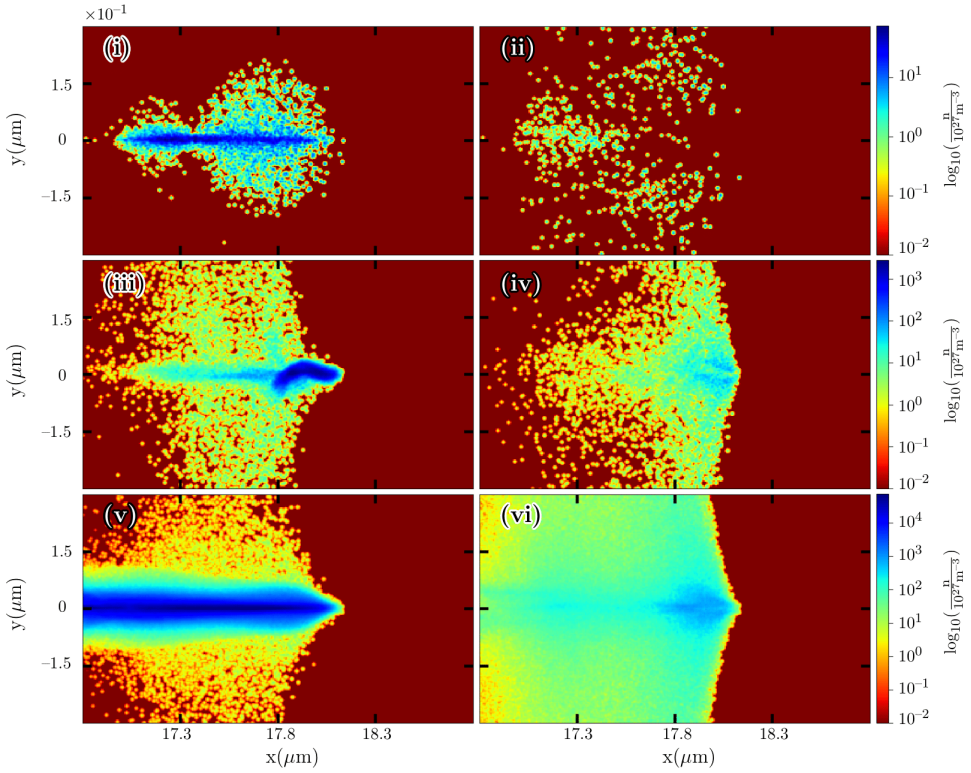

Figure 4.7: Densities (Log scale) of the electrons (panels i, iii and v) and positrons (panels ii, iv and vi), in units of 10^{27} m^{-3}, generated via NBW after the primary electron beam has propagated 10 μm inside the target. Panels i-ii correspond to the collision between the 8.9 GeV beam and the Li target, panels iii-iv to that between the 8.9 GeV beam and the Au target, and panels v-vi correspond to the interaction between the 89 GeV beam and Au target. Note the different scales on the x and y axis.

are an important step towards probing the microphysics governing extreme astrophysical environments and open up research in conditions under which atomic, plasma, and strong-field QED physics interweave.

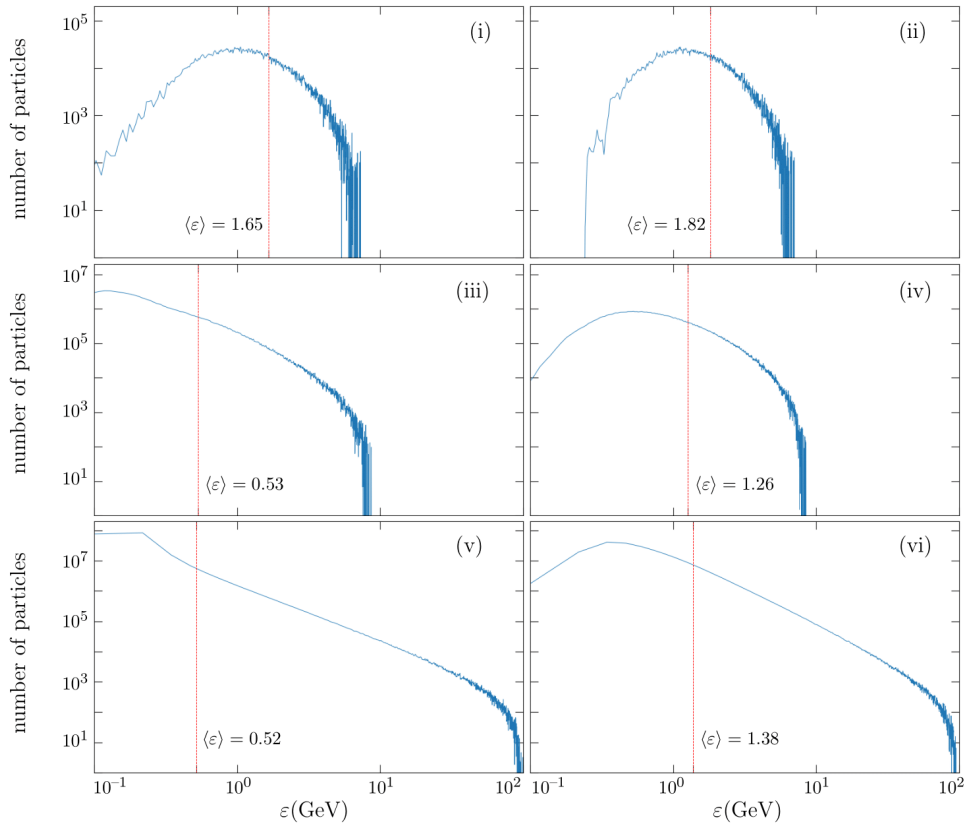

Figure 4.8: Energy distributions (Log scale) of the electrons (panels i, iii and v) and positrons (panels ii, iv and vi) generated via NBW after the primary electron beam has propagated 10 μm inside the target. Panels i-ii correspond to the collision between the 8.9 GeV beam and the Li target, panels iii-iv to that between the 8.9 GeV beam and the Au target, and panels v-vi correspond to the interaction between the 89 GeV beam and Au target. The red vertical line corresponds to the average energy value associated to the given distribution.

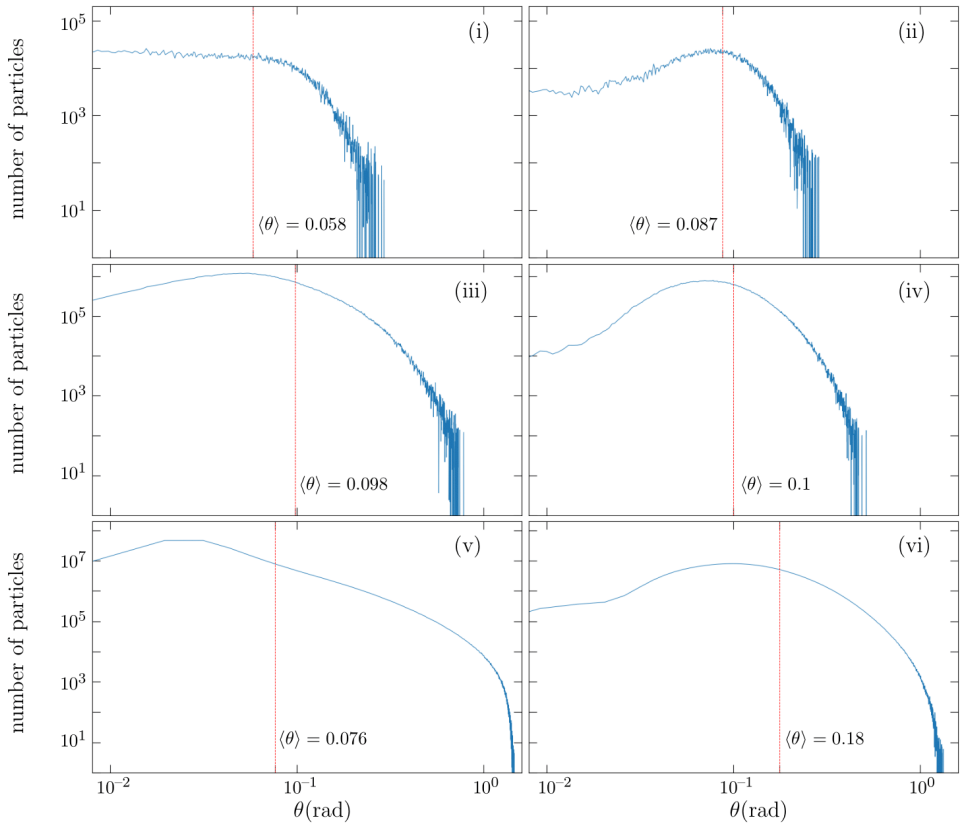

Figure 4.9: Divergence distributions (Log scale) for NBW electrons (panels i, iii, and v) and positrons (panels ii, iv, and vi) are shown after approximately 10 μm of beam propagation through the target. Panels i-ii correspond to the collision between the 8.9 GeV beam and the Li target, panels iii-iv to that between the 8.9 GeV beam and the Au target, and panels v-vi correspond to the interaction between the 89 GeV beam and Au target. In each case, the vertical red line indicates the average value.

Chapter 5

Fully resolved NIC and NBW processes

The modeling of Strong-Field (SF) QED particles (positrons, electrons, and photons) and their interactions within particle-in-cell (PIC) and Monte-Carlo (MC) codes is the primary tool available for studying extreme plasma conditions and astrophysical compact objects. Reference [44] provides a comprehensive summary of our current understanding of SFQED processes, to the extent that state-of-the-art codes often rely on directly implementing the results reported there. However, a major limitation of this approach is that photon polarizations and lepton spins, as well as particles' angular distribution, are neglected. Various groups [99–105] have proposed methods to address these issues, but the scientific community still lacks an SFQED library that comprehensively tackles all these limitations.

In the following sections, we begin with a brief introduction to Baier and Katkov's quasiclassical operator method (QOM), then apply this technique to compute the squared transition amplitudes assocated to the NIC and NBW processes. Specifically, we consider two scenarios: one where we integrate these squared amplitudes over the entire solid angle $d\Omega$, and one where we do not. In contrast to the approach taken in [44], we will neither average over the initial states nor sum over the final spin/polarization states. By tracking the complete set of particle parameters, we derive NIC and NBW differential distributions that are fully resolved in terms of the spins and polarizations of the involved particles, while their momenta are characterized in full detail, including both energy and angular properties. We will refer to these distributions as FNIC and FNBW[1]. We will also demonstrate that by summing the FNIC and FNBW distributions over the inner (spin and polarization) and angular degrees of freedom, we can recover the results presented in Chapter 3, and originally in [44]. Finally, we will show that the FNIC and FNBW distributions are improper, potentially negative, and lack their usual probabilistic interpretation. The only way to restore a stochastic meaning is by considering their contributions from the entire formation length λ_f (or time τ_f) of the quasiclassical trajectory followed by the particle undergoing the NIC or NBW process.

Throughout this chapter, we introduce a series of SFQED analytical distributions capable of characterizing physical particles in every respect. We also present a suite of algorithms designed to generate numerical particles with spin/polarization resolution and detailed angular distributions. For clarity, we adopt naming conventions

[1] The "F" stands for *Fully resolved*.

consistent with those used in Chapter 3 and Appendix A for the `SFQEDtoolkit` routines. In fact, the techniques described here are intended to be part of `SFQEDtoolkit`'s advanced computational module. Although we will showcase some examples of its application, this module has not yet been released. Consequently, unlike in Chapter A, we will not provide an explicit list of the routines' arguments.

5.1 The Quasiclassical operator method

Developed by Baier and Katkov in the late 60s, the quasiclassical operator method is a theoretical framework used to describe the interaction of relativistic particles (typically electrons or positrons) with strong EM fields. Considering the case of an electron with energy ε moving within a purely magnetic field of intensity H, the foundations of the QOM lie in the awareness that two quantum effects contribute to the emission of high-energy photons:

- related to the quantization of the electron's motion inside the field, the first effect concerns the noncommutability of the dynamic variables associated to the particle. As a matter of fact, the commutator of any two operators $\hat{A}$ and $\hat{B}$ describing its motion has the order $\frac{\hbar\omega_0}{\varepsilon}$, i.e.,

$$[\hat{A}, \hat{B}] \sim \frac{\hbar\omega_0}{\varepsilon}, \tag{5.1}$$

  where $c = 1$ has been used, and $\omega_0 = \frac{eH}{\varepsilon}$ is the particle's Larmor frequency. This result generalizes to any EM field and suggests that the motion of the particle becomes more and more classical as its energy ε increases ($[\hat{A}, \hat{B}] \xrightarrow[\varepsilon\to\infty]{} 0$);

- the second effect is connected to the fermion's recoil after radiation. Indicating with ω the emitted photon's frequency, the order of the recoil is easily seen to be $\frac{\hbar\omega}{\varepsilon}$.

Due to the fact that the second kind of effect dominates over the first, as $\omega \gg \omega_0$, we are allowed to treat the electron's physics semiclassically, determining its trajectory using classical mechanics while addressing its interactions with the external field through quantum transition amplitudes. According to the Feynman rules, at first order in perturbation theory the matrix element corresponding to NIC, i.e. the photon emission process by an electron in SF, is

$$U_{fi} = \frac{ie}{2\pi\sqrt{\hbar\omega}} \int dt \int d\vec{r} F^{\dagger}_{f,\zeta'}(\vec{r}) \exp\Big(\frac{i\varepsilon_f t}{\hbar}\Big) e^*_\mu J^\mu \exp\Big(i\omega t - i\vec{k}\cdot\vec{r}\Big) \exp\Big(\frac{-i\varepsilon_i t}{\hbar}\Big) F_{i,\zeta}(\vec{r}), \tag{5.2}$$

where e^μ and $k^\mu(\omega, \vec{k})$ are the photon polarization and four-momentum, $F_{i,\zeta}(\vec{r})$ is the solution to the wave equation in the backgorund SF (with energy ε_i and spin state ζ), while J^μ is the *generalized* density current four-vector[2].

Replacing the classical variables $\vec{p}$ and ε with the corresponding operators[3]

$$p^\mu \to \hat{p}^\mu = i\hbar\partial^\mu - eA^\mu \qquad \text{and} \qquad \varepsilon \to \hat{\mathcal{H}} = \sqrt{\hat{\vec{p}}^{\,2} + m^2}, \tag{5.3}$$

it is then possible to switch eq. (5.2) to its operator form. In this way the initial and final fermion states become

$$\begin{aligned} \exp\Big(\frac{-i\varepsilon_i t}{\hbar}\Big) F_{i,\zeta}(\vec{r}) &= \Psi_\zeta(\hat{\vec{p}}) \exp\Big(\frac{-i\hat{\mathcal{H}}t}{\hbar}\Big)|i\rangle \\ F_{f,\zeta'}(\vec{r}) \exp\Big(\frac{i\varepsilon_f t}{\hbar}\Big) &= \langle f| \exp\Big(\frac{i\hat{\mathcal{H}}t}{\hbar}\Big)\Psi_{\zeta'}(\hat{\vec{p}}\,'), \end{aligned} \tag{5.4}$$

where $\Psi_\zeta(\hat{\vec{p}})$ is the operatorial form of the wave functions $F_{i,\zeta}(\vec{r})$; when applied to $|i\rangle$, the initial particle state[4], the operator $\Psi_\zeta(\hat{\vec{p}})$ describes a particle in a state with defined momentum and spin, $\vec{p}$ and ζ in this case; the exact same argument translates quite naturally to $\Psi_{\zeta'}(\hat{\vec{p}}\,')$ and the final state $\langle f|$. Finally, the exponential terms $\pm\exp\Big(\frac{i\hat{\mathcal{H}}t}{\hbar}\Big)$ enforce the time dependence of the given state and, after substituting (5.4) into (5.2), their presence makes it natural to shift all the operators to the Heisenberg picture: U_{fi} becomes

$$U_{fi} = \frac{ie}{2\pi\sqrt{\hbar\omega}} \langle f| \int dt \exp(i\omega t) M(t) |i\rangle\,, \tag{5.5}$$

with

$$M(t) = \Psi^\dagger_{\zeta'}(\hat{\vec{p}}\,')\{e^*_\mu \hat{J}^\mu, \exp\Big(-i\vec{k}\cdot\hat{\vec{r}}\Big)\}\Psi_\zeta(\hat{\vec{p}}). \tag{5.6}$$

The particle's momentum $\hat{\vec{p}}(t)$, density current $\hat{J}^\mu(t)$ and position $\hat{\vec{r}}(t)$ quantum operators in eq. (5.6) are all expressed in the time dependent Heisenberg picture; furthermore, we introduced the symmetrized product of operators through the brackets $\{\bullet, \bullet\}$, corresponding to half of the anticommutator. Not affecting the matrix element in (5.2), this choice is motivated by the fact that Eqs. (5.5)-(5.6) are now suitable for the description of any interaction between the field and particles with spin ζ, especially in those case where ζ does not equal $\frac{1}{2}$. As a matter of fact,

[2]Note that in this context, J^μ does not represent the *proper* density current. For example, in QED for spin-$\frac{1}{2}$ states, the density current is given by $\bar{\Psi}\gamma^\mu\Psi$; here, however, the J^μ is simply identified with the Dirac γ matrices, i.e., $J^\mu = \gamma^\mu$.

[3]Actually this approximation is valid only for particles dwelling in large orbital momenta states, where the spin-field interaction term $\frac{e\hbar}{2}\sigma^{\mu\nu}F_{\mu\nu}$ can be neglected.

[4]Notice that, in the coordinate representation, $|i\rangle$ and $|f\rangle$ are solutions of the Klein-Gordon equation in an external field. Also, we point out that $|i\rangle$ and $|f\rangle$ do not describe the spin part of the particle's state, which is instead taken care of by the operators $\Psi_\zeta(\hat{\vec{p}})$ and $\Psi_{\zeta'}(\hat{\vec{p}}\,')$.

symmetrized products of this kind naturally arise in lagrangian density interaction terms of ($\zeta \neq \frac{1}{2}$)-QFTs[5], thus justifying their appearence in eq. (5.6).

The probability for the NIC emission of a photon with momentum $\vec{k}$ can easily be found as the squared matrix element $\frac{dw_{NIC}^{fi}}{d^3k} = U_{fi}^{\dagger}U_{fi}$. Moreover, as we are not concerned with resolving the final Klein-Gordon states $|f\rangle$ in their entirety, but only their spin and polarization parts, we exploit the completeness relation $\sum_f |f\rangle\langle f| = 1$ to rerender $\frac{dw_{NIC}^{fi}}{d^3k}$ as

$$\frac{dw_{NIC}}{d^3k} = \sum_f U_{fi}^{\dagger}U_{fi} = \\ = \frac{e^2}{(2\pi)^2\hbar\omega}\langle i|\int dt_1 \int dt_2 \exp\{i\omega(t_1 - t_2)\}M^{\dagger}(t_2)M(t_1)|i\rangle . \tag{5.7}$$

Despite $M(t_1)$ and $M(t_2)$ taken at different times don't commute in general, a series of algebraic operations known as "disentanglement"[6] can prove their commutativity with $\frac{1}{\gamma^2}$-order accuracy

$$[M(t_1), M(t_2)] = O\Big(\frac{1}{\gamma^2}\Big), \tag{5.8}$$

together with the commutativity (with the same accuracy) of all the operators involved in (5.6), $\gamma = \frac{\varepsilon}{m}$ being the initial electron's Lorentz gamma factor. This means all the dynamic operators in eq. (5.7) commute with a $\max(\frac{1}{\gamma^2}, \frac{\hbar\omega_0}{\varepsilon})$-order accuracy[7], and their operatorial form may now be replaced by the corresponding classical values; M can thus be rewritten as

$$M(t) = R(t)\exp\Big\{i\frac{\varepsilon}{\varepsilon'}k_\mu x^\mu(t)\Big\} \tag{5.9}$$

and eq. (5.7) becomes

$$dw_{NIC} = d^3k\frac{e^2}{(2\pi)^2\hbar\omega}\int dt_1 \int dt_2 R^*(t_2)R(t_1)\exp\Big\{-i\frac{\varepsilon}{\varepsilon'}k_\mu[x^\mu(t_2) - x^\mu(t_1)]\Big\}. \tag{5.10}$$

While $\varepsilon' = \varepsilon - \hbar\omega$ denotes the electron's energy after the NIC photon emission, $R(t)$ is a time dependent function containing all the spin characteristics; upon completing the necessary mathematical steps, it is demonstred to coincide with the

[5] An obvious example is given by scalar QED, where $\zeta = 0$ and $\hat{J}^\mu = D^\mu \equiv \partial^\mu + ieA^\mu$ corresponds to the covariant derivative. This time the Lagrangian interaction term is proportional to $\mathcal{L}_{int} \propto \phi^* \overleftrightarrow{D}^\mu \phi$, with ϕ being the complex scalar field and $\phi^* \overleftrightarrow{D}^\mu \phi \equiv \phi^*(D^\mu\phi) - (D^{*\mu}\phi^*)\phi$. $\mathcal{L}_{int}$ then takes part to the S-matrix, defined as $S = T\exp\{-\frac{i}{\hbar}\int d^4x\mathcal{L}_{int}(x)\}$ (T is the time ordering operator), which after the due algebra makes a symmetrized $\{\bullet,\bullet\}$-like term appear in (5.6).

[6] See section 2.2 of [44] for further details.

[7] Let us not forget that the entire QOM framework is based on the neglect of $\frac{\hbar\omega_0}{\varepsilon}$-order quantum effects.

transition matrix element for the spin vectors of free particles. As such its general form will be

$$R(t) = \frac{1}{2}\psi^{\dagger}_{\zeta'}(p'(t))[e^{*}_{\mu}J^{\mu}(p'(t)) + e^{*}_{\mu}J^{\mu}(p(t))]\psi_{\zeta}(p(t)), \tag{5.11}$$

where $\psi_{\zeta}(p(t)) \equiv \psi_{\zeta}(\varepsilon(t), \vec{p}(t))$ defines a generic four-component Dirac spinor.

Equations (5.10)-(5.11) represent the crowning achievement of the QOM, providing us with a general expression for evaluating transition probabilities of any SFQED process (up to a few minor tweaks which we will see in sec. 5.2.2). In a nutshell, the QOM is a mathematical and physical tool that can be used to study synchrotron radiation, bremsstrahlung and pair production processes in external SF. Essential in high-strength fields scenarios, this approach defines particle's motion through classical trajectory equations, while resorting to quantum operators to assess transition probabilities.

In the following sections we will apply this method to the two paradigmatic cases of NIC and NBW.

5.2 The full-resolution NIC and NBW distributions

5.2.1 The fully-resolved NIC differential distribution

At the end of previous section we saw that, according to the QOM, the NIC's transition probability has the form reported in eq. (5.10)-(5.11). We proceed with the introduction of the generic Dirac spinor $\psi_{\zeta}(p) = \frac{1}{\sqrt{2\varepsilon}}u_{\zeta}(p)$, where

$$u_{\zeta}(p) = u_{\zeta}(\varepsilon, \vec{p}) = \sqrt{\varepsilon + m}\begin{pmatrix} \varphi_{\zeta} \\ \frac{\vec{p}\cdot\vec{\sigma}}{\varepsilon+m}\,\varphi_{\zeta} \end{pmatrix} = \begin{pmatrix} \sqrt{\varepsilon+m}\,\varphi_{\zeta} \\ \sqrt{\varepsilon-m}\,(\vec{n}_p\cdot\vec{\sigma})\,\varphi_{\zeta} \end{pmatrix} \tag{5.12}$$

is a solution of the Dirac eq. (3.9) normalized to $\bar{u}_{\zeta'}(p)u_{\zeta}(p) = 2m\delta_{\zeta'\zeta}$, $\vec{n}_p = \frac{\vec{p}}{|\vec{p}|}$ and φ_{ζ} is the two-component spinor ($\varphi^{\dagger}_{\zeta}\varphi_{\zeta} = 1$) describing the polarization state of the fermion; ζ (ζ') describes the spin of the electron before (after) the emission. By replacing $J^{\mu} = \gamma^{\mu}$ and eq. (5.12) into (5.11), it is quite straightforward to see that $R(t)$ reduces to[8]

$$R(t) = \varphi^{\dagger}_{\zeta'}(p'(t))[A(t) + i\vec{\sigma}\cdot\vec{B}(t)]\varphi_{\zeta}(p(t)), \tag{5.13}$$

with the coefficients A and $\vec{B}$ directly depending on the emitted photon's polarization e^{μ}

$$A(t) = \frac{\vec{e}^{\star}\cdot\vec{p}(t)}{2\sqrt{\varepsilon\varepsilon'}}\Big[\Big(\frac{\varepsilon'+m}{\varepsilon+m}\Big)^{\frac{1}{2}} + \Big(\frac{\varepsilon+m}{\varepsilon'+m}\Big)^{\frac{1}{2}}\Big] \tag{5.14}$$

[8] Keep in mind that any 2×2 matrix m can be decomposed as the sum of the unit and Pauli matrices $m = a\mathbb{I}_{2\times 2} + i\vec{\sigma}\cdot\vec{b}$

$$\vec{B}(t) = \frac{\vec{e}^{\star}}{2\sqrt{\varepsilon\varepsilon'}} \wedge \Big[\Big(\frac{\varepsilon' + m}{\varepsilon + m}\Big)^{\frac{1}{2}} \vec{p}(t) - \Big(\frac{\varepsilon + m}{\varepsilon' + m}\Big)^{\frac{1}{2}} (\vec{p}(t) - \vec{k})\Big], \tag{5.15}$$

$\vec{p}$ and $\vec{v}$ being respectively the momentum and velocity of the starting electron. We now exploit the definition of the spin density matrix $\rho_\zeta = \varphi_\zeta \varphi_\zeta^\dagger = \frac{1}{2}(1 + \vec{\zeta} \cdot \vec{\sigma})$ to recast the combination $R^*(t_2)R(t_1)$ as

$$\begin{aligned} R^*(t_2)R(t_1) &= \frac{1}{4} tr[(1 + \vec{\zeta} \cdot \vec{\sigma})(A^{\star}(t_2) - i\vec{\sigma} \cdot \vec{B}^{\star}(t_2))(1 + \vec{\zeta}' \cdot \vec{\sigma})(A(t_1) + i\vec{\sigma} \cdot \vec{B}(t_1))] = \\ &= \frac{1}{2}\{A(t_1)A^*(t_2)\,(1 + \vec{\zeta} \cdot \vec{\zeta}') + \vec{B}(t_1) \cdot \vec{B}^*(t_2)\,(1 - \vec{\zeta} \cdot \vec{\zeta}') + i(\vec{\zeta}' - \vec{\zeta}) \cdot [\vec{B}(t_1) \wedge \vec{B}^*(t_2)] + \\ &\quad + i(\vec{\zeta}' + \vec{\zeta}) \cdot [\vec{B}(t_1)A^*(t_2) - A(t_1)\vec{B}^*(t_2)] + (\vec{\zeta}' \wedge \vec{\zeta}) \cdot [\vec{B}(t_1)A^*(t_2) + A(t_1)\vec{B}^*(t_2)] + \\ &\quad + [\vec{\zeta} \cdot \vec{B}^*(t_2)][\vec{\zeta}' \cdot \vec{B}(t_1)] + [\vec{\zeta}' \cdot \vec{B}^*(t_2)][\vec{\zeta} \cdot \vec{B}(t_1)]\}. \end{aligned} \tag{5.16}$$

Next we take the ultrarelativistic limit ($\varepsilon \gg m$) of Eqs. (5.14) and (5.15), that is

$$A(t) \to \frac{\varepsilon + \varepsilon'}{2\varepsilon'} \left(\vec{e}^{\star} \cdot \vec{v}(t)\right) \tag{5.17}$$

$$\vec{B}(t) \to \frac{\omega}{2\varepsilon'}\Big[\vec{e}^{\star} \wedge (\vec{n} - \vec{v}(t) + \frac{\vec{n}}{\gamma})\Big], \tag{5.18}$$

with $\vec{n} = \frac{\vec{k}}{|\vec{k}|}$ the photon's direction of propagation, and substitute in (5.16); switching the time integration variables from (t_1, t_2) to

$$\tilde{t} = \frac{t_1 + t_2}{2} \tag{5.19}$$

$$\tau = t_2 - t_1, \tag{5.20}$$

we can expand any instance of $\vec{x}(t)$ and $\vec{v}(t)$, the electron's position and velocity that feature in Eqs. (5.17)-(5.18), according to

$$\vec{x}(\tilde{t} \pm \frac{\tau}{2}) = \vec{x}(\tilde{t}) \pm \vec{v}(\tilde{t})\frac{\tau}{2} + \vec{w}(\tilde{t})\frac{\tau^2}{8} \tag{5.21}$$

$$\vec{v}(\tilde{t} \pm \frac{\tau}{2}) = \vec{v}(\tilde{t}) \pm \vec{w}(\tilde{t})\frac{\tau}{2} + \dot{\vec{w}}(\tilde{t})\frac{\tau^2}{8}, \tag{5.22}$$

so that eq. (5.10) is rewritten as

$$dw_{NIC} = \frac{\alpha}{(2\pi)^2}\frac{d^3k}{\omega}\int d\tilde{t}\int d\tau[R_0(\tilde{t}) + R_I(\tilde{t})\tau + R_{II}(\tilde{t})\tau^2]\exp\Big\{-i\frac{\varepsilon}{\varepsilon'}\omega\Big[\lambda(\tilde{t})\tau + \frac{\tau^3}{24}|\vec{w}(\tilde{t})|^2\Big]\Big\}. \tag{5.23}$$

Here $\vec{w}(t)$ represents the electron acceleration and $\lambda(\tilde{t}) = (1 - \vec{n} \cdot \vec{v}(\tilde{t}))$ is a variable characterizing the disrtibution's angular behavior.

At this stage, a selection of a proper system of axes upon which one can project all vector quantities is the only thing we miss: fortunately $\hat{v}$ (the direction of the initial electron's velocity), $\vec{s}$ (the transverse normalized initial electron's acceleration) and

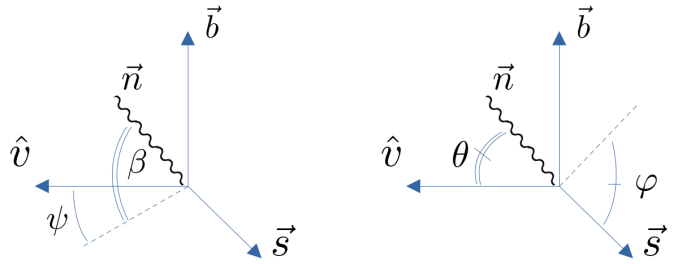

Figure 5.1: Two angular coordinate systems are used to describe the orientation of the emitted radiation $\vec{n}$ relative to the electron's direction $\hat{v}$. On the left, β is the angle between $\vec{n}$ and the plane $\mathcal{P}_{(\hat{v}-\vec{s})}$, and φ is the angle between the projection of $\vec{n}$ onto $\mathcal{P}_{(\hat{v}-\vec{s})}$ and $\hat{v}$. On the right, θ is the angle between $\vec{n}$ and $\hat{v}$, and φ is the angle between the projection of $\vec{n}$ onto the plane $\mathcal{P}_{(\vec{b}-\vec{s})}$ and $\vec{s}$.

$\vec{b} = \hat{v} \wedge \vec{s}$ constitute a particularly convenient choice to do so. In particular, the position of any vector $\vec{V}$ with respect to the triplet $(\hat{v}, \vec{s}, \vec{b})$ will be expressed in terms of the angles (ψ, β). As it is depicted in fig. 5.1, β is the angle between $\vec{V}$ and the plane $\mathcal{P}_{(\hat{v}-\vec{s})}$ shared by $\hat{v}$ and $\vec{s}$, while $\vec{V}$'s projection on $\mathcal{P}_{(\hat{v}-\vec{s})}$ forms with $\hat{v}$ the angle ψ. Hence, the photon's direction $\vec{n}$ is outlined as

$$\vec{n} = (\cos\beta\cos\psi, \cos\beta\sin\psi, \sin\beta) \tag{5.24}$$

and the differential on the photon momentum d^3k reads

$$d^3k = \omega^2 d\omega d\Omega_{(\psi,\beta)}, \tag{5.25}$$

with $d\Omega_{(\psi,\beta)} = d\psi d\beta$ the angular part of the integral measure. Consequently, eq. (5.23) can be rearranged into

$$\frac{dw_{NIC}}{d\tilde{t}d\omega d\Omega_{(\psi,\beta)}} \equiv \frac{dW_{NIC}}{d\omega d\Omega_{(\psi,\beta)}} = \frac{\alpha\omega}{(2\pi)^2}\int d\tau[R_0(\tilde{t})+R_I(\tilde{t})\tau+R_{II}(\tilde{t})\tau^2]\exp\Big\{-i\frac{\varepsilon}{\varepsilon'}\omega\Big[\lambda(\tilde{t})\tau+\frac{\tau^3}{24}|\vec{w}(\tilde{t})|^2\Big]\Big\}, \tag{5.26}$$

in which the integral over τ can be finally performed through the identities [99]

$$\begin{aligned}
\int_{-\infty}^{\infty} d\tau \exp\Big\{-i\frac{\varepsilon}{\varepsilon'}\omega\Big[\lambda(\tilde{t})\tau + \frac{\tau^3}{24}|\vec{w}(\tilde{t})|^2\Big]\Big\} &= \frac{4\sqrt{2}}{\sqrt{3}}\frac{1}{|\vec{w}(\tilde{t})|}\lambda^{\frac{1}{2}}(\tilde{t})K_{\frac{1}{3}}(\xi_e)\\
\int_{-\infty}^{\infty} d\tau\tau \exp\Big\{-i\frac{\varepsilon}{\varepsilon'}\omega\Big[\lambda(\tilde{t})\tau + \frac{\tau^3}{24}|\vec{w}(\tilde{t})|^2\Big]\Big\} &= -i\frac{16}{\sqrt{3}}\frac{1}{|\vec{w}(\tilde{t})|^2}\lambda(\tilde{t})K_{\frac{2}{3}}(\xi_e)\\
\int_{-\infty}^{\infty} d\tau\tau^2 \exp\Big\{-i\frac{\varepsilon}{\varepsilon'}\omega\Big[\lambda(\tilde{t})\tau + \frac{\tau^3}{24}|\vec{w}(\tilde{t})|^2\Big]\Big\} &= -\frac{32\sqrt{2}}{\sqrt{3}}\frac{1}{|\vec{w}(\tilde{t})|^3}\lambda^{\frac{3}{2}}(\tilde{t})K_{\frac{1}{3}}(\xi_e),
\end{aligned} \tag{5.27}$$

where $\xi_e = \frac{4\sqrt{2}}{3}\frac{\omega\gamma^3}{\varepsilon'\chi_e}\lambda^{\frac{3}{2}}$ and we made use of the fact that[9] $|\vec{w}| = \frac{\chi_e\varepsilon}{\gamma^3}$. Since the electron is foreseen to radiate in a cone with opening angle $\eta \sim \frac{1}{\gamma}$, ψ and β are

[9] This relation between the acceleration modulus $|\vec{w}|$ and the quantum nonlinearity parameter χ_e can be straightforwardly derived from eq. (3.21)

expected to be very small (the same order as η, i.e. $\psi, \beta \sim \frac{1}{\gamma}$). Therefore, through an expansion at leading order in ψ and β, we obtain the total angular/polarization/spin resolved NIC differential probability

$$\frac{dW_{NIC}^{(\zeta\zeta'\xi)}}{d\omega d\Omega_{(\psi,\beta)}} = C_{NIC}(dW_0 + \xi_1 dW_1 + \xi_2 dW_2 + \xi_3 dW_3), \tag{5.28}$$

in which $C_{NIC} = \frac{\alpha\omega}{4\pi^2}\sqrt{\frac{2}{3}}\lambda^{\frac{1}{2}}\frac{\gamma^3}{\chi_e\varepsilon'}$, the ξ_i are the Stokes parameters associated to the photon polarization (see Sec. 5.3) and

$$\begin{aligned} dW_0 = K_{\frac{1}{3}}(\xi_e)\Big\{2\lambda\Big[\frac{\varepsilon^2+\varepsilon'^2}{\varepsilon\varepsilon'} + 2(\vec{\zeta}\cdot\vec{\zeta}')\Big] - \frac{1}{\gamma^2}\Big[\frac{\varepsilon^2+\varepsilon'^2}{2\varepsilon\varepsilon'}(\vec{\zeta}\cdot\vec{\zeta}') + 1\Big] + \frac{\varepsilon^2-\varepsilon'^2}{2\varepsilon\varepsilon'}\frac{1}{\gamma}\Big[\beta\vec{s} - \psi\vec{b}\Big]\cdot(\vec{\zeta}\wedge\vec{\zeta}') + \\ + \Big(4\lambda - \frac{1}{\gamma^2}\Big)\frac{\omega^2}{2\varepsilon\varepsilon'}(\vec{\zeta}\cdot\hat{v})(\vec{\zeta}'\cdot\hat{v}) - \frac{\omega^2}{2\varepsilon\varepsilon'}\frac{\beta}{\gamma}[(\vec{\zeta}\cdot\hat{v})(\vec{\zeta}'\cdot\vec{b}) + (\vec{\zeta}\cdot\vec{b})(\vec{\zeta}'\cdot\hat{v})] + \\ - \frac{\omega^2}{2\varepsilon\varepsilon'}\frac{\psi}{\gamma}[(\vec{\zeta}\cdot\hat{v})(\vec{\zeta}'\cdot\vec{s}) + (\vec{\zeta}\cdot\vec{s})(\vec{\zeta}'\cdot\hat{v})] + \frac{\omega^2}{2\varepsilon\varepsilon'\gamma^2}[(\vec{\zeta}\cdot\vec{b})(\vec{\zeta}'\cdot\vec{b}) + (\vec{\zeta}\cdot\vec{s})(\vec{\zeta}'\cdot\vec{s})]\Big\} + \\ + K_{\frac{2}{3}}(\xi_e)\sqrt{2\lambda}\Big\{\beta\frac{\varepsilon^2-\varepsilon'^2}{\varepsilon\varepsilon'}[\vec{\zeta}+\vec{\zeta}']\cdot\hat{v} - \frac{\vec{b}}{\gamma}\cdot[\frac{\omega}{\varepsilon}\vec{\zeta} + \frac{\omega}{\varepsilon'}\vec{\zeta}']\Big\}; \end{aligned} \tag{5.29}$$

$$\begin{aligned} dW_1 = K_{\frac{1}{3}}(\xi_e)\Big\{2\beta\psi\Big[\frac{\varepsilon^2+\varepsilon'^2}{2\varepsilon\varepsilon'}(\vec{\zeta}\cdot\vec{\zeta}') + 1\Big] + \frac{\varepsilon^2-\varepsilon'^2}{2\varepsilon\varepsilon'}(\vec{\zeta}\wedge\vec{\zeta}')\cdot\Big[(\beta^2-\psi^2-2\lambda)\hat{v} + \frac{\psi}{\gamma}\vec{s} - \frac{\beta}{\gamma}\vec{b}\Big] + \\ - \beta\psi\frac{\omega^2}{\varepsilon\varepsilon'}(\vec{\zeta}\cdot\hat{v})(\vec{\zeta}'\cdot\hat{v}) + \frac{\omega^2}{2\varepsilon\varepsilon'}\frac{\beta}{\gamma}[(\vec{\zeta}\cdot\hat{v})(\vec{\zeta}'\cdot\vec{s}) + (\vec{\zeta}\cdot\vec{s})(\vec{\zeta}'\cdot\hat{v})] + \\ + \frac{\omega^2}{2\varepsilon\varepsilon'}\frac{\psi}{\gamma}[(\vec{\zeta}\cdot\hat{v})(\vec{\zeta}'\cdot\vec{b}) + (\vec{\zeta}\cdot\vec{b})(\vec{\zeta}'\cdot\hat{v})] - \frac{\omega^2}{2\varepsilon\varepsilon'\gamma^2}[(\vec{\zeta}\cdot\vec{s})(\vec{\zeta}'\cdot\vec{b}) + (\vec{\zeta}\cdot\vec{b})(\vec{\zeta}'\cdot\vec{s})]\Big\} + \\ + K_{\frac{2}{3}}(\xi_e)\sqrt{2\lambda}\frac{\omega}{\gamma}\Big\{\Big[\frac{\vec{\zeta}'}{\varepsilon} + \frac{\vec{\zeta}}{\varepsilon'}\Big]\cdot\vec{s}\Big\}; \end{aligned} \tag{5.30}$$

$$\begin{aligned} dW_2 = K_{\frac{1}{3}}(\xi_e)\Big\{\Big[\Big(2\lambda\frac{\varepsilon^2-\varepsilon'^2}{\varepsilon\varepsilon'} - \frac{\omega}{\gamma^2\varepsilon}\Big)\hat{v} - \frac{\beta}{\gamma}\frac{\omega}{\varepsilon}\vec{b} - \frac{\psi}{\gamma}\frac{\omega}{\varepsilon}\vec{s}\Big]\cdot\vec{\zeta} + \\ + \Big[\Big(2\lambda\frac{\varepsilon^2-\varepsilon'^2}{\varepsilon\varepsilon'} - \frac{\omega}{\gamma^2\varepsilon'}\Big)\hat{v} - \frac{\beta}{\gamma}\frac{\omega}{\varepsilon'}\vec{b} - \frac{\psi}{\gamma}\frac{\omega}{\varepsilon'}\vec{s}\Big]\cdot\vec{\zeta}'\Big\} + \\ + K_{\frac{2}{3}}(\xi_e)\sqrt{2\lambda}\Big\{\beta\Big[\frac{\varepsilon^2+\varepsilon'^2}{\varepsilon\varepsilon'} + 2(\vec{\zeta}\cdot\vec{\zeta}')\Big] + \frac{\varepsilon^2-\varepsilon'^2}{2\varepsilon\varepsilon'}\frac{1}{\gamma}(\vec{\zeta}\wedge\vec{\zeta}')\cdot\vec{s} + \beta\frac{\omega^2}{\varepsilon\varepsilon'}(\vec{\zeta}\cdot\hat{v})(\vec{\zeta}'\cdot\hat{v}) + \\ - \frac{\omega^2}{2\varepsilon\varepsilon'\gamma}[(\vec{\zeta}\cdot\hat{v})(\vec{\zeta}'\cdot\vec{b}) + (\vec{\zeta}\cdot\vec{b})(\vec{\zeta}'\cdot\hat{v})]\Big\}; \end{aligned} \tag{5.31}$$

$$dW_3 = K_{\frac{1}{3}}(\xi_e)\Big\{\Big[\frac{\varepsilon^2+\varepsilon'^2}{2\varepsilon\varepsilon'}(\vec{\zeta}\cdot\vec{\zeta}') + 1\Big](\psi^2-\beta^2+2\lambda) + \frac{\varepsilon^2-\varepsilon'^2}{2\varepsilon\varepsilon'}(\vec{\zeta}\wedge\vec{\zeta}')\cdot\Big[2\beta\psi\hat{v} - \frac{\beta}{\gamma}\vec{s} - \frac{\psi}{\gamma}\vec{b}\Big] +$$

$$- \frac{\omega^2}{2\varepsilon\varepsilon'}(\psi^2 - \beta^2 + 2\lambda)(\vec{\zeta}\cdot\hat{v})(\vec{\zeta}'\cdot\hat{v}) + \frac{\omega^2}{2\varepsilon\varepsilon'}\frac{\psi}{\gamma}[(\vec{\zeta}\cdot\hat{v})(\vec{\zeta}'\cdot\vec{s}) + (\vec{\zeta}\cdot\vec{s})(\vec{\zeta}'\cdot\hat{v})] +$$
$$- \frac{\omega^2}{2\varepsilon\varepsilon'}\frac{\beta}{\gamma}[(\vec{\zeta}\cdot\hat{v})(\vec{\zeta}'\cdot\vec{b}) + (\vec{\zeta}\cdot\vec{b})(\vec{\zeta}'\cdot\hat{v})] - \frac{\omega^2}{2\varepsilon\varepsilon'\gamma^2}[(\vec{\zeta}\cdot\vec{s})(\vec{\zeta}'\cdot\vec{s}) - (\vec{\zeta}\cdot\vec{b})(\vec{\zeta}'\cdot\vec{b})]\Big\} +$$
$$-K_{\frac{2}{3}}(\xi_e)\sqrt{2\lambda}\frac{\omega}{\gamma}\Big\{\Big[\frac{\vec{\zeta}'}{\varepsilon} + \frac{\vec{\zeta}}{\varepsilon'}\Big]\cdot\vec{b}\Big\}; \tag{5.32}$$

notice that in eq. (5.28) the brackets in the superscript of dW_{NIC} make explicit all the inner spin and polarization states the distribution depends on. Potentially, with the implementation of (5.28)-(5.32), `SFQEDtoolkit` (the library we introduced in chapter 3) not only will be capable of producing a photon whose momentum is distributed according to the proper angular and energy distributions, but it will also track and describe the polarization or spin of all the particles involved in the process.

However, before being able to do so, Eqs. (5.28)-(5.32) must be put into a more suitable form, achieved by switching from the small angles (ψ,β)-system to the more natural polar and azimuthal (θ,φ) spherical angles. The conversion between the two may be performed by comparing the expression of $\vec{n}$ in both angles systems, that is eq. (5.24) and $\vec{n}_{(\theta,\varphi)} = (\cos\theta, \sin\theta\cos\phi, \sin\theta\sin\phi)$. This leads us to the following component by component equalities

$$\cos\beta\cos\psi = \cos\theta, \tag{5.33}$$
$$\cos\beta\sin\psi = \sin\theta\cos\varphi, \tag{5.34}$$
$$\sin\beta = \sin\theta\sin\varphi, \tag{5.35}$$

and, in the limit $\psi,\beta,\theta \sim \frac{1}{\gamma}$ with $\frac{1}{\gamma} \to 0$, (5.34) and (5.35) reduce to

$$\psi \sim \theta\cos\varphi, \tag{5.36}$$
$$\beta \sim \theta\sin\varphi, \tag{5.37}$$

so that

$$\beta^2 + \psi^2 \sim \theta^2,$$
$$\lambda = \frac{\psi^2}{2} + \frac{\beta^2}{2} + \frac{1}{2\gamma^2} \sim \frac{\theta^2}{2} + \frac{1}{2\gamma^2} \tag{5.38}$$

and (5.28)-(5.32) become

$$\frac{dW_{NIC}^{(\zeta\zeta'\xi)}}{d\omega d\Omega} = C_{NIC}(dW'_0 + \xi_1 dW'_1 + \xi_2 dW'_2 + \xi_3 dW'_3), \tag{5.39}$$

with

$$dW'_0 = K_{\frac{1}{3}}(\xi_e)\Big\{2\lambda\frac{\varepsilon^2+\varepsilon'^2}{\varepsilon\varepsilon'} + \Big(4\lambda - \frac{1}{\gamma^2}\Big)(\vec{\zeta}\cdot\vec{\zeta}') - \frac{1}{\gamma^2} + \frac{\varepsilon^2-\varepsilon'^2}{2\varepsilon\varepsilon'}\frac{\theta}{\gamma}\Big[\sin\varphi\vec{s} - \cos\varphi\vec{b}\Big]\cdot(\vec{\zeta}\wedge\vec{\zeta}') +$$

$$+\theta^2\frac{\omega^2}{\varepsilon\varepsilon'}(\vec{\zeta}\cdot\hat{v})(\vec{\zeta}'\cdot\hat{v})-\frac{\omega^2}{2\varepsilon\varepsilon'}\frac{\theta\sin\varphi}{\gamma}[(\vec{\zeta}\cdot\hat{v})(\vec{\zeta}'\cdot\vec{b})+(\vec{\zeta}\cdot\vec{b})(\vec{\zeta}'\cdot\hat{v})]+$$
$$-\frac{\omega^2}{2\varepsilon\varepsilon'}\frac{\theta\cos\varphi}{\gamma}[(\vec{\zeta}\cdot\hat{v})(\vec{\zeta}'\cdot\vec{s})+(\vec{\zeta}\cdot\vec{s})(\vec{\zeta}'\cdot\hat{v})]\Big\}+$$
$$+K_{\frac{2}{3}}(\xi_e)\sqrt{2\lambda}\Big\{\theta\sin\varphi\frac{\varepsilon^2-\varepsilon'^2}{\varepsilon\varepsilon'}[\vec{\zeta}+\vec{\zeta}']\cdot\hat{v}-\frac{\vec{b}}{\gamma}\cdot[\frac{\omega}{\varepsilon}\vec{\zeta}+\frac{\omega}{\varepsilon'}\vec{\zeta}']\Big\}; \tag{5.40}$$

$$dW_1'=K_{\frac{1}{3}}(\xi_e)\Big\{\theta^2\sin 2\varphi\Big[\frac{\varepsilon^2+\varepsilon'^2}{2\varepsilon\varepsilon'}(\vec{\zeta}\cdot\vec{\zeta}')+1\Big]+$$
$$+\frac{\varepsilon^2-\varepsilon'^2}{2\varepsilon\varepsilon'}(\vec{\zeta}\wedge\vec{\zeta}')\cdot\Big[(-\theta^2\cos 2\varphi-2\lambda)\hat{v}+\frac{\theta\cos\varphi}{\gamma}\vec{s}-\frac{\theta\sin\varphi}{\gamma}\vec{b}\Big]+$$
$$-\theta^2\sin 2\varphi\frac{\omega^2}{2\varepsilon\varepsilon'}(\vec{\zeta}\cdot\hat{v})(\vec{\zeta}'\cdot\hat{v})+\frac{\omega^2}{2\varepsilon\varepsilon'}\frac{\theta\sin\varphi}{\gamma}[(\vec{\zeta}\cdot\hat{v})(\vec{\zeta}'\cdot\vec{s})+(\vec{\zeta}\cdot\vec{s})(\vec{\zeta}'\cdot\hat{v})]+$$
$$+\frac{\omega^2}{2\varepsilon\varepsilon'}\frac{\theta\cos\varphi}{\gamma}[(\vec{\zeta}\cdot\hat{v})(\vec{\zeta}'\cdot\vec{b})+(\vec{\zeta}\cdot\vec{b})(\vec{\zeta}'\cdot\hat{v})]-\frac{\omega^2}{2\varepsilon\varepsilon'\gamma^2}[(\vec{\zeta}\cdot\vec{s})(\vec{\zeta}'\cdot\vec{b})+(\vec{\zeta}\cdot\vec{b})(\vec{\zeta}'\cdot\vec{s})]\Big\}+$$
$$+K_{\frac{2}{3}}(\xi_e)\sqrt{2\lambda}\frac{\omega}{\gamma}\Big\{\Big[\frac{\vec{\zeta}'}{\varepsilon}+\frac{\vec{\zeta}}{\varepsilon'}\Big]\cdot\vec{s}\Big\}; \tag{5.41}$$

$$dW_2'=K_{\frac{1}{3}}(\xi_e)\Big\{\Big[\Big(2\lambda\frac{\varepsilon^2-\varepsilon'^2}{\varepsilon\varepsilon'}-\frac{\omega}{\gamma^2\varepsilon}\Big)\hat{v}-\frac{\theta\sin\varphi}{\gamma}\frac{\omega}{\varepsilon}\vec{b}-\frac{\theta\cos\varphi}{\gamma}\frac{\omega}{\varepsilon}\vec{s}\Big]\cdot\vec{\zeta}+$$
$$+\Big[\Big(2\lambda\frac{\varepsilon^2-\varepsilon'^2}{\varepsilon\varepsilon'}-\frac{\omega}{\gamma^2\varepsilon'}\Big)\hat{v}-\frac{\theta\sin\varphi}{\gamma}\frac{\omega}{\varepsilon'}\vec{b}-\frac{\theta\cos\varphi}{\gamma}\frac{\omega}{\varepsilon'}\vec{s}\Big]\cdot\vec{\zeta}'\Big\}+$$
$$+K_{\frac{2}{3}}(\xi_e)\sqrt{2\lambda}\Big\{\theta\sin\varphi\Big[\frac{\varepsilon^2+\varepsilon'^2}{\varepsilon\varepsilon'}+2(\vec{\zeta}\cdot\vec{\zeta}')\Big]+\frac{\varepsilon^2-\varepsilon'^2}{2\varepsilon\varepsilon'}\frac{1}{\gamma}(\vec{\zeta}\wedge\vec{\zeta}')\cdot\vec{s}+\theta\sin\varphi\frac{\omega^2}{\varepsilon\varepsilon'}(\vec{\zeta}\cdot\hat{v})(\vec{\zeta}'\cdot\hat{v})+$$
$$-\frac{\omega^2}{2\varepsilon\varepsilon'\gamma}[(\vec{\zeta}\cdot\hat{v})(\vec{\zeta}'\cdot\vec{b})+(\vec{\zeta}\cdot\vec{b})(\vec{\zeta}'\cdot\hat{v})]\Big\}; \tag{5.42}$$

$$dW_3'=K_{\frac{1}{3}}(\xi_e)\Big\{\Big[\frac{\varepsilon^2+\varepsilon'^2}{2\varepsilon\varepsilon'}(\vec{\zeta}\cdot\vec{\zeta}')+1\Big](\theta^2\cos 2\varphi+2\lambda)+$$
$$+\frac{\varepsilon^2-\varepsilon'^2}{2\varepsilon\varepsilon'}(\vec{\zeta}\wedge\vec{\zeta}')\cdot\Big[\theta^2\sin 2\varphi\hat{v}-\frac{\theta\sin\varphi}{\gamma}\vec{s}-\frac{\theta\cos\varphi}{\gamma}\vec{b}\Big]+$$
$$-\frac{\omega^2}{2\varepsilon\varepsilon'}(\theta^2\cos 2\varphi+2\lambda)(\vec{\zeta}\cdot\hat{v})(\vec{\zeta}'\cdot\hat{v})+\frac{\omega^2}{2\varepsilon\varepsilon'}\frac{\theta\cos\varphi}{\gamma}[(\vec{\zeta}\cdot\hat{v})(\vec{\zeta}'\cdot\vec{s})+(\vec{\zeta}\cdot\vec{s})(\vec{\zeta}'\cdot\hat{v})]+$$
$$-\frac{\omega^2}{2\varepsilon\varepsilon'}\frac{\theta\sin\varphi}{\gamma}[(\vec{\zeta}\cdot\hat{v})(\vec{\zeta}'\cdot\vec{b})+(\vec{\zeta}\cdot\vec{b})(\vec{\zeta}'\cdot\hat{v})]-\frac{\omega^2}{2\varepsilon\varepsilon'\gamma^2}[(\vec{\zeta}\cdot\vec{s})(\vec{\zeta}'\cdot\vec{s})-(\vec{\zeta}\cdot\vec{b})(\vec{\zeta}'\cdot\vec{b})]\Big\}+$$
$$-K_{\frac{2}{3}}(\xi_e)\sqrt{2\lambda}\frac{\omega}{\gamma}\Big\{\Big[\frac{\vec{\zeta}'}{\varepsilon}+\frac{\vec{\zeta}}{\varepsilon'}\Big]\cdot\vec{b}\Big\}; \tag{5.43}$$

$d\Omega_{(\psi,\beta)}=d\Omega_{(\theta,\varphi)}=\sin\theta d\theta d\varphi\equiv d\Omega$ is the usual angular spherical coordinates, integral measure.

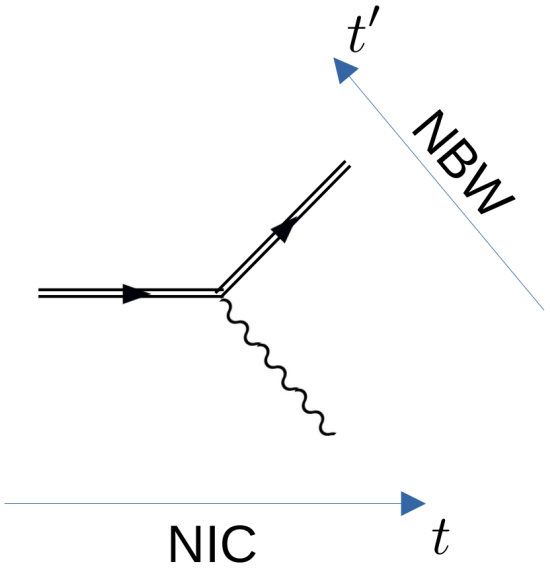

Figure 5.2: By simply reversing the flow of time, the Feynman diagram for the NIC photon emission process transforms into one representing NBW pair production (this time-reversal procedure naturally entails a modification of the momentum conservation law). This property is known as crossing symmetry.

The ensemble of (5.39)-(5.43), denoted from now on as FNIC, matches perfectly the differential distribution reported in [100]: these Eqs. pave the way for different numerical applications, which will be presented in the sections to come. Simultaneously with the development of the fully-resolved NIC distribution, we will establish the NBW counterpart as well. This will help us highlight the differences and similarities between the two SFQED processes.

5.2.2 The fully-resolved NBW differential distribution

As we already stated before, with a few adjustments Eqs. (5.10)-(5.11) can be adapted to describe the NBW transition probabilities of a photon decaying into an electron-positron pair after interacting with a SF. The SFQED vertex associated to the NIC can be mapped onto that representing the NBW process just by changing the time direction (see fig. 5.2), or equivalently by taking advantage of the crossing symmetry. It is thus easy to translate eq. (5.10) into

$$dw_{NBW} = d^3p \frac{\alpha}{(2\pi)^2\omega} \int dt_1 \int dt_2 R^*(t_1)R(t_2) \exp\Big\{i\frac{\varepsilon_-}{\varepsilon_+}k_\mu[x^\mu(t_2) - x^\mu(t_1)]\Big\}, \quad (5.44)$$

with the vertex function $R(t)$ now redefined as

$$R(t) = \frac{1}{2}\psi^\dagger_{\zeta_-}(p_-(t))[e_\mu J^\mu(p_-(t)) + e_\mu J^\mu(-p_+(t))]\psi_{\bar{\zeta}_+}(-p_+(t)). \quad (5.45)$$

Here $\psi_{\bar{\zeta}_+}(-p_+) = \frac{1}{\sqrt{2\varepsilon_+}} u_{\bar{\zeta}_+}(-p_+)$ describes the outgoing antiparticle wave function, with

$$u_{\bar{\zeta}_+}(-p_+) = \begin{pmatrix} \sqrt{\varepsilon_+ - m}\,(\vec{n}_{p_+} \cdot \vec{\sigma})\ \varphi_{\zeta_+} \\ \sqrt{\varepsilon_+ + m}\ \varphi_{\zeta_+} \end{pmatrix}. \tag{5.46}$$

Plugging $J^\mu = \gamma^\mu$ and (5.46) into eq. (5.45) recasts the latter into

$$R(t) = i\varphi^\dagger_{\zeta_-}(p_-(t))[A(t) - i\vec{\sigma} \cdot \vec{B}(t)]\varphi_{\zeta_+}(p_+(t)), \tag{5.47}$$

where the coefficients A and $\vec{B}$ now read

$$A(t) = \frac{\vec{e} \cdot (\vec{k} \wedge \vec{p}_-(t))}{2\sqrt{\varepsilon_-\varepsilon_+(\varepsilon_- + m)(\varepsilon_+ + m)}} \tag{5.48}$$

$$\vec{B}(t) = \frac{\vec{e}[(\varepsilon_- + m)(\varepsilon_+ + m) - \vec{p}_+(t) \cdot \vec{p}_-(t)] + [\vec{p}_+(t) - \vec{p}_-(t)]\vec{e} \cdot \vec{p}_-(t)}{2\sqrt{\varepsilon_-\varepsilon_+(\varepsilon_- + m)(\varepsilon_+ + m)}}. \tag{5.49}$$

Exactly as in section 5.2.1, $k^\mu = (\omega, \vec{k} = \omega\vec{n})$ and e^μ identify the four-wave vector and polarization of the photon, while $\vec{p}_\pm = \gamma_\pm m\vec{v}_\pm$, $\varepsilon_\pm$ and $\vec{\zeta}_\pm$ correspond to the momenta, energies and spins of the outcoming electron $(-)$ and positron $(+)$.

As in the NIC case, we now proceed by taking the ultrarelativistic limit ($\varepsilon_\pm \gg m$) of the coefficients (5.48)-(5.49), obtaining

$$A \to \frac{\omega}{2\varepsilon_+}[\vec{e} \cdot (\vec{n} \wedge \vec{v}_-)\,] \tag{5.50}$$

$$\vec{B} \to \frac{\omega}{2\varepsilon_+}\Big[\frac{\vec{e}}{\gamma_-} + (\vec{e} \cdot \vec{v}_-)\Big(\vec{n} - \frac{2\varepsilon_-}{\omega}\vec{v}_-\Big)\Big]. \tag{5.51}$$

Similarly to (5.21) and (5.22), we then expand all dynamical quantities appearing in Eqs. (5.44) and (5.50)-(5.51) in terms of the time variables t and τ defined in (5.19)-(5.20). As a result equation (5.44) can be manipulated into the fully-resolved (in the decay angles, polarization and spin) differential probability for NBW pair production

$$\frac{dW^{(\xi\zeta_-\zeta_+)}_{NBW}}{d\varepsilon_- d\Omega_{(\psi,\beta)}} = C_{BW}(d\bar{W}_0 + \xi_1 d\bar{W}_1 + \xi_2 d\bar{W}_2 + \xi_3 d\bar{W}_3), \tag{5.52}$$

with the constant $C_{BW} = \frac{\alpha}{4\pi^2}\sqrt{\frac{2}{3}}\lambda_-^{\frac{1}{2}}\frac{\gamma_-^3}{\chi_\gamma}$ and

$$\begin{aligned} d\bar{W}_0 = K_{\frac{1}{3}}(\xi_\gamma)\frac{1}{2\varepsilon_+^2}\Big\{\frac{\omega^2}{\gamma_-^2}\Big(1 + (\vec{\zeta}_- \cdot \vec{\zeta}_+)\Big) + \Big(4\lambda_- - \frac{1}{\gamma_-^2}\Big)\Big[\varepsilon_+^2 + \varepsilon_-^2 - 2\varepsilon_+\varepsilon_-(\vec{\zeta}_- \cdot \vec{\zeta}_+)\Big] + \\ + \frac{\omega^2}{\gamma_-}\Big[\beta\vec{s} - \psi\vec{b}\Big] \cdot (\vec{\zeta}_- \wedge \vec{\zeta}_+) + (\varepsilon_+^2 - \varepsilon_-^2)\frac{\beta}{\gamma_-}[(\vec{\zeta}_- \cdot \hat{v})(\vec{\zeta}_+ \cdot \vec{b}) + (\vec{\zeta}_- \cdot \vec{b})(\vec{\zeta}_+ \cdot \hat{v})] + \\ + (\varepsilon_+^2 - \varepsilon_-^2)\frac{\psi}{\gamma_-}[(\vec{\zeta}_- \cdot \hat{v})(\vec{\zeta}_+ \cdot \vec{s}) + (\vec{\zeta}_- \cdot \vec{s})(\vec{\zeta}_+ \cdot \hat{v})] + \end{aligned}$$

$$- \Big(4\lambda_- - \frac{1}{\gamma_-^2}\Big)(\varepsilon_+ - \varepsilon_-)^2(\vec{\zeta}_- \cdot \hat{v})(\vec{\zeta}_+ \cdot \hat{v}) - \frac{\omega^2}{\gamma_-^2}[(\vec{\zeta_-} \cdot \vec{b})(\vec{\zeta}_+ \cdot \vec{b}) + (\vec{\zeta}_- \cdot \vec{s})(\vec{\zeta}_+ \cdot \vec{s})]\Big\}+$$
$$-K_{\frac{2}{3}}(\xi_\gamma)\frac{\sqrt{2\lambda_-}}{\varepsilon_+^2}\omega\Big\{[\frac{\varepsilon_+}{\gamma_-}\vec{\zeta}_- - \frac{\varepsilon_-}{\gamma_-}\vec{\zeta}_+] \cdot \vec{b} - \beta(\varepsilon_+ - \varepsilon_-)[(\vec{\zeta}_- \cdot \hat{v}) - (\vec{\zeta}_+ \cdot \hat{v})]\Big\}; \quad (5.53)$$

$$d\bar{W}_1 = K_{\frac{1}{3}}(\xi_\gamma)\frac{1}{2\varepsilon_+^2}\Big\{2\beta\psi\Big[(\varepsilon_+^2 + \varepsilon_-^2)(\vec{\zeta}_- \cdot \vec{\zeta}_+) - 2\varepsilon_+\varepsilon_-\Big] + (\varepsilon_+^2 - \varepsilon_-^2)[\psi^2 - \beta^2 + 2\lambda_-](\vec{\zeta}_- \wedge \vec{\zeta}_+) \cdot \hat{v}+$$
$$+ \frac{\omega^2}{\gamma_-}\Big[\beta\vec{b} - \psi\vec{s}\Big] \cdot (\vec{\zeta}_- \wedge \vec{\zeta}_+) + (\varepsilon_+^2 - \varepsilon_-^2)\frac{\beta}{\gamma_-}[(\vec{\zeta}_- \cdot \hat{v})(\vec{\zeta}_+ \cdot \vec{s}) + (\vec{\zeta}_- \cdot \vec{s})(\vec{\zeta}_+ \cdot \hat{v})]+$$
$$+ (\varepsilon_+^2 - \varepsilon_-^2)\frac{\psi}{\gamma_-}[(\vec{\zeta_-} \cdot \hat{v})(\vec{\zeta}_+ \cdot \vec{b}) + (\vec{\zeta}_- \cdot \vec{b})(\vec{\zeta}_+ \cdot \hat{v})] - 2\beta\psi(\varepsilon_+ - \varepsilon_-)^2(\vec{\zeta}_- \cdot \hat{v})(\vec{\zeta}_+ \cdot \hat{v})+$$
$$- \frac{\omega^2}{\gamma_-^2}[(\vec{\zeta}_- \cdot \vec{s})(\vec{\zeta}_+ \cdot \vec{b}) + (\vec{\zeta}_- \cdot \vec{b})(\vec{\zeta}_+ \cdot \vec{s})]\Big\}+$$
$$+K_{\frac{2}{3}}(\xi_\gamma)\frac{\sqrt{2\lambda_-}}{\varepsilon_+^2}\frac{\omega}{\gamma_-}\Big\{\Big[\vec{\zeta}_+\varepsilon_+ - \vec{\zeta}_-\varepsilon_-\Big] \cdot \vec{s}\Big\}; \quad (5.54)$$

$$d\bar{W}_2 = K_{\frac{1}{3}}(\xi_\gamma)\frac{1}{2\varepsilon_+^2}\Big\{\frac{2\beta\omega}{\gamma_-}\Big[(\vec{\zeta}_- \cdot \vec{b})\varepsilon_+ - (\vec{\zeta}_+ \cdot \vec{b})\varepsilon_-\Big] + \frac{2\psi\omega}{\gamma_-}\Big[(\vec{\zeta}_- \cdot \vec{s})\varepsilon_+ - (\vec{\zeta}_+ \cdot \vec{s})\varepsilon_-\Big]+$$
$$+ \frac{2\omega}{\gamma_-^2}\Big[(\vec{\zeta}_- \cdot \hat{v})\varepsilon_+ + (\vec{\zeta}_+ \cdot \hat{v})\varepsilon_-\Big] - 4\lambda_-(\varepsilon_+^2 - \varepsilon_-^2)\Big[(\vec{\zeta}_- \cdot \hat{v}) - (\vec{\zeta}_+ \cdot \hat{v})\Big]\Big\}+$$
$$-K_{\frac{2}{3}}(\xi_\gamma)\frac{\sqrt{2\lambda_-}}{\varepsilon_+^2}\Big\{\beta\Big[\varepsilon_+^2 + \varepsilon_-^2 - 2\varepsilon_+\varepsilon_-(\vec{\zeta}_- \cdot \vec{\zeta}_+)\Big] + \frac{\omega^2}{2\gamma_-}(\vec{\zeta}_- \wedge \vec{\zeta}_+) \cdot \vec{s} - \beta(\varepsilon_+ - \varepsilon_-)^2(\vec{\zeta}_- \cdot \hat{v})(\vec{\zeta}_+ \cdot \hat{v})+$$
$$+ \frac{(\varepsilon_+^2 - \varepsilon_-^2)}{2\gamma_-}[(\vec{\zeta_-} \cdot \hat{v})(\vec{\zeta}_+ \cdot \vec{b}) + (\vec{\zeta}_- \cdot \vec{b})(\vec{\zeta}_+ \cdot \hat{v})]\Big\}; \quad (5.55)$$

$$d\bar{W}_3 = K_{\frac{1}{3}}(\xi_\gamma)\frac{1}{2\varepsilon_+^2}\Big\{\Big[(\varepsilon_+^2 + \varepsilon_-^2)(\vec{\zeta}_- \cdot \vec{\zeta}_+) - 2\varepsilon_+\varepsilon_-\Big](\psi^2 - \beta^2 + 2\lambda_-) - 2\beta\psi(\varepsilon_+^2 - \varepsilon_-^2)(\vec{\zeta}_- \wedge \vec{\zeta}_+) \cdot \hat{v}+$$
$$+ \frac{\omega^2}{\gamma_-}\Big[\beta\vec{s} + \psi\vec{b}\Big] \cdot (\vec{\zeta}_- \wedge \vec{\zeta}_+) - (\varepsilon_+^2 - \varepsilon_-^2)\frac{\beta}{\gamma_-}[(\vec{\zeta_-} \cdot \hat{v})(\vec{\zeta}_+ \cdot \vec{b}) + (\vec{\zeta}_- \cdot \vec{b})(\vec{\zeta}_+ \cdot \hat{v})]+$$
$$+ (\varepsilon_+^2 - \varepsilon_-^2)\frac{\psi}{\gamma_-}[(\vec{\zeta}_- \cdot \hat{v})(\vec{\zeta}_+ \cdot \vec{s}) + (\vec{\zeta}_- \cdot \vec{s})(\vec{\zeta}_+ \cdot \hat{v})]+$$
$$- \frac{\omega^2}{\gamma_-^2}[(\vec{\zeta}_- \cdot \vec{s})(\vec{\zeta}_+ \cdot \vec{s}) - (\vec{\zeta_-} \cdot \vec{b})(\vec{\zeta}_+ \cdot \vec{b})] - (\psi^2 - \beta^2 + 2\lambda_-)(\varepsilon_+ - \varepsilon_-)^2(\vec{\zeta}_- \cdot \hat{v})(\vec{\zeta}_+ \cdot \hat{v})\Big\}+$$
$$-K_{\frac{2}{3}}(\xi_\gamma)\frac{\sqrt{2\lambda_-}}{\varepsilon_+^2}\frac{\omega}{\gamma_-}\Big\{\Big[\vec{\zeta}_+\varepsilon_+ - \vec{\zeta}_-\varepsilon_-\Big] \cdot \vec{b}\Big\}. \quad (5.56)$$

The parameter $\lambda_- = (1 - \vec{n} \cdot \vec{v}_-)$ encodes in itself the angular details of the process, $\xi_\gamma = \frac{4\sqrt{2}}{3}\frac{\omega^2\gamma_-^3}{\varepsilon_-\varepsilon_+\chi_\gamma}\lambda_-^{\frac{3}{2}}$ is the argument of the modified Bessel functions of the second kind and $\omega = \varepsilon_- + \varepsilon_+$. In writing down Eq. (5.52), we choose the following as the reference axis system for projecting all vectors, including spins and polarization:

- the direction of the outgoing electron's velocity, $\frac{\vec{v}_-}{|\vec{v}_-|} \equiv \hat{v}$,
- the transverse normalized acceleration experienced by the just produced electron, $\vec{s}$,
- the vector $\vec{b} = \hat{v} \wedge \vec{s}$.

The momentum differential[10] d^3p_- has been expressed in spherical coordinates through $d^3p_- = \varepsilon_-^2 d\varepsilon_- d\Omega_{(\psi,\beta)}$, where the angular measure $d\Omega_{(\psi,\beta)}$ has been expressed in the (ψ,β)-system of small angles already introduced in section 5.2.1 (fig. 5.1). As in the NIC case, A key aspect of Eqs. (5.52)-(5.56) is that they are differential in the final electron energy ε_-, effectively restricting its use to characterizing electron properties. Consequently, when dealing with positrons, one must retrieve the positron counterpart of Eqs. (5.52)-(5.56). As we shall see, the symmetry of the process allows for a straightforward transition between the two by applying the simple $+ \leftrightarrow -$ prescription (see Section 5.5.2).

Following the same logic as in sec. 5.2.1 we switch to the usual (θ,φ) polar angles by replacing Eqs. (5.36)-(5.37) into (5.52)-(5.56), so that Eq.

$$\frac{dW_{NBW}^{(\xi\zeta_-\zeta_+)}}{d\varepsilon_- d\Omega} = C_{BW}(d\bar{W}'_0 + \xi_1 d\bar{W}'_1 + \xi_2 d\bar{W}'_2 + \xi_3 d\bar{W}'_3) \tag{5.57}$$

is obtanied, with

$$\begin{aligned} d\bar{W}'_0 = K_{\frac{1}{3}}(\xi_\gamma)\Big\{&\frac{\omega^2}{2\varepsilon_+^2\gamma_-^2} + \Big(4\lambda_- - \frac{1}{\gamma_-^2}\Big)\Big[\frac{\varepsilon_+^2+\varepsilon_-^2}{2\varepsilon_+^2} - \frac{\varepsilon_-}{\varepsilon_+}(\vec{\zeta}_-\cdot\vec{\zeta}_+)\Big] + \\ &+ \frac{\omega^2}{2\varepsilon_+^2\gamma_-}\theta\Big[\sin\varphi\vec{s} - \cos\varphi\vec{b}\Big]\cdot(\vec{\zeta}_-\wedge\vec{\zeta}_+) + \\ &+ \frac{(\varepsilon_+^2-\varepsilon_-^2)}{2\varepsilon_+^2}\frac{\theta}{\gamma_-}\Big[\cos\varphi[(\vec{\zeta}_-\cdot\hat{v})(\vec{\zeta}_+\cdot\vec{s}) + (\vec{\zeta}_-\cdot\vec{s})(\vec{\zeta}_+\cdot\hat{v})] + \\ &\qquad + \sin\varphi[(\vec{\zeta}_-\cdot\hat{v})(\vec{\zeta}_+\cdot\vec{b}) + (\vec{\zeta}_-\cdot\vec{b})(\vec{\zeta}_+\cdot\hat{v})]\Big] + \\ &+ \Big[\frac{\omega^2}{2\varepsilon_+^2\gamma_-^2} - \Big(4\lambda_- - \frac{1}{\gamma_-^2}\Big)\frac{(\varepsilon_+-\varepsilon_-)^2}{2\varepsilon_+^2}\Big](\vec{\zeta}_-\cdot\hat{v})(\vec{\zeta}_+\cdot\hat{v})\Big\} + \\ -K_{\frac{2}{3}}(\xi_\gamma)\sqrt{2\lambda_-}\Big\{&\frac{\omega}{\varepsilon_+\gamma_-}\Big[(\vec{\zeta}_-\cdot\vec{b}) - \frac{\varepsilon_-}{\varepsilon_+}(\vec{\zeta}_+\cdot\vec{b})\Big] - \theta\sin\varphi\frac{(\varepsilon_+^2-\varepsilon_-^2)}{\varepsilon_+^2}[(\vec{\zeta}_-\cdot\hat{v}) - (\vec{\zeta}_+\cdot\hat{v})]\Big\}; \end{aligned} \tag{5.58}$$

$$\begin{aligned} d\bar{W}'_1 = K_{\frac{1}{3}}(\xi_\gamma)\Big\{&\theta^2\sin 2\varphi\Big[\frac{(\varepsilon_+^2+\varepsilon_-^2)}{2\varepsilon_+^2}(\vec{\zeta}_-\cdot\vec{\zeta}_+) - \frac{\varepsilon_-}{\varepsilon_+} - \frac{(\varepsilon_+-\varepsilon_-)^2}{2\varepsilon_+^2}(\vec{\zeta}_-\cdot\hat{v})(\vec{\zeta}_+\cdot\hat{v})\Big] + \\ &+ \Big[\frac{(\varepsilon_+^2-\varepsilon_-^2)}{2\varepsilon_+^2}(\theta^2\cos 2\varphi + 2\lambda_-)\hat{v} + \frac{\omega^2}{2\varepsilon_+^2\gamma_-}\theta(\sin\varphi\vec{b} - \cos\varphi\vec{s})\Big]\cdot(\vec{\zeta}_-\wedge\vec{\zeta}_+) + \end{aligned}$$

[10] The approximation $\varepsilon_- = \sqrt{p_-^2 + m_e^2} \sim p_-$ has been used.

$$+\frac{(\varepsilon_+^2-\varepsilon_-^2)}{2\varepsilon_+^2}\frac{\theta}{\gamma_-}\Big[\sin\varphi[(\vec{\zeta}_-\cdot\hat{v})(\vec{\zeta}_+\cdot\vec{s})+(\vec{\zeta}_-\cdot\vec{s})(\vec{\zeta}_+\cdot\hat{v})]+$$
$$+\cos\varphi[(\vec{\zeta}_-\cdot\hat{v})(\vec{\zeta}_+\cdot\vec{b})+(\vec{\zeta}_-\cdot\vec{b})(\vec{\zeta}_+\cdot\hat{v})]\Big]+$$
$$-\frac{\omega^2}{2\varepsilon_+^2\gamma_-^2}[(\vec{\zeta}_-\cdot\vec{s})(\vec{\zeta}_+\cdot\vec{b})+(\vec{\zeta}_-\cdot\vec{b})(\vec{\zeta}_+\cdot\vec{s})]\Big\}+$$
$$+K_{\frac{2}{3}}(\xi_\gamma)\sqrt{2\lambda_-}\frac{\omega}{\varepsilon_+\gamma_-}\Big\{\Big[(\vec{\zeta}_+\cdot\vec{s})-(\vec{\zeta}_-\cdot\vec{s})\frac{\varepsilon_-}{\varepsilon_+}\Big]\Big\}; \tag{5.59}$$

$$d\bar{W}_2' = K_{\frac{1}{3}}(\xi_\gamma)\Big\{\Big[\Big(\frac{\omega}{\varepsilon_+\gamma_-^2}-2\lambda_-\frac{\varepsilon_+^2-\varepsilon_-^2}{\varepsilon_+^2}\Big)\hat{v}+\frac{\theta}{\varepsilon_+}\frac{\omega}{\gamma_-}(\sin\varphi\vec{b}+\cos\varphi\vec{s})\Big]\cdot\vec{\zeta}_-+$$
$$-\Big[-\Big(\frac{\omega\varepsilon_-}{\varepsilon_+^2\gamma_-^2}+2\lambda_-\frac{\varepsilon_+^2-\varepsilon_-^2}{\varepsilon_+^2}\Big)\hat{v}+\frac{\theta\varepsilon_-}{\varepsilon_+^2}\frac{\omega}{\gamma_-}(\sin\varphi\vec{b}+\cos\varphi\vec{s})\Big]\cdot\vec{\zeta}_+\Big\}+$$
$$-K_{\frac{2}{3}}(\xi_\gamma)\sqrt{2\lambda_-}\Big\{\theta\sin\varphi\Big[\frac{\varepsilon_+^2+\varepsilon_-^2}{\varepsilon_+^2}-\frac{2\varepsilon_-}{\varepsilon_+}(\vec{\zeta}_-\cdot\vec{\zeta}_+)-\frac{(\varepsilon_+-\varepsilon_-)^2}{\varepsilon_+^2}(\vec{\zeta}_-\cdot\hat{v})(\vec{\zeta}_+\cdot\hat{v})\Big]+$$
$$+\frac{1}{2\gamma_-}\Big[\frac{\omega^2}{\varepsilon_+^2}(\vec{\zeta}_-\wedge\vec{\zeta}_+)\cdot\vec{s}+\frac{(\varepsilon_+^2-\varepsilon_-^2)}{\varepsilon_+^2}[(\vec{\zeta}_-\cdot\hat{v})(\vec{\zeta}_+\cdot\vec{b})+(\vec{\zeta}_-\cdot\vec{b})(\vec{\zeta}_+\cdot\hat{v})]\Big]\Big\}; \tag{5.60}$$

$$d\bar{W}_3' = K_{\frac{1}{3}}(\xi_\gamma)\Big\{\Big[\frac{(\varepsilon_+^2+\varepsilon_-^2)}{2\varepsilon_+^2}(\vec{\zeta}_-\cdot\vec{\zeta}_+)-\frac{\varepsilon_-}{\varepsilon_+}-\frac{(\varepsilon_+-\varepsilon_-)^2}{2\varepsilon_+^2}(\vec{\zeta}_-\cdot\hat{v})(\vec{\zeta}_+\cdot\hat{v})\Big](\theta^2\cos2\varphi+2\lambda_-)+$$
$$+\Big[\frac{\theta\omega^2}{2\varepsilon_+^2\gamma_-}(\sin\varphi\vec{s}+\cos\varphi\vec{b})-\theta^2\sin2\varphi\frac{(\varepsilon_+^2-\varepsilon_-^2)}{2\varepsilon_+^2}\hat{v}\Big]\cdot(\vec{\zeta}_-\wedge\vec{\zeta}_+)+$$
$$+\frac{(\varepsilon_+^2-\varepsilon_-^2)}{2\varepsilon_+^2}\frac{\theta}{\gamma_-}\Big[\cos\varphi[(\vec{\zeta}_-\cdot\hat{v})(\vec{\zeta}_+\cdot\vec{s})+(\vec{\zeta}_-\cdot\vec{s})(\vec{\zeta}_+\cdot\hat{v})]+$$
$$-\sin\varphi[(\vec{\zeta}_-\cdot\hat{v})(\vec{\zeta}_+\cdot\vec{b})+(\vec{\zeta}_-\cdot\vec{b})(\vec{\zeta}_+\cdot\hat{v})]\Big]$$
$$-\frac{\omega^2}{2\varepsilon_+^2\gamma_-^2}[(\vec{\zeta}_-\cdot\vec{s})(\vec{\zeta}_+\cdot\vec{s})-(\vec{\zeta}_-\cdot\vec{b})(\vec{\zeta}_+\cdot\vec{b})]\Big\}+$$
$$-K_{\frac{2}{3}}(\xi_\gamma)\sqrt{2\lambda_-}\frac{\omega}{\varepsilon_+\gamma_-}\Big\{\Big[(\vec{\zeta}_+\cdot\vec{b})-(\vec{\zeta}_-\cdot\vec{b})\frac{\varepsilon_-}{\varepsilon_+}\Big]\Big\}. \tag{5.61}$$

Just as Eqs. (5.39)-(5.43) were essential for the NIC, Eqs. (5.57)-(5.61) are crucial for modeling a fully-resolved NBW photon decay into pairs, and will thus be referred to as the FNBW distribution.

In the upcoming sections, we will systematically outline the steps necessary to develop an approach capable of characterizing both the NIC and NBW processes in their entirety. Starting with the two sets of equations, (5.39)-(5.43) and (5.57)-(5.61), we will perform subsequent integrations and/or summations to reduce the number of degrees of freedom, deriving a new differential probability distribution at each stage that can be used to extract information about the final particles. By

simultaneously addressing the NIC and NBW processes from both physical and numerical perspectives, we will first determine the probability per unit time for these processes to occur. We will then assess the energies and directions of the final particles, culminating in the determination of their spin and polarization states. By the end of this chapter, we will recognize that the FNIC and FNBW distributions, as presented in sections 5.2.1-5.2.2, are, in fact, improper, as they can potentially take on negative values. In Section 5.6, we will propose a method to resolve this issue, demonstrating that by integrating the FNIC distribution over the process's formation region, we successfully obtain a new, physically meaningful differential probability. This can then be used to accurately determine the final internal states of the outgoing particles

5.3 The pure and mixed spin-states approach

Throughout the following sections, we describe electron spin and photon polarization states. Before delving into this topic—following the example set by [57, 106]—we briefly introduce the physical and mathematical model that, *on average*, captures the behavior of spin and polarization states.

As is customary, we begin our discussion with the 2×2 polarization density matrix for electrons (or positrons)

$$\rho_{ij} = \langle \varphi_i \varphi_j^{\dagger} \rangle, \tag{5.62}$$

where φ denotes the particle's two-component spinor (see Sec. 5.2.1) and $\langle \bullet \rangle$ represents the average over a particle ensemble. Since ρ is Hermitian, it admits the following expansion

$$\rho = \frac{1}{2}(1 + \vec{\zeta} \cdot \vec{\sigma}) \tag{5.63}$$

where $\vec{\zeta}$ is the polarization (or spin) three-vector and $\vec{\sigma}$ are the Pauli matrices

$$\sigma^1 = \begin{pmatrix} 0 & 1 \\ 1 & 0 \end{pmatrix}, \qquad \sigma^2 = \begin{pmatrix} 0 & -i \\ i & 0 \end{pmatrix}, \qquad \sigma^3 = \begin{pmatrix} 1 & 0 \\ 0 & -1 \end{pmatrix}. \tag{5.64}$$

When Eq. (5.63) describes a single electron, φ can be expressed as a superposition of spin-up (+) and spin-down (-) states with respect to a chosen quantization axis

$$\varphi = c_1 \varphi_+ + c_2 \varphi_- \quad \text{with} \quad |c_1|^2 + |c_2|^2 = 1, \tag{5.65}$$

and thus the magnitude of $\vec{\zeta}$ is unity ($|\vec{\zeta}| = 1$). In this case, the electron is said to be in a *pure* state. However, an ensemble of particles may be in an undefined, or *mixed*, spin state, for which $|\vec{\zeta}| \leq 1$. This scenario typically occurs with numerical macro-particles, where each entity represents multiple real-world particles sharing identical energy-momentum and space-time coordinates.

A similar argument applies to photon polarization. Since a generic photon polarization three-vector $\vec{e}$ can be expressed in terms of its components along the two

unit vectors $\vec{e}_1$ and $\vec{e}_2$, which are orthogonal[11] to the photon momentum $\vec{k}$, the corresponding Hermitian polarization density matrix is given by

$$\rho_{ij} = \langle (\vec{e} \cdot e_i)(\vec{e}^* \cdot e_j) \rangle. \tag{5.66}$$

As in the electron case, the standard expansion in Pauli matrices allows Eq. (5.66) to be rewritten as

$$\rho = \frac{1}{2}(1 + \vec{\xi} \cdot \sigma), \tag{5.67}$$

where $\vec{\xi}$ is the polarization three-vector, whose components correspond to the Stokes parameters[12]. As before, a single photon is always in a completely polarized pure state, characterized by $|\xi| = 1$. Conversely, a collection of photons, such as those in a photon beam, may exhibit a mixed polarization state, for which $|\xi| \leq 1$.

In what follows, we will examine the particles from both pure and mixed perspectives.

5.4 Spin-resolved NIC and polarization-resolved NBW probability and final energies

Any state-of-the-art SFQED-oriented MC code begins by assessing whether a process occurs; if it does, the next step is to determine the energies of all the particles involved in the event. This section will focus on deriving the NIC and NBW probabilities, as well as discussing the mechanisms that enable the extraction of the final particle energies. In contrast to Chapter 3, this time we will explore the potential dependence on both the initial electron's spin and the photon's polarization. These considerations will give rise to new coupling terms, which will have significant implications even in cases where the processes do not occur.

In the first part of the section, we will begin by discussing the NIC, before moving on to the NBW in the second.

---

[11] $\vec{e}_1$, $\vec{e}_2$ and $\vec{n} = \frac{\vec{k}}{|\vec{k}|}$ form a three-dimensional orthonormal basis.

[12] The Stokes vector components depend on the choice of the unit polarization vectors $\vec{e}_1$ and $\vec{e}_2$ and are interpreted as follows:

- ξ_1 describes linear polarization along the direction $\frac{1}{2}(\vec{e}_1 + \vec{e}_2)$ ($\xi_1 > 0$) or $\frac{1}{2}(\vec{e}_1 - \vec{e}_2)$ ($\xi_1 < 0$);
- ξ_2 describes circular polarization;
- ξ_3 describes linear polarization along the direction $\vec{e}_1$ ($\xi_3 > 0$) or $\vec{e}_2$ ($\xi_3 < 0$).

Unlike the electron case, the polarization of a photon with a given momentum $\vec{k}$ cannot be fully described by $\vec{\xi}$ alone; one must also specify a polarization axis, either $\vec{e}_1$ or $\vec{e}_2$.

5.4.1 The initial spin-resolved NIC photon emission rate and energy distribution

The total NIC photon emission probability per unit time $R^{(\zeta)}_{NIC}$ can depend on neither the inner states of the final particles, nor their momenta, as at the stage where this quantity is used, no process has yet taken place. $R^{(\zeta)}_{NIC}$ is obtained by first summing the FNIC differential functions (5.39)-(5.43) over the final polarization ξ and spin ζ' configurations, then integrating over all the possible photon energies ω and all the possible angles of emission[13] Ω

$$\begin{aligned} R^{(\zeta)}_{NIC} &= \int_0^{\varepsilon} d\omega \int_\Omega d\Omega \sum_{\zeta',\xi} \frac{dW^{(\zeta\zeta'\xi)}_{NIC}}{d\omega d\Omega} = \\ &= \frac{\alpha m}{\sqrt{3}\pi\gamma}\Big(\frac{c^2}{\hbar}\Big)\int_0^{\infty}\Big[K_{\frac{2}{3}}(z_q)\frac{2+2u+u^2}{(1+u)^3} - \frac{1}{(1+u)^2}\int_{z_q}^{\infty} dx K_{\frac{1}{3}}(x) + \\ &\qquad - K_{\frac{1}{3}}(z_q)\frac{u}{(1+u)^3}(\vec{\zeta}\cdot\vec{b})\Big]du = \\ &= R_{NIC} + g(\vec{\zeta}\cdot\vec{b}), \end{aligned} \tag{5.71}$$

with $z_q = \frac{2u}{3\chi_e}$ and $u = \frac{\omega}{\varepsilon-\omega}$; the vector $\vec{b} = \hat{v}\wedge\vec{s}$ is computed using the direction of the emitting electron ($\hat{v}$) and its transverse acceleration ($\vec{s}$) at the instant of emission. In (5.71) we isolated the usual spin-unresolved LCFA photon emission probability R_{NIC} (see below)

$$R_{NIC} = \frac{\alpha m}{\sqrt{3}\pi\gamma}\Big(\frac{c^2}{\hbar}\Big)\int_0^{\infty}\Big[K_{\frac{2}{3}}(z_q)\frac{2+2u+u^2}{(1+u)^3} - \frac{1}{(1+u)^2}\int_{z_q}^{\infty} dx K_{\frac{1}{3}}(x)\Big]du \tag{5.72}$$

from the spin dependent term $g(\vec{\zeta}\cdot\vec{b})$, where

$$g = -\frac{\alpha m}{\sqrt{3}\pi\gamma}\Big(\frac{c^2}{\hbar}\Big)\int_0^{\infty} K_{\frac{1}{3}}(z_q)\frac{u}{(1+u)^3}du. \tag{5.73}$$

We equipped `SFQEDtoolkit`'s advanced module with a routine, `function_phtn_emission_rate_initial_spin`, capable of returning the Chebyshev approxima-

[13] The integration of Eqs. (5.39)-(5.43) over the whole solid angle can be performed through the integral identities

$$\int d\Omega\lambda^{\frac{1}{2}}K_{\frac{1}{3}}(\xi_e) = \frac{\pi}{\sqrt{2}}\frac{\varepsilon'\chi_e}{\omega\gamma^3}\int_{z_q}^{\infty} dx K_{\frac{1}{3}}(x); \tag{5.68}$$

$$\int d\Omega\lambda K_{\frac{2}{3}}(\xi_e) = \frac{\pi}{2}\frac{\varepsilon'\chi_e}{\omega\gamma^4}K_{\frac{1}{3}}(z_q); \tag{5.69}$$

$$\int d\Omega\lambda^{\frac{3}{2}}K_{\frac{1}{3}}(\xi_e) = \frac{\pi}{2\sqrt{2}}\frac{\varepsilon'\chi_e}{\omega\gamma^5}K_{\frac{2}{3}}(z_q) \tag{5.70}$$

valid for the modified Bessel functions of the second kind. These relations will come in handy in section 5.6.1.

tion of the function[14]

$$W_{NIC}(\gamma_e,\chi_e,\vec{\zeta},\vec{b}) = \frac{R^{(\zeta)}_{NIC}}{\omega_r} = \frac{\alpha}{\sqrt{3}\pi}\frac{\lambda_r}{\lambda_C}\frac{\chi_e}{\gamma_e}\tilde{W}_{TOT}(\chi_e,\vec{\zeta},\vec{b})$$
$$= \frac{\alpha}{\sqrt{3}\pi}\frac{\lambda_r}{\lambda_C}\frac{\chi_e}{\gamma_e}(\tilde{W}_{LCFA}(\chi_e)+\tilde{g}(\chi_e,\vec{\zeta},\vec{b})), \tag{5.74}$$

where

$$\tilde{W}_{LCFA}(\chi_e) = \frac{1}{\chi_e}\int_0^\infty \Big[K_{\frac{2}{3}}(z_q)\frac{2+2u+u^2}{(1+u)^3} - \frac{1}{(1+u)^2}\int_{z_q}^\infty dx K_{\frac{1}{3}}(x)\Big]du =$$
$$= \int_0^\infty \frac{45(v\chi)^2+42v\chi+20}{(2+3v\chi)^3}K_{\frac{2}{3}}(v)dv \tag{5.75}$$

corresponds to the usual LCFA differential probability already disclosed in eq. (3.26), while

$$\tilde{g}(\chi_e,\vec{\zeta},\vec{b}) = -\frac{(\vec{\zeta}\cdot\vec{b})}{\chi_e}\int_0^\infty K_{\frac{1}{3}}(z_q)\frac{u}{(1+u)^3}du = -\frac{27}{4}\chi_e(\vec{\zeta}\cdot\vec{b})\int_0^\infty \frac{w^5}{\left(1+\frac{3}{2}\chi_e w^3\right)^3}K_{\frac{1}{3}}(w^3)dw \tag{5.76}$$

represents the rearranged spin dependent term (5.73). The variable changes $u = \frac{3}{2}\chi_e v$ and $u = \frac{3}{2}\chi_e w^3$ were applied within the integrals in Eqs. (5.75) and (5.76) to smooth the function being approximated and simplify the Chebyshev polynomials required for its representation. Figure 5.3 illustrates the relative error between the numerical evaluation of Eq. (5.74) and its corresponding Chebyshev approximation as implemented in `SFQEDtoolkit`.

Once the occurrence of the emission has been established according to the methods of chapter 3, the photon's energy can be finally determined. We incorporated in `SFQEDtoolkit` the numerical roiutine `function_phtn_emission_nrg_initial_spin` which returns the energy ω of a photon emitted through NIC. Defining the spin-resolved cumulative distribution as

$$\tilde{I}_{NIC}(\bar{w},\chi_e,\vec{\zeta},\vec{b}) = \int_0^{\bar{w}}\frac{9dw}{2(1+\frac{3\chi_e w^3}{2})^3}\Bigg[\Bigg[1+\left(1+\frac{3\chi_e w^3}{2}\right)^2\Bigg]w^2K_{\frac{2}{3}}(w^3)+$$
$$- w^2\left(1+\frac{3\chi_e w^3}{2}\right)\int_{w^3}^\infty K_{\frac{1}{3}}(y)dy\Bigg]+$$
$$- \frac{27}{4}\chi_e(\vec{\zeta}\cdot\vec{b})\int_0^{\bar{w}}\frac{w^5}{\left(1+\frac{3}{2}\chi_e w^3\right)^3}K_{\frac{1}{3}}(w^3)dw, \tag{5.77}$$

[14] In writing Eq. (5.74), we utilized the concepts of the reference wavelength λ_r and frequency ω_r, which were introduced in Chapter 3. These quantities are entirely arbitrary, subject only to the constraint $\lambda_r\omega_r = c$, and in computational physics they define the scale of a given simulation.

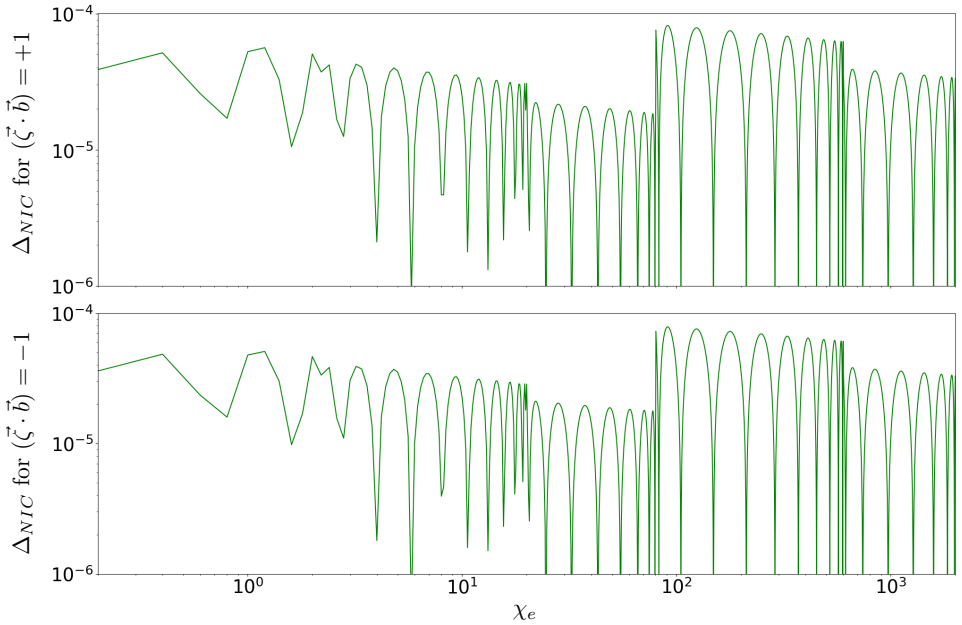

Figure 5.3: Relative error between the analytical and numerical `SFQEDtoolkit` implementation of the spin-dependent photon emission rate in Eq. (5.74), for two different initial spin orientations: fully aligned (up) or anti-aligned (down) with respect to $\vec{b}$. Not only is the difference between the two cases negligible, but they are also indistinguishable from Fig. 3.2. The error function has been computed at 10^4 evenly spaced points over the range $0 \leq \chi_e \leq 2000$.

`function_phtn_emission_nrg_initial_spin` proceeds as in section 3.3.3 by solving the integral equation

$$\begin{aligned}\tilde{I}_{NIC}(\bar{w},\chi_e,\vec{\zeta},\vec{b}) &= r\tilde{I}_{NIC}(\infty,\chi_e,\vec{\zeta},\vec{b}) \\ &= r(\tilde{W}_{LCFA}(\chi_e)+\tilde{g}(\chi_e,\vec{\zeta},\vec{b})) \\ &= r\tilde{W}_{TOT}(\chi_e,\vec{\zeta},\vec{b}) \end{aligned} \tag{5.78}$$

for $\bar{w}$, where r is a random number uniformly distributed between $0 < r < 1$. Depending on the value of r, the above routine will behave differently:

- for $r < r_{low}$, eq. (5.78) can be simplified using the corresponding asymptotic expansions and, at lowest order in w, is analitically inverted to give

$$\bar{w} = r\tilde{W}_{TOT}(\chi_e,\vec{\zeta},\vec{b})\left[\frac{9}{2^{1/3}}\Gamma\left(\frac{2}{3}\right)\right]^{-1}; \tag{5.79}$$

- for $r_{low} \leq r \leq r_{high}$ `SFQEDtoolkit` actually solves (5.78) numerically by applying the Van Wijngaarden Dekker-Brent method [50];

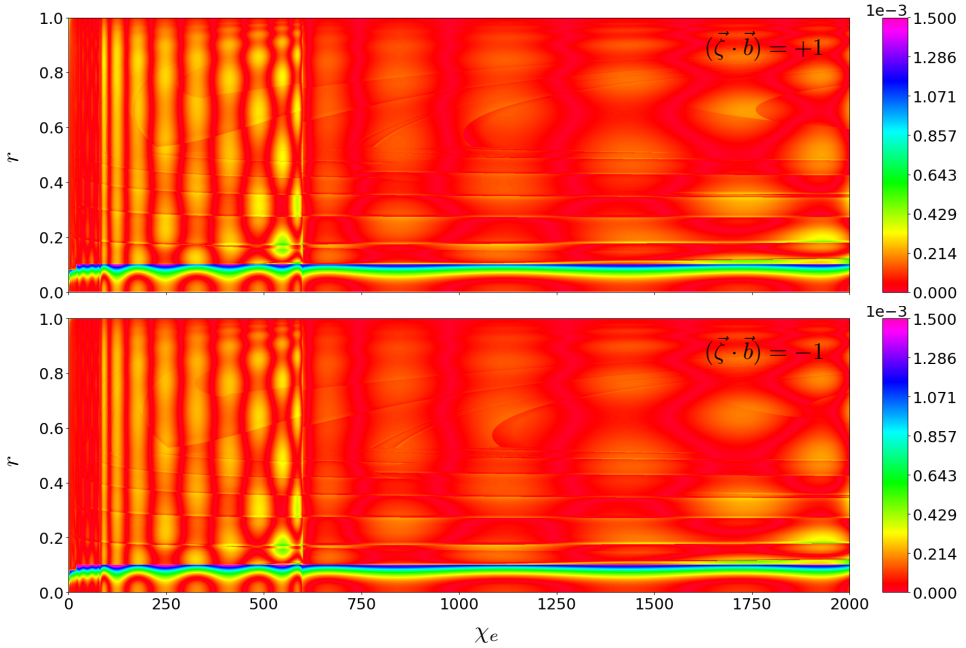

Figure 5.4: Analogous to Fig. 3.4, this plot shows the relative difference between the exact and `SFQEDtoolkit`-computed spin-dependent photon emission energies. The contour plot was generated by evaluating the error function at 10^4 points in χ_e and 10^3 points in r over the domain $0 \leq \chi_e \leq 2000$ and $0 \leq r \leq 1$. Similarly to Fig. 5.3, two initial spin orientations relative to $\vec{b}$ were considered: fully aligned (up) and anti-aligned (down).

- for $r > r_{high}$, in a way completely analogous to eq. (3.40), the exponential tail

$$\tilde{I}_{NIC}(\bar{w},\chi_e,\vec{\zeta},\vec{b}) \approx \tilde{W}_{TOT}(\chi_e,\vec{\zeta},\vec{b})(1-e^{-(\bar{w}^3-w_0^3)}) + \tilde{I}_{NIC}(w_0,\chi_e,\vec{\zeta},\vec{b})e^{-(\bar{w}^3-w_0^3)} \tag{5.80}$$

  is employed to represent (5.77) in the highest portion of the spectrum. Replacing (5.80) into (5.78) gives

$$\bar{w} = \sqrt[3]{w_0^3 - \log\left[\frac{\tilde{W}_{TOT}(\chi_e,\vec{\zeta},\vec{b})(1-r)}{\tilde{W}_{TOT}(\chi_e,\vec{\zeta},\vec{b}) - \tilde{I}_{NIC}(w_0,\chi_e,\vec{\zeta},\vec{b})}\right]}. \tag{5.81}$$

Now, the variables r_{low}, r_{high} and w_0 are χ_e-dependent quantities whose values were decided ad hoc and summarized in table 5.1. Whichever the r-interval, or the method followed to achieve $\bar{w}$, `function_phtn_emission_nrg_initial_spin` replaces any function appearing in (5.77)-(5.81) with the corresponding Chebyshev approximations. Once $\bar{w}^3$ is known, the emitted photon's energy $\omega = \frac{3\chi_e\bar{w}^3}{2+3\chi_e\bar{w}^3}\varepsilon$ is returned. The colormap in fig. 5.4 shows how the accuracy of this method is well below the predefined 0.1% accuracy threshold.

χ_e	r_{low}	r_{high}	w_0
$0 \leq \chi_e < 2$	0.1	0.999993	1.45
$2 \leq \chi_e < 20$	0.1	0.999986	1.55
$20 \leq \chi_e < 80$	0.1	0.999986	1.6
$80 \leq \chi_e < 600$	0.08	0.999994	1.9
$600 \leq \chi_e \leq 2000$	0.05	0.999992	2.1

Table 5.1: The numerical values of r_{low}, r_{high} and w_0 for each of the five intervals of χ_e.

No emission spin flip

The introduction of new spin coupling terms, such as that shown in (5.73), within the emission probability of eq. (5.71) establishes a genuine selection rule which may flip the electron's spin even in the absence of photon emission. As pointed out in [103], these terms might also be seen to emerge from the interference of the one loop self-energy diagram with the forward scattered one. In any case, the process is governed by the probability

$$P_{NIC}^{(\zeta),NE} = 1 - R_{NIC}^{(\zeta)} dt = 1 - R_{NIC} dt - g(\vec{\zeta} \cdot \vec{b}) dt \tag{5.82}$$

that an electron with a certain spin ζ does not emit a photon, i.e., the complementary probability of Eq. (5.71). Here, dt represents a generic time interval[15], ensuring that $R_{NIC}^{(\zeta)}$ has the correct dimensionality for a probability. As shown in the literature [103], we could now introduce the average nonradiating electron spin vector $\vec{\zeta}^{NE}$ and recast eq. (5.82) as[16]

$$P_{NIC}^{(\zeta\zeta^{NE}),NE} = \frac{1}{2}\Big[P_{NIC}^{(\zeta),NE} + (\vec{\zeta}^{NE} \cdot \vec{S}^{NE})\Big], \tag{5.83}$$

where

$$\vec{S}^{NE} = \vec{\zeta}(1 - R_{NIC} dt) - g\vec{b} dt. \tag{5.84}$$

Before proceeding any further, a few remarks are in order. To begin with, $\vec{\zeta}^{NE}$ represents the spin of the electron as it gets selected by a generic detector after no photon emission occurs. Moreover, the probability in eq. (5.83) is a relativistically invariant quantity that must take the same form in any reference frame, particularly in the rest frame of the electron. Hence, we introduce two density matrices:

$$\rho' = \frac{1}{2}(1 + \vec{\sigma} \cdot \vec{\zeta}^{NE}) \tag{5.85}$$

[15] In PIC codes $\omega_r dt = \Delta t$ will represent the time step of the simulations.

[16] We stress out that by summing (5.83) over all the possible spin configurations

$$P_{NIC}^{(\zeta\zeta^{NE}),NE}|_{\vec{\zeta}^{NE}=\uparrow} + P_{NIC}^{(\zeta\zeta^{NE}),NE}|_{\vec{\zeta}^{NE}=\downarrow} = P_{NIC}^{(\zeta),NE}$$

one can successfully retrieve eq. (5.82) ($\uparrow$ and $\downarrow$ denote the orientation of $\vec{\zeta}^{NE}$ with respect to some spin quantization axis).

$$\rho^{(r)} = \frac{1}{2}(1 + \vec{\sigma} \cdot \vec{\zeta}^{(r)}) \tag{5.86}$$

describing the spin states of both the detector and the electron in the rest frame of the latter. In this frame, Eq. (5.83) takes the form

$$P_{NIC}^{(\zeta\zeta^{NE}),NE} \equiv P \sim tr(\rho' \rho^{(r)}) \sim 1 + \vec{\zeta}^{NE} \cdot \vec{\zeta}^{(r)}. \tag{5.87}$$

Comparing (5.83) with (5.87), it is clear that the proper final electron spin state, as we mean it in its rest frame, is given by [57]

$$\vec{\zeta}^{(r)} = \frac{\vec{S}^{NE}}{P_{NIC}^{(\zeta),NE}}, \tag{5.88}$$

which we will refer to as the spin quantization axis (SQA). Due to the arbitrariness of the detector, we will choose its orientation to coincide with that of the SQA (5.227), and thus

$$\vec{\zeta}^{NE} = \vec{\zeta}^{(r)}; \tag{5.89}$$

when referring to the final electron's spin we will use $\vec{\zeta}^{NE}$ and $\vec{\zeta}^{(r)}$ interchangeably. Equivalently, one could notice that the combination (see [106])

$$\frac{P_{NIC}^{(\zeta\zeta^{NE}),NE}|_{\vec{\zeta}^{NE}=\uparrow} - P_{NIC}^{(\zeta\zeta^{NE}),NE}|_{\vec{\zeta}^{NE}=\downarrow}}{P_{NIC}^{(\zeta\zeta^{NE}),NE}|_{\vec{\zeta}^{NE}=\uparrow} + P_{NIC}^{(\zeta\zeta^{NE}),NE}|_{\vec{\zeta}^{NE}=\downarrow}} = \vec{\zeta}^{NE} \cdot \frac{\vec{S}^{NE}}{P_{NIC}^{(\zeta),NE}} \tag{5.90}$$

gives precisely the projection of the SQA onto the detector's spin state $\vec{\zeta}^{NE}$, and can thus be used to infer $\vec{\zeta}^{(r)}$. Eq. (5.89) is a perfectly valid *mixed* spin state, with $|\vec{\zeta}^{NE}| \leq 1$.

If one were interested in *pure* states only ($|\vec{\zeta}^{NE}| = 1$), the following condition is used to assess the system

$$\frac{P_{NIC}^{(\zeta\zeta^{NE}),NE}|_{\vec{\zeta}^{NE}=\uparrow}}{P_{NIC}^{(\zeta\zeta^{NE}),NE}|_{\vec{\zeta}^{NE}=\uparrow} + P_{NIC}^{(\zeta\zeta^{NE}),NE}|_{\vec{\zeta}^{NE}=\downarrow}} = \frac{P_{NIC}^{(\zeta),NE} + |\vec{S}^{NE}|}{2P_{NIC}^{(\zeta),NE}} > r_{NE}, \tag{5.91}$$

where r_{NE} a random number such that $0 \leq r_{NE} \leq 1$; if the inequality (5.91) holds than $\vec{\zeta}^{NE} = \frac{\vec{S}^{NE}}{|\vec{S}^{NE}|}$, otherwise $\vec{\zeta}^{NE} = -\frac{\vec{S}^{NE}}{|\vec{S}^{NE}|}$. The functions `function_no_emission_spin_flip_mix` and `function_no_emission_spin_flip_pure` implemented in `SFQEDtoolkit` reenact the mechanisms we just described.

In the next section we tackle these same arguments but from the perspective of the NBW process, while the electron spin-flip after the photon emission is delayed until section 5.6.

5.4.2 The polarization-resolved NBW pair production rate and energy distribution

The NBW probability per unit time $R^{(\xi)}_{NBW}$ regulates the occurrence of pair production within strong electromagnetic fields. Likewise to the NIC case described in 5.4.1, $R^{(\xi)}_{NBW}$ can depend only on the photon's polarization ξ at the moment of decay, besides its quantum parameter χ_γ and energy ω of course: all the other variables appearing in Eqs. (5.57)-(5.61) are unnecessary. Retracing the steps of sec. 5.4.1, we thus derive an expression for $R^{(\xi)}_{NBW}$ by summing the FNBW distributions over the electron and poitron spin states ($\zeta_\pm$) and integrating over the final electron's (ε_-) or poistron's ($\varepsilon_+ = \omega - \varepsilon_-$) energy and angles of emission[17] (θ and φ). This procedure extinguishes the superfluous degrees of freedom and the polarization-resolved probability per unit time emerges as

$$R^{(\xi)}_{NBW} = \frac{\alpha m^2}{\sqrt{3}\pi\omega^2}\left(\frac{c^4}{\hbar}\right)\int_0^\omega d\varepsilon_-\Big[K_{\frac{2}{3}}(z_p)\frac{\varepsilon_+^2+\varepsilon_-^2}{\varepsilon_+\varepsilon_-} + \int_{z_p}^\infty dx K_{\frac{1}{3}}(x) - \xi_3 K_{\frac{2}{3}}(z_p)\Big], \tag{5.95}$$

with $z_p = \frac{2}{3\chi_\gamma}\frac{\omega^2}{\varepsilon_-\varepsilon_+}$. Through algebraic manipulations we can rewrite eq. (5.95) into the more convenient

$$W_{NBW}(\omega,\chi_\gamma,\vec{\xi}) = \frac{R^{(\xi)}_{NBW}}{\omega_r} = W^{LCFA}_{NBW}(\omega,\chi_\gamma) + \xi_3 W^{\xi}_{NBW}(\omega,\chi_\gamma) \tag{5.96}$$

in which we isolated the usual NBW probability rate in eq. (3.28)

$$\begin{aligned} W^{LCFA}_{NBW}(\omega,\chi_\gamma) &= \frac{1}{\omega_r}\frac{\alpha m^2}{\sqrt{3}\pi\omega^2}\left(\frac{c^4}{\hbar}\right)\int_0^\omega d\varepsilon_-\Big[K_{\frac{2}{3}}(z_p)\frac{\varepsilon_+^2+\varepsilon_-^2}{\varepsilon_+\varepsilon_-} + \int_{z_p}^\infty dx K_{\frac{1}{3}}(x)\Big] = \\ &= \frac{\alpha}{\sqrt{3}\pi}\frac{\lambda_r}{\lambda_C}\frac{1}{\gamma_\gamma}\int_0^1 dv \frac{9-v^2}{3(1-v^2)}K_{\frac{2}{3}}\left(\frac{8}{3\chi_\gamma(1-v^2)}\right) \end{aligned} \tag{5.97}$$

from the polarization dependent term

$$W^{\xi}_{NBW}(\omega,\chi_\gamma) = -\frac{\alpha m^2}{\sqrt{3}\pi\omega^2}\left(\frac{c^4}{\hbar}\right)\int_0^\omega d\varepsilon_- K_{\frac{2}{3}}(z_p) =$$

[17] Similarly to the set of Eqs. (5.68)-(5.70), the integral identities

$$\int d\Omega\lambda^{\frac{1}{2}}K_{\frac{1}{3}}(\xi_\gamma) = \frac{\pi}{\sqrt{2}}\frac{\varepsilon_-\varepsilon_+\chi_\gamma}{\omega^2\gamma^3}\int_{z_p}^\infty dx K_{\frac{1}{3}}(x) \tag{5.92}$$

$$\int d\Omega\lambda K_{\frac{2}{3}}(\xi_\gamma) = \frac{\pi}{2}\frac{\varepsilon_-\varepsilon_+\chi_\gamma}{\omega^2\gamma^4}K_{\frac{1}{3}}(z_p) \tag{5.93}$$

$$\int d\Omega\lambda^{\frac{3}{2}}K_{\frac{1}{3}}(\xi_\gamma) = \frac{\pi}{2\sqrt{2}}\frac{\varepsilon_-\varepsilon_+\chi_\gamma}{\omega^2\gamma^5}K_{\frac{2}{3}}(z_p) \tag{5.94}$$

are fundamental for the integration of (5.57)-(5.61) over the solid angle. Eqs. (5.92)-(5.94) will be useful in section 5.6.1.

$$= -\frac{1}{\omega_r}\frac{\alpha}{\sqrt{3}\pi}\frac{\lambda_r}{\lambda_C}\frac{1}{\gamma_\gamma}\int_0^1 dv K_{\frac{2}{3}}\Big(\frac{8}{3\chi_\gamma(1-v^2)}\Big). \tag{5.98}$$

Here, in addition to the standard relations involving modified Bessel functions of the second kind, we applied the change of variable $\varepsilon_- = \frac{\omega}{2}(1+v)$ to regularize the integrals. As in the previous section, we equipped our new component of `SFQEDtoolkit` with the routine `function_rate_spin_bw`, which returns the Chebyshev approximation of the polarization-resolved probability defined in Eq. (5.96). Following the methods outlined in Section 3.3.2, `function_rate_spin_bw` is then used to infer the occurrence of NBW events in PIC and MC codes. Its accuracy as a function of χ_γ matches that shown in Fig. 3.3, indicating that the approximation for the new polarization-dependent term is more accurate than the approximation of the original term in Eq. (5.97).

Once the photon decays via the NBW channel, the final energies of the resulting electron and positron must be sampled from the appropriate distribution. To achieve this, we equipped `SFQEDtoolkit` with a function `function_nrg_spin_bw`, which applies the inverse transform sampling algorithm (ITS) to the cumulative distribution derived from eq. (5.95)

$$\tilde{I}_{NBW}(\bar{\varepsilon}_-,\chi_e,\vec{\xi}) = \frac{1}{\omega}\int_0^{\bar{\varepsilon}_-} d\varepsilon_-\Big[K_{\frac{2}{3}}(z_p)\frac{\varepsilon_+^2+\varepsilon_-^2}{\varepsilon_+\varepsilon_-} + \int_{z_p}^{\infty} dx K_{\frac{1}{3}}(x) - \xi_3 K_{\frac{2}{3}}(z_p)\Big]. \tag{5.99}$$

By redefining (5.99) using the energy relation $\bar{\varepsilon}_- = \frac{\omega}{2}(1+\bar{v})$ we obtain

$$\tilde{I}_{NBW}(\bar{v},\chi_e,\vec{\xi}) = \int_0^{\bar{v}} dv\Big[\Big(\frac{2(1+v^2)}{1-v^2} - \xi_3\Big)K_{\frac{2}{3}}\Big(\frac{8}{3\chi_\gamma(1-v^2)}\Big) + \int_{\frac{8}{3\chi_\gamma(1-v^2)}}^{\infty} dx K_{\frac{1}{3}}(x)\Big]. \tag{5.100}$$

The function `function_nrg_spin_bw` solves the integral equation

$$\begin{aligned}\tilde{I}_{NBW}(\bar{v},\chi_e,\vec{\xi}) &= r\tilde{I}_{NBW}(1,\chi_e,\vec{\xi}) \\ &= r\tilde{W}^{TOT}_{NBW}(\chi_\gamma,\vec{\xi})\end{aligned} \tag{5.101}$$

$$\tilde{W}^{TOT}_{NBW}(\chi_\gamma,\vec{\xi}) = \int_0^1 dv \frac{9-v^2}{3(1-v^2)}K_{\frac{2}{3}}\Big(\frac{8}{3\chi_\gamma(1-v^2)}\Big) - \int_0^1 dv K_{\frac{2}{3}}\Big(\frac{8}{3\chi_\gamma(1-v^2)}\Big), \tag{5.102}$$

r being the usual random number uniformly distributed between $0 < r < 1$. As in sec. (5.4.1), `SFQEDtoolkit` adapts its approach based on the value of r:

- for $r < r^{BW}_{low}$ (i.e., at low energies $v \to 0$), the integrand of eq. (5.100) is replaced by its asymptotic expansion, and eq. (5.101) is inverted analytically, yielding

$$\bar{v} = \frac{r\tilde{W}^{TOT}_{NBW}(\chi_\gamma,\vec{\xi})}{(2-\xi_3)K_{\frac{2}{3}}(\frac{8}{3\chi_\gamma}) + \int_{\frac{8}{3\chi_\gamma}}^{\infty} dx K_{\frac{1}{3}}(x)}; \tag{5.103}$$

χ_γ	r_{low}^{BW}	v_0
$0.24 \leq \chi_\gamma < 0.4$	0.0105	0.9996
$0.4 \leq \chi_\gamma < 2$	0.0109	0.9993
$2 \leq \chi_\gamma < 20$	0.013	0.996
$20 \leq \chi_\gamma < 80$	0.023	0.987
$80 \leq \chi_\gamma < 600$	0.0295	0.908
$600 \leq \chi_\gamma \leq 2000$	0.029	0.908

Table 5.2: The numerical values of r_{low}^{BW} and v_0 for each of the five intervals of χ_γ.

- for $r_{low}^{BW} \leq r \leq r_{high}^{BW}$ eq. (5.101) is solved numerically using the standard Wijngaarden Dekker-Brent algorithm [50];
- for $r > r_{high}^{BW}$ (i.e., at the highmost energy values $v \to 1$), the integrand in Eq. (5.100) is assumed to follow an exponential tail:

$$\tilde{I}_{NBW}(v,\chi_e,\vec{\xi}) \approx \tilde{W}_{NBW}^{TOT}(\chi_\gamma,\vec{\xi})\Big[1 - e^{-\left(\frac{8}{3\chi_\gamma(1-v^2)} - \frac{8}{3\chi_\gamma(1-v_0^2)}\right)}\Big] + \\ + \tilde{I}_{NBW}(v_0,\chi_e,\vec{\xi})e^{-\left(\frac{8}{3\chi_\gamma(1-v^2)} - \frac{8}{3\chi_\gamma(1-v_0^2)}\right)}. \tag{5.104}$$

By substituting Eq. (5.104) into Eq. (5.101), we can solve analytically for $\bar{v}$:

$$\bar{v} = \sqrt{1 - \left(\frac{1}{1-v_0^2} - \frac{3\chi_\gamma}{8}\log\left[\frac{\tilde{W}_{BW}^{TOT}(\chi_\gamma,\vec{\xi})(1-r)}{\tilde{W}_{BW}^{TOT}(\chi_\gamma,\vec{\xi}) - \tilde{I}_{BW}(v_0,\chi_e,\vec{\xi})}\right]\right)^{-1}}. \tag{5.105}$$

Once $\bar{v}$ is determined, the corresponding energies are obtained via $\bar{\varepsilon}_- = \frac{\omega}{2}(1+\bar{v})$.

The values for r_{low}^{BW} and v_0 were identified by comparing the relative error between the proposed solutions (Eqs. (5.103) and (5.104)) and the numerical solution. These values strongly depend on the quantum parameter χ_γ and are summarized in Table 5.2. Conversely, r_{high}^{BW} is recopmuted at each iteration

$$r_{high}^{BW} = \frac{\tilde{I}_{NBW}(v_0,\chi_e,\vec{\xi})}{\tilde{W}_{NBW}^{TOT}(\chi_\gamma,\vec{\xi})}. \tag{5.106}$$

Regardless of which of the three methods `SFQEDtoolkit` employs, all the distributions in the formulas from Eqs. (5.99) to (5.106) are evaluated using their Chebyshev approximations. Fig. 5.5 summarizes the accuracy of `function_nrg_spin_bw` all over its domain of validity.

No decay polarization flip

Repeating the same reasoning as in sec. 5.4.1, the dependence of (5.95) on the photon polarization $\vec{\xi}$ serves as a selection rule that may flip the photon polarization

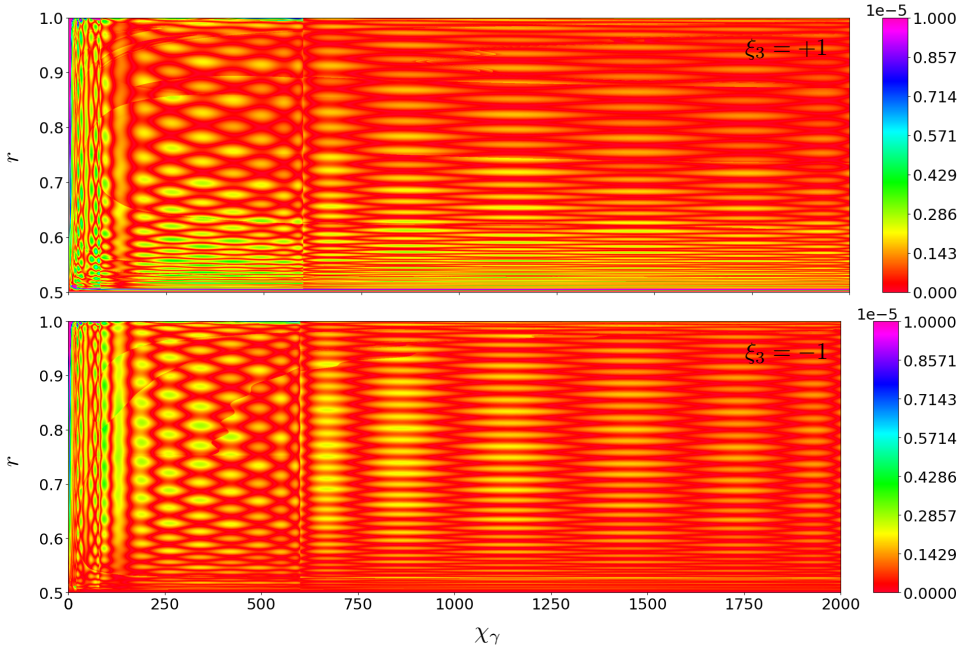

Figure 5.5: Analogous to Fig. 3.6, this figure displays the relative difference between the exact polarization-dependent energy of one of the leptons produced during the NBW process and the energy computed with `SFQEDtoolkit`. The contour plot was generated by evaluating the error function at 10^4 points in χ_γ and 10^3 points in r over the domain $0.3 \leq \chi_\gamma \leq 2000$ and $0.5 \leq r \leq 1$ (by symmetry, the range $0 \leq r < 0.5$ corresponds to the antilepton's energy). Two limiting cases for the Stokes parameter ξ_3 are considered: $\xi_3 = +1$ (up) and $\xi_3 = -1$ (down).

vector if the NBW process does not occur. This kind of scheme is ruled by the probability $P_{NBW}^{(\xi),ND}$ that a photon with a certain polarization ξ does not decay

$$P_{NBW}^{(\xi),ND} = 1 - R_{NBW}^{(\xi)} dt, \tag{5.107}$$

where the time interval dt is required to render Eq. (5.95) a proper probability. Following arguments analogous to those already used in section 5.4.1, equation (5.107) is reworked into

$$P_{NBW}^{(\xi\xi^{ND}),ND} = \frac{1}{2}\Big[P_{NBW}^{(\xi),ND} + (\vec{\xi}^{ND} \cdot \vec{S}^{ND})\Big], \tag{5.108}$$

in which the detector polarization vector $\vec{\xi}^{ND}$ after the rejected NBW decay is introduced, and its coupling to the polarization quantization axis (PQA) $\vec{S}^{ND}$

$$\vec{S}^{ND} = \vec{\xi}(1 - R_{BW}^{LCFA} dt) - R_{BW}^{\xi} dt(0, 0, 1) \tag{5.109}$$

is made explicit. In eq. (5.109) the terms

$$R_{BW}^{LCFA} = \frac{\alpha}{\sqrt{3}\pi} \frac{\lambda_r}{\lambda_C} \frac{\omega_r}{\gamma_\gamma} \int_0^1 dv \frac{9 - v^2}{3(1 - v^2)} K_{\frac{2}{3}}\left(\frac{8}{3\chi_\gamma(1 - v^2)}\right) \tag{5.110}$$

and

$$R^{\xi}_{BW} = -\frac{\alpha}{\sqrt{3}\pi}\frac{\lambda_r}{\lambda_C}\frac{\omega_r}{\gamma_\gamma}\int_0^1 dv K_{\frac{2}{3}}\Big(\frac{8}{3\chi_\gamma(1-v^2)}\Big) \tag{5.111}$$

are such that $R^{(\xi)}_{NBW} = R^{LCFA}_{NBW} + \xi_3 R^{\xi}_{NBW}$. To emphasize the consistency of (5.108) with (5.107), we point out that

$$P^{(\xi\vec{\xi}^{ND}),ND}_{NBW}|_{\vec{\xi}^{ND}=\uparrow} + P^{(\xi\vec{\xi}^{ND}),ND}_{NBW}|_{\vec{\xi}^{ND}=\downarrow} = P^{(\xi),ND}_{NBW}\,.$$

Similarly to the procedure outlined in sec. 5.4.1[18], the ratio

$$\frac{P^{(\xi\vec{\xi}^{ND}),ND}_{NBW}|_{\vec{\xi}^{ND}=\uparrow} - P^{(\xi\vec{\xi}^{ND}),ND}_{NBW}|_{\vec{\xi}^{ND}=\downarrow}}{P^{(\xi\vec{\xi}^{ND}),ND}_{NBW}|_{\vec{\xi}^{ND}=\uparrow} + P^{(\xi\vec{\xi}^{ND}),ND}_{NBW}|_{\vec{\xi}^{ND}=\downarrow}} = \vec{\xi}^{ND}\cdot\frac{\vec{S}^{ND}}{P^{(\xi),ND}_{NBW}} \tag{5.112}$$

suggests to align the detector polarization vector $\vec{\xi}^{ND}$ along the PQA $= \frac{\vec{S}^{ND}}{P^{(\xi),ND}_{NBW}}$, thus identifying the photon polarization mixed state as

$$\vec{\xi}^{ND} = \frac{\vec{S}^{ND}}{P^{(\xi),ND}_{NBW}}. \tag{5.113}$$

For pure states, a random number r is drawn from the interval $0 \le r \le 1$ and the following condition is evaluated:

$$\frac{P^{(\xi\vec{\xi}^{ND}),ND}_{NBW}|_{\vec{\xi}^{ND}=\uparrow}}{P^{(\xi\vec{\xi}^{ND}),ND}_{NBW}|_{\vec{\xi}^{ND}=\uparrow} + P^{(\xi\vec{\xi}^{ND}),ND}_{NBW}|_{\vec{\xi}^{ND}=\downarrow}} = \frac{P^{(\xi),ND}_{NBW} + |\vec{S}^{ND}|}{2P^{(\xi),ND}_{NBW}} > r. \tag{5.114}$$

If (5.114) holds true than $\vec{\xi}^{ND} = \frac{\vec{S}^{ND}}{|\vec{S}^{ND}|}$, otherwise $\vec{\xi}^{ND} = -\frac{\vec{S}^{ND}}{|\vec{S}^{ND}|}$. `SFQEDtoolkit` can carry out either algorithm via the routine `function_no_decay_pola_flip_mix` or `function_no_decay_pola_flip_pure`.

5.5 Angular distribution algorithms

The mechanisms developed thus far for the NIC and NBW processes allow us to determine whether a photon emission or pair creation event occurs, along with

[18] We can use the same strategy as described in Sec. 5.4.1 to detect any potential polarization flip in the absence of NBW decay. This is because, even for photons, the transition probability between different polarization states can be expressed as

$$|\mathcal{M}_{fi}|^2 \sim a + \vec{b}\cdot\vec{\xi}^{ND}.$$

the energies of the resulting particles. However, we still lack a method for sampling the momenta of the newly created particles in a way that ensures they follow the correct angular distribution. This section is dedicated to the theoretical and numerical description of the unreleased `SFQEDtoolkit` functions that, by addressing this challenge, significantly enhance the trajectory characterization of particles involved in SFQED processes. Having Monte Carlo and PIC codes capable of producing spin- or polarization-resolved particles within the theoretical $\frac{1}{\gamma}$-cone (and thus no longer relying on the collinear approximation) provides a significant advantage. This capability facilitates precision studies in SFQED and may deepen our understanding of already known phenomena.

5.5.1 NIC: Photons' angular distribution from spin resolved electrons

After a NIC event is deemed to occur and the energies of the outgoing particles are determined, the available information can be further enriched by computing the photon emission angles, which also influence the recoil of the emitting particle. This requires deriving a differential probability with an angular dependence that can be implemented in numerical computations. However, as we will see in Sec. 5.7.1, the FNIC ensemble described by Eqs. (5.39)-(5.43) is not a viable candidate, as it leads to an ill-defined and potentially negative distribution. To reformulate Eqs. (5.39)-(5.43) into a form suitable for practical calculations, we assert the following:

- Resolving the final spin and polarization states is unnecessary for determining the particles' momenta after a NIC or NBW event.
- Conversely, resolving the final momenta is crucial for determining the orientation of their corresponding spin and polarization states.

In other words, the spin and polarization of outgoing particles cannot influence the direction of their momenta, whereas the latter can certainly influence the former. One might argue, based on the *physical logic* underlying SFQED processes, that nature could operate in the opposite manner—meaning that while (*i*) spin and polarization quantization axes are entirely independent of the final momenta, (*ii*) the final momenta of particles could strongly depend on their internal states. We consider this notion conceptually flawed: spin inherently carries a sense of orientation that is inseparable from the direction of momentum. From this perspective, particles emitted in specific directions are more likely to have their spin or polarization aligned in particular ways.

In light of the above considerations, the differential probability we seek must be obtained by summing (5.39)-(5.43) over all final particles' internal states $\vec{\zeta}'$ and $\vec{\xi}$,

yielding

$$\frac{dW_{NIC}^{(\zeta)}}{d\omega d\varphi d\theta} \equiv \sum_{\zeta',\xi} \frac{dW_{NIC}^{(\zeta\zeta'\xi)}}{d\omega d\varphi d\theta} = \frac{\alpha\omega}{\pi^2}\sqrt{\frac{2}{3}}\lambda^{\frac{1}{2}}\sin\theta\frac{\gamma^3}{\chi_e\varepsilon'}a, \tag{5.115}$$

where

$$a = K_{\frac{1}{3}}(\xi_e)\Big[2\lambda\frac{\varepsilon^2+\varepsilon'^2}{\varepsilon\varepsilon'} - \frac{1}{\gamma^2}\Big] + K_{\frac{2}{3}}(\xi_e)\sqrt{2\lambda}\Big[\theta\sin\varphi\frac{\varepsilon^2-\varepsilon'^2}{\varepsilon\varepsilon'}\hat{v} - \frac{\omega}{\gamma\varepsilon}\vec{b}\Big]\cdot\vec{\zeta}. \tag{5.116}$$

To facilitate numerical computations, equations (5.115)-(5.116) can be reformulated as follows:

- change of variable for the polar angle θ by defining

$$z = 2\sqrt{2}\gamma^3\lambda^{\frac{3}{2}} = [2\gamma^2(1-\vec{n}\cdot\vec{v})]^{\frac{3}{2}} \tag{5.117}$$

$$dz = \frac{3}{2}z^{\frac{1}{3}}2\gamma^2\beta\sin\theta d\theta = \frac{3}{2}[2\gamma^2(1-\vec{n}\cdot\vec{v})]^{\frac{1}{2}}2\gamma^2\beta\sin\theta d\theta = 3\sqrt{2}\gamma^3\lambda^{\frac{1}{2}}\beta\sin\theta d\theta. \tag{5.118}$$

  Since[19] $\vec{n}\cdot\vec{v} = |\vec{\beta}|\cos\theta$ and

$$\vec{\beta} = \frac{\vec{v}}{c} \sim \hat{v} \tag{5.119}$$

  the variable z naturally encodes the dependence on θ, which determines the angular separation between the emitted photon and the emitting electron. Given $0 \le \theta \le \pi$, the range of z is

$$\Big(\frac{2}{1+\beta}\Big)^{\frac{3}{2}} \le z \le \Big(\frac{2}{1-\beta}\Big)^{\frac{3}{2}}. \tag{5.120}$$

  In the ultrarelativistic limit (to lowest order in $\beta = |\vec{\beta}|$), this simplifies to $1 \le z \le \infty$.

- change of variable for photon energy ω introducing

$$u = \frac{\omega}{\varepsilon-\omega} \tag{5.121}$$

  and the corresponding differential

$$d\omega = \frac{\varepsilon du}{(1+u)^2}. \tag{5.122}$$

- integration over the azimuthal angle φ

$$\int_0^{2\pi}\frac{dW_{NIC}^{(\zeta)}}{d\omega d\varphi d\theta}d\varphi \tag{5.123}$$

[19] In this and the following section, the vector $\vec{\beta}$ represents the electron's velocity $\vec{v}$ normalized by the speed of light c, rather than the angle β introduced in Sec. 5.2.1.

(all the terms depending on trigonometric functions of φ vanish upon integration). Since the photon's momentum is confined within the $\frac{1}{\gamma}$-cone around the emitting electron, it is expected to be uniformly distributed in the azimuthal angle φ. This justifies the integration.

Enforcing (5.117)-(5.123), on equation (5.115), it becomes (at the lowest order in $\beta \sim 1 - \frac{1}{2\gamma^2}$)

$$\int_0^{2\pi} \frac{dW_{NIC}^{(\zeta)}}{d\omega d\varphi d\theta} d\varphi = \frac{dW_{NIC}^{(\zeta)}}{dudz} = \frac{\alpha}{\pi} \frac{2}{3\sqrt{3}} \frac{1}{\chi_e \varepsilon'} \varepsilon^2 \frac{u}{(1+u)^2} \frac{1}{\gamma^2} a'. \tag{5.124}$$

Here $a = \frac{a'}{\gamma^2}$ and

$$a' = K_{\frac{1}{3}}(\xi_e)\Big[z^{\frac{2}{3}} \frac{2+2u+u^2}{(1+u)} - 1\Big] - K_{\frac{2}{3}}(\xi_e) z^{\frac{1}{3}} \Big[\frac{u}{(1+u)} \vec{\zeta} \cdot \vec{b}\Big], \tag{5.125}$$

where the argument of the Bessel functions is recasted as $\xi_e = \frac{4\sqrt{2}}{3} \frac{\omega \gamma^3}{\varepsilon' \chi_e} \lambda^{\frac{3}{2}} = \frac{2u}{3\chi_e} z$.

At this stage, the ITS algorithm (already used in Chap. 3) ensures that by solving the equation

$$\int_{\bar{z}}^{\infty} \frac{dW_{NIC}^{(\zeta)}}{dudz} dz - r \int_1^{\infty} \frac{dW_{NIC}^{(\zeta)}}{dudz} dz = 0 \tag{5.126}$$

for $\bar{z}$ (where r is a random number between 0 and 1), the resulting values will be distributed according to (5.124). For simplicity, we change the integration variable in eq. (5.126) from z to

$$\sigma = \frac{2u}{3\chi_e} z, \tag{5.127}$$

with the corresponding differentials related by $dz = \frac{3\chi_e}{2u} d\sigma$. This transforms (5.126) into

$$\int_{\bar{\sigma}}^{\infty} \frac{dW_{NIC}^{(\zeta)}}{dud\sigma} d\sigma - r \int_{\frac{2u}{3\chi_e}}^{\infty} \frac{dW_{NIC}^{(\zeta)}}{dud\sigma} d\sigma = 0 \tag{5.128}$$

where

$$\frac{dW_{NIC}^{(\zeta)}}{dud\sigma} = \frac{\alpha}{\pi} \frac{1}{\sqrt{3}} \frac{1}{\varepsilon'} \varepsilon^2 \frac{1}{(1+u)^2} \frac{1}{\gamma^2} a^{\sigma} \tag{5.129}$$

$$a^{\sigma} = K_{\frac{1}{3}}(\sigma)\Big[\Big(\frac{3\chi_e}{2u}\Big)^{\frac{2}{3}} \sigma^{\frac{2}{3}} \frac{2+2u+u^2}{(1+u)} - 1\Big] - K_{\frac{2}{3}}(\sigma)\Big(\frac{3\chi_e}{2u}\Big)^{\frac{1}{3}} \sigma^{\frac{1}{3}} \Big[\frac{u}{(1+u)} \vec{\zeta} \cdot \vec{b}\Big]. \tag{5.130}$$

To prevent numerical underflow during the application of the inverse transform sampling (ITS), we cap the upper integration bound at $\sigma = 30$ instead of ∞. Using the differential relation

$$\frac{d}{dx}[x^{\nu}K_{\nu}(x)] = -x^{\nu}K_{\nu-1}(x), \tag{5.131}$$

which holds for modified Bessel functions of the second kind, we derive the integral identities

$$\int_a^b x^{\frac{2}{3}}K_{\frac{1}{3}}(x)dx = -\int_a^b \frac{d}{dx}[x^{\frac{2}{3}}K_{\frac{2}{3}}(x)]dx = -b^{\frac{2}{3}}K_{\frac{2}{3}}(b) + a^{\frac{2}{3}}K_{\frac{2}{3}}(a) \tag{5.132}$$

$$\int_a^b x^{\frac{1}{3}}K_{\frac{2}{3}}(x)dx = -\int_a^b \frac{d}{dx}[x^{\frac{1}{3}}K_{\frac{1}{3}}(x)]dx = -b^{\frac{1}{3}}K_{\frac{1}{3}}(b) + a^{\frac{1}{3}}K_{\frac{1}{3}}(a). \tag{5.133}$$

This allows us to rewrite Eq. (5.128)

$$a^r(\bar{\sigma}) - ra^r\Big(\frac{2u}{3\chi_e}\Big) = 0, \tag{5.134}$$

where the function $a^r(x)$ is defined as

$$\begin{aligned} a^r(x) =& \Big(\frac{3\chi_e}{2u}\Big)^{\frac{2}{3}}[-K_{\frac{2}{3}}(30)30^{\frac{2}{3}} + K_{\frac{2}{3}}(x)x^{\frac{2}{3}}]\Big[\frac{2+2u+u^2}{(1+u)}\Big] - \int_x^{30} K_{\frac{1}{3}}(\sigma)d\sigma\Big[1\Big] + \\ & - \Big(\frac{3\chi_e}{2u}\Big)^{\frac{1}{3}}[-K_{\frac{1}{3}}(30)30^{\frac{1}{3}} + K_{\frac{1}{3}}(x)x^{\frac{1}{3}}]\Big[\frac{u}{(1+u)}\vec{\zeta}\cdot\vec{b}\Big]. \end{aligned} \tag{5.135}$$

Explicitly writing out all terms in Eqs. (5.134)-(5.135), the final integral equation takes the form

$$\begin{aligned} &\Big\{\Big(\frac{3\chi_e}{2u}\Big)^{\frac{2}{3}}[-K_{\frac{2}{3}}(30)30^{\frac{2}{3}}(1-r) + K_{\frac{2}{3}}(\bar{\sigma})\bar{\sigma}^{\frac{2}{3}}] - rK_{\frac{2}{3}}\Big(\frac{2u}{3\chi_e}\Big)\Big\}A_r + \\ &\qquad -\Big\{\int_{\bar{\sigma}}^{30} K_{\frac{1}{3}}(\sigma)d\sigma - r\int_{\frac{2u}{3\chi_e}}^{30} K_{\frac{1}{3}}(\sigma)d\sigma\Big\}B_r + \\ &-\Big\{\Big(\frac{3\chi_e}{2u}\Big)^{\frac{1}{3}}[-K_{\frac{1}{3}}(30)30^{\frac{1}{3}}(1-r) + K_{\frac{1}{3}}(\bar{\sigma})\bar{\sigma}^{\frac{1}{3}}] - rK_{\frac{1}{3}}\Big(\frac{2u}{3\chi_e}\Big)\Big\}C_r = 0, \end{aligned} \tag{5.136}$$

with the constants A_r, B_r and C_r are given by

$$A_r = \frac{2+2u+u^2}{(1+u)}, \tag{5.137}$$

$$B_r = 1, \tag{5.138}$$

$$C_r = \frac{u}{(1+u)}(\vec{\zeta}\cdot\vec{b}). \tag{5.139}$$

The `SFQEDtoolkit` provides the function `function_initial_spin_phtn_emission_polar_angle`, which numerically solves Eq. (5.136) for $\bar{\sigma}$ using the Van Wijngaarden-Dekker-Brent method[20]. Once $\bar{\sigma}$ is obtained, the corresponding cosine of the polar

[20] When solving Eq. (5.136), the random number r, the transformed photon energy u, and the initial electron spin ζ are fixed parameters.

angle θ is computed as

$$\cos\theta = \Big[1 - (\frac{3\chi}{2u}\bar{\sigma})^{\frac{2}{3}}\frac{1}{2\gamma^2}\Big]\frac{1}{\beta}. \tag{5.140}$$

If the initial electron's spin is unresolved, as is the case in most modern simulation codes, Eq. (5.124) is averaged over all possible spin configurations:

$$\begin{aligned}\frac{dW_{NIC}}{dudz} &\equiv \frac{1}{2}\sum_{\zeta}\frac{dW^{(\zeta)}_{NIC}}{dudz} \\ &= \frac{\alpha}{\pi}\frac{2}{3\sqrt{3}}\frac{1}{\chi_e\varepsilon'}\varepsilon^2\frac{u}{(1+u)^3}\frac{1}{\gamma^2}K_{\frac{1}{3}}(\xi_e)\Big[z^{\frac{2}{3}}(2+2u+u^2)-(1+u)\Big].\end{aligned} \tag{5.141}$$

Under this assumption, Eq. (5.136) simplifies to

$$\begin{aligned}\Big\{\Big(\frac{3\chi_e}{2u}\Big)^{\frac{2}{3}}[-K_{\frac{2}{3}}(30)30^{\frac{2}{3}}(1-r)+K_{\frac{2}{3}}(\bar{\sigma})\bar{\sigma}^{\frac{2}{3}}]-rK_{\frac{2}{3}}\Big(\frac{2u}{3\chi_e}\Big)\Big\}A_r+ \\ -\Big\{\int_{\bar{\sigma}}^{30}K_{\frac{1}{3}}(\sigma)d\sigma - r\int_{\frac{2u}{3\chi_e}}^{30}K_{\frac{1}{3}}(\sigma)d\sigma\Big\}B_r = 0.\end{aligned} \tag{5.142}$$

The new module of `SFQEDtoolkit` implements the routine `function_phtn_emission_polar_angle`, specifically designed to solve Eq. (5.142). In Fig. 5.6, we present the angular distribution of photons emitted via NIC during the collision of a 500 MeV electron beam with a linearly polarized laser wave with intensity $I = 5\times10^{21}$ W/cm^2. The figure compares the photon distributions obtained using the collinear approximation with those generated by `SFQEDtoolkit`'s `function_phtn_emission_polar_angle`. The results are consistent with those reported in [104].

5.5.2 NBW: Angular distribution from polarization resolved photons

By extending the arguments presented in Sec. 5.5.1 to the FNBW distribution described by Eqs. (5.57)-(5.61), we derive a differential probability with angular dependence that enables us to identify nontrivial emission directions for the pairs produced via NBW. The derivation follows closely that of the previous section. First, we sum over the final electron and positron spin states $\zeta^{\pm}$, integrate over the azimuthal angle φ, and then replace the polar coordinate θ with $z = 2\sqrt{2}\gamma_-^3\lambda_-^{\frac{3}{2}}$, which, from this point onward, carries all the information regarding the angular separation between the initial photon's trajectory and that of the electron. As a result, Eqs. (5.57)-(5.61) become

$$\frac{dW^{(\xi)}_{BW}}{dzd\varepsilon_-} = \int_0^{2\pi}\sum_{\zeta^+\zeta^-}\frac{dW^{(\xi\zeta_-\zeta_+)}_{BW}}{d\varepsilon_- d\Omega}d\varphi$$

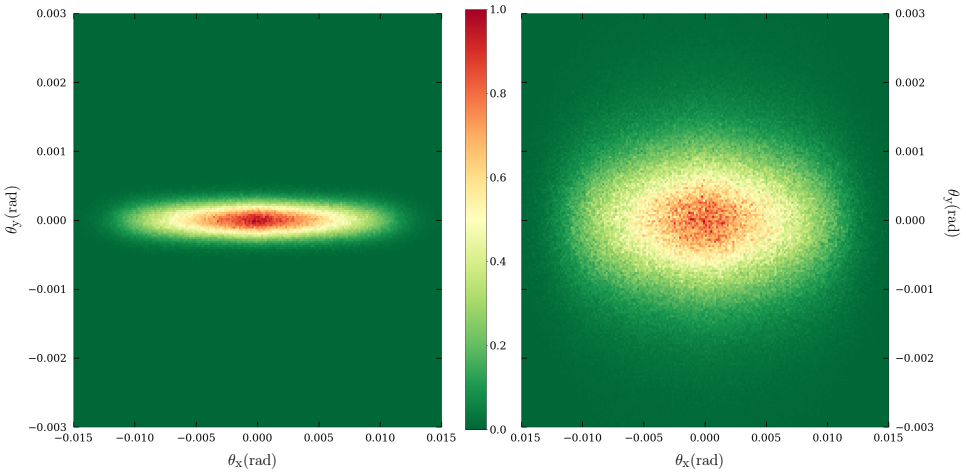

Figure 5.6: The figure illustrates the θ_x-θ_y distribution of NIC photons produced during a MC simulation of a collision between a 500 MeV electron beam and a linearly polarized laser pulse ($I = 5 \times 10^{21}$ W/cm^2). Two simulation approaches are compared: the collinear approximation (left panel) and the angle-resolved module of `SFQEDtoolkit` (right panel). The results, expressed in normalized simulation weights, agree with those reported in [104].

$$= \frac{2\alpha}{\pi}\frac{1}{3\sqrt{3}}\frac{1}{\chi_\gamma}\frac{1}{\gamma_-^2}(d\bar{W}_0'' + \xi_3 d\bar{W}_3''), \tag{5.143}$$

where

$$d\bar{W}_0'' = K_{\frac{1}{3}}(\xi_\gamma)\Big\{\frac{\omega^2}{2\varepsilon_+^2} + \Big(2z^{\frac{2}{3}} - 1\Big)\frac{\varepsilon_+^2 + \varepsilon_-^2}{2\varepsilon_+^2}\Big\}, \tag{5.144}$$

$$d\bar{W}_3'' = -K_{\frac{1}{3}}(\xi_\gamma)\frac{\varepsilon_-}{\varepsilon_+}z^{\frac{2}{3}}. \tag{5.145}$$

The argument of the modified Bessel functions is rewritten as $\xi_\gamma = \frac{2\omega^2}{3\varepsilon_-\varepsilon_+\chi_\gamma}z$. Although the change to the variable z helps us identify potential similarities between the NIC and NBW distributions, this transformation is only temporary. For numerical convenience, we define instead

$$\eta = \frac{2\omega^2}{3\varepsilon_-\varepsilon_+\chi_\gamma}z, \tag{5.146}$$

and apply the ITS algorithm to the distribution

$$\frac{dW_{BW}^{(\xi)}}{d\eta d\varepsilon_-} = \frac{\alpha}{\pi}\frac{1}{\sqrt{3}}\frac{\varepsilon_-\varepsilon_+}{\omega^2}\frac{1}{\gamma_-^2}(d\bar{W}_0^\eta + \xi_3 d\bar{W}_3^\eta), \tag{5.147}$$

with

$$d\bar{W}_0^\eta = K_{\frac{1}{3}}(\eta)\Big\{\frac{\omega^2}{2\varepsilon_+^2} + \Big[2\Big(\frac{3\varepsilon_-\varepsilon_+\chi_\gamma}{2\omega^2}\Big)^{\frac{2}{3}}\eta^{\frac{2}{3}} - 1\Big]\frac{\varepsilon_+^2 + \varepsilon_-^2}{2\varepsilon_+^2}\Big\} \tag{5.148}$$

$$d\bar{W}_3^{\eta} = -K_{\frac{1}{3}}(\eta)\frac{\varepsilon_-}{\varepsilon_+}\Big(\frac{3\varepsilon_-\varepsilon_+\chi_\gamma}{2\omega^2}\Big)^{\frac{2}{3}}\eta^{\frac{2}{3}}. \tag{5.149}$$

In `SFQEDtoolkit`, the routine `function_initial_pola_pair_production_polar_angle` solves the integral equation

$$\int_{\bar{\eta}}^{\infty}\frac{dW_{BW}^{(\xi)}}{d\eta d\varepsilon_-}d\eta - r\int_{\frac{2\omega^2}{3\varepsilon_-\varepsilon_+\chi_\gamma}}^{\infty}\frac{dW_{BW}^{(\xi)}}{d\eta d\varepsilon_-}d\eta = 0 \tag{5.150}$$

which generates η values distributed according to eq. (5.147) over the interval $\frac{2\omega^2}{3\varepsilon_-\varepsilon_+\chi_\gamma} \leq \eta \leq \infty$. Using the identities in Eqs. (5.132)-(5.133) and capping the upper integration bound to $\eta = 30$ (instead of $\eta = \infty$), Eq. (5.150) can be recast as

$$d\bar{W}_0^r(\bar{\eta}) + \xi_3 d\bar{W}_3^r(\bar{\eta}) = r\Big[d\bar{W}_0^r\Big(\frac{2\omega^2}{3\varepsilon_-\varepsilon_+\chi_\gamma}\Big) + \xi_3 d\bar{W}_3^r\Big(\frac{2\omega^2}{3\varepsilon_-\varepsilon_+\chi_\gamma}\Big)\Big], \tag{5.151}$$

with the functions $d\bar{W}_0^r(x)$ and $d\bar{W}_3^r(x)$ defined as

$$d\bar{W}_0^r(x) = [-K_{\frac{2}{3}}(30)30^{\frac{2}{3}} + K_{\frac{2}{3}}(x)x^{\frac{2}{3}}]\Big(\frac{3\varepsilon_-\varepsilon_+\chi_\gamma}{2\omega^2}\Big)^{\frac{2}{3}}\frac{\varepsilon_+^2+\varepsilon_-^2}{\varepsilon_+^2} + \int_x^{30}K_{\frac{1}{3}}(x)dx\Big\{\frac{\varepsilon_-}{\varepsilon_+}\Big\} \tag{5.152}$$

$$d\bar{W}_3^r(x) = [-K_{\frac{2}{3}}(30)30^{\frac{2}{3}} + K_{\frac{2}{3}}(x)x^{\frac{2}{3}}]\Big(\frac{3\varepsilon_-\varepsilon_+\chi_\gamma}{2\omega^2}\Big)^{\frac{2}{3}}\Big[-\frac{\varepsilon_-}{\varepsilon_+}\Big]. \tag{5.153}$$

Simple algebraic manipulations put equation (5.151) into the more manageable form

$$\Big\{\Big(\frac{3\varepsilon_-\varepsilon_+\chi_\gamma}{2\omega^2}\Big)^{\frac{2}{3}}[-K_{\frac{2}{3}}(30)30^{\frac{2}{3}}(1-r) + K_{\frac{2}{3}}(\bar{\eta})\bar{\eta}^{\frac{2}{3}}] - rK_{\frac{2}{3}}\Big(\frac{2\omega^2}{3\varepsilon_-\varepsilon_+\chi_\gamma}\Big)\Big\}\bar{A}_r + \\ + \Big\{\int_{\bar{\eta}}^{30}K_{\frac{1}{3}}(\eta)d\eta - r\int_{\frac{2\omega^2}{3\varepsilon_-\varepsilon_+\chi_\gamma}}^{30}K_{\frac{1}{3}}(\eta)d\eta\Big\}\bar{B}_r = 0, \tag{5.154}$$

where the constants $\bar{A}_r$ and $\bar{B}_r$ are

$$\bar{A}_r = \frac{\varepsilon_+^2+\varepsilon_-^2}{\varepsilon_+^2} - \frac{\varepsilon_-}{\varepsilon_+}\xi_3 \tag{5.155}$$

$$\bar{B}_r = \frac{\varepsilon_-}{\varepsilon_+}. \tag{5.156}$$

The function `function_initial_pola_pair_production_polar_angle` solves (5.154) numerically for $\bar{\eta}$ and then returns the cosine of the unknown polar angle θ as

$$\cos\theta = \Big[1 - (\frac{3\varepsilon_-\varepsilon_+\chi_\gamma}{2\omega^2}\bar{\eta})^{\frac{2}{3}}\frac{1}{2\gamma_-^2}\Big]\frac{1}{\beta_-}. \tag{5.157}$$

If the initial photon's polarization $\vec{\xi}$ is either unresolved or irrelevant, the distribution in Eq. (5.143) is averaged over all polarization configurations, so that Eq. (5.154) reduces to

$$\Big\{\Big(\frac{3\varepsilon_-\varepsilon_+\chi_\gamma}{2\omega^2}\Big)^{\frac{2}{3}}[-K_{\frac{2}{3}}(30)30^{\frac{2}{3}}(1-r)+K_{\frac{2}{3}}(\bar{\eta})\bar{\eta}^{\frac{2}{3}}]-rK_{\frac{2}{3}}\Big(\frac{2\omega^2}{3\varepsilon_-\varepsilon_+\chi_\gamma}\Big)\Big\}\bar{\bar{A}}_r+ \\ +\Big\{\int_{\bar{\eta}}^{30}K_{\frac{1}{3}}(\eta)d\eta-r\int_{\frac{2\omega^2}{3\varepsilon_-\varepsilon_+\chi_\gamma}}^{30}K_{\frac{1}{3}}(\eta)d\eta\Big\}\bar{B}_r=0, \tag{5.158}$$

with $\bar{\bar{A}}_r=\frac{\varepsilon_+^2+\varepsilon_-^2}{\varepsilon_+^2}$. `SFQEDtoolkit`'s advanced function `function_pair_production_polar_angle` is purposedly designed to solve (5.158) for $\bar{\eta}$ and return the corresponding $\cos\theta$ in accordance with eq. (5.157).

5.6 Determination of the final inner states

Up to this point in the thesis, we have provided the reader with the theoretical and numerical tools necessary to determine the occurrence of SFQED events, the energies of the resulting particles, and their subsequent directions. The stage is now set to explore the evolution of the spin and polarization states of these particles. However, this topic is somewhat delicate, so we will proceed gradually. In Sec. 5.5, we briefly mentioned the possibility of inferring spins and polarizations independently from the angular characterization of momenta, specifically when particles are generated under the collinear approximation. While we have identified this approach as conceptually flawed, and given that many modern codes in the literature still rely on it, the first part of this section will discuss its implementation for both the NIC and NBW channels.

This will be instrumental to the second part, where we will use the FNIC and FNBW distributions, Eqs. (5.39)-(5.43) and (5.57)-(5.61), to resolve the internal states of particles that have a complete angular characterization, following the methods outlined in Sec. 5.5.

In the third part, we will demonstrate that, under certain conditions, those FNIC and FNBW distributions may result in negative probabilities. We will thoroughly examine the corresponding differentials and propose a novel approach to treat them in a way that restores their probabilistic interpretation.

5.6.1 Internal states for particles without angular resolution

Particles produced under the collinear approximation have their spin or polarization states extracted from a differential probability in which all angular information has been integrated out.

Final electron spin and photon polarization after the collinear NIC photon emission

For the NIC process, this distribution is obtained by integrating eqs. (5.39)-(5.43) over the possible emission angles. By applying the identities in eqs. (5.68)-(5.70), the FNIC collapses into

$$\begin{aligned}\frac{dW_{NIC}^{(\zeta\zeta'\xi)}}{d\omega} &= \int_\Omega \frac{dW_{NIC}^{(\zeta\zeta'\xi)}}{d\omega d\Omega} d\Omega \\ &= \frac{\alpha}{4\sqrt{3}\pi\gamma^2}(dW_0^\star + \xi_1 dW_1^\star + \xi_2 dW_2^\star + \xi_3 dW_3^\star),\end{aligned} \tag{5.159}$$

where

$$\begin{aligned}dW_0^\star =& \Big[K_{\frac{2}{3}}(z_q)\frac{\varepsilon^2+\varepsilon'^2}{\varepsilon\varepsilon'} - \int_{z_q}^\infty dx K_{\frac{1}{3}}(x)\Big] + \Big[2K_{\frac{2}{3}}(z_q) - \int_{z_q}^\infty dx K_{\frac{1}{3}}(x)\Big](\vec{\zeta}\cdot\vec{\zeta}') + \\ &+ \Big[K_{\frac{2}{3}}(z_q) - \int_{z_q}^\infty dx K_{\frac{1}{3}}(x)\Big]\frac{\omega^2}{\varepsilon\varepsilon'}(\vec{\zeta}\cdot\hat{v})(\vec{\zeta}'\cdot\hat{v}) - K_{\frac{1}{3}}(z_q)\Big[\frac{\omega}{\varepsilon}(\vec{\zeta}\cdot\vec{b}) + \frac{\omega}{\varepsilon'}(\vec{\zeta}'\cdot\vec{b})\Big],\end{aligned} \tag{5.160}$$

$$\begin{aligned}dW_1^\star =& -K_{\frac{2}{3}}(z_q)\frac{\varepsilon^2-\varepsilon'^2}{2\varepsilon\varepsilon'}(\vec{\zeta}\wedge\vec{\zeta}')\cdot\hat{v} - \frac{\omega^2}{2\varepsilon\varepsilon'}\int_{z_q}^\infty dx K_{\frac{1}{3}}(x)[(\vec{\zeta}\cdot\vec{s})(\vec{\zeta}'\cdot\vec{b}) + (\vec{\zeta}\cdot\vec{b})(\vec{\zeta}'\cdot\vec{s})] + \\ &+ K_{\frac{1}{3}}(z_q)\Big[\frac{\omega}{\varepsilon}(\vec{\zeta}'\cdot\vec{s}) + \frac{\omega}{\varepsilon'}(\vec{\zeta}\cdot\vec{s})\Big],\end{aligned} \tag{5.161}$$

$$\begin{aligned}dW_2^\star =& \Big[K_{\frac{2}{3}}(z_q)\frac{\varepsilon^2-\varepsilon'^2}{\varepsilon\varepsilon'} - \frac{\omega}{\varepsilon}\int_{z_q}^\infty dx K_{\frac{1}{3}}(x)\Big](\hat{v}\cdot\vec{\zeta}) + \Big[K_{\frac{2}{3}}(z_q)\frac{\varepsilon^2-\varepsilon'^2}{\varepsilon\varepsilon'} - \frac{\omega}{\varepsilon'}\int_{z_q}^\infty dx K_{\frac{1}{3}}(x)\Big](\hat{v}\cdot\vec{\zeta}') + \\ &+ K_{\frac{1}{3}}(z_q)\Big\{\frac{\varepsilon^2-\varepsilon'^2}{2\varepsilon\varepsilon'}(\vec{\zeta}\wedge\vec{\zeta}')\cdot\vec{s} - \frac{\omega^2}{2\varepsilon\varepsilon'}[(\vec{\zeta}\cdot\hat{v})(\vec{\zeta}'\cdot\vec{b}) + (\vec{\zeta}\cdot\vec{b})(\vec{\zeta}'\cdot\hat{v})]\Big\},\end{aligned} \tag{5.162}$$

$$\begin{aligned}dW_3^\star =& K_{\frac{2}{3}}(z_q)\Big[\frac{\varepsilon^2+\varepsilon'^2}{2\varepsilon\varepsilon'}(\vec{\zeta}\cdot\vec{\zeta}') + 1 - \frac{\omega^2}{2\varepsilon\varepsilon'}(\vec{\zeta}\cdot\hat{v})(\vec{\zeta}'\cdot\hat{v})\Big] + \\ &- \frac{\omega^2}{2\varepsilon\varepsilon'}\int_{z_q}^\infty dx K_{\frac{1}{3}}(x)[(\vec{\zeta}\cdot\vec{s})(\vec{\zeta}'\cdot\vec{s}) - (\vec{\zeta}\cdot\vec{b})(\vec{\zeta}'\cdot\vec{b})]\Big\} + \\ &- K_{\frac{1}{3}}(z_q)\Big[\frac{\omega}{\varepsilon}(\vec{\zeta}'\cdot\vec{b}) + \frac{\omega}{\varepsilon'}(\vec{\zeta}\cdot\vec{b})\Big].\end{aligned} \tag{5.163}$$

Eqs. (5.159)-(5.163), which retain a dependence on the initial and final spin- and polarization-states only, is perfectly consistent with the differential in [99]. For the sake of future convenience we switch from the variable ω to u (5.121), getting

$$\frac{dW_{NIC}^{(\zeta\zeta'\xi)}}{du} = \frac{\alpha}{4\sqrt{3}\pi\gamma^2}\frac{\varepsilon}{(1+u)^2}(dW_0^\star + \xi_1 dW_1^\star + \xi_2 dW_2^\star + \xi_3 dW_3^\star), \tag{5.164}$$

and

$$dW_0^\star = \Big[K_{\frac{2}{3}}(z_q)\frac{2+2u+u^2}{(1+u)} - \int_{z_q}^{\infty} dx K_{\frac{1}{3}}(x)\Big] + \Big[2K_{\frac{2}{3}}(z_q) - \int_{z_q}^{\infty} dx K_{\frac{1}{3}}(x)\Big](\vec{\zeta}\cdot\vec{\zeta}') + \\ + \Big[K_{\frac{2}{3}}(z_q) - \int_{z_q}^{\infty} dx K_{\frac{1}{3}}(x)\Big]\frac{u^2}{1+u}(\vec{\zeta}\cdot\hat{v})(\vec{\zeta}'\cdot\hat{v}) - K_{\frac{1}{3}}(z_q)\Big[\frac{u}{1+u}(\vec{\zeta}\cdot\vec{b}) + u(\vec{\zeta}'\cdot\vec{b})\Big]; \tag{5.165}$$

$$dW_1^\star = -K_{\frac{2}{3}}(z_q)\frac{2u+u^2}{2(1+u)}(\vec{\zeta}\wedge\vec{\zeta}')\cdot\hat{v} - \frac{u^2}{2(1+u)}\int_{z_q}^{\infty} dx K_{\frac{1}{3}}(x)[(\vec{\zeta}\cdot\vec{s})(\vec{\zeta}'\cdot\vec{b}) + (\vec{\zeta}\cdot\vec{b})(\vec{\zeta}'\cdot\vec{s})] + \\ + K_{\frac{1}{3}}(z_q)\Big[\frac{u}{1+u}(\vec{\zeta}'\cdot\vec{s}) + u(\vec{\zeta}\cdot\vec{s})\Big]; \tag{5.166}$$

$$dW_2^\star = \Big[K_{\frac{2}{3}}(z_q)\frac{2u+u^2}{1+u} - \frac{u}{1+u}\int_{z_q}^{\infty} dx K_{\frac{1}{3}}(x)\Big](\hat{v}\cdot\vec{\zeta}) + \Big[K_{\frac{2}{3}}(z_q)\frac{2u+u^2}{1+u} - u\int_{z_q}^{\infty} dx K_{\frac{1}{3}}(x)\Big](\hat{v}\cdot\vec{\zeta}') + \\ + K_{\frac{1}{3}}(z_q)\Big\{\frac{2u+u^2}{2(1+u)}(\vec{\zeta}\wedge\vec{\zeta}')\cdot\vec{s} - \frac{u^2}{2(1+u)}[(\vec{\zeta}\cdot\hat{v})(\vec{\zeta}'\cdot\vec{b}) + (\vec{\zeta}\cdot\vec{b})(\vec{\zeta}'\cdot\hat{v})]\Big\}; \tag{5.167}$$

$$dW_3^\star = K_{\frac{2}{3}}(z_q)\Big[\frac{2+2u+u^2}{2(1+u)}(\vec{\zeta}\cdot\vec{\zeta}') + 1 - \frac{u^2}{2(1+u)}(\vec{\zeta}\cdot\hat{v})(\vec{\zeta}'\cdot\hat{v})\Big] + \\ - \frac{u^2}{2(1+u)}\int_{z_q}^{\infty} dx K_{\frac{1}{3}}(x)\Big[(\vec{\zeta}\cdot\vec{s})(\vec{\zeta}'\cdot\vec{s}) - (\vec{\zeta}\cdot\vec{b})(\vec{\zeta}'\cdot\vec{b})\Big] + \\ - K_{\frac{1}{3}}(z_q)\Big[\frac{u}{1+u}(\vec{\zeta}'\cdot\vec{b}) + u(\vec{\zeta}\cdot\vec{b})\Big]. \tag{5.168}$$

We can now outline an algorithm to determine the electron's spin and the photon's polarization after the NIC event. By summing eq. (5.164) over the final photon polarizations $\vec{\xi}$, we obtain the differential probability

$$\frac{dW_{NIC}^{(\zeta\zeta')}}{du} = \sum_{\xi}\frac{dW_{NIC}^{(\zeta\zeta'\xi)}}{du} = \frac{\alpha}{2\sqrt{3}\pi\gamma^2}\frac{\varepsilon}{(1+u)^2}dW_0^\star \tag{5.169}$$

which depends only on the electron's spin $\vec{\zeta}'$ (at this stage, we neglect the dependence on u and $\vec{\zeta}$, assuming them to be fixed). The term $dW_0^\star$ is given by

$$dW_0^\star = a^\star + \vec{\zeta}'\cdot\vec{S}^\star, \tag{5.170}$$

$$a^\star = \Big[K_{\frac{2}{3}}(z_q)\frac{2+2u+u^2}{(1+u)} - \int_{z_q}^{\infty} dx K_{\frac{1}{3}}(x)\Big] - K_{\frac{1}{3}}(z_q)\frac{u}{1+u}(\vec{\zeta}\cdot\vec{b}) \tag{5.171}$$

$$\vec{S}^{\star} = \Big[2K_{\frac{2}{3}}(z_q) - \int_{z_q}^{\infty} dx K_{\frac{1}{3}}(x)\Big]\vec{\zeta} + \Big[K_{\frac{2}{3}}(z_q) - \int_{z_q}^{\infty} dx K_{\frac{1}{3}}(x)\Big]\frac{u^2}{1+u}(\vec{\zeta}\cdot\hat{v})\hat{v} - K_{\frac{1}{3}}(z_q)u\vec{b}. \tag{5.172}$$

From the discussion in sec. 5.4.1, we know that, up to a constant factor, dW_0^* corresponds to the NIC cross-section summed over the final photon's polarization and emission angles

$$\int_{\Omega}\sum_{\xi}|\mathcal{M}_{fi}|^2 \sim dW_0^* = a^* + \vec{\zeta}'\cdot\vec{S}^*, \tag{5.173}$$

where $\vec{\zeta}'$ represents the final electron spin as selected by an arbitrary detector. Since the quantity in eq. (5.173) is a Lorentz invariant which takes the form[21]

$$\int_{\Omega}\sum_{\xi}|\mathcal{M}_{fi}|^2 \sim 1 + \vec{\zeta}'\cdot\vec{\zeta}^{(r)} \tag{5.174}$$

in the final electron's rest frame, it is natural to recognize the final electron spin state $\vec{\zeta}^{(r)}$ in its rest frame[22] as [57]

$$\vec{\zeta}^{(r)} = \frac{\vec{S}^*}{a^*}. \tag{5.175}$$

The quantity in eq. (5.175) is the proper SQA of the final electron: given the arbitrariness in choosing $\vec{\zeta}'$, we will henceforth make no distinction between the detector's spin axis and the SQA:

$$\vec{\zeta}' = \vec{\zeta}^{(r)} = \frac{\vec{S}^*}{a^*} \tag{5.176}$$

(this is a common abuse of notation that simplifies the forthcoming expressions). Alternatively, one could define the SQA as the direction onto which the detector's spin axis $\vec{\zeta}'$ projects when considering the ratio

$$\frac{\frac{dW_{NIC}^{(\zeta\zeta')}}{du}\Big|_{\vec{\zeta}'=\uparrow} - \frac{dW_{NIC}^{(\zeta\zeta')}}{du}\Big|_{\vec{\zeta}'=\downarrow}}{\frac{dW_{NIC}^{(\zeta\zeta')}}{du}\Big|_{\vec{\zeta}'=\uparrow} + \frac{dW_{NIC}^{(\zeta\zeta')}}{du}\Big|_{\vec{\zeta}'=\downarrow}} = \vec{\zeta}'\cdot\frac{\vec{S}^{\star}}{a^{\star}}, \tag{5.177}$$

which again leads to eq. (5.176).

The same reasoning applies directly to the photon polarization: depending on whether the quantum system is in a mixed spin/polarization state or a pure one, two possible approaches arise:

[21] See argument above eq. (5.87) in sec 5.4.1.

[22] Notice that in Eqs. (5.28), (5.39) and (5.174) the vectors $\vec{\zeta}$ and $\vec{\zeta}'$ are already expressed in the frames at rest with the incoming and outgoing electrons, respectively.

- For mixed states, we begin by identifying the spin quantization axis (SQA) as given in Eq. (5.176). The next step involves evaluating the ratio:

$$\frac{\frac{dW_{NIC}^{(\zeta\zeta'\xi)}}{du}\Big|_{\vec{\xi}=\uparrow} - \frac{dW_{NIC}^{(\zeta\zeta'\xi)}}{du}\Big|_{\vec{\xi}=\downarrow}}{\frac{dW_{NIC}^{(\zeta\zeta'\xi)}}{du}\Big|_{\vec{\xi}=\uparrow} + \frac{dW_{NIC}^{(\zeta\zeta'\xi)}}{du}\Big|_{\vec{\xi}=\downarrow}} = \vec{\xi}\cdot\frac{\vec{P}^{\star}}{a^{\star}+\vec{\zeta}'\cdot\vec{S}^{\star}}, \tag{5.178}$$

  which leads to the PQA

$$\vec{\xi} = \frac{\vec{P}^{\star}}{a^{\star}+\vec{\zeta}'\cdot\vec{S}^{\star}}. \tag{5.179}$$

  Here, the electron spin from Eq. (5.177) is used within the polarization-resolved distribution (5.164), now rewritten as:

$$\frac{dW_{NIC}^{(\zeta\zeta'\xi)}}{du} = \frac{\alpha}{4\sqrt{3}\pi\gamma^2}\frac{\varepsilon}{(1+u)^2}(a^{\star}+\vec{\zeta}'\cdot\vec{S}^{\star}+\vec{\xi}\cdot\vec{P}^{\star}) \tag{5.180}$$

$$\vec{P}^{\star} = (dW_1^{\star}, dW_2^{\star}, dW_3^{\star}). \tag{5.181}$$

- For pure states, the spin and polarization are determined sequentially by evaluating the conditions:

$$\frac{\frac{dW_{NIC}^{(\zeta\zeta')}}{du}\Big|_{\vec{\zeta}'=\uparrow}}{\frac{dW_{NIC}^{(\zeta\zeta')}}{du}\Big|_{\vec{\zeta}'=\uparrow} + \frac{dW_{NIC}^{(\zeta\zeta')}}{du}\Big|_{\vec{\zeta}'=\downarrow}} = \frac{a^{\star}+|\vec{S}^{\star}|}{2a^{\star}} > r_{\zeta'} \tag{5.182}$$

  and

$$\frac{\frac{dW_{NIC}^{(\zeta\zeta'\xi)}}{du}\Big|_{\vec{\xi}=\uparrow}}{\frac{dW_{NIC}^{(\zeta\zeta'\xi)}}{du}\Big|_{\vec{\xi}=\uparrow} + \frac{dW_{NIC}^{(\zeta\zeta'\xi)}}{du}\Big|_{\vec{\xi}=\downarrow}} = \frac{a^{\star}+\vec{\zeta}'\cdot\vec{S}^{\star}+|\vec{P}^{\star}|}{2(a^{\star}+\vec{\zeta}'\cdot\vec{S}^{\star})} > r_{\xi}, \tag{5.183}$$

  where $r_{\zeta'}$ and r_{ξ} random numbers uniformly distributed between 0 and 1. If Eq. (5.182) [Eq. (5.183)] holds, then the spin (polarization) state is assigned as $\vec{\zeta}' = \frac{\vec{S}^{\star}}{|S^{\star}|}$ ($\vec{\xi} = \frac{\vec{P}^{\star}}{|P^{\star}|}$), otherwise they take the opposite values $\vec{\zeta}' = -\frac{\vec{S}^{\star}}{|S^{\star}|}$ ($\vec{\xi} = -\frac{\vec{P}^{\star}}{|P^{\star}|}$).

`SFQEDtoolkit`'s advanced module implements two functions:

- `function_spin_and_pola_no_angles_mixed_states`, that tracks the evolution of mixed spin- and polarization-states for particles created in the collinear approximation, reproducing the mechanisms corresponding to Eqs. (5.176) and (5.179);

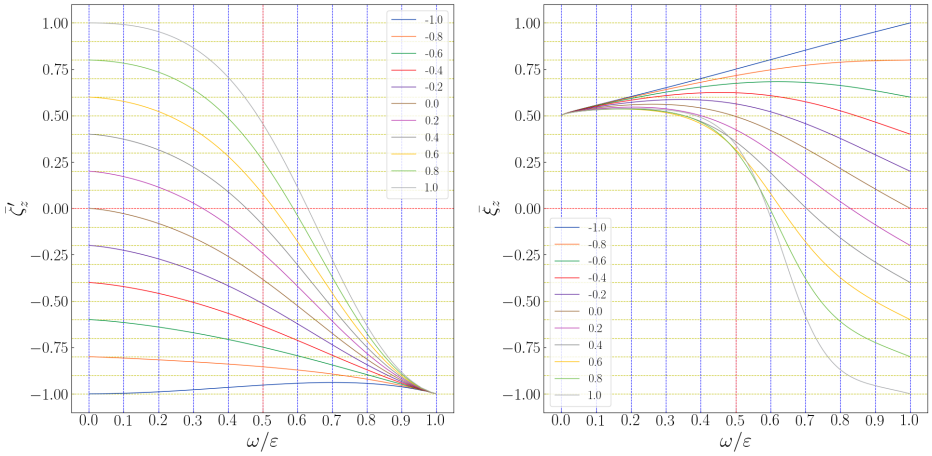

Figure 5.7: Mixed-state curves for spin (ζ_z', left) and photon polarization (ξ_z, right) were obtained by simulating a 1 GeV electron moving in a magnetic field, $\vec{B} = (0, 0, B_z)$. Both ζ_z' and ξ_z are plotted as functions of the photon-to-electron energy ratio, $\frac{\omega}{\varepsilon}$, for various initial spin component values, ζ_z (specified in the inset and indicated by different colors). The anomalous behavior observed in the polarization curve arises from its dependence on the spin value (see eq. (5.178)).

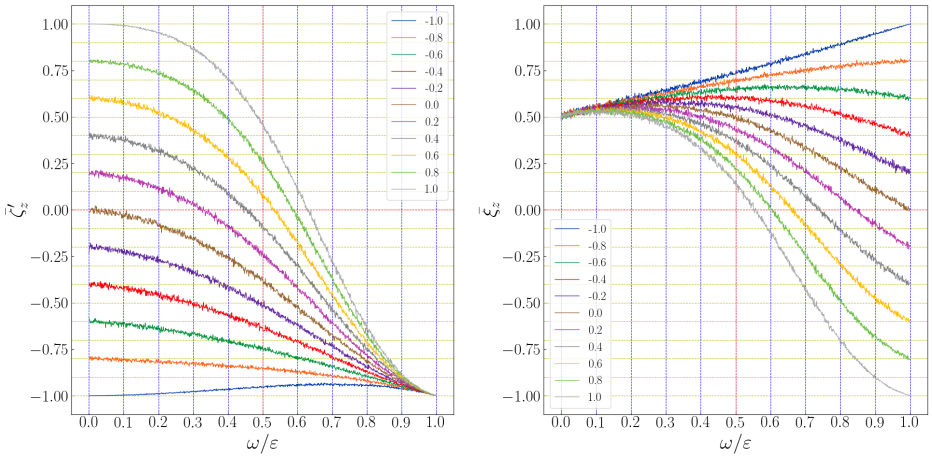

Figure 5.8: As in fig. 5.7, but this time pure states have been employed for spin and polarization. Each data point on the curves represents the average outcome of 10^3 NIC photon emissions with the identical parameters (initial electron spin ζ, energy ε, quantum parameter χ_e and photon-to-electron energy ratio $\frac{\omega}{\varepsilon}$).

- `function_spin_and_pola_no_angles_pure_states` which performs the same task but for pure states, therefore evaluating (5.182) and (5.183).

Figures 5.7 and 5.8 were generated using the advanced version of the `SFQEDtoolkit` and illustrate the spin- (left) and polarization–photon energy (right) curves obtained

from simulating a $\varepsilon = 1$ GeV electron moving in a magnetic field, $\vec{B} = (0, 0, B_z)$, with quantum parameter $\chi_e = 2$,. In Figure 5.7, the spin component ζ'_z and the polarization component ξ_z (both measured along the magnetic field) are obtained via the routine `function_spin_and_pola_no_angles_mixed_states`. In contrast, Figure 5.8 shows the averages of these quantities over multiple emissions, computed using `function_spin_and_pola_no_angles_pure_states`. In both cases, ζ'_z and ξ_z are plotted as functions of the photon-to-electron energy ratio, $\frac{\omega}{\varepsilon}$, for various initial spin component values, ζ_z (indicated by the different colors of the curves). An interesting observation emerges: while the results in Figure 5.8 and the final-spin (left panel) of Figure 5.7 are perfectly consistent with those reported in [107], the photon polarization mixed state exhibits an anomalous behavior. This discrepancy arises from our approach: the fact that the PQA depends on the SQA computed in Eq. (5.175) undermines the physical logic of the problem. In effect, it is ambiguous whether nature first fixes the final electron's spin and then the photon's polarization, or vice versa. One could indeed return to Eq. (5.39), sum over the ζ' states, and first determine the PQA via

$$\vec{\xi} = \frac{\vec{P}'^{\star}}{a^{\star}}, \tag{5.184}$$

where $\vec{P}'^{\star} = (dW'^{\star}_1, dW'^{\star}_2, dW'^{\star}_3)$ and

$$dW'^{\star}_0 = K_{\frac{2}{3}}(z_q)\frac{\varepsilon^2 + \varepsilon'^2}{\varepsilon\varepsilon'} - \int_{z_q}^{\infty} dx K_{\frac{1}{3}}(x) - K_{\frac{1}{3}}(z_q)\frac{\omega}{\varepsilon}(\vec{\zeta}\cdot\vec{b}), \tag{5.185}$$

$$dW'^{\star}_1 = K_{\frac{1}{3}}(z_q)\frac{\omega}{\varepsilon'}(\vec{\zeta}\cdot\vec{s}), \tag{5.186}$$

$$dW'^{\star}_2 = \Big[K_{\frac{2}{3}}(z_q)\frac{\varepsilon^2 - \varepsilon'^2}{\varepsilon\varepsilon'} - \frac{\omega}{\varepsilon}\int_{z_q}^{\infty} dx K_{\frac{1}{3}}(x)\Big](\hat{v}\cdot\vec{\zeta}), \tag{5.187}$$

$$dW'^{\star}_3 = -K_{\frac{1}{3}}(z_q)\frac{\omega}{\varepsilon'}(\vec{\zeta}\cdot\vec{b}). \tag{5.188}$$

Only then one proceeds with the calculation of the SQA. Although the two methods differ, they are expected to yield equivalent results on *average*; however, no averaging process is applied here. It is important to note that the results presented in Figure 5.8 are derived from a stochastic procedure involving pure spin and polarization states, while the mixed state method used in Figure 5.7 is entirely deterministic: given a set of simulation parameters, the final mixed state is always computed in the same way. The simplest solution to the issue, from now on referred to as the "dependence problem", is to compute the mixed states ζ'_z and ξ_z independently, using Eqs. (5.176) and (5.184). The routine `function_spin_and_pola_no_angles_mixed_states_independent` implements this approach, and its results are shown in Figure 5.9, thereby restoring consistency. In contrast, pure states do not require such a modification because their intrinsic probabilistic nature inherently addresses this issue.

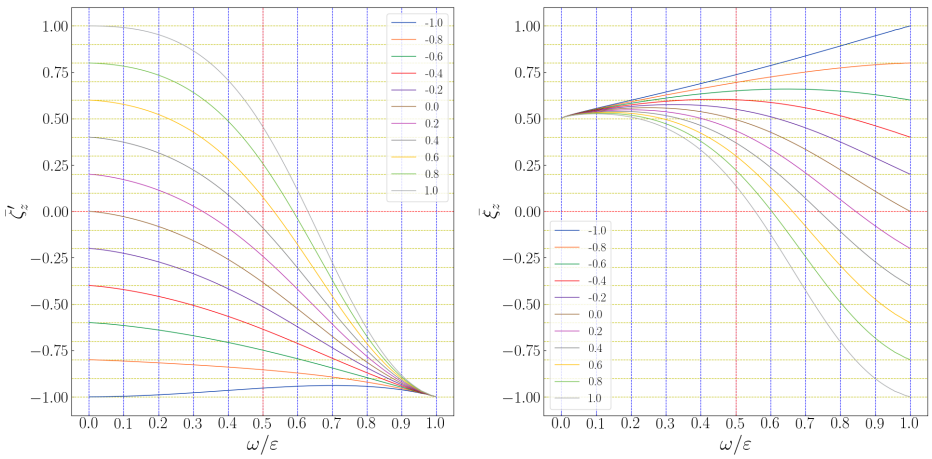

Figure 5.9: As in fig. 5.7. This time the SQA and PQA are computed independently from one another, and the results are consistent with those found in the literature.

Final electron and positron spins after the collinear NBW pair production

Defining the spin states of pair particles produced under the NBW collinear approximation follows the same procedure as that proposed in the previous section for the NIC. The process begins by integrating the FNBW distribution (Eqs. (5.57)–(5.61)) over the solid angle. This integration, performed using the identities in Eqs. (5.92)–(5.94), eliminates the redundant angular dependence, yielding

$$\begin{aligned}\frac{d\bar{W}_{NBW}^{(\xi\zeta_-\zeta_+)}}{d\varepsilon_-} &= \int_\Omega \frac{d\bar{W}_{NBW}^{(\xi\zeta_-\zeta_+)}}{d\varepsilon_- d\Omega} d\Omega \\ &= \frac{\alpha m^2}{4\sqrt{3}\pi\omega^2}(d\bar{W}_0^\star + \xi_1 d\bar{W}_1^\star + \xi_2 d\bar{W}_2^\star + \xi_3 d\bar{W}_3^\star),\end{aligned} \tag{5.189}$$

in which

$$\begin{aligned}d\bar{W}_0^\star =& \Big[K_{\frac{2}{3}}(z_p)\frac{\varepsilon_+^2+\varepsilon_-^2}{\varepsilon_+\varepsilon_-} + \int_{z_p}^\infty dx K_{\frac{1}{3}}(x)\Big] - \Big[2K_{\frac{2}{3}}(z_p) - \int_{z_p}^\infty dx K_{\frac{1}{3}}(x)\Big](\vec{\zeta}_-\cdot\vec{\zeta}_+)+ \\ &+ \Big[\frac{\varepsilon_+^2+\varepsilon_-^2}{\varepsilon_+\varepsilon_-}\int_{z_p}^\infty dx K_{\frac{1}{3}}(x) - K_{\frac{2}{3}}(z_p)\frac{(\varepsilon_+-\varepsilon_-)^2}{\varepsilon_+\varepsilon_-}\Big](\vec{\zeta}_-\cdot\hat{v})(\vec{\zeta}_+\cdot\hat{v})+ \\ &- K_{\frac{1}{3}}(z_p)\Big\{\Big[\frac{\omega}{\varepsilon_-}(\vec{\zeta}_-\cdot\vec{b}) - \frac{\omega}{\varepsilon_+}(\vec{\zeta}_+\cdot\vec{b})\Big]\Big\};\end{aligned} \tag{5.190}$$

$$\begin{aligned}d\bar{W}_1^\star =& \Big[\frac{(\varepsilon_+^2-\varepsilon_-^2)}{2\varepsilon_+\varepsilon_-}K_{\frac{2}{3}}(z_p)\Big]\hat{v}\cdot(\vec{\zeta}_-\wedge\vec{\zeta}_+)+ \\ &- \frac{\omega^2}{2\varepsilon_+\varepsilon_-}\int_{z_p}^\infty dx K_{\frac{1}{3}}(x)[(\vec{\zeta}_-\cdot\vec{s})(\vec{\zeta}_+\cdot\vec{b}) + (\vec{\zeta}_-\cdot\vec{b})(\vec{\zeta}_+\cdot\vec{s})]+\end{aligned}$$

$$+ K_{\frac{1}{3}}(z_p)\Big\{\Big[\frac{\omega}{\varepsilon_-}(\vec{\zeta}_+\cdot\vec{s}) - \frac{\omega}{\varepsilon_+}(\vec{\zeta}_-\cdot\vec{s})\Big]\Big\}; \tag{5.191}$$

$$\begin{aligned} d\bar{W}_2^{\star} =& \Big[\frac{\omega}{\varepsilon_-}\int_{z_p}^{\infty} dx K_{\frac{1}{3}}(x) - K_{\frac{2}{3}}(z_p)\frac{\varepsilon_+^2-\varepsilon_-^2}{\varepsilon_+\varepsilon_-}\Big](\hat{v}\cdot\vec{\zeta}_-)+ \\ &+ \Big[\frac{\omega}{\varepsilon_+}\int_{z_p}^{\infty} dx K_{\frac{1}{3}}(x) + K_{\frac{2}{3}}(z_p)\frac{\varepsilon_+^2-\varepsilon_-^2}{\varepsilon_+\varepsilon_-}\Big](\hat{v}\cdot\vec{\zeta}_+)+ \\ &- K_{\frac{1}{3}}(z_p)\Big\{\Big[\frac{\omega^2}{2\varepsilon_+\varepsilon_-}(\vec{\zeta}_-\wedge\vec{\zeta}_+)\cdot\vec{s} + \frac{(\varepsilon_+^2-\varepsilon_-^2)}{2\varepsilon_+\varepsilon_-}[(\vec{\zeta}_-\cdot\hat{v})(\vec{\zeta}_+\cdot\vec{b}) + (\vec{\zeta}_-\cdot\vec{b})(\vec{\zeta}_+\cdot\hat{v})]\Big]\Big\}; \end{aligned} \tag{5.192}$$

$$\begin{aligned} d\bar{W}_3^{\star} =& \Big[\frac{(\varepsilon_+^2+\varepsilon_-^2)}{2\varepsilon_+\varepsilon_-}(\vec{\zeta}_-\cdot\vec{\zeta}_+) - 1 - \frac{(\varepsilon_+-\varepsilon_-)^2}{2\varepsilon_+\varepsilon_-}(\vec{\zeta}_-\cdot\hat{v})(\vec{\zeta}_+\cdot\hat{v})\Big]K_{\frac{2}{3}}(z_p)+ \\ &- \frac{\omega^2}{2\varepsilon_+\varepsilon_-}\int_{z_p}^{\infty} dx K_{\frac{1}{3}}(x)[(\vec{\zeta}_-\cdot\vec{s})(\vec{\zeta}_+\cdot\vec{s}) - (\vec{\zeta}_-\cdot\vec{b})(\vec{\zeta}_+\cdot\vec{b})]\Big\}+ \\ &- K_{\frac{1}{3}}(z_p)\Big[\frac{\omega}{\varepsilon_-}(\vec{\zeta}_+\cdot\vec{b}) - (\vec{\zeta}_-\cdot\vec{b})\frac{\omega}{\varepsilon_+}\Big]. \end{aligned} \tag{5.193}$$

One then continues by summing (5.189)-(5.193) over the positron's spin ($\vec{\zeta}^{\,+}$)

$$\frac{dW_{NBW}^{(\xi\zeta_-)}}{d\varepsilon_-} = \frac{\alpha m^2}{2\sqrt{3}\pi\omega^2}(d\bar{W}_0^{\circ} + \xi_1 d\bar{W}_1^{\circ} + \xi_2 d\bar{W}_2^{\circ} + \xi_3 d\bar{W}_3^{\circ}), \tag{5.194}$$

where

$$d\bar{W}_0^{\circ} = \Big[K_{\frac{2}{3}}(z_p)\frac{\varepsilon_+^2+\varepsilon_-^2}{\varepsilon_+\varepsilon_-} + \int_{z_p}^{\infty} dx K_{\frac{1}{3}}(x)\Big] - K_{\frac{1}{3}}(z_p)\frac{\omega}{\varepsilon_-}(\vec{\zeta}_-\cdot\vec{b}) \tag{5.195}$$

$$d\bar{W}_1^{\circ} = -K_{\frac{1}{3}}(z_p)\frac{\omega}{\varepsilon_+}(\vec{\zeta}_-\cdot\vec{s}) \tag{5.196}$$

$$d\bar{W}_2^{\circ} = \Big[\frac{\omega}{\varepsilon_-}\int_{z_p}^{\infty} dx K_{\frac{1}{3}}(x) - K_{\frac{2}{3}}(z_p)\frac{\varepsilon_+^2-\varepsilon_-^2}{\varepsilon_+\varepsilon_-}\Big](\hat{v}\cdot\vec{\zeta}_-) \tag{5.197}$$

$$d\bar{W}_3^{\circ} = -K_{\frac{2}{3}}(z_p) + K_{\frac{1}{3}}(z_p)(\vec{\zeta}_-\cdot\vec{b})\frac{\omega}{\varepsilon_+}. \tag{5.198}$$

At this stage, a few key remarks are in order. Physical and numerical reasoning suggests that once the spin of one particle is determined, this information should then be used to establish the polarization of the other. However, it is essential to remember that the electron and positron are created simultaneously. Since there is no fundamental reason to begin with the electron, we arbitrarily choose to determine

the positron's spin first[23]. With this choice in mind, also keeping into account the underlying symmetry of the problem, the differential distribution in the positron energy $\frac{dW_{NBW}^{(\xi\zeta_+)}}{d\varepsilon_+}$, analogous to (5.194)-(5.198), can be obtained by swapping every occurrence of the + and − subscripts in the relevant variables. Applying this prescription yields:

$$\frac{dW_{BW}^{(\xi\zeta_+)}}{d\varepsilon_+} = \frac{\alpha m^2}{2\sqrt{3}\pi\omega^2}(d\bar{W}_0^+ + \xi_1 d\bar{W}_1^+ + \xi_2 d\bar{W}_2^+ + \xi_3 d\bar{W}_3^+), \tag{5.199}$$

in which

$$d\bar{W}_0^+ = \Big[K_{\frac{2}{3}}(z_p)\frac{\varepsilon_+^2+\varepsilon_-^2}{\varepsilon_+\varepsilon_-} + \int_{z_p}^{\infty} dx K_{\frac{1}{3}}(x)\Big] - K_{\frac{1}{3}}(z_p)\frac{\omega}{\varepsilon_+}(\vec{\zeta}_+\cdot\vec{b}) \tag{5.200}$$

$$d\bar{W}_1^+ = -K_{\frac{1}{3}}(z_p)\frac{\omega}{\varepsilon_-}(\vec{\zeta}_+\cdot\vec{s}) \tag{5.201}$$

$$d\bar{W}_2^+ = \Big[\frac{\omega}{\varepsilon_+}\int_{z_p}^{\infty} dx K_{\frac{1}{3}}(x) + K_{\frac{2}{3}}(z_p)\frac{\varepsilon_+^2-\varepsilon_-^2}{\varepsilon_+\varepsilon_-}\Big](\hat{v}\cdot\vec{\zeta}_+) \tag{5.202}$$

$$d\bar{W}_3^+ = -K_{\frac{2}{3}}(z_p) + K_{\frac{1}{3}}(z_p)(\vec{\zeta}_+\cdot\vec{b})\frac{\omega}{\varepsilon_-}. \tag{5.203}$$

As usual, we recast Eqs. (5.199)-(5.203) in the form

$$\frac{dW_{NBW}^{(\xi\zeta_+)}}{d\varepsilon_+} = \frac{\alpha m^2}{2\sqrt{3}\pi\omega^2}(a_+^\star + \vec{\zeta}_+\cdot\vec{S}_+^\star), \tag{5.204}$$

where we have separated the spin-independent term

$$a_+^\star = \Big[K_{\frac{2}{3}}(z_p)\frac{\varepsilon_+^2+\varepsilon_-^2}{\varepsilon_+\varepsilon_-} + \int_{z_p}^{\infty} dx K_{\frac{1}{3}}(x)\Big] - K_{\frac{2}{3}}(z_p)\xi_3 \tag{5.205}$$

from the term that couples to the spin

$$\vec{S}_+^\star = \Big[\frac{\omega}{\varepsilon_+}\int_{z_p}^{\infty} dx K_{\frac{1}{3}}(x) + K_{\frac{2}{3}}(z_p)\frac{\varepsilon_+^2-\varepsilon_-^2}{\varepsilon_+\varepsilon_-}\Big]\xi_2\hat{v} + K_{\frac{1}{3}}(z_p)\Big[\frac{\omega}{\varepsilon_-}(\xi_3\vec{b}-\xi_1\vec{s}) - \frac{\omega}{\varepsilon_+}\vec{b}\Big]. \tag{5.206}$$

In this way, we exploit the relationship between $\frac{dW_{NBW}^{(\xi\zeta_+)}}{d\varepsilon_+}$ and the squared transition matrix element associated with the positron spin, namely

$$\frac{dW_{NBW}^{(\xi\zeta_+)}}{d\varepsilon_+} \sim |\mathcal{M}_{fi}^{\zeta_+}|^2.$$

[23] On average, the results remain unchanged whether one computes $\vec{\zeta}_+$ before $\vec{\zeta}_-$ or vice versa.

By the same logic of previous section, through the ratio

$$\frac{\frac{dW^{(\xi\zeta_+)}_{NBW}}{d\varepsilon_+}\Big|_{\vec{\zeta}_+=\uparrow} - \frac{dW^{(\xi\zeta_+)}_{NBW}}{d\varepsilon_+}\Big|_{\vec{\zeta}_+=\downarrow}}{\frac{dW^{(\xi\zeta_+)}_{NBW}}{d\varepsilon_+}\Big|_{\vec{\zeta}_+=\uparrow} + \frac{dW^{(\xi\zeta_+)}_{NBW}}{d\varepsilon_+}\Big|_{\vec{\zeta}_+=\downarrow}} = \vec{\zeta}_+ \cdot \frac{\vec{S}^\star_+}{a^\star_+} \tag{5.207}$$

we can identify the positron's mixed state as

$$\vec{\zeta}_+ = \frac{\vec{S}^\star_+}{a^\star_+}. \tag{5.208}$$

Conversely, to determine the pure state corresponding to (5.208), one evaluates

$$\frac{\frac{dW^{(\xi\zeta_+)}_{NBW}}{d\varepsilon_+}\Big|_{\vec{\zeta}_+=\uparrow}}{\frac{dW^{(\xi\zeta_+)}_{NBW}}{d\varepsilon_+}\Big|_{\vec{\zeta}_+=\uparrow} + \frac{dW^{(\xi\zeta_+)}_{NBW}}{d\varepsilon_+}\Big|_{\vec{\zeta}_+=\downarrow}} = \frac{a^\star_+ + |\vec{S}^\star_+|}{2a^\star_+} > r^\star_+, \tag{5.209}$$

$r^\star_+$ being a random number such that $0 \leq r^\star_+ \leq 1$; if the inequality in (5.209) holds then $\vec{\zeta}_+ = \frac{\vec{S}^\star_+}{|\vec{S}^\star_+|}$, if it does not $\vec{\zeta}_+ = -\frac{\vec{S}^\star_+}{|\vec{S}^\star_+|}$.

Regardless of whether $\vec{\zeta}_+$ is mixed or pure, we insert its value back into Eqs. (5.190)-(5.193), which by rearranging the terms become

$$\begin{aligned} d\bar{W}^\star_0 =& \Big[K_{\frac{2}{3}}(z_p)\frac{\varepsilon^2_+ + \varepsilon^2_-}{\varepsilon_+\varepsilon_-} + \int_{z_p}^{\infty} dx K_{\frac{1}{3}}(x)\Big] + K_{\frac{1}{3}}(z_p)\frac{\omega}{\varepsilon_+}(\vec{\zeta}_+ \cdot \vec{b}) + \\ & \vec{\zeta}_- \cdot \Big\{\Big[\frac{\varepsilon^2_+ + \varepsilon^2_-}{\varepsilon_+\varepsilon_-}\int_{z_p}^{\infty} dx K_{\frac{1}{3}}(x) - K_{\frac{2}{3}}(z_p)\frac{(\varepsilon_+ - \varepsilon_-)^2}{\varepsilon_+\varepsilon_-}\Big](\vec{\zeta}_+ \cdot \hat{v})\hat{v} + \\ & - \Big[2K_{\frac{2}{3}}(z_p) - \int_{z_p}^{\infty} dx K_{\frac{1}{3}}(x)\Big]\vec{\zeta}_+ - K_{\frac{1}{3}}(z_p)\frac{\omega}{\varepsilon_-}\vec{b}\Big\} \end{aligned} \tag{5.210}$$

$$\begin{aligned} d\bar{W}^\star_1 =& K_{\frac{1}{3}}(z_p)\frac{\omega}{\varepsilon_-}(\vec{\zeta}_+ \cdot \vec{s}) + \\ & + \vec{\zeta}_- \cdot \Big\{\frac{(\varepsilon^2_+ - \varepsilon^2_-)}{2\varepsilon_+\varepsilon_-}K_{\frac{2}{3}}(z_p)(\vec{\zeta}_+ \wedge \hat{v}) - K_{\frac{1}{3}}(z_p)\frac{\omega}{\varepsilon_+}\vec{s} + \\ & - \frac{\omega^2}{2\varepsilon_+\varepsilon_-}\int_{z_p}^{\infty} dx K_{\frac{1}{3}}(x)[(\vec{\zeta}_+ \cdot \vec{b})\vec{s} + (\vec{\zeta}_+ \cdot \vec{s})\vec{b}]\Big\} \end{aligned} \tag{5.211}$$

$$\begin{aligned} d\bar{W}^\star_2 =& \Big[\frac{\omega}{\varepsilon_+}\int_{z_p}^{\infty} dx K_{\frac{1}{3}}(x) + K_{\frac{2}{3}}(z_p)\frac{\varepsilon^2_+ - \varepsilon^2_-}{\varepsilon_+\varepsilon_-}\Big](\hat{v} \cdot \vec{\zeta}_+) + \\ & + \vec{\zeta}_- \cdot \Big\{\Big[\frac{\omega}{\varepsilon_-}\int_{z_p}^{\infty} dx K_{\frac{1}{3}}(x) - K_{\frac{2}{3}}(z_p)\frac{\varepsilon^2_+ - \varepsilon^2_-}{\varepsilon_+\varepsilon_-}\Big]\hat{v} + \end{aligned}$$

$$- K_{\frac{1}{3}}(z_p)\Big(\frac{\omega^2}{2\varepsilon_+\varepsilon_-}(\vec{\zeta}_+ \wedge \vec{s}) + \frac{(\varepsilon_+^2 - \varepsilon_-^2)}{2\varepsilon_+\varepsilon_-}[(\vec{\zeta}_+ \cdot \vec{b})\hat{v} + (\vec{\zeta}_+ \cdot \hat{v})\vec{b}]\Big)\Big\} \quad (5.212)$$

$$\begin{aligned} d\bar{W}_3^\star =& - K_{\frac{2}{3}}(z_p) - K_{\frac{1}{3}}(z_p)\frac{\omega}{\varepsilon_-}(\vec{\zeta}_+ \cdot \vec{b}) + \\ &+ \vec{\zeta}_- \cdot \Big\{K_{\frac{2}{3}}(z_p)\Big[\frac{(\varepsilon_+^2 + \varepsilon_-^2)}{2\varepsilon_+\varepsilon_-}\vec{\zeta}_+ - \frac{(\varepsilon_+ - \varepsilon_-)^2}{2\varepsilon_+\varepsilon_-}(\vec{\zeta}_+ \cdot \hat{v})\hat{v}\Big] + \\ &- \frac{\omega^2}{2\varepsilon_+\varepsilon_-}\int_{z_p}^{\infty} dx K_{\frac{1}{3}}(x)[(\vec{\zeta}_+ \cdot \vec{s})\vec{s} - (\vec{\zeta}_+ \cdot \vec{b})\vec{b}] + K_{\frac{1}{3}}(z_p)\frac{\omega}{\varepsilon_+}\vec{b}\Big\}. \end{aligned} \quad (5.213)$$

As we did with eq. (5.204), we rewrite (5.189)-(5.193) in the conventional transition matrix form

$$\frac{dW_{NBW}^{(\xi\zeta_-\zeta_+)}}{d\varepsilon_-} = \frac{\alpha m^2}{4\sqrt{3}\pi\omega^2}(a_-^\star + \vec{\zeta}_- \cdot \vec{S}_-^\star), \quad (5.214)$$

with

$$\begin{aligned} a_0^\star =& \Big[K_{\frac{2}{3}}(z_p)\frac{\varepsilon_+^2 + \varepsilon_-^2}{\varepsilon_+\varepsilon_-} + \int_{z_p}^{\infty} dx K_{\frac{1}{3}}(x)\Big] + K_{\frac{1}{3}}(z_p)\frac{\omega}{\varepsilon_+}(\vec{\zeta}_+ \cdot \vec{b}) + \\ &+ \xi_1 K_{\frac{1}{3}}(z_p)\frac{\omega}{\varepsilon_-}(\vec{\zeta}_+ \cdot \vec{s}) + \xi_2\Big[\frac{\omega}{\varepsilon_+}\int_{z_p}^{\infty} dx K_{\frac{1}{3}}(x) + K_{\frac{2}{3}}(z_p)\frac{\varepsilon_+^2 - \varepsilon_-^2}{\varepsilon_+\varepsilon_-}\Big](\hat{v} \cdot \vec{\zeta}_+) \\ &- \xi_3\Big[K_{\frac{2}{3}}(z_p) + K_{\frac{1}{3}}(z_p)\frac{\omega}{\varepsilon_-}(\vec{\zeta}_+ \cdot \vec{b})\Big], \end{aligned} \quad (5.215)$$

and $\vec{S}_-^\star$ given by

$$\vec{S}_-^\star = \vec{S}_0^\star + \xi_1\vec{S}_1^\star + \xi_2\vec{S}_2^\star + \xi_3\vec{S}_3^\star, \quad (5.216)$$

$$\begin{aligned} \vec{S}_0^\star =& \Big[\frac{\varepsilon_+^2 + \varepsilon_-^2}{\varepsilon_+\varepsilon_-}\int_{z_p}^{\infty} dx K_{\frac{1}{3}}(x) - K_{\frac{2}{3}}(z_p)\frac{(\varepsilon_+ - \varepsilon_-)^2}{\varepsilon_+\varepsilon_-}\Big](\vec{\zeta}_+ \cdot \hat{v})\hat{v} + \\ &- \Big[2K_{\frac{2}{3}}(z_p) - \int_{z_p}^{\infty} dx K_{\frac{1}{3}}(x)\Big]\vec{\zeta}_+ - K_{\frac{1}{3}}(z_p)\frac{\omega}{\varepsilon_-}\vec{b} \end{aligned} \quad (5.217)$$

$$\begin{aligned} \vec{S}_1^\star =& \frac{(\varepsilon_+^2 - \varepsilon_-^2)}{2\varepsilon_+\varepsilon_-}K_{\frac{2}{3}}(z_p)(\vec{\zeta}_+ \wedge \hat{v}) - K_{\frac{1}{3}}(z_p)\frac{\omega}{\varepsilon_+}\vec{s} + \\ &- \frac{\omega^2}{2\varepsilon_+\varepsilon_-}\int_{z_p}^{\infty} dx K_{\frac{1}{3}}(x)[(\vec{\zeta}_+ \cdot \vec{b})\vec{s} + (\vec{\zeta}_+ \cdot \vec{s})\vec{b}] \end{aligned} \quad (5.218)$$

$$\begin{aligned} \vec{S}_2^\star =& \Big[\frac{\omega}{\varepsilon_-}\int_{z_p}^{\infty} dx K_{\frac{1}{3}}(x) - K_{\frac{2}{3}}(z_p)\frac{\varepsilon_+^2 - \varepsilon_-^2}{\varepsilon_+\varepsilon_-}\Big]\hat{v} + \\ &- K_{\frac{1}{3}}(z_p)\Big(\frac{\omega^2}{2\varepsilon_+\varepsilon_-}(\vec{\zeta}_+ \wedge \vec{s}) + \frac{(\varepsilon_+^2 - \varepsilon_-^2)}{2\varepsilon_+\varepsilon_-}[(\vec{\zeta}_+ \cdot \vec{b})\hat{v} + (\vec{\zeta}_+ \cdot \hat{v})\vec{b}]\Big) \end{aligned} \quad (5.219)$$

$$\begin{aligned} \vec{S}_3^\star =& K_{\frac{2}{3}}(z_p)\Big[\frac{(\varepsilon_+^2 + \varepsilon_-^2)}{2\varepsilon_+\varepsilon_-}\vec{\zeta}_+ - \frac{(\varepsilon_+ - \varepsilon_-)^2}{2\varepsilon_+\varepsilon_-}(\vec{\zeta}_+ \cdot \hat{v})\hat{v}\Big] + \\ &- \frac{\omega^2}{2\varepsilon_+\varepsilon_-}\int_{z_p}^{\infty} dx K_{\frac{1}{3}}(x)[(\vec{\zeta}_+ \cdot \vec{s})\vec{s} - (\vec{\zeta}_+ \cdot \vec{b})\vec{b}] + K_{\frac{1}{3}}(z_p)\frac{\omega}{\varepsilon_+}\vec{b}. \end{aligned} \quad (5.220)$$

Finally, from

$$\frac{\left.\frac{dW_{NBW}^{(\xi\zeta-\zeta+)}}{d\varepsilon_-}\right|_{\vec{\zeta}_-=\uparrow} - \left.\frac{dW_{NBW}^{(\xi\zeta-\zeta+)}}{d\varepsilon_-}\right|_{\vec{\zeta}_-=\downarrow}}{\left.\frac{dW_{NBW}^{(\xi\zeta-\zeta+)}}{d\varepsilon_-}\right|_{\vec{\zeta}_-=\uparrow} + \left.\frac{dW_{NBW}^{(\xi\zeta-\zeta+)}}{d\varepsilon_-}\right|_{\vec{\zeta}_-=\downarrow}} = \vec{\zeta}_- \cdot \frac{\vec{S}_-^\star}{a_-^\star} \tag{5.221}$$

we can infer that the final electron's mixed spin state is given by

$$\vec{\zeta}_- = \frac{\vec{S}_-^\star}{a_-^\star}. \tag{5.222}$$

Conversely, to ascertain its pure state counterpart, we must evaluate

$$\frac{\left.\frac{dW_{NBW}^{(\xi\zeta-\zeta+)}}{d\varepsilon_-}\right|_{\vec{\zeta}_-=\uparrow}}{\left.\frac{dW_{NBW}^{(\xi\zeta-\zeta+)}}{d\varepsilon_-}\right|_{\vec{\zeta}_-=\uparrow} + \left.\frac{dW_{NBW}^{(\xi\zeta-\zeta+)}}{d\varepsilon_-}\right|_{\vec{\zeta}_-=\downarrow}} = \frac{a_-^\star + |S_-^\star|}{2a_-^\star} > r_-^\star, \tag{5.223}$$

with $r_-^\star$ another random value drawn from the interval $(0, 1)$. If this condition holds, then $\vec{\zeta}_- = \frac{\vec{S}_-^\star}{|S_-^\star|}$; otherwise $\vec{\zeta}_- = -\frac{\vec{S}_-^\star}{|S_-^\star|}$.

In the new unreleased computational module of `SFQEDtoolkit`, we implemented two functions:

- `function_pola_and_spin_BW_no_angles_mixed_states`,
- `function_pola_and_spin_BW_no_angles_pure_states`.

These functions numerically reproduce the algorithms described above for the mixed and pure spin states, respectively. An example of their application is shown in Figures 5.10 and 5.11, which depict the electron (left) and positron (right) spin curves obtained from the simulation of the NBW decay of a $\omega = 1$ GeV photon in a magnetic field, $\vec{B} = (0, 0, B_z)$, with quantum parameter $\chi_\gamma = 2$. In Figure 5.10, the mixed spin state components of the electron and positron, ζ_{+z} and ζ_{-z}, along $\vec{B}$ are computed using `function_pola_and_spin_BW_no_angles_mixed_states`. Similarly, Figure 5.11 presents the averages of these quantities over multiple pair production processes, obtained in the pure state approach using `function_pola_and_spin_BW_no_angles_pure_states`. In both cases, ζ_{+z} and ζ_{-z} are plotted as functions of the electron-to-photon energy ratio, $\frac{\varepsilon_-}{\omega}$, for different initial polarization component values, ξ_z (indicated by the various curve colors). As in the NIC case, the positron mixed-state curves in Figure 5.10 (right panel) do not align with those in Figure 5.11 [107]. This is another instance of the "dependence problem" we encountered in the previous section. By computing the two leptons' spins independently, i.e., using Eq. (5.208) along with its counterpart obtained via the $+ \leftrightarrow -$ prescription, we can restore the correctness of the results. The `SFQEDtoolkit` addresses this through the advanced routine `function_pola_and_spin_BW_no_angles_mixed_states_independent`, whose results are presented in Figure 5.12. These curves are fully consistent with those in Figure 5.11.

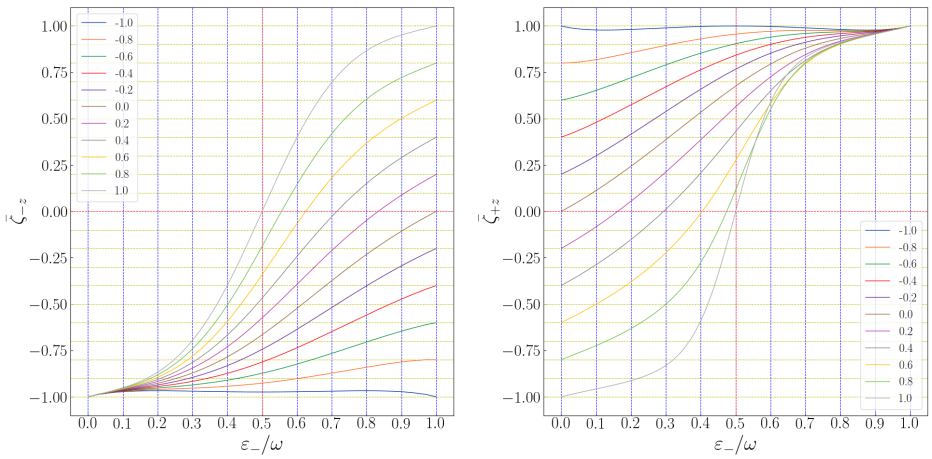

Figure 5.10: Mixed-state spin curves for the electron (ζ_{-z}, left) and positron (ζ_{+z}, right) obtained from the simulation of a 1 GeV photon propagating in a magnetic field, $\vec{B} = (0, 0, B_z)$. Both ζ_{-z} and ζ_{+z} are plotted as functions of the electron-to-photon energy ratio, $\frac{\varepsilon_-}{\omega}$, for various initial polarization component values, ξ_z (specified in the inset and indicated by different colors). The anomalous behavior observed in the positron spin curves arises from its dependence on the electron spin. Important: although in the text we describe a procedure where the positron spin is computed first, followed by the electron's, the routine `function_pola_and_spin_BW_no_angles_mixed_states` performs these calculations in the opposite order. Due to the symmetry of the pair production process, switching between these two approaches is straightforward.

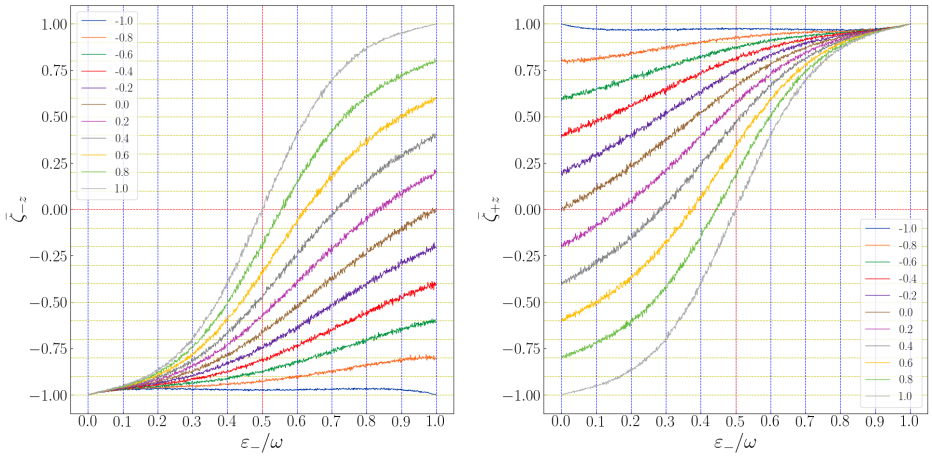

Figure 5.11: As in fig. 5.10, but this time pure states have been employed for characterizing the two leptons' spins. Each data point on the curves represents the average outcome of 10^3 NBW photon emissions with the identical parameters (initial photon polarization ξ, energy ω, quantum parameter χ_γ and electron-to-photon energy ratio $\frac{\varepsilon_-}{\omega}$).

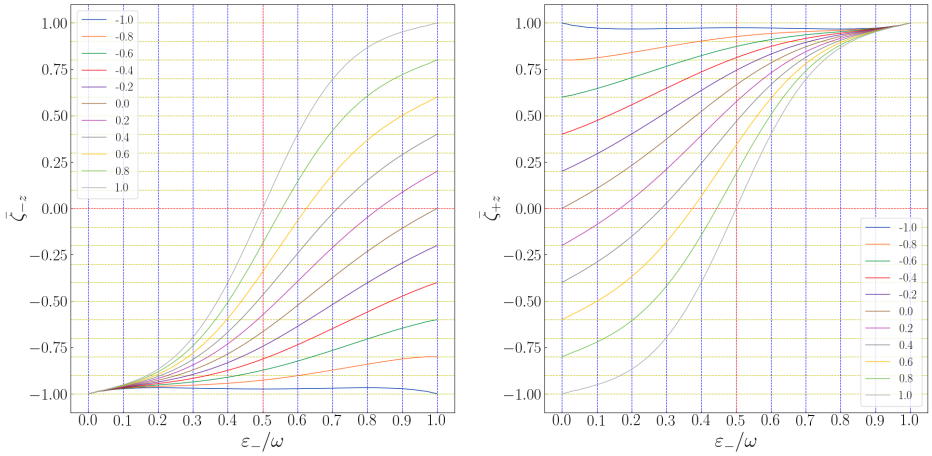

Figure 5.12: As in fig. 5.10. This time the electron and positron SQAs are computed independently from one another. The results are consistent with those in fig. 5.11 and [107].

5.6.2 Internal states for particles with angular resolution

Allowing spin-resolved electrons and positrons, along with polarization-resolved photons, to evolve within PIC and Monte Carlo codes may open up unexplored aspects of plasma physics. The inclusion of new internal degrees of freedom could provide new informations on the dynamics of interactions between matter and electromagnetic fields at high densities and energies. In this section, we address the determination of the internal states of particles whose directional properties have been rigorously characterized according to the methods detailed in Sec. 5.5. The procedures outlined here closely mirror those presented in Secs. 5.6.1 and 5.6.1; however, we now employ the FNIC and FNBW distributions (i.e., Eqs. (5.39)–(5.43) and (5.57)–(5.61)). Henceforth, we assume that the final particles' energies and directions are fully determined and can be treated as constants (see Secs. 5.4 and 5.5 for further details).

Final electron spin and photon polarization after the angular NIC photon emission

As mentioned earlier, the algorithm for determining the final inner states in the NIC process is based on Eqs. (5.39)–(5.43). By summing these equations over the final photon polarization vector $\vec{\xi}$, we obtain the differential probability

$$\frac{dW_{NIC}^{(\zeta\zeta')}}{d\omega d\varphi d\theta} = \frac{\alpha\omega}{2\pi^2}\sqrt{\frac{2}{3}}\lambda^{\frac{1}{2}}\frac{\gamma^3}{\chi_e\varepsilon'}\sin\theta dW_0', \tag{5.224}$$

which we will use to ascertain the final electron's spin. The quantity dW'_0, defined in eq. (5.40), can be reformulated to isolate its dependence on the final spin vector $\vec{\zeta}'$

$$\begin{aligned} dW'_0 = K_{\frac{1}{3}}(\xi_e)\Big[2\lambda\frac{\varepsilon^2+\varepsilon'^2}{\varepsilon\varepsilon'} - \frac{1}{\gamma^2}\Big] + K_{\frac{2}{3}}(\xi_e)\sqrt{2\lambda}\Big[\theta\sin\varphi\frac{\varepsilon^2-\varepsilon'^2}{\varepsilon\varepsilon'}\hat{v} - \frac{\omega}{\gamma\varepsilon}\vec{b}\Big]\cdot\vec{\zeta} + \\ + \vec{\zeta}'\cdot\Big\{K_{\frac{1}{3}}(\xi_e)\Big[\Big(4\lambda - \frac{1}{\gamma^2}\Big)\vec{\zeta} + \frac{\varepsilon^2-\varepsilon'^2}{2\varepsilon\varepsilon'}\frac{\theta}{\gamma}\Big(\sin\varphi(\vec{s}\wedge\vec{\zeta}) - \cos\varphi(\vec{b}\wedge\vec{\zeta})\Big) + \\ + \theta^2\frac{\omega^2}{\varepsilon\varepsilon'}(\vec{\zeta}\cdot\hat{v})\hat{v} - \frac{\omega^2}{2\varepsilon\varepsilon'}\frac{\theta\sin\varphi}{\gamma}\Big((\vec{\zeta}\cdot\hat{v})\vec{b} + (\vec{\zeta}\cdot\vec{b})\hat{v}\Big) + \\ - \frac{\omega^2}{2\varepsilon\varepsilon'}\frac{\theta\cos\varphi}{\gamma}\Big((\vec{\zeta}\cdot\hat{v})\vec{s} + (\vec{\zeta}\cdot\vec{s})\hat{v}\Big)\Big] + \\ + K_{\frac{2}{3}}(\xi_e)\sqrt{2\lambda}\Big[\theta\sin\varphi\frac{\varepsilon^2-\varepsilon'^2}{\varepsilon\varepsilon'}\hat{v} - \frac{\omega}{\gamma\varepsilon'}\vec{b}\Big]\Big\} = \\ = a + \vec{\zeta}'\cdot\vec{S}, \end{aligned} \tag{5.225}$$

where the spin-independent part a was defined in eq. (5.116), and

$$\begin{aligned} \vec{S} = K_{\frac{1}{3}}(\xi_e)\Big[\Big(4\lambda - \frac{1}{\gamma^2}\Big)\vec{\zeta} + \frac{\varepsilon^2-\varepsilon'^2}{2\varepsilon\varepsilon'}\frac{\theta}{\gamma}\Big(\sin\varphi(\vec{s}\wedge\vec{\zeta}) - \cos\varphi(\vec{b}\wedge\vec{\zeta})\Big)\Big] + \\ + K_{\frac{1}{3}}(\xi_e)\frac{\omega^2}{\varepsilon\varepsilon'}\Big[\theta^2(\vec{\zeta}\cdot\hat{v}) - \frac{\theta}{2\gamma}\Big(\sin\varphi(\vec{\zeta}\cdot\vec{b}) + \cos\varphi(\vec{\zeta}\cdot\vec{s})\Big)\Big]\hat{v} + K_{\frac{2}{3}}(\xi_e)\sqrt{2\lambda}\theta\sin\varphi\frac{\varepsilon^2-\varepsilon'^2}{\varepsilon\varepsilon'}\hat{v} + \\ - K_{\frac{1}{3}}(\xi_e)\frac{\omega^2}{2\varepsilon\varepsilon'}\frac{\theta\cos\varphi}{\gamma}(\vec{\zeta}\cdot\hat{v})\vec{s} - K_{\frac{1}{3}}(\xi_e)\frac{\omega^2}{2\varepsilon\varepsilon'}\frac{\theta\sin\varphi}{\gamma}(\vec{\zeta}\cdot\hat{v})\vec{b} - K_{\frac{2}{3}}(\xi_e)\sqrt{2\lambda}\frac{\omega}{\gamma\varepsilon'}\vec{b}. \end{aligned} \tag{5.226}$$

As in sec. 5.6.1 one can proceed in two ways:

- for mixed spin and polarization states, satisfying $|\vec{\zeta}'| \leq 1$ and $|\vec{\xi}| \leq 1$, we start by evaluating the ratio

$$\frac{\frac{dW_{NIC}^{(\zeta\zeta')}}{d\omega d\varphi d\theta}\Big|_{\vec{\zeta}'=\uparrow} - \frac{dW_{NIC}^{(\zeta\zeta')}}{d\omega d\varphi d\theta}\Big|_{\vec{\zeta}'=\downarrow}}{\frac{dW_{NIC}^{(\zeta\zeta')}}{d\omega d\varphi d\theta}\Big|_{\vec{\zeta}'=\uparrow} + \frac{dW_{NIC}^{(\zeta\zeta')}}{d\omega d\varphi d\theta}\Big|_{\vec{\zeta}'=\downarrow}} = \frac{dW'_0\Big|_{\vec{\zeta}'=\uparrow} - dW'_0\Big|_{\vec{\zeta}'=\downarrow}}{dW'_0\Big|_{\vec{\zeta}'=\uparrow} + dW'_0\Big|_{\vec{\zeta}'=\downarrow}} = \vec{\zeta}'\cdot\frac{\vec{S}}{a}, \tag{5.227}$$

  which ultimately allows us to identify the Spin Quantization Axis (SQA) as

$$\vec{\zeta}' = \frac{\vec{S}}{a}. \tag{5.228}$$

  Subsequently, we substitute Eq. (5.228) back into the system of Eqs. (5.39)–(5.43), which can then be rewritten as

$$\frac{dW_{NIC}^{(\zeta\zeta'\xi)}}{d\omega d\Omega} = C_{NIC}(a + \vec{\zeta}'\cdot\vec{S} + \vec{\xi}\cdot\vec{P}), \tag{5.229}$$

in which we set

$$\vec{P} = (dW'_1, dW'_2, dW'_3). \tag{5.230}$$

Following the same approach as for the SQA, we then assess the ratio

$$\frac{\frac{dW_{NIC}^{(\zeta\zeta'\xi)}}{d\omega d\Omega}\Big|_{\vec{\xi}=\uparrow} - \frac{dW_{NIC}^{(\zeta\zeta'\xi)}}{d\omega d\Omega}\Big|_{\vec{\xi}=\downarrow}}{\frac{dW_{NIC}^{(\zeta\zeta'\xi)}}{d\omega d\Omega}\Big|_{\vec{\xi}=\uparrow} + \frac{dW_{NIC}^{(\zeta\zeta'\xi)}}{d\omega d\Omega}\Big|_{\vec{\xi}=\downarrow}} = \vec{\xi} \cdot \frac{\vec{P}}{a + \vec{\zeta}' \cdot \vec{S}} \tag{5.231}$$

which leads to the following PQA

$$\vec{\xi} = \frac{\vec{P}}{a + \vec{\zeta}' \cdot \vec{S}}. \tag{5.232}$$

However, in light of the "dependence problem" already introduced in sec. 5.6.1, we also provide an expression for the PQA which is independent of the final electron spin. Starting from Eq. (5.39) and summing over the ζ' states, we obtain

$$\frac{dW_{NIC}^{(\zeta\xi)}}{d\omega d\varphi d\theta} = \frac{\alpha\omega}{2\pi^2}\sqrt{\frac{2}{3}}\lambda^{\frac{1}{2}}\frac{\gamma^3}{\chi_e\varepsilon'}\sin\theta(a + \vec{\xi}\cdot\vec{h}), \tag{5.233}$$

with

$$h_1 = K_{\frac{1}{3}}(\xi_e)\theta^2\sin 2\varphi + K_{\frac{2}{3}}(\xi_e)\sqrt{2\lambda}\frac{\omega}{\gamma\varepsilon'}(\vec{\zeta}\cdot\vec{s}) \tag{5.234}$$

$$h_2 = K_{\frac{1}{3}}(\xi_e)\Big[\Big(2\lambda\frac{\varepsilon^2 - \varepsilon'^2}{\varepsilon\varepsilon'} - \frac{\omega}{\gamma^2\varepsilon}\Big)\hat{v} - \frac{\theta\omega}{\gamma\varepsilon}(\sin\varphi\vec{b} + \cos\varphi\vec{s})\Big]\cdot\vec{\zeta} + K_{\frac{2}{3}}(\xi_e)\sqrt{2\lambda}\theta\sin\varphi\frac{\varepsilon^2 + \varepsilon'^2}{\varepsilon\varepsilon'} \tag{5.235}$$

$$h_3 = K_{\frac{1}{3}}(\xi_e)(\theta^2\cos 2\varphi + 2\lambda) - K_{\frac{2}{3}}(\xi_e)\sqrt{2\lambda}\frac{\omega}{\gamma\varepsilon'}(\vec{\zeta}\cdot\vec{b}). \tag{5.236}$$

Following reasoning similar to that leading to Eq. (5.228), we can then define an alternative PQA as

$$\vec{\xi} = \frac{\vec{h}}{a}. \tag{5.237}$$

- for pure states, on the other side, we first draw two random numbers ($0 \leq r_{\zeta'}, r_\xi \leq 1$) and then evaluate the conditions

$$\frac{\frac{dW_{NIC}^{(\zeta\zeta')}}{d\omega d\varphi d\theta}\Big|_{\vec{\zeta}'=\uparrow}}{\frac{dW_{NIC}^{(\zeta\zeta')}}{d\omega d\varphi d\theta}\Big|_{\vec{\zeta}'=\uparrow} + \frac{dW_{NIC}^{(\zeta\zeta')}}{d\omega d\varphi d\theta}\Big|_{\vec{\zeta}'=\downarrow}} = \frac{a + |S|}{2a} > r_{\zeta'} \tag{5.238}$$

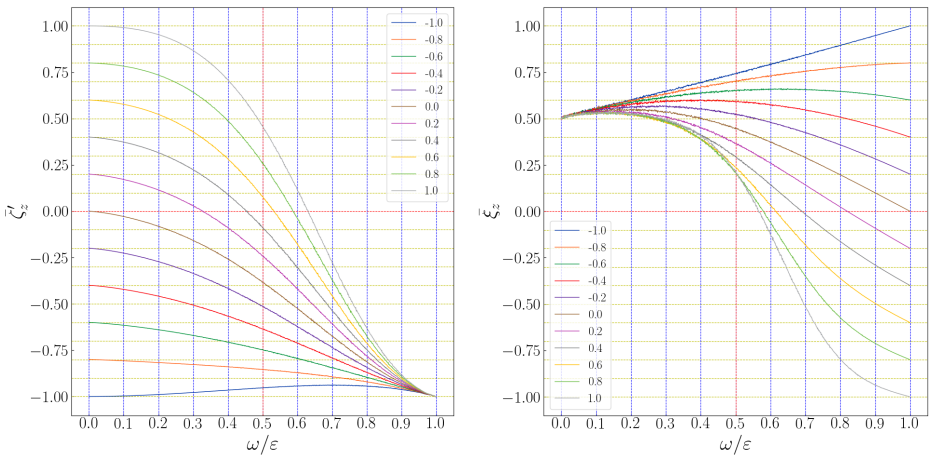

Figure 5.13: Mixed-state curves for electron spin (ζ'_z, left) and photon polarization (ξ_z, right) were generated by simulating a 1 GeV electron moving in a magnetic field, $\vec{B} = (0, 0, B_z)$. Each NIC emission is repeated 10^4 times, with each repetition emitting a photon in a different direction (as described in Sec. 5.5.1) while maintaining the same photon-to-electron energy ratio, $\frac{\omega}{\varepsilon}$. The resulting values of ζ'_z and ξ_z are averaged over these emissions and plotted as functions of $\frac{\omega}{\varepsilon}$ for various initial spin component values, ζ' (specified in the inset and indicated by different colors). The anomalous behavior observed in the polarization curve arises from both its dependence on the spin value and the fact the states are not physical.

and

$$\frac{\left.\frac{dW_{NIC}^{(\zeta\zeta'\xi)}}{d\omega d\Omega}\right|_{\vec{\xi}=\uparrow}}{\left.\frac{dW_{NIC}^{(\zeta\zeta'\xi)}}{d\omega d\Omega}\right|_{\vec{\xi}=\uparrow} + \left.\frac{dW_{NIC}^{(\zeta\zeta'\xi)}}{d\omega d\Omega}\right|_{\vec{\xi}=\downarrow}} = \frac{a + \vec{\zeta}' \cdot \vec{S} + |P|}{2(a + \vec{\zeta}' \cdot \vec{S})} > r_\xi, \tag{5.239}$$

one after the other (notice that eq. (5.239) depends on the value of $\vec{\zeta}'$ explicitely). If they hold, then $\vec{\zeta}' = \frac{\vec{S}}{|S|}$ and $\vec{\xi} = \frac{\vec{P}}{|P|}$, otherwise $\vec{\zeta}' = -\frac{\vec{S}}{|S|}$ and $\vec{\xi} = -\frac{\vec{P}}{|P|}$.

In `SFQEDtoolkit` we have made available three routines:

- `function_spin_and_pola_angles_mixed_states`
- `function_spin_and_pola_angles_mixed_states_independent`
- `function_spin_and_pola_angles_pure_states`

which replicate the algorithms for mixed and pure states discussed above. We combined them with the functions introduced at the end of Sec. 5.5.1 to generate the photon emission angles. To test the implementation, we set up a simulation in

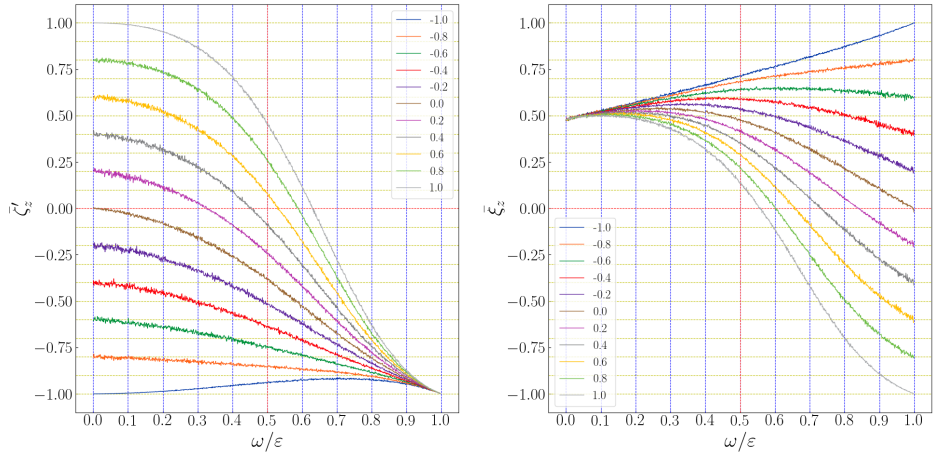

Figure 5.14: Similar to Figure 5.13, but in this case pure-states were used: each emission along a given direction is repeated 10^3 times (with the same parameters), and the outcomes are averaged accordingly.

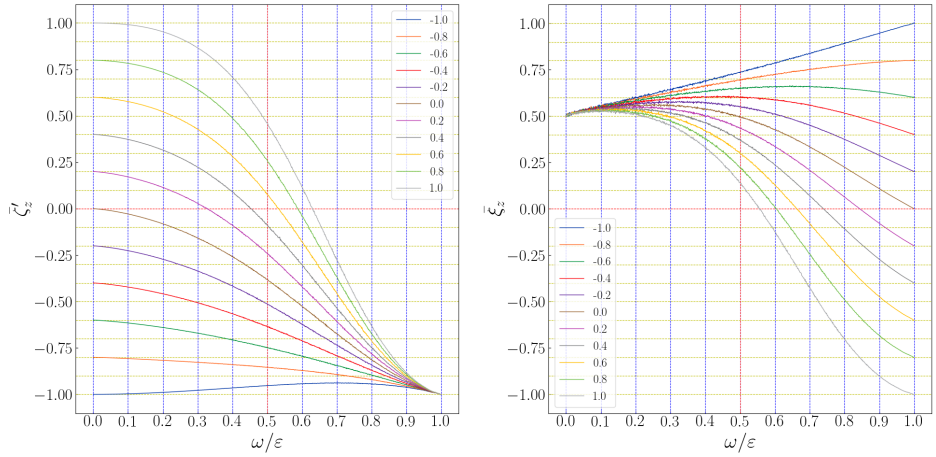

Figure 5.15: As in Fig. 5.13, but with the SQA and PQA computed independently. The results appear consistent with those in Sec. 5.6.1, which correspond to the angle-unresolved NIC emission process. However, most of the spin and polarization states are, in fact, non-physical.

which an electron, moving in a magnetic field $\vec{B} = (0, 0, B_z)$ with energy $\varepsilon = 1$ GeV and quantum parameter $\chi_e = 2$, is forced to emit photons via NIC.

Specifically, the electron is made to emit a photon 10^4 times, each emission occurring in a different direction but with the same photon-to-electron energy ratio $\frac{\omega}{\varepsilon}$. The final spin ($\zeta_z'$) and polarization ($\xi_z$) components along the magnetic field are then averaged over these emissions. By repeating this process for all possible $\frac{\omega}{\varepsilon}$ ratios and several values of the initial spin projection ζ_z, we obtained the spin-

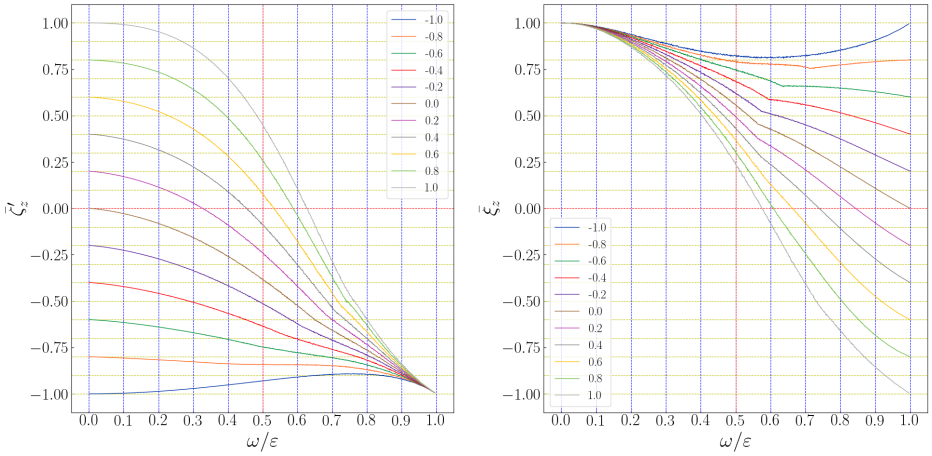

Figure 5.16: As in fig. 5.15, but rejecting all the non-physical states.

and polarization-photon energy curves shown in Figs. 5.13–5.15. Surprisingly, only the independent mixed-state results from Fig. 5.15 appear to agree with the angle-unresolved curves in Fig. 5.9 [107]. In addition to the usual "dependence problem" observed in the right panel of Fig. 5.13, this time even the pure-state curves in Fig. 5.14 appear slightly shifted from those in fig. 5.8. As a matter of fact, a more detailed analysis reveals that the magnitudes of some of the computed spin and polarization states (determined via Eqs. (5.228), (5.232) and (5.237)) can exceed unity:

$$|\vec{\zeta}'| > 1 \quad \text{and} \quad |\vec{\xi}| > 1. \tag{5.240}$$

Unfortunately, rejecting the states that satisfy (5.240) is not a valid solution, as the corresponding curves would transform into those portrayed in Figs. 5.16. This discrepancy points to an underlying ill-defined negative differential probability, which will be discussed in Section 5.7.

Final electron and positron spin after the angular NBW pair production

If the NBW process generates positrons and electrons in accordance with the angular distribution described in Section 5.5.2, then the following method is appropriate for determining their spins. The algorithm starts by summing the FNBW distribution described in (5.57)-(5.61) over the final positron's spin states ζ_+, yielding

$$\frac{dW_{NBW}^{(\xi\zeta_-)}}{d\theta d\varphi d\varepsilon_-} = \frac{\alpha}{2\pi^2}\sqrt{\frac{2}{3}}\lambda_-^{\frac{1}{2}}\frac{\gamma_-^3}{\chi_\gamma} sin\theta(d\bar{W}_0^- + \xi_1 d\bar{W}_1^- + \xi_2 d\bar{W}_2^- + \xi_3 d\bar{W}_3^-) \tag{5.241}$$

with

$$d\bar{W}_0^- = K_{\frac{1}{3}}(\xi_\gamma)\Big\{\frac{\omega^2}{2\varepsilon_+^2\gamma_-^2} + \Big(4\lambda_- - \frac{1}{\gamma_-^2}\Big)\frac{\varepsilon_+^2+\varepsilon_-^2}{2\varepsilon_+^2}\Big\}+$$

$$- K_{\frac{2}{3}}(\xi_\gamma)\sqrt{2\lambda_-}\vec{\zeta}_-\cdot\Big\{\frac{\omega}{\varepsilon_+\gamma_-}\vec{b}-\theta\sin\varphi\frac{\varepsilon_+^2-\varepsilon_-^2}{\varepsilon_+^2}\hat{v}\Big\}, \tag{5.242}$$

$$d\bar{W}_1^- = - K_{\frac{1}{3}}(\xi_\gamma)\theta^2\sin 2\varphi\frac{\varepsilon_-}{\varepsilon_+} - K_{\frac{2}{3}}(\xi_\gamma)\sqrt{2\lambda_-}\frac{\omega\varepsilon_-}{\varepsilon_+^2\gamma_-}(\vec{\zeta}_-\cdot\vec{s}), \tag{5.243}$$

$$\begin{aligned} d\bar{W}_2^- =& K_{\frac{1}{3}}(\xi_\gamma)\Big[\Big(\frac{\omega}{\varepsilon_+\gamma_-^2}-2\lambda_-\frac{\varepsilon_+^2-\varepsilon_-^2}{\varepsilon_+^2}\Big)\hat{v}+\frac{\omega}{\varepsilon_+\gamma_-}\theta(\sin\varphi\vec{b}+\cos\varphi\vec{s})\Big]\cdot\vec{\zeta}_-+ \\ & - K_{\frac{2}{3}}(\xi_\gamma)\sqrt{2\lambda_-}\theta\sin\varphi\frac{\varepsilon_+^2+\varepsilon_-^2}{\varepsilon_+^2}, \end{aligned} \tag{5.244}$$

$$d\bar{W}_3^- = - K_{\frac{1}{3}}(\xi_\gamma)\frac{\varepsilon_-}{\varepsilon_+}(\theta^2\cos 2\varphi+2\lambda_-) + K_{\frac{2}{3}}(\xi_\gamma)\sqrt{2\lambda_-}\frac{\omega\varepsilon_-}{\varepsilon_+^2\gamma_-}(\vec{\zeta}_-\cdot\vec{b}); \tag{5.245}$$

we immediately recast this quantity in the usual transition probability form

$$\frac{dW_{NBW}^{(\xi\zeta_-)}}{d\theta d\varphi d\varepsilon_-} = \frac{\alpha}{2\pi^2}\sqrt{\frac{2}{3}}\lambda_-^{\frac{1}{2}}\frac{\gamma_-^3}{\chi_\gamma}sin\theta(a_-+\vec{\zeta}_-\cdot\vec{S}_-), \tag{5.246}$$

where we defined

$$\begin{aligned} a_- =& K_{\frac{1}{3}}(\xi_\gamma)\Big\{\frac{\omega^2}{2\varepsilon_+^2\gamma_-^2}+\Big(4\lambda_--\frac{1}{\gamma_-^2}\Big)\frac{\varepsilon_+^2+\varepsilon_-^2}{2\varepsilon_+^2}-\frac{\varepsilon_-}{\varepsilon_+}\Big[\xi_1\theta^2\sin 2\varphi+\xi_3(\theta^2\cos 2\varphi+2\lambda_-)\Big]\Big\}+ \\ & - K_{\frac{2}{3}}(\xi_\gamma)\sqrt{2\lambda_-}\xi_2\theta\sin\varphi\frac{\varepsilon_+^2+\varepsilon_-^2}{\varepsilon_+^2} \end{aligned} \tag{5.247}$$

$$\begin{aligned} \vec{S}_- =& K_{\frac{1}{3}}(\xi_\gamma)\xi_2\Big[\Big(\frac{\omega}{\varepsilon_+\gamma_-^2}-2\lambda_-\frac{\varepsilon_+^2-\varepsilon_-^2}{\varepsilon_+^2}\Big)\hat{v}+\frac{\omega}{\varepsilon_+\gamma_-}\theta(\sin\varphi\vec{b}+\cos\varphi\vec{s})\Big]+ \\ & + K_{\frac{2}{3}}(\xi_\gamma)\sqrt{2\lambda_-}\Big\{-\frac{\omega}{\varepsilon_+\gamma_-}\vec{b}+\theta\sin\varphi\frac{\varepsilon_+^2-\varepsilon_-^2}{\varepsilon_+^2}\hat{v}+\frac{\omega\varepsilon_-}{\varepsilon_+^2\gamma_-}(\xi_3\vec{b}-\xi_1\vec{s})\Big\}. \end{aligned} \tag{5.248}$$

Then we apply the "$+\leftrightarrow-$" prescription to retrieve the positron differential distribution equivalent to Eqs. (5.246)-(5.248), i.e.,

$$\frac{dW_{NBW}^{(\xi\zeta_+)}}{d\theta d\varphi d\varepsilon_+} = \frac{\alpha}{2\pi^2}\sqrt{\frac{2}{3}}\lambda_+^{\frac{1}{2}}\frac{\gamma_+^3}{\chi_\gamma}sin\theta(a_++\vec{\zeta}_+\cdot\vec{S}_+), \tag{5.249}$$

where

$$\begin{aligned} a_+ =& K_{\frac{1}{3}}(\xi_\gamma)\Big\{\frac{\omega^2}{2\varepsilon_-^2\gamma_+^2}+\Big(4\lambda_+-\frac{1}{\gamma_+^2}\Big)\frac{\varepsilon_+^2+\varepsilon_-^2}{2\varepsilon_-^2}-\frac{\varepsilon_+}{\varepsilon_-}\Big[\xi_1\theta^2\sin 2\varphi+\xi_3(\theta^2\cos 2\varphi+2\lambda_+)\Big]\Big\}+ \\ & - K_{\frac{2}{3}}(\xi_\gamma)\sqrt{2\lambda_+}\xi_2\theta\sin\varphi\frac{\varepsilon_+^2+\varepsilon_-^2}{\varepsilon_-^2}. \end{aligned} \tag{5.250}$$

$$\vec{S}_+ = K_{\frac{1}{3}}(\xi_\gamma)\xi_2\Big[\Big(\frac{\omega}{\varepsilon_-\gamma_+^2} + 2\lambda_+\frac{\varepsilon_+^2-\varepsilon_-^2}{\varepsilon_-^2}\Big)\hat{v} + \frac{\omega}{\varepsilon_-\gamma_+}\theta(\sin\varphi\vec{b} + \cos\varphi\vec{s})\Big] + \\ + K_{\frac{2}{3}}(\xi_\gamma)\sqrt{2\lambda_+}\Big\{-\frac{\omega}{\varepsilon_-\gamma_+}\vec{b} - \theta\sin\varphi\frac{\varepsilon_+^2-\varepsilon_-^2}{\varepsilon_-^2}\hat{v} + \frac{\omega\varepsilon_+}{\varepsilon_-^2\gamma_+}(\xi_3\vec{b} - \xi_1\vec{s})\Big\}. \tag{5.251}$$

As done multiple times before, the positron's mixed spin state is defined as

$$\vec{\zeta}_+ = \frac{\vec{S}_+}{a_+}; \tag{5.252}$$

whereas, to determine its pure spin state, we must verify whether the inequality

$$\frac{\frac{dW_{NBW}^{(\xi\zeta_+)}}{d\theta d\varphi d\varepsilon_+}\Big|_{\vec{\zeta}_+=\uparrow}}{\frac{dW_{NBW}^{(\xi\zeta_+)}}{d\theta d\varphi d\varepsilon_+}\Big|_{\vec{\zeta}_+=\uparrow} + \frac{dW_{NBW}^{(\xi\zeta_+)}}{d\theta d\varphi d\varepsilon_+}\Big|_{\vec{\zeta}_+=\downarrow}} = \frac{a_+ + |S_+|}{2a_+} > r_+ \tag{5.253}$$

is satisfied (r_+ is a random number uniformly distributed in $0 \leq r_+ \leq 1$). If the condition holds, the positron's spin is assigned as $\vec{\zeta}_+ = \frac{\vec{S}_+}{|S_+|}$; otherwise, it is set to $\vec{\zeta}_+ = -\frac{\vec{S}_+}{|S_+|}$. It is important to note that the values of θ, φ, $\hat{v}$, $\vec{s}$ and $\vec{b}$, which appear in (5.246)-(5.248) and (5.249)-(5.251), are species-specific. Although not explicitly stated, they are inherently updated according to the prescription above. However, once assigned, these values remain unchanged throughout the application of (5.252) and (5.253).

With the purpose of extracting the final electron spin $\vec{\zeta}_-$, we rewrite (5.58)-(5.61) in such a way that their coupling to $\vec{\zeta}_-$ is made manifest

$$d\bar{W}'_0 = K_{\frac{1}{3}}(\xi_\gamma)\Big[\frac{\omega^2}{2\varepsilon_+^2\gamma_-^2} + \Big(4\lambda_- - \frac{1}{\gamma_-^2}\Big)\frac{\varepsilon_+^2+\varepsilon_-^2}{2\varepsilon_+^2}\Big] + \\ + K_{\frac{2}{3}}(\xi_\gamma)\sqrt{2\lambda_-}\Big[\frac{\omega\varepsilon_-}{\varepsilon_+^2\gamma_-}(\vec{\zeta}_+\cdot\vec{b}) - \theta\sin\varphi\frac{(\varepsilon_+^2-\varepsilon_-^2)}{\varepsilon_+^2}(\vec{\zeta}_+\cdot\hat{v})\Big] + \\ + \vec{\zeta}_-\cdot\Big\{K_{\frac{1}{3}}(\xi_\gamma)\Big[-\Big(4\lambda_- - \frac{1}{\gamma_-^2}\Big)\frac{\varepsilon_-}{\varepsilon_+}\vec{\zeta}_+ + \frac{\omega^2}{2\varepsilon_+^2\gamma_-}\theta\Big(\sin\varphi(\vec{\zeta}_+\wedge\vec{s}) - \cos\varphi(\vec{\zeta}_+\wedge\vec{b})\Big) + \\ + \frac{(\varepsilon_+^2-\varepsilon_-^2)}{2\varepsilon_+^2}\frac{\theta}{\gamma_-}\Big(\cos\varphi[(\vec{\zeta}_+\cdot\vec{s})\hat{v} + (\vec{\zeta}_+\cdot\hat{v})\vec{s}] + \sin\varphi[(\vec{\zeta}_+\cdot\vec{b})\hat{v} + (\vec{\zeta}_+\cdot\hat{v})\vec{b}]\Big) + \\ + \Big(\frac{\omega^2}{2\varepsilon_+^2\gamma_-^2} - [4\lambda_- - \frac{1}{\gamma_-^2}]\frac{(\varepsilon_+-\varepsilon_-)^2}{2\varepsilon_+^2}\Big)(\vec{\zeta}_+\cdot\hat{v})\hat{v}\Big] + \\ - K_{\frac{2}{3}}(\xi_\gamma)\sqrt{2\lambda_-}\Big[\frac{\omega}{\varepsilon_+\gamma_-}\vec{b} - \theta\sin\varphi\frac{\varepsilon_+^2-\varepsilon_-^2}{\varepsilon_+^2}\hat{v}\Big]\Big\} \tag{5.254}$$

$$d\bar{W}'_1 = -K_{\frac{1}{3}}(\xi_\gamma)\theta^2\sin 2\varphi\frac{\varepsilon_-}{\varepsilon_+} + K_{\frac{2}{3}}(\xi_\gamma)\sqrt{2\lambda_-}\frac{\omega}{\varepsilon_+\gamma_-}(\vec{\zeta}_+\cdot\vec{s}) +$$

$$+\vec{\zeta}_-\cdot\Big\{K_{\frac{1}{3}}(\xi_\gamma)\Big[\theta^2\sin 2\varphi\Big(\frac{\varepsilon_+^2+\varepsilon_-^2}{2\varepsilon_+^2}\vec{\zeta}_+-\frac{(\varepsilon_+-\varepsilon_-)^2}{2\varepsilon_+^2}(\vec{\zeta}_+\cdot\hat{v})\hat{v}\Big)+$$
$$-\frac{\omega^2}{2\varepsilon_+^2\gamma_-^2}[(\vec{\zeta}_+\cdot\vec{b})\vec{s}+(\vec{\zeta}_+\cdot\vec{s})\vec{b}]+\frac{\omega^2}{2\varepsilon_+^2\gamma_-}\theta[\sin\varphi(\vec{\zeta}_+\wedge\vec{b})-\cos\varphi(\vec{\zeta}_+\wedge\vec{s})]+$$
$$+\frac{\varepsilon_+^2-\varepsilon_-^2}{2\varepsilon_+^2}(\theta^2\cos 2\varphi+2\lambda_-)(\vec{\zeta}_+\wedge\hat{v})+$$
$$+\frac{(\varepsilon_+^2-\varepsilon_-^2)}{2\varepsilon_+^2}\frac{\theta}{\gamma_-}\Big(\sin\varphi[(\vec{\zeta}_+\cdot\vec{s})\hat{v}+(\vec{\zeta}_+\cdot\hat{v})\vec{s}]+\cos\varphi[(\vec{\zeta}_+\cdot\vec{b})\hat{v}+(\vec{\zeta}_+\cdot\hat{v})\vec{b}]\Big)\Big]+$$
$$-K_{\frac{2}{3}}(\xi_\gamma)\sqrt{2\lambda_-}\frac{\omega\varepsilon_-}{\varepsilon_+^2\gamma_-}\vec{s}\Big\} \tag{5.255}$$

$$d\bar{W}_2'=K_{\frac{1}{3}}(\xi_\gamma)\Big[\Big(\frac{\omega\varepsilon_-}{\varepsilon_+^2\gamma_-^2}+2\lambda_-\frac{\varepsilon_+^2-\varepsilon_-^2}{\varepsilon_+^2}\Big)\hat{v}-\frac{\theta\varepsilon_-}{\varepsilon_+^2}\frac{\omega}{\gamma_-}(\sin\varphi\vec{b}+\cos\varphi\vec{s})\Big]\cdot\vec{\zeta}_+ +$$
$$-K_{\frac{2}{3}}(\xi_\gamma)\sqrt{2\lambda_-}\theta\sin\varphi\frac{\varepsilon_+^2+\varepsilon_-^2}{\varepsilon_+^2}+$$
$$+\vec{\zeta}_-\cdot\Big\{K_{\frac{1}{3}}(\xi_\gamma)\Big[\Big(\frac{\omega}{\varepsilon_+\gamma_-^2}-2\lambda_-\frac{\varepsilon_+^2-\varepsilon_-^2}{\varepsilon_+^2}\Big)\hat{v}+\frac{\theta}{\varepsilon_+}\frac{\omega}{\gamma_-}(\sin\varphi\vec{b}+\cos\varphi\vec{s})\Big]+$$
$$+K_{\frac{2}{3}}(\xi_\gamma)\sqrt{2\lambda_-}\Big[\theta\sin\varphi\Big(\frac{2\varepsilon_-}{\varepsilon_+}\vec{\zeta}_++\frac{(\varepsilon_+-\varepsilon_-)^2}{\varepsilon_+^2}(\vec{\zeta}_+\cdot\hat{v})\hat{v}\Big)+$$
$$-\frac{1}{2\gamma_-}\Big(\frac{\omega^2}{\varepsilon_+^2}(\vec{\zeta}_+\wedge\vec{s})+\frac{\varepsilon_+^2-\varepsilon_-^2}{\varepsilon_+^2}[(\vec{\zeta}_+\cdot\vec{b})\hat{v}+(\vec{\zeta}_+\cdot\hat{v})\vec{b}]\Big)\Big]\Big\} \tag{5.256}$$

$$d\bar{W}_3'=-K_{\frac{1}{3}}(\xi_\gamma)\frac{\varepsilon_-}{\varepsilon_+}(\theta^2\cos 2\varphi+2\lambda_-)-K_{\frac{2}{3}}(\xi_\gamma)\sqrt{2\lambda_-}\frac{\omega}{\varepsilon_+\gamma_-}(\vec{\zeta}_+\cdot\vec{b})+$$
$$+\vec{\zeta}_-\cdot\Big\{K_{\frac{1}{3}}(\xi_\gamma)\Big[\Big(\frac{\varepsilon_+^2+\varepsilon_-^2}{2\varepsilon_+^2}\vec{\zeta}_+-\frac{(\varepsilon_+-\varepsilon_-)^2}{2\varepsilon_+^2}(\vec{\zeta}_+\cdot\hat{v})\hat{v}\Big)(\theta^2\cos 2\varphi+2\lambda_-)+$$
$$+\Big(\frac{\theta\omega^2}{2\varepsilon_+^2\gamma_-}[\sin\varphi(\vec{\zeta}_+\wedge\vec{s})+\cos\varphi(\vec{\zeta}_+\wedge\vec{b})]-\theta^2\sin 2\varphi\frac{\varepsilon_+^2-\varepsilon_-^2}{2\varepsilon_+^2}(\vec{\zeta}_+\wedge\hat{v})\Big)+$$
$$+\frac{\varepsilon_+^2-\varepsilon_-^2}{2\varepsilon_+^2}\frac{\theta}{\gamma_-}\Big(\cos\varphi[(\vec{\zeta}_+\cdot\vec{s})\hat{v}+(\vec{\zeta}_+\cdot\hat{v})\vec{s}]-\sin\varphi[(\vec{\zeta}_+\cdot\vec{b})\hat{v}+(\vec{\zeta}_+\cdot\hat{v})\vec{b}]\Big)$$
$$-\frac{\omega^2}{2\varepsilon_+^2\gamma_-^2}[(\vec{\zeta}_+\cdot\vec{s})\vec{s}-(\vec{\zeta}_+\cdot\vec{b})\vec{b}]\Big]+$$
$$+K_{\frac{2}{3}}(\xi_\gamma)\sqrt{2\lambda_-}\frac{\omega\varepsilon_-}{\varepsilon_+^2\gamma_-}\vec{b}\Big\}, \tag{5.257}$$

so that eq. (5.57) can be recasted into its transition probability form

$$\frac{dW_{NBW}^{(\xi\zeta_-\zeta_+)}}{d\varepsilon_-d\Omega}=C_{BW}(d\bar{W}_0'+\xi_1d\bar{W}_1'+\xi_2d\bar{W}_2'+\xi_3d\bar{W}_3')=$$

$$= C_{BW}(a'_- + \vec{\zeta}_- \cdot \vec{S}'_-), \tag{5.258}$$

where

$$\begin{aligned}
a'_- =& K_{\frac{1}{3}}(\xi_\gamma)\Big\{\frac{\omega^2}{2\varepsilon_+^2\gamma_-^2} + \Big(4\lambda_- - \frac{1}{\gamma_-^2}\Big)\frac{\varepsilon_+^2+\varepsilon_-^2}{2\varepsilon_+^2} - \frac{\varepsilon_-}{\varepsilon_+}\Big[\xi_1\theta^2\sin 2\varphi + \xi_3(\theta^2\cos 2\varphi + 2\lambda_-)\Big]+ \\
&+ \xi_2\Big[\Big(\frac{\omega\varepsilon_-}{\varepsilon_+^2\gamma_-^2} + 2\lambda_-\frac{\varepsilon_+^2-\varepsilon_-^2}{\varepsilon_+^2}\Big)(\vec{\zeta}_+\cdot\hat{v}) - \frac{\theta\varepsilon_-}{\varepsilon_+^2}\frac{\omega}{\gamma_-}(\sin\varphi(\vec{\zeta}_+\cdot\vec{b}) + \cos\varphi(\vec{\zeta}_+\cdot\vec{s}))\Big]\Big\}+ \\
&+ K_{\frac{2}{3}}(\xi_\gamma)\sqrt{2\lambda_-}\Big\{\frac{\omega\varepsilon_-}{\varepsilon_+^2\gamma_-}(\vec{\zeta}_+\cdot\vec{b}) - \theta\sin\varphi\frac{(\varepsilon_+^2-\varepsilon_-^2)}{\varepsilon_+^2}(\vec{\zeta}_+\cdot\hat{v}) + \xi_1\frac{\omega}{\varepsilon_+\gamma_-}(\vec{\zeta}_+\cdot\vec{s})+ \\
&- \xi_2\theta\sin\varphi\frac{\varepsilon_+^2+\varepsilon_-^2}{\varepsilon_+^2} - \xi_3\frac{\omega}{\varepsilon_+\gamma_-}(\vec{\zeta}_+\cdot\vec{b})\Big\}
\end{aligned} \tag{5.259}$$

and

$$\vec{S}'_- = \vec{S}_0 + \xi_1\vec{S}_1 + \xi_2\vec{S}_2 + \xi_3\vec{S}_3, \tag{5.260}$$

$$\begin{aligned}
\vec{S}_0 =& K_{\frac{1}{3}}(\xi_\gamma)\Big[-\Big(4\lambda_- - \frac{1}{\gamma_-^2}\Big)\frac{\varepsilon_-}{\varepsilon_+}\vec{\zeta}_+ + \frac{\omega^2}{2\varepsilon_+^2\gamma_-}\theta\Big(\sin\varphi(\vec{\zeta}_+\wedge\vec{s}) - \cos\varphi(\vec{\zeta}_+\wedge\vec{b})\Big)+ \\
&+ \frac{(\varepsilon_+^2-\varepsilon_-^2)}{2\varepsilon_+^2}\frac{\theta}{\gamma_-}\Big(\cos\varphi[(\vec{\zeta}_+\cdot\vec{s})\hat{v} + (\vec{\zeta}_+\cdot\hat{v})\vec{s}] + \sin\varphi[(\vec{\zeta}_+\cdot\vec{b})\hat{v} + (\vec{\zeta}_+\cdot\hat{v})\vec{b}]\Big)+ \\
&+ \Big(\frac{\omega^2}{2\varepsilon_+^2\gamma_-^2} - [4\lambda_- - \frac{1}{\gamma_-^2}]\frac{(\varepsilon_+-\varepsilon_-)^2}{2\varepsilon_+^2}\Big)(\vec{\zeta}_+\cdot\hat{v})\hat{v}\Big]+ \\
&- K_{\frac{2}{3}}(\xi_\gamma)\sqrt{2\lambda_-}\Big[\frac{\omega}{\varepsilon_+\gamma_-}\vec{b} - \theta\sin\varphi\frac{\varepsilon_+^2-\varepsilon_-^2}{\varepsilon_+^2}\hat{v}\Big]
\end{aligned} \tag{5.261}$$

$$\begin{aligned}
\vec{S}_1 =& K_{\frac{1}{3}}(\xi_\gamma)\Big[\theta^2\sin 2\varphi\Big(\frac{\varepsilon_+^2+\varepsilon_-^2}{2\varepsilon_+^2}\vec{\zeta}_+ - \frac{(\varepsilon_+-\varepsilon_-)^2}{2\varepsilon_+^2}(\vec{\zeta}_+\cdot\hat{v})\hat{v}\Big) - \frac{\omega^2}{2\varepsilon_+^2\gamma_-^2}[(\vec{\zeta}_+\cdot\vec{b})\vec{s} + (\vec{\zeta}_+\cdot\vec{s})\vec{b}]+ \\
&+ \Big(\frac{\varepsilon_+^2-\varepsilon_-^2}{2\varepsilon_+^2}(\theta^2\cos 2\varphi + 2\lambda_-)(\vec{\zeta}_+\wedge\hat{v}) + \frac{\omega^2}{2\varepsilon_+^2\gamma_-}\theta[\sin\varphi(\vec{\zeta}_+\wedge\vec{b}) - \cos\varphi(\vec{\zeta}_+\wedge\vec{s})]\Big)+ \\
&+ \frac{(\varepsilon_+^2-\varepsilon_-^2)}{2\varepsilon_+^2}\frac{\theta}{\gamma_-}\Big(\sin\varphi[(\vec{\zeta}_+\cdot\vec{s})\hat{v} + (\vec{\zeta}_+\cdot\hat{v})\vec{s}] + \cos\varphi[(\vec{\zeta}_+\cdot\vec{b})\hat{v} + (\vec{\zeta}_+\cdot\hat{v})\vec{b}]\Big)\Big]+ \\
&- K_{\frac{2}{3}}(\xi_\gamma)\sqrt{2\lambda_-}\frac{\omega\varepsilon_-}{\varepsilon_+^2\gamma_-}\vec{s}
\end{aligned} \tag{5.262}$$

$$\begin{aligned}
\vec{S}_2 =& K_{\frac{1}{3}}(\xi_\gamma)\Big[\Big(\frac{\omega}{\varepsilon_+\gamma_-^2} - 2\lambda_-\frac{\varepsilon_+^2-\varepsilon_-^2}{\varepsilon_+^2}\Big)\hat{v} + \frac{\theta}{\varepsilon_+}\frac{\omega}{\gamma_-}(\sin\varphi\vec{b} + \cos\varphi\vec{s})\Big]+ \\
&+ K_{\frac{2}{3}}(\xi_\gamma)\sqrt{2\lambda_-}\Big[\theta\sin\varphi\Big(\frac{2\varepsilon_-}{\varepsilon_+}\vec{\zeta}_+ + \frac{(\varepsilon_+-\varepsilon_-)^2}{\varepsilon_+^2}(\vec{\zeta}_+\cdot\hat{v})\hat{v}\Big)+ \\
&- \frac{1}{2\gamma_-}\Big(\frac{\omega^2}{\varepsilon_+^2}(\vec{\zeta}_+\wedge\vec{s}) + \frac{\varepsilon_+^2-\varepsilon_-^2}{\varepsilon_+^2}[(\vec{\zeta}_+\cdot\vec{b})\hat{v} + (\vec{\zeta}_+\cdot\hat{v})\vec{b}]\Big)\Big]
\end{aligned} \tag{5.263}$$

$$\vec{S}_3 = K_{\frac{1}{3}}(\xi_\gamma)\Big[\Big(\frac{\varepsilon_+^2+\varepsilon_-^2}{2\varepsilon_+^2}\vec{\zeta}_+ - \frac{(\varepsilon_+-\varepsilon_-)^2}{2\varepsilon_+^2}(\vec{\zeta}_+\cdot\hat{v})\hat{v}\Big)(\theta^2\cos 2\varphi + 2\lambda_-)+$$

$$+\Big(\frac{\theta\omega^2}{2\varepsilon_+^2\gamma_-}[\sin\varphi(\vec{\zeta}_+\wedge\vec{s})+\cos\varphi(\vec{\zeta}_+\wedge\vec{b})]-\theta^2\sin 2\varphi\frac{\varepsilon_+^2-\varepsilon_-^2}{2\varepsilon_+^2}(\vec{\zeta}_+\wedge\hat{v})\Big)+$$
$$+\frac{\varepsilon_+^2-\varepsilon_-^2}{2\varepsilon_+^2}\frac{\theta}{\gamma_-}\Big(\cos\varphi[(\vec{\zeta}_+\cdot\vec{s})\hat{v}+(\vec{\zeta}_+\cdot\hat{v})\vec{s}]-\sin\varphi[(\vec{\zeta}_+\cdot\vec{b})\hat{v}+(\vec{\zeta}_+\cdot\hat{v})\vec{b}]\Big)$$
$$-\frac{\omega^2}{2\varepsilon_+^2\gamma_-^2}[(\vec{\zeta}_+\cdot\vec{s})\vec{s}-(\vec{\zeta}_+\cdot\vec{b})\vec{b}]\Big]+$$
$$+K_{\frac{2}{3}}(\xi_\gamma)\sqrt{2\lambda_-}\frac{\omega\varepsilon_-}{\varepsilon_+^2\gamma_-}\vec{b}. \tag{5.264}$$

By substituting throughout Eqs. (5.258)–(5.264) the mixed (or pure) state value for $\vec{\zeta}_+$ obtained via Eq. (5.252) (or Eq. (5.253)), we obtain the final electron's spin quantization axis (SQA) as

$$\vec{\zeta}_- = \frac{\vec{S}'_-}{a'_-}. \tag{5.265}$$

For the mixed state, this expression directly represents the final electron spin. In contrast, for the pure state, the electron spin is assigned as $\vec{\zeta}_- = \frac{\vec{S}'_-}{|\vec{S}'_-|}$ (or $\vec{\zeta}_- = -\frac{\vec{S}'_-}{|\vec{S}'_-|}$), depending on whether the inequality

$$\frac{\frac{dW_{NBW}^{(\xi\zeta_-\zeta_+)}}{d\varepsilon_- d\Omega}\Big|_{\vec{\zeta}_-=\uparrow}}{\frac{dW_{NBW}^{(\xi\zeta_-\zeta_+)}}{d\varepsilon_- d\Omega}\Big|_{\vec{\zeta}_-=\uparrow}+\frac{dW_{NBW}^{(\xi\zeta_-\zeta_+)}}{d\varepsilon_- d\Omega}\Big|_{\vec{\zeta}_-=\downarrow}}=\frac{a'_-+|\vec{S}'_-|}{2a'_-}>r_- \tag{5.266}$$

holds (or does not). Here r_- is a random number uniformly distributed in $0\le r_-\le 1$. Alternatively, one can compute the final electron mixed state $\vec{\zeta}_-$ by applying the "$+\leftrightarrow-$" prescription to eq. (5.252). In this way, the two $\vec{\zeta}_+$ and $\vec{\zeta}_-$ states would be independent.

We have enhanced `SFQEDtoolkit` by adding three additional routines:

- `function_pola_and_spin_BW_angles_mixed_states`;
- `function_pola_and_spin_BW_angles_mixed_states_independent`;
- `function_pola_and_spin_BW_angles_pure_states`.

These routines generate the spins of the leptons produced in the NBW pair process according to the mixed and pure state mechanisms described above. To validate the NBW numerical framework we have developed, we conducted a simulation analogous to the one performed at the end of Sec. 5.6.2. A photon, propagating in a magnetic field $\vec{B}=(0,0,B_z)$ with energy $\omega=1$ GeV and quantum parameter $\chi_\gamma=2$, is forced to decay into an electron-positron pair via NBW. Every photon decay is reiterated 10^4 times: using the `SFQEDtoolkit`'s functions introduced in Sec. 5.5.2, a different emission direction is chosen for the created electron, while the electron-to-photon energy ratio $\frac{\varepsilon_-}{\omega}$ remains fixed throughout. The final

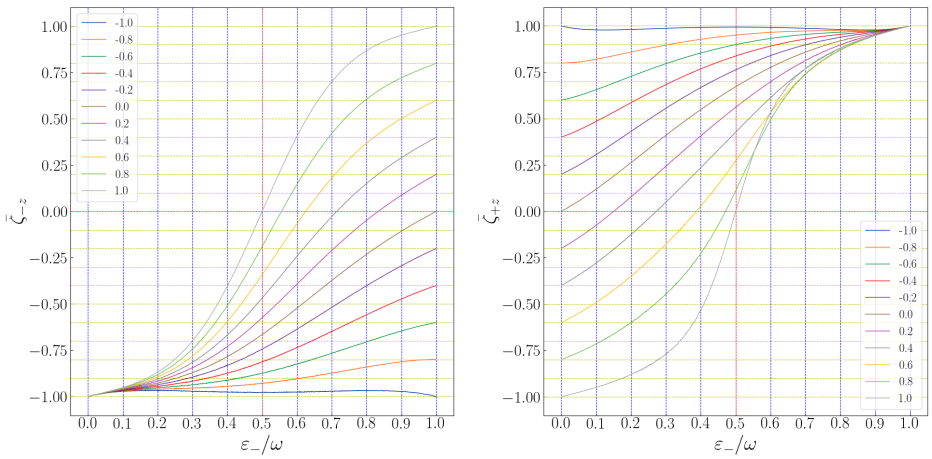

Figure 5.17: Mixed-state curves for the electron (ζ_{-z}, left) and positron (ζ_{+z}, right) spin generated by simulating the NBW decay of a 1 GeV photon moving in a magnetic field, $\vec{B} = (0, 0, B_z)$. Each NBW decay is repeated 10^4 times, each time selecting a different direction for the electron (as described in Sec. 5.5.2) while maintaining the same electron-to-photon energy ratio, $\frac{\varepsilon_-}{\omega}$. The resulting values of ζ_{-z} and ζ_{+z} are averaged over these emissions and plotted as functions of $\frac{\varepsilon_-}{\omega}$ for various initial spin component values, ξ_z (specified in the inset and indicated by different colors). Important: although in the text we describe a procedure where the positron spin is computed first, followed by the electron's, the routine `function_pola_and_spin_BW_angles_mixed_states` performs these calculations in the opposite order. Due to the symmetry of the pair production process, switching between these two approaches is straightforward. This time, the anomalous behavior observed in the right panel is due not only to the "dependence problem" but also to the fact that most states are non-physical.

spin components (ζ_{-z} and ζ_{+z}) along the magnetic field are then averaged over all these decays. By repeating this process for all possible values of $\frac{\varepsilon_-}{\omega}$ and initial polarization projections ξ_z, we obtained the electron-spin and positron-spin versus electron-energy curves shown in Figs. 5.17–5.19. In this case, the pure-state curves in Fig. 5.18 differ significantly from the angle-unresolved results presented in Sec. 5.6.1. Only the independent mixed-states approach shown in Fig. 5.19 appears to agree with those results (see Figs. 5.11–5.12). Nonetheless, similarly to the NIC counterpart, not all spin states computed via Eqs. (5.265)-(5.266) are physically valid, as some exceed unity in magnitude:

$$|\vec{\zeta}_-| > 1 \quad \text{and} \quad |\vec{\zeta}_+| > 1. \tag{5.267}$$

Again, discarding these unphysical states modifies the curves into those shown in Fig. 5.20, highlighting the same underlying issue affecting the FNIC distribution. A potential resolution to this issue is explored in the next section, within the context of the NIC process.

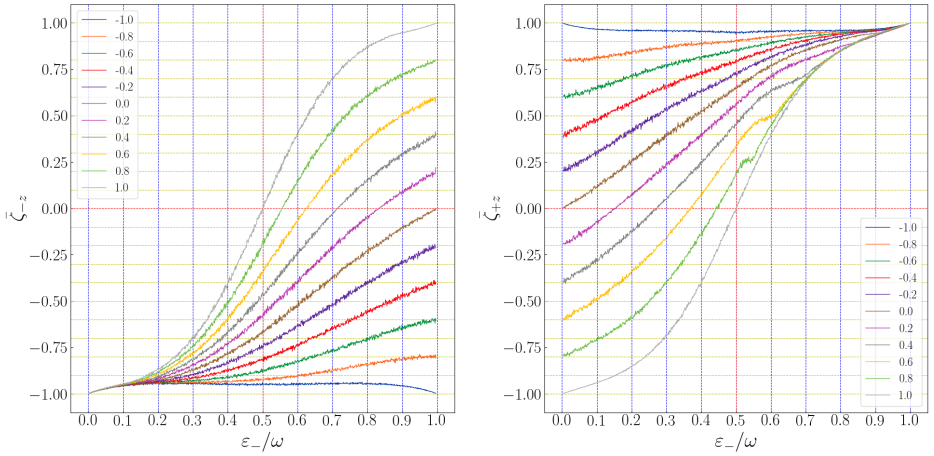

Figure 5.18: Similar to Fig. 5.13, but pure states are used here to track the inner particles' states. Each NBW event, in which an electron is produced along a specific direction, is repeated 10^3 times with all parameters held constant. Every data point in the plot represents the average outcome of these repetitions.

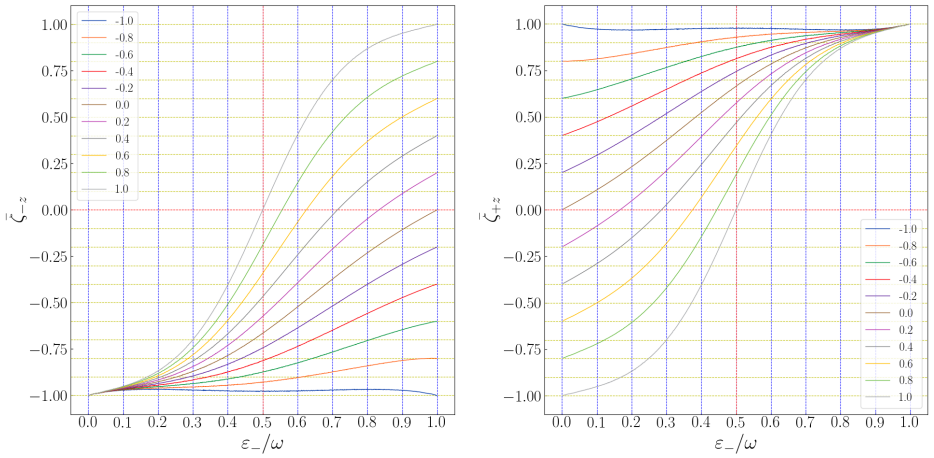

Figure 5.19: As in Fig. 5.17, but with the leptons' SQAs computed independently of each other. Although the results appear consistent with those in Sec. 5.6.1, most of the computed spin states exhibit a modulus greater than unity, rendering them non-physical.

5.7 An ill-defined differential probability

The issue introduced at the end of the previous section might arise because of the use of the QOM approximation. To rule out this possibility, we recomputed the differential probability in Eq. (5.7), following the rigorous first order SFQED S-matrix element approach [108]. Using the Volkov states in Eq. (3.12), we applied the SFQED Feynman rules to derive the invariant S-matrix element $\mathcal{M}_{fi}$ for the

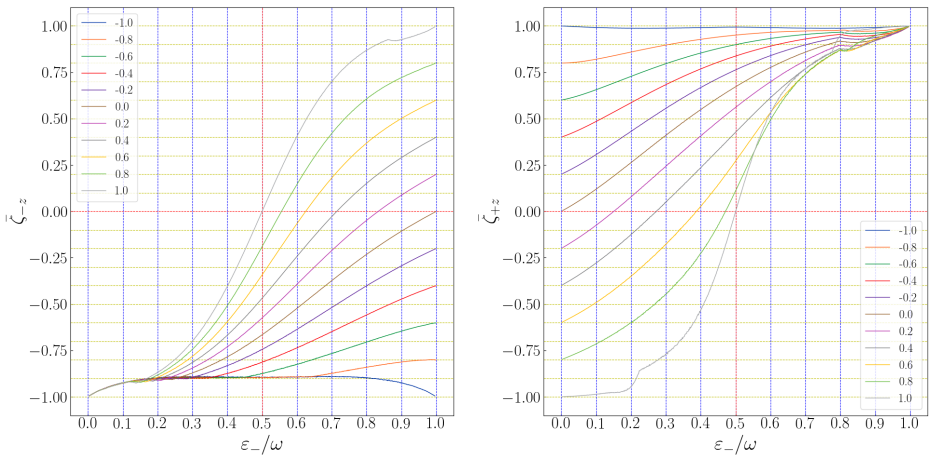

Figure 5.20: As in fig. 5.17, but rejecting all the non-physical electron and positron spin states.

NIC process occurring in a plane wave propagating along $d^\mu = (1, \vec{d})$

$$\mathcal{M}_{fi} = -e\sqrt{\frac{\pi}{2V^3\varepsilon\varepsilon'\omega}}\int d\phi\Big[\bar{u}_{p',\zeta'}\Big(1 - \frac{\not{d}\not{\mathcal{A}}(\phi)}{2p'_-}\Big)\not{\epsilon}^*\Big(1 + \frac{\not{d}\not{\mathcal{A}}(\phi)}{2p_-}\Big)u_{p,\zeta}\Big]\exp\Big\{\Big\{if(\phi)\Big\}\Big\}. \tag{5.268}$$

Here, the exponential term

$$f(\phi) = (p'_+ + k_+ - p_+)\phi + \int_0^\phi d\phi'\Big[\frac{p'_\mu\mathcal{A}^\mu(\phi')}{p'_-} - \frac{p_\mu\mathcal{A}^\mu(\phi')}{p_-} - \frac{\mathcal{A}^2(\phi')}{2}\Big(\frac{1}{p'_-} - \frac{1}{p_-}\Big)\Big], \tag{5.269}$$

depends on the phase $\phi = d_\mu x^\mu$ instead of the space-time position x^μ. Additionally, we used the notation

$$\begin{aligned} V_- &\equiv d_\mu V^\mu = V_0 - \vec{V}\cdot\vec{d} \\ V_+ &\equiv \tilde{d}_\mu V^\mu = \frac{1}{2}(V_0 + \vec{V}\cdot\vec{d}) \\ \not{V} &\equiv \gamma^\mu V_\mu \end{aligned} \tag{5.270}$$

to represent various contractions[24] of a generic four-vector V^μ. The external field four-potential A^μ, scaled by the electron charge[25] $e < 0$, is denoted by $\mathcal{A}^\mu = eA^\mu$.

[24]The use of the + and − subscripts in this notation should not be confused with those employed in sections 5.2.2, 5.4.2, 5.5.2, 5.6.1, and 5.6.2, where these subscripts distinguish species-specific variables. In the current context, however, which pertains to the NIC process, the only lepton species under consideration is the electron. Therefore, any variable will be associated with the electron species.

[25]Note that the four-vector e^μ represents the polarization of the emitted photon.

Exploiting the commutation properties of the Clifford algebra the integrand can be rewritten as

$$\Big(1-\frac{\not{d}\mathcal{A}(\phi)}{2p'_-}\Big)\not{\epsilon}^*\Big(1+\frac{\not{d}\mathcal{A}(\phi)}{2p_-}\Big)=\not{\epsilon}^*+\frac{1}{2}\Big(\frac{\mathcal{A}(\phi)\not{d}\not{\epsilon}^*}{p'_-}+\frac{\not{\epsilon}^*\not{d}\mathcal{A}(\phi)}{p_-}\Big)-\frac{\mathcal{A}^2(\phi)\not{d}\not{e}^*_-}{2p'_-p_-}, \tag{5.271}$$

allowing us to evaluate the square of Eq. (5.268)

$$\begin{aligned}|\mathcal{M}_{fi}|^2=\frac{e^2\pi}{2V^3\varepsilon\varepsilon'\omega}\int d\phi\int d\phi'\,\exp\Big\{\Big\{i[f(\phi)-f(\phi')]\Big\}\Big\}\times\\ \times\frac{1}{4}tr\Big\{\Big[\not{\epsilon}^*+\frac{1}{2}\Big(\frac{\mathcal{A}(\phi)\not{d}\not{\epsilon}^*}{p'_-}+\frac{\not{\epsilon}^*\not{d}\mathcal{A}(\phi)}{p_-}\Big)-\frac{\mathcal{A}^2(\phi)\not{d}\not{e}^*_-}{2p'_-p_-}\Big](\not{p}+m)(1+\gamma^5\not{\zeta})\times\\ \times\Big[\not{\epsilon}+\frac{1}{2}\Big(\frac{\mathcal{A}(\phi')\not{d}\not{\epsilon}}{p'_-}+\frac{\not{\epsilon}\not{d}\mathcal{A}(\phi')}{p_-}\Big)-\frac{\mathcal{A}^2(\phi')\not{d}\not{e}_-}{2p'_-p_-}\Big](\not{p}'+m)(1+\gamma^5\not{\zeta}')\Big\}.\end{aligned} \tag{5.272}$$

Here

$$\begin{aligned}u_{p,\zeta}\bar{u}_{p,\zeta}&=\frac{1}{2}(\not{p}+m)(1+\gamma^5\not{\zeta})\\ u_{p',\zeta'}\bar{u}_{p',\zeta'}&=\frac{1}{2}(\not{p}'+m)(1+\gamma^5\not{\zeta}')\end{aligned} \tag{5.273}$$

are the density matrices of the initial and final partially polarized electrons, respectively.

Without compromising too much the generality of the problem, we decide to simplify the calculations through a series of assumptions:

- the quantization volume is normalized to unity $V=1$;
- introducing the two four-vectors

  $$a_i^\mu=(0,\vec{a}_i)\quad\text{with}\quad i=1,2\quad\text{and such that}\quad a_{\mu\,i}a_j^\mu=-\delta_{ij}, \tag{5.274}$$

  the external plane wave is lineraly polarized along $\vec{a}_1$ and gauge-fixed to $A^\mu(\phi)=(0,A_0\psi(\phi)\vec{a}_1)$. While $\psi(\phi)$ is the pulse shape function, A_0 is linked to the electric field amplitude through

  $$E(\phi)=|\vec{E}(\phi)|=-\vec{A}'(\phi)=-A_0\psi'(\phi), \tag{5.275}$$

  and hence we have $A_0<0$. The wave counter-propagates with respect to the starting electron $\vec{d}=-\frac{\vec{p}}{|\vec{p}|}\equiv-\hat{v}$;
- The two possible polarization states of the outgoing photon are selected as

  $$e_i^\mu=\frac{(d^\mu a_i^\nu-d^\nu a_i^\mu)k_\nu}{k_-}\quad\text{with}\quad i=1,2 \tag{5.276}$$

while

$$\zeta^\mu = -\frac{(d^\mu a_2^\nu - d^\nu a_2^\mu)p_\nu}{p_-} \tag{5.277}$$

$$\zeta'^\mu = -\frac{(d^\mu a_2^\nu - d^\nu a_2^\mu)p'_\nu}{p'_-} \tag{5.278}$$

are chosen as the electron's SQA before and after the emission. In the following we will use the scalar $s = \pm 1$ ($s' = \pm 1$) to denote the alignment of the initial (final) spin along the corresponding axis.

Switching the integration variables in eq. (5.272) to (ϕ_+, ϕ_-), that are related to the original pair (ϕ, ϕ') through

$$\begin{aligned} \phi &= \phi_+ + \frac{\phi_-}{2} \\ \phi' &= \phi_+ - \frac{\phi_-}{2}, \end{aligned} \tag{5.279}$$

we replace in $|\mathcal{M}_{fi}|^2$ all the assumptions (5.274)-(5.278), also expanding[26]

$$\begin{aligned} \mathcal{A}(\phi) &= \mathcal{A}(\phi_+ + \frac{\phi_-}{2}) = \mathcal{A}(\phi_+) + \mathcal{A}'(\phi_+)\frac{\phi_-}{2} \\ \mathcal{A}(\phi') &= \mathcal{A}(\phi_+ - \frac{\phi_-}{2}) = \mathcal{A}(\phi_+) - \mathcal{A}'(\phi_+)\frac{\phi_-}{2}. \end{aligned} \tag{5.280}$$

Reintroducing the proper S-matrix element

$$S_{fi} = (2\pi)^3\delta^{(2)}(\vec{p}'_\perp + \vec{k}_\perp - \vec{p}_\perp)\delta(p'_- + k_- - p_-)i\mathcal{M}_{fi}, \tag{5.281}$$

where the notation $\vec{V}_\perp$ identifies the component perpendicular to the wave's direction $\vec{d}$ of any vector $\vec{V}$, we retrieve (check [108] for details) an expression for the average probability $dP^{(e^-\to e^-\gamma)}_{j,s,s'}$ that a photon is emitted with momentum between k and $k+dk$ in the j-th polarization state (5.276), by an electron whose spin alignment goes from being s along (5.277) to s' with respect to (5.278):

$$\begin{aligned} dP^{(e^-\to e^-\gamma)}_{j,s,s'} &= \frac{d^3k}{(2\pi)^3}\int\frac{d^3p'}{(2\pi)^3}|S_{fi}|^2 = \\ &= d^3k\frac{\alpha}{16\pi^2 p_- p'_-\omega}\int_{-\infty}^{\infty}d\phi_+\int_{-\infty}^{\infty}d\phi_- e^{i\frac{m^2k_-}{2p_-p'_-}\left([1+\vec{\pi}_\perp^2(\phi_+)]\phi_- + \frac{\mathcal{E}^2(\phi_+)\phi_-^3}{m^2 12}\right)}T_{j,s,s'} \end{aligned} \tag{5.282}$$

where

$$\vec{\pi}_\perp(\phi_+) = \frac{1}{m}(\vec{p}_\perp - \vec{\mathcal{A}}_\perp(\phi_+)) - \frac{p_-}{k_- m}\vec{q}_\perp. \tag{5.283}$$

[26] The Taylor expansions in eq. (5.280) are valid in LCFA's conditions.

The two $T_{j,s,s'}$, one for each polarization state in (5.276), are inferred[27] by performing the trace in eq.(5.272), and read

$$\begin{aligned} T_{1,s,s'} = &-2(1+ss')m^2 - \Big(2+2ss'+ss'\frac{k_-}{p_-}\frac{k_-}{p_- - k_-}\Big)\Big(p_2 - \frac{p_-}{k_-}k_2\Big)^2 + \\ &- i(s+s')\frac{m}{2}\mathcal{E}(\phi_+)\phi_-\frac{k_-}{p_-}\Big(2+\frac{k_-}{p_- - k_-}\Big) + \\ &- (1+ss')\Big(4+\frac{k_-}{p_-}\frac{k_-}{p_- - k_-}\Big)\mathcal{E}^2(\phi_+)\frac{\phi_-^2}{4} \end{aligned} \tag{5.284}$$

$$\begin{aligned} T_{2,s,s'} = &\Big(2+2ss'+ss'\frac{k_-}{p_-}\frac{k_-}{p_- - k_-}\Big)\Big(p_2 - \frac{p_-}{k_-}k_2\Big)^2 + \\ &+ i(s-s')\frac{m}{2}\mathcal{E}(\phi_+)\phi_-\frac{k_-}{p_-}\frac{k_-}{p_- - k_-} + \\ &- (1-ss')\frac{k_-}{p_-}\frac{k_-}{p_- - k_-}\mathcal{E}^2(\phi_+)\frac{\phi_-^2}{4}, \end{aligned} \tag{5.285}$$

with $\mathcal{E}(\phi_+) = -eA_0\psi'(\phi_+) = eE(\phi_+) < 0$ representing the product between electron charge and electric field intensity.

Finally defining

$$\phi_- = 2\tilde{\phi}\Big(\frac{p_-p'_-}{k_-\mathcal{E}^2(\phi_+)}\Big)^{\frac{1}{3}} \tag{5.286}$$

$$z(\phi_+) = m^2\Big(\frac{k_-}{p_-p'_-\mathcal{E}(\phi_+)}\Big)^{\frac{2}{3}}[1+\vec{\pi}_\perp^2(\phi_+)], \tag{5.287}$$

and making use of the Airy functions definitions[28]

$$\mathrm{Ai}(z) = \int_{-\infty}^{\infty}\frac{d\phi}{2\pi}e^{iz\phi+i\frac{\phi^3}{3}}$$

[27] In Eqs. (5.284)-(5.285) the sign of the terms proportional to $\mathcal{E}(\phi_+)$ is opposite to that of reference [108]. The misalignment is due to a mistake made (and admitted) by the authors.

[28] In the current footnote the integral form of the squared Airy functions

$$\begin{aligned} \mathrm{Ai}^2(z) &= \frac{4^{\frac{1}{3}}}{2\pi}\int_{-\infty}^{+\infty}\mathrm{Ai}(4^{\frac{1}{3}}(z+x^2))dx \\ \mathrm{Ai}'^2(z) &= \frac{4^{\frac{1}{3}}}{\pi}\int_{-\infty}^{+\infty}x^2\,\mathrm{Ai}(4^{\frac{1}{3}}(z+x^2))dx + z\frac{4^{\frac{1}{3}}}{2\pi}\int_{-\infty}^{+\infty}\mathrm{Ai}(4^{\frac{1}{3}}(z+x^2))dx \end{aligned} \tag{5.288}$$

and their relations with the modified Bessel funtions of the second kind

$$\begin{aligned} \mathrm{Ai}(z) &= \frac{\sqrt{z}}{\pi\sqrt{3}}K_{\frac{1}{3}}\Big(\frac{2}{3}z^{\frac{3}{2}}\Big) \\ \mathrm{Ai}'(z) &= -\frac{z}{\pi\sqrt{3}}K_{\frac{2}{3}}\Big(\frac{2}{3}z^{\frac{3}{2}}\Big) \\ \mathrm{Ai}_1(z) &= \frac{1}{\pi\sqrt{3}}\int_z^\infty\sqrt{x}K_{\frac{1}{3}}\Big(\frac{2}{3}x^{\frac{3}{2}}\Big)dx = \frac{1}{\pi\sqrt{3}}\int_{\frac{2}{3}z^{\frac{3}{2}}}^\infty K_{\frac{1}{3}}(a)da \end{aligned} \tag{5.289}$$

are also provided.

$$\begin{aligned}\mathrm{Ai}'(z) &= i\int_{-\infty}^{\infty}\frac{d\phi}{2\pi}\phi e^{iz\phi+i\frac{\phi^3}{3}}\\ \mathrm{Ai}''(z) &= i^2\int_{-\infty}^{\infty}\frac{d\phi}{2\pi}\phi^2 e^{iz\phi+i\frac{\phi^3}{3}} = z\,\mathrm{Ai}(z),\end{aligned}\tag{5.290}$$

we can solve the integral in $d\phi_-$ and rewrite eq. (5.282) as

$$dP^{(e^-\to e^-\gamma)}_{j,s,s'} = d^3k\frac{\alpha}{4\pi p_- p'_-\omega}\int_{-\infty}^{\infty}d\phi_+\bar{T}_{j,s,s'},\tag{5.291}$$

where this time

$$\begin{aligned}\bar{T}_{1,s,s'}(\phi_+) = -\Big[2(1+ss')m^2 + \Big(2+2ss'+ss'\frac{k_-}{p_-}\frac{k_-}{p_--k_-}\Big)\Big(p_2-\frac{p_-}{k_-}k_2\Big)^2\Big]\Big(\frac{p_-p'_-}{k_-\mathcal{E}^2(\phi_+)}\Big)^{\frac{1}{3}}\mathrm{Ai}(z)+\\ -(s+s')m\mathcal{E}(\phi_+)\frac{k_-}{p_-}\Big(2+\frac{k_-}{p_--k_-}\Big)\Big(\frac{p_-p'_-}{k_-\mathcal{E}^2(\phi_+)}\Big)^{\frac{2}{3}}\mathrm{Ai}'(z)+\\ +(1+ss')\Big(4+\frac{k_-}{p_-}\frac{k_-}{p_--k_-}\Big)\Big(\frac{p_-p'_-}{k_-}\Big)z\,\mathrm{Ai}(z)\end{aligned}\tag{5.292}$$

and

$$\begin{aligned}\bar{T}_{2,s,s'}(\phi_+) = \Big(2+2ss'+ss'\frac{k_-}{p_-}\frac{k_-}{p_--k_-}\Big)\Big(p_2-\frac{p_-}{k_-}k_2\Big)^2\Big(\frac{p_-p'_-}{k_-\mathcal{E}^2(\phi_+)}\Big)^{\frac{1}{3}}\mathrm{Ai}(z)+\\ +(s-s')m\mathcal{E}(\phi_+)\frac{k_-}{p_-}\frac{k_-}{p_--k_-}\Big(\frac{p_-p'_-}{k_-\mathcal{E}^2(\phi_+)}\Big)^{\frac{2}{3}}\mathrm{Ai}'(z)+\\ +(1-ss')\frac{k_-}{p_-}\frac{k_-}{p_--k_-}\Big(\frac{p_-p'_-}{k_-}\Big)z\,\mathrm{Ai}(z).\end{aligned}\tag{5.293}$$

For the sake of simplicity, from this point onward we will focus on the unpolarized photon emission probability

$$\frac{dP^{(e^-\to e^-\gamma)}_{s,s'}}{d\omega d\varphi d\theta} = \frac{\alpha\omega}{4\pi p_- p'_-}\sin\theta\int_{-\infty}^{\infty}d\phi_+\bar{T}_{s,s'}(\phi_+)\tag{5.294}$$

obtained by summing (5.291) over the possible photon polarizations, and thus

$$\begin{aligned}\bar{T}_{s,s'}(\phi_+) = \bar{T}_{1,s,s'}(\phi_+)+\bar{T}_{2,s,s'}(\phi_+) = -2(1+ss')m^2\Big(\frac{p_-p'_-}{k_-\mathcal{E}^2(\phi_+)}\Big)^{\frac{1}{3}}\mathrm{Ai}(z)+\\ -2m\mathcal{E}(\phi_+)\frac{k_-}{p_-}\Big(s+\frac{p_-}{p_--k_-}s'\Big)\Big(\frac{p_-p'_-}{k_-\mathcal{E}^2(\phi_+)}\Big)^{\frac{2}{3}}\mathrm{Ai}'(z)+\\ +\Big[4(1+ss')+2\frac{k_-^2}{p_-(p_--k_-)}\Big]\Big(\frac{p_-p'_-}{k_-}\Big)z\,\mathrm{Ai}(z).\end{aligned}\tag{5.295}$$

From (5.294) we can build the differential probability

$$\frac{dP^{(e^-\to e^-\gamma)}_{s,s'}}{d\phi_+ d\omega d\varphi d\theta} = \frac{\alpha\omega}{4\pi p_- p'_-}\sin\theta\bar{T}_{s,s'}(\phi_+)\tag{5.296}$$

which is completely equivalent to eq. (5.224)-(5.225) under the assumptions outlined at the beginning of the section.

In the next section we will analytically show that (5.296) becomes negative over a certain range of phase values, and that properly speaking cannot be considered a differential probability.

5.7.1 Analytical study

We start our analysis by determining which values of the phase ϕ_+ render eq. (5.295) positive

$$\bar{T}_{s,s'}(\phi_+) \geq 0. \tag{5.297}$$

We will limit ourselves to the perfectly valid scenario in which the spin alignment flips after the emission ($s = -s'$). In this case only the last 2 terms of eq. (5.293) contribute (the others vanish either because of $s = -s'$ or because of the summation over the final photon polarization), and the inequality (5.297) is then recasted as

$$(s-s')m\mathcal{E}(\phi_+)\frac{k_-}{p_-}\frac{k_-}{p_- - k_-}\Big(\frac{p_-p'_-}{k_-\mathcal{E}^2(\phi_+)}\Big)^{\frac{2}{3}}\mathrm{Ai}'(z) + (1-ss')\frac{k_-}{p_-}\frac{k_-}{p_- - k_-}\Big(\frac{p_-p'_-}{k_-}\Big)z\,\mathrm{Ai}(z) \geq 0. \tag{5.298}$$

Since the quantity z defined in eq. (5.287) is always positive

$$\mathrm{Ai}(z) > 0 \quad \text{and} \quad \mathrm{Ai}'(z) < 0 \quad \forall z \in \mathbb{R}^+,$$

eq. (5.298) can be manipulated into

$$z\frac{\mathrm{Ai}(z)}{\mathrm{Ai}'(z)} \leq -\frac{s-s'}{1-ss'}\Big(\frac{k_-m^3}{p_-p'_-\mathcal{E}(\phi_+)}\Big)^{\frac{1}{3}}. \tag{5.299}$$

Now, one of the basic assumptions of the LCFA consists in considering the external EM fields as varying on timescales much greater then those needed by the NIC photon to form. In such circumstances any plane wave, and actually *any field*[29], can be considered as an instantaneous constant crossed field (CCF) in which $|\vec{E}| = |\vec{B}|$ and $\frac{\vec{E}}{|\vec{E}|} \wedge \frac{\vec{B}}{|\vec{B}|} = \vec{d}$: under these conditions the pulse shape of the plane wave reduces to

$$\psi(\phi) = \phi \tag{5.300}$$

and the RHS of (5.299) can be treated as a constant

$$-\frac{s-s'}{1-ss'}\Big(\frac{k_-m^3}{p_-p'_-\mathcal{E}}\Big)^{\frac{1}{3}} \equiv -\frac{s-s'}{1-ss'}C_3. \tag{5.301}$$

[29] In this statement lies the key to retrieve Eqs. (5.225) and (5.296)'s probabilistic interpretation.

At the lowest order in $\frac{1}{\gamma}$ (and $\theta \sim \frac{1}{\gamma}$) the quantum nonlinearity parameter of a relativistic electron[30] inside a CCF undergoing a NIC event is

$$\chi = \frac{\gamma}{E_{cr}} \sqrt{\left(\vec{E} + \frac{\vec{v}}{\gamma} \wedge \vec{B}\right)^2 - \left(\frac{\vec{v}}{\gamma} \cdot \vec{E}\right)^2} \sim 2\frac{\gamma E}{E_{cr}} = 2\gamma E|e| = -2\gamma\mathcal{E}, \tag{5.302}$$

while $p_- \sim 2\gamma m$ and $k_- \sim 2\omega$; at the same order, the constant introduced in eq. (5.301)

$$C_3 \equiv \left(\frac{k_- m^3}{p_- p'_- \mathcal{E}}\right)^{\frac{1}{3}} \sim -\left[\frac{m^2 \frac{\omega}{\gamma}}{(m - \frac{\omega}{\gamma})\chi}\right]^{\frac{1}{3}} \tag{5.303}$$

depends only on the photon-electron energy ratio $\frac{\omega}{\gamma}$ and the quantum nonlinearity paramter χ. Graphically, the LHS and RHS of eq. (5.299) are displayed in figure 5.21, while the evolution of the "constant" $C_3(\frac{\omega}{\gamma},\chi)$ is shown for fixed[31] χ in fig.

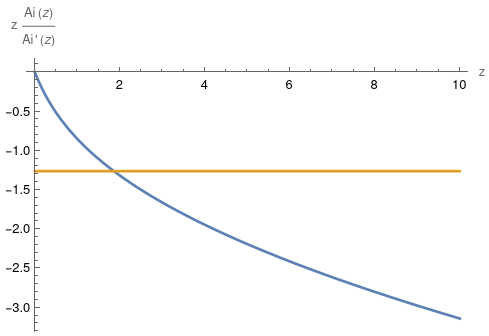

Figure 5.21: The two sides of (5.299): the blue curve descrbes the evolution of $z\frac{\mathrm{Ai}(z)}{\mathrm{Ai}'(z)}$, while the orange represents one possible value of the constant at the RHS.

5.22.

Solving (5.299) requires some numerical methods: despite $z\frac{\mathrm{Ai}(z)}{\mathrm{Ai}'(z)}$ admits rather simple asymptotic expansions for $z \to 0$

$$z\Big[-\frac{\Gamma(\frac{1}{3})}{3^{\frac{1}{3}}\Gamma(\frac{2}{3})} + z - \frac{\Gamma^2(\frac{1}{3})}{2\times 3^{\frac{2}{3}}\Gamma^2(\frac{2}{3})}z^2 + \frac{2\Gamma(\frac{1}{3})}{3^{\frac{4}{3}}\Gamma(\frac{2}{3})}z^3 - \Big(\frac{1}{4} + \frac{\Gamma^3(\frac{1}{3})}{12\Gamma^3(\frac{2}{3})}\Big)z^4 + \frac{7\Gamma^2(\frac{1}{3})}{15\times 3^{\frac{2}{3}}\Gamma^2(\frac{2}{3})}z^5 + O(z^6)\Big] \tag{5.304}$$

and $z \to \infty$

$$z\Big[-\frac{1}{\sqrt{z}} + \frac{1}{4z^2} - \frac{7}{32z^{\frac{7}{2}}} + \frac{21}{64z^5} - \frac{1463}{2048z^{\frac{13}{2}}} + O\Big(\frac{1}{z^{\frac{15}{2}}}\Big)\Big] \tag{5.305}$$

which can lead to straightforward solutions, its modeling in the intermediate region is not traceable to any known function. In any case, a solution to (5.299) will

[30] For positrons eq. (5.302) would be $\chi \sim 2\gamma\mathcal{E}$.

[31] Notice that changing the value of the parameter χ doesn't alter the shape depicted in fig. 5.22, which instead gets simply rescaled.

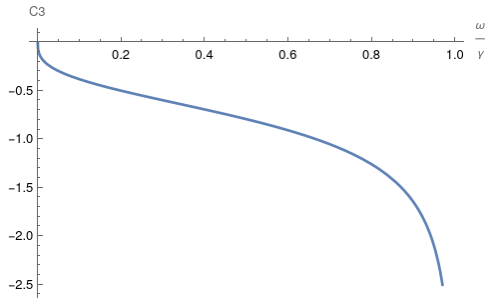

Figure 5.22: Dependence of the parameter (5.303) from the ratio $\frac{\omega}{\gamma}$.

inevitably have the form

$$z(\phi_+) \geq \bar{z}, \tag{5.306}$$

with $\bar{z}$ corresponding to the point in fig. 5.21 where the two curves intersect each other. Replacing the definitions (5.287), (5.283) and (5.300) for $z(\phi_+)$, $\vec{\pi}_\perp(\phi_+)$ and the CCF's wave pulse $\psi(\phi_+)$, eq. (5.306) narrows down to a degree 2 polynomial inequality in ϕ_+, whose solutions are found in the usual form

$$\phi_+ \leq \frac{-\bar{b} - \sqrt{\bar{b}^2 - 4\bar{a}\bar{d}}}{2\bar{a}} \quad \vee \quad \phi_+ \geq \frac{-\bar{b} + \sqrt{\bar{b}^2 - 4\bar{a}\bar{d}}}{2\bar{a}}. \tag{5.307}$$

The parameters $\bar{a}$, $\bar{b}$ and $\bar{d}$ depend on the mutual orientation between the starting electron's and CCF wave's direction: when they are initially counterpropagating, we have

$$\bar{a} = \Big(-\frac{eE}{m}\Big)^2; \tag{5.308}$$

$$\bar{b} = 2\Big(-\frac{eE}{m}\Big)\Big(2\gamma\frac{\sin\theta}{1+\cos\theta}\Big)\cos\varphi; \tag{5.309}$$

$$\bar{c} = \Big(2\gamma\frac{\sin\theta}{1+\cos\theta}\Big)^2; \tag{5.310}$$

$$\bar{d} = \bar{c} + 1 - \frac{\bar{z}}{C_3^2}. \tag{5.311}$$

Naturally, due to the prefactor $-\frac{s-s'}{1-ss'}$ in eq. (5.301), eq. (5.299) does also admit trivial solutions depending on the alignment s and s' of the spin before and after the process. As a matter of fact, only the differential probability $\bar{T}_{-1,+1}(\phi_+)$ associated to electrons (particles with negative charge) has (5.307)-like solutions, while $\bar{T}_{+1,-1}(\phi_+)$ is always positive (the opposite is true for positrons). This is confirmed by fig. 5.23, where $\bar{T}_{-1,+1}(\phi_+)$'s behavior in the phase ϕ_+ is showed, any other parameter (like $\chi = 2$, $\frac{\omega}{\gamma} = 0.1$ and the emitted photon's direction $\vec{n}$) remaining fixed.

Analogous arguments hold for the case $s = s'$ too, despite this time the equation to solve features the presence of further terms

$$(1+ss')\Big[-2m^2\Big(\frac{p_-p'_-}{k_-\mathcal{E}^2(\phi_+)}\Big)^{\frac{1}{3}} + \Big(4 + \frac{k_-}{p_-}\frac{k_-}{p_- - k_-}\Big)\Big(\frac{p_-p'_-}{k_-}\Big)z\Big]\,\mathrm{Ai}(z) +$$

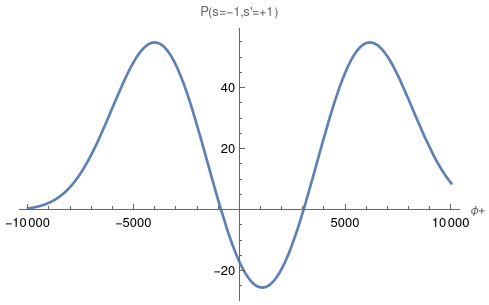

Figure 5.23: Behavior of the function $\bar{T}_{-1,+1}(\phi_+)$. Supposedly, this function represents a differential transition probability but is negative over an extended range of phases ϕ_+.

$$-(s+s')m\mathcal{E}(\phi_+)\frac{k_-}{p_-}\Big(2+\frac{k_-}{p_- - k_-}\Big)\Big(\frac{p_-p'_-}{k_-\mathcal{E}^2(\phi_+)}\Big)^{\frac{2}{3}}\,\mathrm{Ai}'(z)\geq 0. \quad (5.312)$$

Through some manipulations, eq. (5.312) becomes

$$[-2C_3^2C_4+(4C_4+1)z]\frac{\mathrm{Ai}(z)}{\mathrm{Ai}'(z)}\leq\Big(\frac{s+s'}{1+ss'}\Big)C_3(2C_5+1), \quad (5.313)$$

where the parameters

$$C_4\equiv\frac{p_-p'_-}{k_-^2}\xrightarrow[\gamma\gg 1]{}\frac{m(m-\frac{\omega}{\gamma})}{(\frac{\omega}{\gamma})^2}, \quad (5.314)$$

$$C_5\equiv\frac{p'_-}{k_-}\xrightarrow[\gamma\gg 1]{}\frac{(m-\frac{\omega}{\gamma})}{\frac{\omega}{\gamma}} \quad (5.315)$$

in the ultrarelativistic limit depend only on the photon-electron energy ratio $\frac{\omega}{\gamma}$. Unfortunately, a straightforward visual representation like that given in fig. 5.21 for eq. (5.299) is precluded, nonethelss inspecting the limits $\frac{\omega}{\gamma}\to 0,1$ will result to be quite pedagogical:

- for $\frac{\omega}{\gamma}\to 0$ and $\gamma\gg 1$ the term in C_4 will dominate eq. (5.313), being the one with the highest order in $(\frac{\omega}{\gamma})^{-1}$, since

$$C_3^2C_4\to\frac{m^{\frac{7}{3}}(m-\frac{\omega}{\gamma})^{\frac{1}{3}}}{(\frac{\omega}{\gamma})^{\frac{4}{3}}\chi^{\frac{2}{3}}} \quad (5.316)$$

$$C_3C_5\to-\Big[\frac{m^2(m-\frac{\omega}{\gamma})^2}{(\frac{\omega}{\gamma})^2\chi}\Big]^{\frac{1}{3}}. \quad (5.317)$$

  The corresponding inequality reduces to the more trivial

$$4C_4z\frac{\mathrm{Ai}(z)}{\mathrm{Ai}'(z)}\leq 0, \quad (5.318)$$

  which is satisfied by every value of z, and thus every phase ϕ_+;

- for $\frac{\omega}{\gamma} \to 1$, on the other hand, almost all the terms vanish and eq. (5.313) is traced back to the more familiar

$$z\frac{\mathrm{Ai}(z)}{\mathrm{Ai}'(z)} \leq \Big(\frac{s+s'}{1+ss'}\Big)C_3, \tag{5.319}$$

whose solution won't be any different from the (5.307) found for (5.299). Indeed, figure 5.24 shows that already at $\frac{\omega}{\gamma} = 0.8$ the differential probability $\bar{T}_{+1,+1}(\phi_+)$ behaves exactly like $\bar{T}_{-1,+1}(\phi_+)$, plotted in fig. 5.23 for $\frac{\omega}{\gamma} = 0.1$.

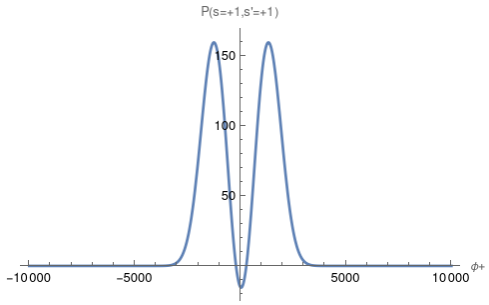

Figure 5.24: As in fig. 5.23: this time the transition probability plotted is $\bar{T}_{+1,+1}(\phi_+)$.

This rather coarse analysis seems to suggest that when $s = s'$, as the energy ratio $\frac{\omega}{\gamma}$ increases, the corresponding angle- and spin-resolved differential probability transitions from being positive over the whole phases ϕ_+ domain, to have regions in which it is ill-defined and negative. This same behavior occurs for $s = -s'$ as well, but due to the presence of much less terms (and thus less contributions), the transition takes place already at lower values of the energy ratio ($\frac{\omega}{\gamma} \sim 0.1$).

5.7.2 Recovering the probabilistic meaning behind the fully-resolved distribution

From the conclusion of Sec. 5.7.1, it is evident that Eqs. (5.39) and (5.282) cannot be regarded as proper differential probabilities. Undeniably, these expressions exhibit negative values over extended parameter ranges, rendering them unsuitable for describing any SFQED process. However, this improper behavior disappears once the distribution is integrated over the solid angle. Specifically, integrating Eq. (5.39) over the entire solid angle $d\Omega$ (see Sec. 5.6) seems to restore its differential probabilistic interpretation[32]. A similar outcome is achieved by summing Eq. (5.39) over the internal states of the final particles. The literature indeed contains numerous examples where distributions that are either 'angle-unresolved but spin-and-polarization-resolved' or 'spin-and-polarization-unresolved but angle-resolved' operate as proper differential probabilities [99, 104].

[32]The corresponding angle-unresolved distribution computed in Sec. 5.6 can be shown to remain non-negative.

In this section, we propose a novel approach to address this issue— a method to predict the spins and polarizations after the NIC process using the fully resolved distributions we have developed so far. What we have designed is a comprehensive algorithm, conceived as the most straightforward generalization of the procedure outlined in Chapter 3, which currently represents the state-of-the-art in modern PIC and MC simulations. As such, it offers the potential for seamless integration into SFQED-oriented libraries, such as `SFQEDtoolkit`. The cornerstone of our approach lies in the recognition that, by its very construction, only Eq. (5.272) (or equivalently Eq. (5.294)) can be regarded as a proper probability, while there is no guarantee that the integrand function is always positive. Before presenting our solution, we first summarize the strategy commonly employed by existing codes to enforce SFQED processes:

1. the event is deemed to occur through the corresponding emission probability per unit time;
2. the energies of the final particles are determined according to the energy differential distributions associated to the processes.

In the collinear approximation 1.) and 2.) are perfectly enough to describe the event, otherwise one can continue with

3. the determination of the final momentum's direction (through the angles θ and φ), see sec. 5.5;
4. the determination of the final spin and polarization states ($\vec{\zeta}'$ and $\vec{\xi}$), see sec.s 5.6.1 and 5.6.2.

Advanced SFQED codes typically perform step 3.) without step 4.), or vice versa. To the best of our knowledge, no codes or algorithms exist in the literature that successfully implement all four steps (1. to 4.). Additionally, each step is expected to be executed locally: by inserting the fields' values experienced by particles at a given time and position into the corresponding differential distributions, one can extract the required informations about the process. However, this approach does not work with step 4.), where fully-resolved probabilities may become locally negative. Although the concept of formation time and/or length has been known since the inception of the theory, it is often neglected in numerical routines that calculate the details of SFQED processes (such as final energies, directions, spins, and polarizations). These fundamental physical quantities, which are inherently considered by nature whenever a process develops, are not typically accounted for in the locally constant field approximation. However, full-resolution differential probabilities appear to acquire physical significance only after considering their contribution over the entire formation length of the process. It is precisely this integration procedure, over the formation length or formation time, that will convert any ill-defined differential object back into a well-defined local probability.

The SFQED technique we developed to address these issues provides an ideal alternative to the four-step process outlined above. Referring to that same list of steps, our algorithm proceeds unchanged from steps 1.) to 3.), determining the occurrence of the event, the final particle energies, and their angular distribution. However, instead of locally applying equation (5.39) to determine the final inner states as described in section 5.6.2, we *replace* the generic electromagnetic fields acting on the particle with a *fictitious* CCF. This CCF is defined such that:

- Its field intensity, given by
$$E = \frac{\chi}{2\gamma|e|} \tag{5.320}$$
produces the same quantum nonlinearity parameter χ on the emitting particle as it experiences within the original fields (where γ is the particle's Lorentz factor).

- Its polarization is aligned with the transverse acceleration vector $\vec{s}$ induced on the particle by the original fields:
$$\vec{E} = \pm\vec{s} \tag{5.321}$$
(the orientation depends on the sign of the charge: + for positrons and − for electrons).

In fact, the invariant χ alone dictates the occurrence of the SFQED event and determines the energies of the outgoing particles. At the same time, the fields' polarization plays a crucial role in shaping the final spin and polarization. It should now be clear that the plane-wave and CCF considerations presented in sections 5.7 and 5.7.1 are fully consistent with the underlying nature of the problem we are currently addressing.

While transitioning to such a CCF does not alter the fundamental nature of the quantum process, it significantly simplifies the protocol that resolves the ill-defined nature of the negative differentials. Indeed, the complexity is reduced to such an extent that, instead of performing the integral over only the formation region, we could even extend it over the entire quasiclassical trajectory[33]! While this would certainly guarantee the positivity of the resulting distributions, we know that the total NIC probability receives no contribution from portions of the trajectory outside the formation region. Therefore, we update the set of assumptions made in Section 5.7 by further imposing:

- that the plane wave colliding head-on with the electron becomes a CCF[34]
$$A_\mu(\phi) = a_\mu\phi \tag{5.322}$$

[33] It is worth to mention that, within the scope of our method, the trajectory which we refer to is supposed to be the one followed by the charged particle as it moves inside the fictitious CCF.

[34] A CCF is essentially a constant plane wave, or equivalently, a plane wave with zero frequency.

(and thus $\vec{E} = -\vec{A}'(\phi_+) = -\vec{a}$). For convenience, the plane wave direction is still denoted by $\vec{d} = \frac{\vec{E}}{|\vec{E}|} \wedge \frac{\vec{B}}{|\vec{B}|}$. Although this may initially seem like a cumbersome constraint, it will soon become apparent that it is a natural choice;

- the following gauge fixing conditions on the emitted photon polarization

$$k_\mu e^\mu = 0 \tag{5.323}$$
$$d_\mu e^\mu \equiv e_- = 0, \tag{5.324}$$

with the associated completeness relation given by

$$\sum_{i=1,2} e^*_{i,\mu} e_{i,\nu} = -g_{\mu\nu} + \frac{k_\mu d_\nu + d_\mu k_\nu}{k_-} \tag{5.325}$$

(the polarization indices i are explicitly indicated).

To further generalize our result, we relax the assumptions (5.276)–(5.278) regarding the specific forms proposed for the outgoing inner states ζ' and ξ. Under this new set of assumptions, the matrix element (5.268) can be refined accordingly. In particular, the phase integration in the exponential function (5.269) can be explicitly evaluated, yielding:

$$f(\phi) = \alpha\phi + \beta\phi^2 + \kappa\phi^3, \tag{5.326}$$

with the variables

$$\begin{aligned} \alpha &= p'_+ + k_+ - p_+, \\ \beta &= \frac{e}{2}\Big(\frac{p'_\mu}{p'_-} - \frac{p_\mu}{p_-}\Big)a^\mu, \\ \kappa &= -\frac{e^2}{6}a^2\Big(\frac{1}{p'_-} - \frac{1}{p_-}\Big) \end{aligned} \tag{5.327}$$

introduced for simplicity. Thereafter, the shift

$$\phi \to \Big(\frac{1}{3\kappa}\Big)^{\frac{1}{3}}\varphi - \phi_0 \quad \text{with} \quad \phi_0 = \frac{\beta}{3\kappa} \tag{5.328}$$

is carried out in eq. (5.268)

$$\begin{aligned} \mathcal{M}_{fi} = -e\sqrt{\frac{\pi}{2V^3\varepsilon\varepsilon'\omega}}\Big(\frac{1}{3\kappa}\Big)^{\frac{1}{3}} \exp\{i\tilde{\alpha}\}\times \\ \times \int d\varphi \bar{u}_{p',\zeta'}\Big\{\not{e}^* - \frac{e}{2}\Big(\frac{\not{a}\not{d}\not{e}^*}{p'_-} + \frac{\not{e}^*\not{d}\not{a}}{p_-}\Big)\phi_0 - \frac{e^2a^2\not{d}\not{e}^*_-}{2p'_-p_-}\phi_0^2 + \\ + \Big[\frac{e}{2}\Big(\frac{\not{a}\not{d}\not{e}^*}{p'_-} + \frac{\not{e}^*\not{d}\not{a}}{p_-}\Big) + \frac{e^2a^2\not{d}\not{e}^*_-}{p'_-p_-}\phi_0\Big]\frac{\varphi}{(3\kappa)^{\frac{1}{3}}} \end{aligned}$$

$$- \frac{e^2 a^2 \not{d} \not{e}^*_-}{2p'_- p_-} \frac{\varphi^2}{(3\kappa)^{\frac{2}{3}}} \Big\} u_{p,\zeta} \times \exp\Big\{ i\Big(z\varphi + \frac{\varphi^3}{3} \Big) \Big\}, \tag{5.329}$$

where $\tilde{\alpha} = \frac{2\beta^3}{27\kappa^2} - \frac{\alpha\beta}{3\kappa}$ and $z = (\alpha - \frac{\beta^2}{3\kappa})(\frac{1}{3\kappa})^{\frac{1}{3}}$; most of the terms vanish out by enforcing the second gauge condition (5.324), while the integral in $d\varphi$ can be solved using the Airy function defintions in (5.290)

$$\begin{aligned} \mathcal{M}_{fi} = -e \sqrt{\frac{\pi}{2V^3 \varepsilon\varepsilon' \omega}} \Big(\frac{1}{3\kappa} \Big)^{\frac{1}{3}} \exp\{i\tilde{\alpha}\} \times \\ \times \bar{u}_{p',\zeta'} \Big\{ \Big[\not{\epsilon}^* - \frac{e}{2} \Big(\frac{\not{\phi} \not{d} \not{\epsilon}^*}{p'_-} + \frac{\not{\epsilon}^* \not{d} \not{\phi}}{p_-} \Big) \phi_0 \Big] \mathrm{Ai}(z) - \frac{ie}{2} \Big(\frac{\not{\phi} \not{d} \not{\epsilon}^*}{p'_-} + \frac{\not{\epsilon}^* \not{d} \not{\phi}}{p_-} \Big) \frac{\mathrm{Ai}'(z)}{(3\kappa)^{\frac{1}{3}}} \Big\} u_{p,\zeta}. \end{aligned} \tag{5.330}$$

Omitting the initial constant, which is irrelevant to our purpose, the squared matrix element of the NIC in a CCF takes the form

$$\begin{aligned} |\mathcal{M}_{fi}|^2 \sim \frac{1}{4} Tr\Big\langle \Big\{ \not{\epsilon}^* \,\mathrm{Ai}(z) - \frac{e}{2} \Big(\frac{\not{\phi} \not{d} \not{\epsilon}^*}{p'_-} + \frac{\not{\epsilon}^* \not{d} \not{\phi}}{p_-} \Big) \Big[\phi_0 \,\mathrm{Ai}(z) + i \frac{\mathrm{Ai}'(z)}{(3\kappa)^{\frac{1}{3}}} \Big] \Big\} (\not{p} + m)(1 + \gamma^5 \not{\zeta}) \times \\ \times \Big\{ \not{\epsilon} \,\mathrm{Ai}(z) - \frac{e}{2} \Big(\frac{\not{\epsilon} \not{d} \not{\phi}}{p'_-} + \frac{\not{\phi} \not{d} \not{\epsilon}}{p_-} \Big) \Big[\phi_0 \,\mathrm{Ai}(z) - i \frac{\mathrm{Ai}'(z)}{(3\kappa)^{\frac{1}{3}}} \Big] \Big\} (\not{p}' + m)(1 + \gamma^5 \not{\zeta}') \Big\rangle. \end{aligned} \tag{5.331}$$

Equation (5.331) serves as the cornerstone of our approach. By applying the procedures outlined below eq. (5.173), it can be reliably used to extract well-defined SQA and PQA for the final particles. Specifically, using (5.325) to sum over photon polarizations recasts the squared matrix element into:

$$\sum_{\xi} |\mathcal{M}_{fi}|^2 \sim I + \zeta' \cdot l, \tag{5.332}$$

where we adopted the notation $V \cdot W = V_\mu W^\mu$ to identify the Minkowskian product between two four-vectors. Here

$$l^\mu = A\zeta^\mu + Ba^\mu + Ck^\mu + Dd^\mu + Ep^\mu + F\epsilon^{\mu\nu\rho\sigma} a_\nu k_\rho d_\sigma + G\epsilon^{\mu\nu\rho\sigma} a_\nu d_\rho p_\sigma + H\epsilon^{\mu\nu\rho\sigma} a_\nu d_\rho p'_\sigma \tag{5.333}$$

represents the intricate SQA four-vector arising from the expansion of the trace in (5.331)[35]. The set of constants $(I, A, B, C, D, E, F, G, H)$ appearing in (5.332)-(5.333) is provided below

$$\begin{aligned} A = 2k_-(a \cdot a) e^2 \Big[\frac{\mathrm{Ai}'(z)^2}{(3\kappa)^{\frac{2}{3}}} + \phi_0^2 \,\mathrm{Ai}(z)^2 \Big] + \\ + 2e\phi_0 \,\mathrm{Ai}(z)^2 (-p_-(a \cdot k) - p'_-(a \cdot k) + k_-(a \cdot p')) + \end{aligned}$$

[35] The details of the trace computation are left to the reader.

$$+ 2\,\mathrm{Ai}(z)^2(k_-(p\cdot p') - p'_-(k\cdot p) - p_-(k\cdot p')) \tag{5.334}$$

$$\begin{aligned} B = 2e\phi_0\,\mathrm{Ai}(z)^2\Big(&- p_-(\zeta\cdot k) + p'_-(\zeta\cdot k) - k_-(\zeta\cdot p') + \zeta_-(k\cdot p) + \\ &+ \frac{\zeta_- k_-}{p_-}(p\cdot p') - \frac{\zeta_- k_-}{p'_-}m^2 - \frac{\zeta_- p'_-}{p_-}(k\cdot p)\Big) \end{aligned} \tag{5.335}$$

$$\begin{aligned} C = {} & 2e\phi_0(\zeta\cdot a)\,\mathrm{Ai}(z)^2(p_- - p'_-) + \\ & + 2\,\mathrm{Ai}(z)^2(-\zeta_-(p\cdot p') + \zeta_- m^2 + p_-(\zeta\cdot p')) \end{aligned} \tag{5.336}$$

$$\begin{aligned} D = {} & -2(\zeta\cdot a)k_- e\phi_0\,\mathrm{Ai}(z)^2\Big(\frac{m^2}{p_-} - \frac{(p\cdot p')}{p'_-}\Big) \\ & - 2e\phi_0\,\mathrm{Ai}(z)^2\Big(\frac{p_-}{p'_-} - 1\Big)((\zeta\cdot a)(k\cdot p') - (\zeta\cdot k)(a\cdot p')) \\ & - 2(\zeta\cdot k)\,\mathrm{Ai}(z)^2((p\cdot p') - m^2) \\ & - \zeta_- k_-(a\cdot a)e^2m^2\Big[\frac{\mathrm{Ai}'(z)^2}{(3\kappa)^{\frac{2}{3}}} + \phi_0^2\,\mathrm{Ai}(z)^2\Big]\Big(\frac{1}{p_-^2} + \frac{1}{p'^2_-}\Big) \\ & + 2\frac{\zeta_- k_-}{p_- p'_-}(a\cdot a)(p\cdot p')e^2\Big[\frac{\mathrm{Ai}'(z)^2}{(3\kappa)^{\frac{2}{3}}} + \phi_0^2\,\mathrm{Ai}(z)^2\Big] \\ & - 2\zeta_-(a\cdot k)e\phi_0\,\mathrm{Ai}(z)^2\Big(\frac{1}{p_-} + \frac{1}{p'_-}\Big)((p\cdot p') - m^2) \\ & + 2\zeta_-(a\cdot p')(k\cdot p)e\phi_0\,\mathrm{Ai}(z)^2\Big(\frac{1}{p_-} - \frac{1}{p'_-}\Big) \\ & - 2(\zeta\cdot p')(a\cdot a)\frac{k_-}{p'_-}e^2\Big[\frac{\mathrm{Ai}'(z)^2}{(3\kappa)^{\frac{2}{3}}} + \phi_0^2\,\mathrm{Ai}(z)^2\Big] \\ & + 2(\zeta\cdot p')(a\cdot k)e\phi_0\,\mathrm{Ai}(z)^2\Big(\frac{p_-}{p'_-} + 1\Big) \\ & + 2(\zeta\cdot p')(k\cdot p)\,\mathrm{Ai}(z)^2 \end{aligned} \tag{5.337}$$

$$\begin{aligned} E = {} & -2k_-(\zeta\cdot a)e\phi_0\,\mathrm{Ai}(z)^2 \\ & - 2\frac{\zeta_- k_-}{p_-}(a\cdot a)e^2\Big[\frac{\mathrm{Ai}'(z)^2}{(3\kappa)^{\frac{2}{3}}} + \phi_0^2\,\mathrm{Ai}(z)^2\Big] \\ & + 2\zeta_- e\phi_0\,\mathrm{Ai}(z)^2\Big(\frac{p'_-}{p_-}(a\cdot k) + (a\cdot k) - \frac{k_-}{p_-}(a\cdot p')\Big) \\ & + 2\,\mathrm{Ai}(z)^2(\zeta_-(k\cdot p') - k_-(\zeta\cdot p') + p'_-(\zeta\cdot k)) \end{aligned} \tag{5.338}$$

$$F = -2em\,\mathrm{Ai}(z)\frac{\mathrm{Ai}'(z)}{(3\kappa)^{\frac{1}{3}}}\Big(1 - \frac{p_-}{p'_-}\Big) \tag{5.339}$$

$$G = -2em\,\mathrm{Ai}(z)\Big(\frac{\mathrm{Ai}'(z)}{(3\kappa)^{\frac{1}{3}}}\Big)\frac{k_-}{p_-} \tag{5.340}$$

$$H = +2em\,\mathrm{Ai}(z)\frac{\mathrm{Ai}'(z)}{(3\kappa)^{\frac{1}{3}}}\frac{k_-}{p'_-} \tag{5.341}$$

$$\begin{aligned} I = &-k_- e^2 (a\cdot a)\Big(\frac{p'_-}{p_-}+\frac{p_-}{p'_-}\Big)\Big[\frac{\mathrm{Ai}'(z)^2}{(3\kappa)^{\frac{2}{3}}}+\phi_0^2\,\mathrm{Ai}(z)^2\Big] \\ &+ 2e\phi_0\,\mathrm{Ai}(z)^2(p_-(a\cdot k)+p'_-(a\cdot k)-\frac{k_-p_-}{p'_-}(a\cdot p')) \\ &+ 2\,\mathrm{Ai}(z)^2(-k_-m^2+p'_-(k\cdot p)+p_-(k\cdot p')) \\ &+ 2em\,\mathrm{Ai}(z)\frac{\mathrm{Ai}'(z)}{(3\kappa)^{\frac{1}{3}}}\epsilon^{\mu\nu\rho\sigma}\zeta_\mu a_\nu\Big(k_\rho d_\sigma-\frac{p'_-}{p_-}k_\rho d_\sigma-\frac{k_-}{p_-}d_\rho p_\sigma+\frac{k_-}{p'_-}d_\rho p'_\sigma\Big). \end{aligned} \tag{5.342}$$

Now, using the Pauli-Lubanski spin relations [57]

$$\begin{aligned} \zeta'^0 &= \frac{|\vec{p}\,'|}{m}\eta_\parallel \\ \vec{\zeta}'_\perp &= \vec{\eta}_\perp \\ \zeta'_\parallel &= \frac{\varepsilon'}{m}\eta_\parallel \end{aligned} \tag{5.343}$$

the detector's spin four-vector components in the lab frame $\zeta'^\mu = (\zeta'^0, \vec{\zeta}\,')$ can be rewritten in terms of its components expressed in the final electron's rest frame $\eta^\mu = (0, \vec{\eta})$, so that eq. (5.332) becomes

$$\begin{aligned} \sum_\xi |\mathcal{M}_{fi}|^2 \sim I + \zeta'\cdot l = I + \zeta'_\mu l^\mu = \\ = I + \zeta'^0 l^0 - \vec{\zeta}\,'\cdot\vec{l} = \\ = I + \zeta'^0 l^0 - (\vec{\zeta}'_\perp + \zeta'_\parallel\hat{v}')\cdot\vec{l} = \\ = I + \frac{|\vec{p}\,'|}{m}\eta_\parallel l^0(\hat{v}'\cdot\hat{v}') - (\vec{\eta}_\perp + \frac{\varepsilon'}{m}\eta_\parallel\hat{v}')\cdot\vec{l} = \\ = I + \eta_\parallel\hat{v}'\cdot(\frac{|\vec{p}\,'|}{m}l^0\hat{v}' - \frac{\varepsilon'}{m}\vec{l}\,) - \vec{\eta}_\perp\cdot\vec{l} = \\ = I + \eta_\parallel\hat{v}'\cdot\Big(\frac{|\vec{p}\,'|}{m}l^0 - \frac{\varepsilon'}{m}l_\parallel\Big)\hat{v}' - \vec{\eta}_\perp\cdot\vec{l}_\perp = \\ = I + \eta_\parallel\hat{v}'\cdot\Big[\Big(\frac{|\vec{p}\,'|}{m}l^0 - \frac{\varepsilon'}{m}l_\parallel\Big)\hat{v}' - \vec{l}_\perp\Big] + \vec{\eta}_\perp\cdot\Big[\Big(\frac{|\vec{p}\,'|}{m}l^0 - \frac{\varepsilon'}{m}l_\parallel\Big)\hat{v}' - \vec{l}_\perp\Big] = \\ = I + (\eta_\parallel\hat{v}' + \vec{\eta}_\perp)\cdot\Big[\Big(\frac{|\vec{p}\,'|}{m}l^0 - \frac{\varepsilon'}{m}l_\parallel\Big)\hat{v}' - \vec{l}_\perp\Big] = \end{aligned}$$

$$\equiv I + \vec{\eta}\cdot\vec{\delta} = I\Big(1 + \vec{\eta}\cdot\frac{\vec{\delta}}{I}\Big), \tag{5.344}$$

where we defined

$$\vec{\delta} \equiv \Big(\frac{|\vec{p}\,'|}{m}l^0 - \frac{\varepsilon'}{m}l_\parallel\Big)\hat{v}' - \vec{l}_\perp. \tag{5.345}$$

By comparing eq. (5.344) and eq. (5.174), we can directly recognize the SQA to be

$$\vec{\zeta}^{(r)} = \frac{\vec{\delta}}{I}. \tag{5.346}$$

This vector describes a completely legitimate spin state

$$|\vec{\zeta}^{(r)}| \leq 1,$$

that can be used in any PIC or MC simulation. We used this new method to perform the same tests as those described at the end of sec. 5.6.2, thus replacing the algorithms described there. This time, not only the agreement between the new spin-photon energy curves in fig. 5.25 and those in fig. 5.9 is perfect, but all the states are physical.

The same argument applies to photon polarizations. By summing (5.331) over the final spins, we obtain

$$\sum_{\zeta'} |\mathcal{M}_{fi}|^2 \sim I + \xi\cdot y, \tag{5.347}$$

which can be used to extract the corresponding polarization states. We are still in the process of deriving a closed-form expression for the Stokes parameters ξ and the four-vector y, and we plan to present these results in a forthcoming work.

5.8 Conclusions

In this chapter, we have thoroughly derived the fully resolved differential probabilities for the NIC and NBW processes, detailed in energies, spins/polarizations, and angles, using the quasiclassical operator method by Baier and Katkov [44]. We also introduced an advanced version of the `SFQEDtoolkit`, a new computational module capable of comprehensively characterizing numerical particles, and demonstrated various applications of this toolkit. In the final section, we noted that the most general expressions for the NIC, Eqs. (5.39)-(5.43), and NBW, Eqs. (5.57)-(5.61), differentials are not genuine probabilities, as they may assume negative values. Specifically, these "improper" probabilities resolve so many parameters that they cease to be local: this precludes the application typically employed in simulation codes, where SFQED event characteristics are determined by the field

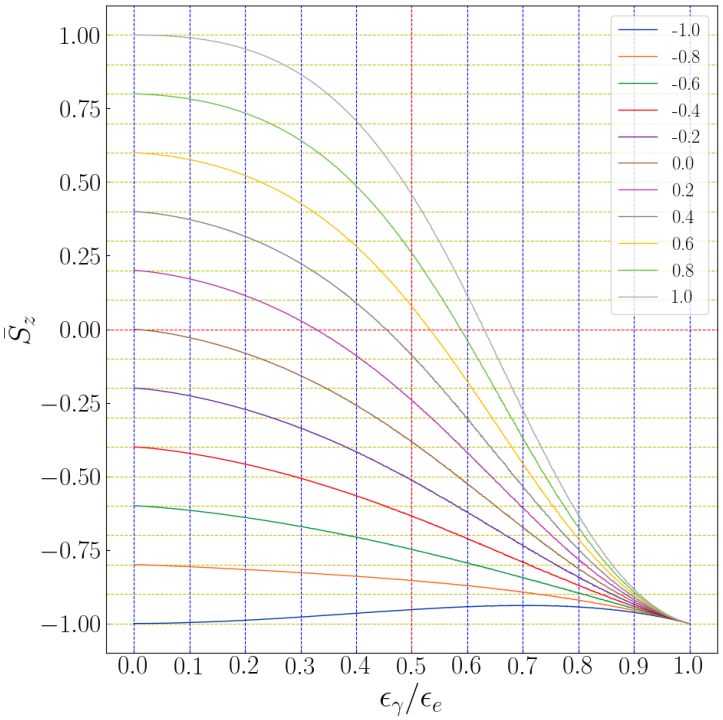

Figure 5.25: As in Fig. 5.16, all states are now physical, contributing to the expected behavior of the spin curves (averaged over the whole solid angle) shown in fig. 5.9.

values at the moment of emission, as they would result in either negative probabilities or unphysical spin and polarization states (with magnitudes exceeding one).

To restore their physical interpretation and overcome this issue, we proposed an LCFA-consistent procedure that reinterprets these otherwise ill-defined probability distributions. At the moment of emission, we construct a Constant Crossed Field (CCF) that ensures the emitting particle experiences the same quantum nonlinearity parameter χ and acceleration as in the original field. By integrating the contributions from the ill-defined emission probabilities along the quasiclassical particle's trajectory (within the new CCF), we obtain a nonlocal, fully resolved probability that can be used to determine a valid SQA and PQA. Although this approach is currently implemented only for the NIC process, the differential expressions (5.57)–(5.61) associated with the NBW process exhibit the same issues and will require a similar treatment. We plan to address this in future work.

Chapter 6

Conclusions and Outlook

In this final chapter, we summarize the key results of our work and outline promising directions for future research. In Chapter 2, we introduced Chebyshev polynomials and explored their properties, laying the groundwork for `ChAppX`, a flexible, parallel-optimized software designed to generate Chebyshev approximations for functions of one, two, or three variables with arbitrarily high accuracy. The Chebyshev approximations produced by `ChAppX` have been extensively incorporated into the strong-field (SF) QED-oriented library `SFQEDtoolkit`, presented in Chapter 3.

Completely open-source and available on GitHub[1], `SFQEDtoolkit` combines Chebyshev, asymptotic, and exponential expansions to efficiently approximate nonlinear Compton emission (NIC) and nonlinear Breit-Wheeler (NBW) pair creation distributions. Designed for seamless integration into existing particle-in-cell (PIC) and Monte Carlo (MC) codes, it provides an efficient implementation of SFQED processes with accuracy better than 0.1% across the entire particle spectrum. Benchmarks performed with the PIC code Smilei (v4.7) demonstrated that `SFQEDtoolkit` outperforms the default 256-point lookup tables and even surpasses the accuracy of 1024-point tables. Currently, NIC and NBW processes are implemented under the locally-constant-field approximation (LCFA), assuming collinear emission of generated particles. For photon emission, we also included the beyond-LCFA method from Ref. [62] (discussed in Section 3.4).

To test `SFQEDtoolkit` under realistic conditions, we integrated it into the PIC code CALDER [43] and, as detailed in Chapter 4, simulated the collision of 9 and 90 GeV electron bunches with thick solid targets composed of lithium (Li) or gold (Au). These simulations demonstrated that "short" electron-positron jets, whose densities exceed those of solid matter, can form within the 10 MT self-generated magnetic fields developing inside the high-Z Au target. In this regime, atomic field ionization, NIC photon emission, and NBW pair production reinforce one another: the processes initially generate a strong magnetic field, which in turn drives the creation of an exceptionally large number of particles.

The simulations described above operate in a completely new regime where SFQED, atomic and plasma physics are strongly intertwined. Yet, this is only one example

[1] https://github.com/QuantumPlasma/SFQEDtoolkit

of a pioneering experiment meant to explore uncharted territory in QED. Consider, for instance, the recently proposed precision studies of radiation reaction[2] in the collisions between a high-intensity laser and an ultrarelativistic electron beam [109–111], or the LUXE [112] and E-320 [113] experiments, which should probe non-perturbative QED in electron- and photon-laser collisions. All these scenarios demand accurate and efficient numerical methods capable of supporting the ever-growing need to explore SFQED by resolving every degree of freedom of the particles involved.

Motivated by this challenge, in Chapter 5 we developed analytical expressions for the NIC and NBW differential distributions, detailing the particles' energy, emission angles, spins and polarizations. We then implemented these functions into a new computational module of `SFQEDtoolkit`, designed to overcome the limitations of state-of-the-art codes by sampling the momenta (in modulus and directions) of numerical particles, together with their spin/polarization-states. During the testing of this module, we discovered that the general expressions for the NIC and NBW differential distributions do not always yield genuine probabilities, as they can become negative, leading to spin and polarization distributions that lack direct physical interpretation. However, by defining a tailored Constant Crossed Field (CCF) around the emitting particle at the moment of emission, and integrating the contributions of these ill-defined quantities along its quasiclassical trajectory, we obtained predictions that are consistent with a stochastic interpretation. Applying this approach to the NIC process allowed us to derive a physically consistent expression for the final spin state. This, combined with the information we can extract about the energy and angular distributions (see Secs. 5.4 and 5.5) enables the determination of the complete final electron state following the event. An equivalent expression for the photon polarization-state is under development. Additionally, the differential expressions (5.57)-(5.61) for the NBW process exhibit similar inconsistencies and will require a comparable treatment, which we plan to address in future work.

6.1 Outlook

The results obtained from the "thick-target" simulation in Chapter 4 could pave the way for research in a new regime, where atomic and plasma physics are strongly interlaced to SFQED. Further refinements to the simulation setup (Fig. 4.1), along with a deeper investigation into the pair production mechanism, could lead to an efficient method for generating neutral pair-plasma. In turn, this would enable us to probe the microphysics governing extreme astrophysical environments, such as those found in pulsars and magnetars.

Regarding the fully resolved NIC and NBW distributions discussed in Chapter 5,

[2] i.e., the self-interaction of a charged lepton with its own electromagnetic field

several open questions remain. Most importantly, the CCF-based technique we developed for extracting physical spin states must be extended to account for the polarization of NIC photons and the spins of NBW pairs. Once this extension is fully implemented in `SFQEDtoolkit`'s advanced module, we can conduct a simulation similar to the thick-target study in Chapter 4, but with a key improvement: each computational particle will be fully characterized in terms of energy, angular distribution, and polarization. We envisage that NIC emissions and NBW decays occurring in different directions could significantly influence the spin and polarization states of the particles. This, in turn, may provide novel observables for the ultrafast diagnostic and characterization of plasma dynamics.

Appendix A

User guide

SFQEDtoolkit is an open source library written in C++. A wrapper for Fortran-based programs which leverages the standardized interoperability of modern Fortran with C is also provided with the current version. SFQEDtoolkit can be used as a black box by following the instructions below and the examples showing its usage provided on GitHub at:
https://github.com/QuantumPlasma/SFQEDtoolkit.

This appendix describes the key steps needed for implementing SFQEDtoolkit, and the main functions currently available. SFQEDtoolkit exposes all functions[1] to the user through the module SFQEDtoolki_Interface.hpp and SFQEDtoolkit_Interface.f90 to C++ and Fortran codes, respectively. We recommend users to read this appendix before implementing the library.

SFQEDtoolkit must be initialized and finalized once at the beginning and at the end of the simulation, respectively. The functions assigned to carry out these two purposes are the only ones that *must* be necessarily implemented in a code employing SFQEDtoolkit: all other available SFQEDtoolkit functions are independent of each other and can be ignored if not required, i.e., only the functions that are desired have to be implemented in a code. Thus, for example, none of the functions of the beyond LCFA method of Sec. 3.4 needs to be implemented if not used. Analogously, for example, if one is interested in photon emission according to the LCFA method but not in pair creation, then the implementation of the function that compute the LCFA photon emission rate and of the function that calculate the LCFA emitted photon energy may suffice. In fact, e.g., for testing purposes, one can even implement only the SFQEDtoolkit function for the LCFA photon emission rate, and use a custom version for calculating the LCFA emitted photon energy, or vice versa. This enables high flexibility and allows users to customize SFQEDtoolkit to their code and to their specific objective without implementing unnecessary functions.

Figure A.1 displays the flowchart of a PIC code embedding SFQEDtoolkit. At initialization all the precomputed Chebyshev coefficients stored in the txt files included with the library are loaded into memory[2]. At this stage the user needs

[1] Possible other minor functions, typically variation of the main functions, are included to address specific requests of some users.

[2] The tables with the Chebyshev coefficients are available in the "coefficients" folder of

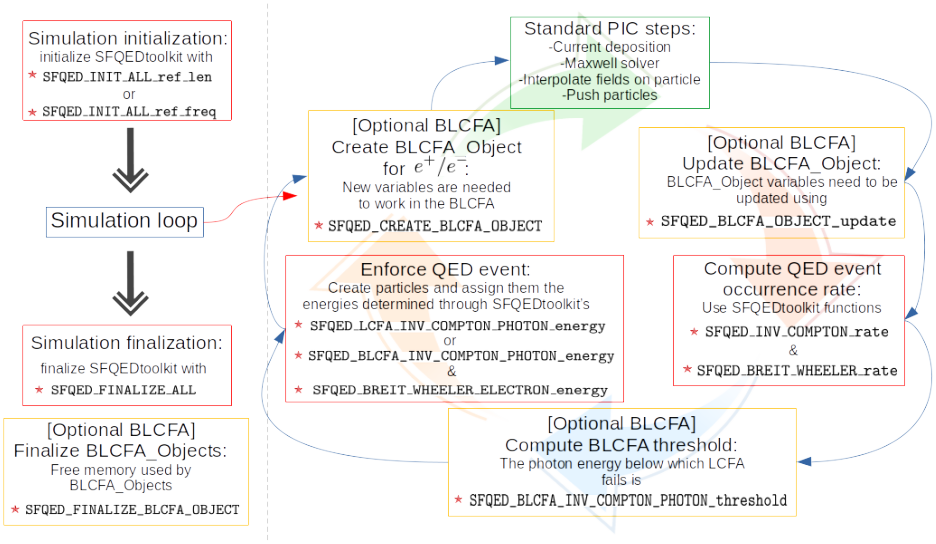

Figure A.1: Workflow of a PIC code implementing the routines provided by `SFQEDtoolkit`.

to specify either the reference length or the reference frequency of the simulation. This is required because in `SFQEDtoolkit` all quantities are given in normalized units, and an angular frequency ω_r is used as a reference. Consequently, the reference time $T_r = 1/\omega_r$, length $\lambda_r = c/\omega_r$, and field $E_r = m_e c\omega_r/|e|$ are obtained, while energy is normalized to $m_e c^2$. In particular, notice that in a problem where lengths are given in units of the laser wavelength λ, then $\lambda_r = \lambda/2\pi$ such that $\omega_r = 2\pi c/\lambda$.

The initialization is carried out through either the first or the second of the two following functions

1: `bool SFQED_INIT_ALL_ref_len(double ref_len, double ts)`: initializes the environment by loading into memory all coefficients needed for modeling SFQED processes. In addition, it stores the reference length `ref_len`= λ_r and the timestep of the simulation `ts`= Δt. The reference length must be given in meters, while the simulation timestep must be given in normalized units, i.e., in units of $T_r = 1/\omega_r$. The simulation timestep is used only by the routines that implement the beyond LCFA photon emission method described in Sec. 3.4. At runtime, `SFQEDtoolkit` reads the required information from files located in the subdirectory "coefficients" from the parent directory where the program is executed. If initialization is successful,

`SFQEDtoolkit` at https://github.com/QuantumPlasma/SFQEDtoolkit. The "coefficients" folder includes a "README.md" file detailing how to interpret the content of each file, and how the Chebyshev coefficients stored in the files are connected to the function that they approximate, including the specific interval of approximation.

the function returns a boolean that is `true`.

2: `bool SFQED_INIT_ALL_ref_freq(double ref_freq, double ts)`: equivalent and alternative to function 1. The only difference is that the scale of the simulation is set by providing the reference angular frequency `ref_freq`= ω_r in SI units.

If the photon emission method beyond LCFA of Sec. 3.4 is employed, `SFQEDtoolkit` provides users with a `C++` object named `BLCFA_Object` that is designed to allocate the additional information that is required to keep track of the force acting on the particle. Namely, a boolean signaling whether the particle was created at the penultimate timestep, and two arrays each with three double precision elements. One array stores the transverse Lorentz force at the penultimate timestep, the other array stores the difference of the Lorentz force between the penultimate and the antipenultimate timestep. This object is created by calling the function

3: `BLCFA_Object* SFQED_CREATE_BLCFA_OBJECT()`: creates an object designed to store the information required to apply the beyond LCFA method to a particle. The boolean is set to `true`, while the two arrays are initialized to zero. The function returns a pointer to the created `BLCFA_Object`.

If this function is implemented, each computational particle should have one `BLCFA_Object` associated. It is up to the user to organize objects in a suitable data structure (array, linked list, etc.) and, if the code in which `SFQEDtoolkit` is implemented uses message passing interface (MPI), to manage the communication of the object data among MPI domains. A recommended choice is to use inheritance to derive from `BLCFA_Object` an object `Particle`, where information such as particle position and momentum is stored, and to create either an array or a `C++` vector to store the data of all particles in the simulation. Another option is to include a pointer to a `BLCFA_Object` in the class or data type used by the existing code to store information about a particle's status. In a parallel code using MPI, the communication of the additional particle data stored in `BLCFA_Object` should follow the same methodology used by the code to communicate other particle information such as particle's position and momentum. In fact, one should simply communicate the elementary datatypes stored in a `BLCFA_Object` instead of the `BLCFA_Object` itself.

Next, the standard steps of a PIC loop are performed: currents are deposited on the grid, Maxwell equations are solved, the resulting fields on the grid are interpolated at the particle's position, and particles are advanced in time according to the Lorentz force with a suitable particle 'pusher' (see, e.g., Ref. [35]). If a leapfrog integrator is used, a convenient choice is to adapt the implementation to its staggered method by first advancing the particle momentum, then call the routines for

modeling SFQED processes, and only afterward advance the particle position and store the new data into memory.

Again, only when using the beyond LCFA method for photon emission of Sec. 3.4, a user employing the `BLCFA_Object` and its features can resort to the function

> 4: `bool SFQED_BLCFA_OBJECT_update(BLCFA_Object* obj, double* p_push, double* p, double delta, double gamma, double chi)`: if the boolean of the `BLCFA_Object` pointed by `obj` is `true`, calculates $\boldsymbol{F}^{(n)}_{L,\perp}$ from Eqs. (3.50)-(3.53) by using the particle momentum before `p` and after `p_push` one timestep, and changes the boolean of `BLCFA_Object` to `false`. In addition, it sets both arrays of the `BLCFA_Object` equal to the computed $\boldsymbol{F}^{(n)}_{L,\perp}$, while the boolean returned by the function is `false` to signal no emission at this timestep. By contrast, if the boolean of the `BLCFA_Object` pointed by `obj` is `false`, uses the particle momentum before `p` and after `p_push` one timestep to perform all calculations in Eqs. (3.50)-(3.57). Then, it returns `delta` as defined in Eq. (3.57), the normalized particle energy `gamma` [Eq. (3.52)], and its quantum parameter `chi` [Eq. (3.54)]. Finally, the two arrays of the `BLCFA_Object` pointed by `obj` are updated by storing $\boldsymbol{F}^{(n)}_{L,\perp}$ and $\boldsymbol{F}^{(n)}_{L,\perp} - \boldsymbol{F}^{(n-1)}_{L,\perp}$, while the boolean returned by the function is `true` only if the necessary conditions for applying the local emission model hold [see the conditions below Eq. (3.57)].

While functions 3 and 4 are optional and relevant only for the photon emission model beyond LCFA of Sec. 3.4, SFQED probability rates must be computed for each particle and at each timestep in the considered LCFA and beyond LCFA models. `SFQEDtoolkit` allows users to efficiently compute the SFQED rates by means of

> 5: `double SFQED_INV_COMPTON_rate(double gamma, double chi)`: uses the normalized electron or positron energy `gamma`, as well as its quantum parameter `chi`, to return the LCFA photon emission probability rate.

> 6: `double SFQED_BREIT_WHEELER_rate(double gamma, double chi)`: uses the normalized photon energy `gamma` as well as its quantum parameter `chi` to return the LCFA probability rate of photon conversion in an electron-positron pair.

> 7: `double SFQED_BREIT_WHEELER_rate_fast(double gamma, double chi)`: same as function 6 but it returns zero if `chi` < 0.3 (see Sec. 3.3.2).

From a purely technical point of view, since the beyond LCFA photon emission method of Sec. 3.4 is based on an acceptance-rejection technique, the optical depth method cannot be used to determine whether a SFQED event is deemed to occur.

In case a SFQED event is deemed to occur according to the LCFA probability rate, the energy of generated particles is computed by calling

> 8: `double SFQED_LCFA_INV_COMPTON_PHOTON_energy(double gamma, double chi, double rnd)`: returns the normalized photon energy by sampling from the LCFA energy distribution. Its input parameters are the normalized electron or positron energy `gamma`, the quantum parameter `chi` of the emitting particle, and a random number `rnd` sampled from a uniform distribution in $(0, 1)$.

> 9: `double SFQED_BREIT_WHEELER_ELECTRON_energy(double gamma, double chi, double rnd)`: returns the normalized energy of the generated electron (positron) by sampling from the LCFA energy distribution for photon conversion into an electron-positron pair. The energy of the positron (electron) is then readily obtained from the difference between the photon and the electron (positron) energy. The normalized photon energy `gamma` and its quantum parameter `chi`, as well as a uniformly distributed random number `rnd` in $(0, 1)$, must be passed as input parameters.

> 10: `double SFQED_BREIT_WHEELER_ELECTRON_energy_fast(double gamma, double chi, double rnd)`: same as function 9, but `chi` < 0.3 is not managed. This function must be used only in combination with function 7.

When the beyond LCFA model of Sec. 3.4 is used, if function 4 returns `true` and a SFQED event is deemed to occur according to the LCFA probability rate (see function 5), the calculation of the local LCFA energy threshold $\gamma_{\gamma,\mathrm{LCFA}}$, as defined in Eq. (3.58), is required to determine the improved photon energy distribution. If `BLCFA_Object`s are created and updated through functions 3 and 4, respectively, then $\gamma_{\gamma,\mathrm{LCFA}}$ can be computed by calling

> 11: `double SFQED_BLCFA_INV_COMPTON_PHOTON_threshold(BLCFA_Object* obj, double delta, double gamma, double chi)`: returns the normalized photon energy threshold below which the LCFA breaks, i.e., the $\gamma_{\gamma,\mathrm{LCFA}}$ defined in Eq. (3.58). The arguments of this routine are those passed to and updated by function 4.

After calling function 11 all required quantities for the beyond LCFA method are available, and the photon energy is obtained from

12: `double SFQED_BLCFA_INV_COMPTON_PHOTON_energy(double limit, double gamma, double chi,double rnd, double rnd2)`: returns the normalized photon energy according to the beyond LCFA model of Sec. 3.4. This function requires as input the same parameters of function 8, plus two additional arguments: (i) the `limit`=$\gamma_{\gamma,\mathrm{LCFA}}$ defined in Eq. (3.58), which users can obtain by calling function 11, and (ii) `rnd2`, which is a uniformly distributed random number in $(0,1)$ independent of `rnd`. If $\gamma_{\gamma,\mathrm{LCFA}} > 0.75\gamma_e$ the function returns zero. Otherwise, it applies the acceptance-rejection technique of Sec. 3.4 and returns zero if the event is rejected.

After the above steps, the computational cycle is complete and is repeated until the end of the simulation is reached. At this point, if the `BLCFA_Object` was used, memory should be deallocated by calling the function

13: `void SFQED_FINALIZE_BLCFA_OBJECT(BLCFA_Object* obj)`: deallocates the memory space reserved for the `BLCFA_Object` pointed by `obj`.

and `SFQEDtoolkit` should be 'finalized' (meaning that the memory reserved by `SFQEDtoolkit` for storing the tables of coefficients should be deallocated, by calling the function

14: `void SFQED_FINALIZE_ALL()`: frees all the memory allocated at initialization.

Finally, `SFQEDtoolkit` provides users with two functions for the computation of the particle quantum nonlinearity parameter χ according to Eq. (3.21), and one function implementing the collinear emission model for the generated particle.

15: `double compute_chi_with_vectors(double gamma, double p[3], double EE[3], double BB[3])`: returns the quantum nonlinearity parameter $\chi_{\gamma/e}$ of a particle with energy `gamma` and momentum `p` in an electric `EE` and magnetic `BB` field. All quantities must be provided in normalized units.

16: `double compute_chi_with_components(double gamma, double px, double py, double pz, double EEx, double EEy, double EEz, double BBx, double BBy, double BBz)`: same as 15 but the electric and magnetic field are passed component-by-component.

17: `void SFQED_build_collinear_momentum(double gamma_out, double p_in[3], double p_out[3])`: returns the momentum of

the generated particle `p_out` aligned with the momentum of the parent particle `p_in` and sets it magnitude according to the energy of the generated particle `gamma_out`. All parameters are in normalized units.

The above functions can be used in combination with functions 5–10.

Appendix B

The Sokolov-Ternov effect

To benchmark the fully resolved NIC numerical module implemented in `SFQEDtoolkit`, see Chap. 5, we simulated a 1 GeV electron beam comprising 10^6 particles circulating in a transverse magnetic field B, corresponding to a nonlinear quantum parameter of $\chi_e = 10^{-3}$. Under these conditions, the differing transition rates for electron spin alignment relative to the magnetic field cause the initially unpolarized beam to develop a net spin polarization opposite to the field direction. However, this polarization does not reach full saturation; its limiting value is explicitly given by [114]

$$\begin{aligned} \zeta(t) &= A\Big(1 - \exp\Big\{-\frac{t}{\tau}\Big\}\Big) \\ \tau &= A\frac{1}{m\alpha\gamma_e^2}\Big(\frac{B_{cr}}{B}\Big)^3 \\ A &= \frac{8\sqrt{3}}{15}, \end{aligned} \tag{B.1}$$

where B_{cr} is the critical Schwinger (magnetic) field. This phenomenon is known as the Sokolov-Ternov effect. Figure B.1 compares the evolution of the bunch's average spin component along the magnetic field (blue line) with the theoretical prediction from Eq. (B.1) (orange dashed line). The agreement between `SFQEDtoolkit` and theory is excellent. Moreover, due to the low value of χ_e, photon emission is minimal, and the change in electron polarization is entirely attributable to the "no emission spin flip" mechanism described in Sec. 5.4.1. Without this effect, the beam's polarization would remain almost unchanged.

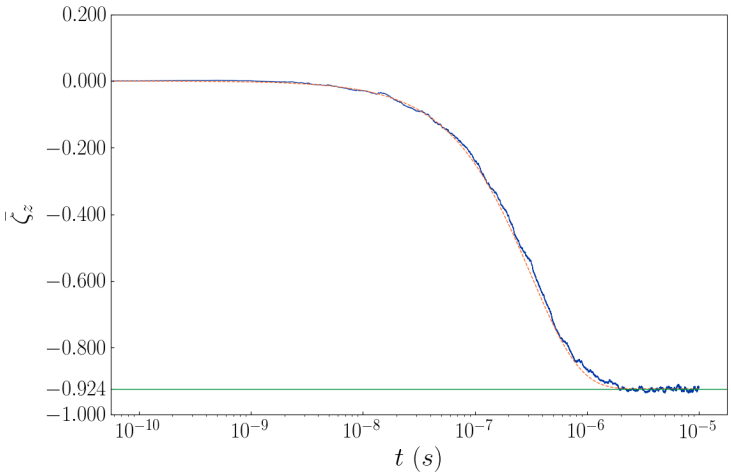

Figure B.1: Sokolov-Ternov Effect: Owing to the selection rule imposed by the spin-dependent terms in the NIC photon emission rate (see Eq. (5.71)), an electron beam moving through a weak magnetic field tends to polarize with its spin aligning antiparallel to the field. This polarization is incomplete and saturates at approximately $A \approx 92.4\%$ (green line). The figure compares the theoretical prediction (orange dashed line) with the numerical results obtained using `SFQEDtoolkit` (blue line).

Appendix C

Bessel functions approximations

Throughout chapter 5, we extensively employed the modified Bessel functions of the second kind, $K_{\frac{1}{3}}(x)$ and $K_{\frac{2}{3}}(x)$, along with the integrals $\int_x^{30} K_{\frac{1}{3}}(y)dy$ and $\int_x^{\infty} K_{\frac{1}{3}}(y)dy$. Since computing these functions can be resource-intensive[1], `SFQEDtoolkit` uses their Chebyshev approximations. To manage this efficiently, we partitioned the domain of x into distinct subdomains, each addressed by a tailored Chebyshev approximation or an asymptotic expansion.

$K_{\frac{1}{3}}(x)$ is implemented in `SFQEDtoolkit` using the following strategy:

- $0 < x \leq 0.1$: Use the asymptotic expansion

$$K_{\frac{1}{3}}(x) \xrightarrow{x\to 0} \frac{\Gamma(\frac{1}{3})}{2^{\frac{2}{3}}x^{\frac{1}{3}}} + \frac{\Gamma(-\frac{1}{3})x^{\frac{1}{3}}}{2^{\frac{4}{3}}} + \frac{3\Gamma(\frac{1}{3})x^{\frac{5}{3}}}{2^{\frac{11}{3}}}. \tag{C.1}$$

- for $0.1 < x \leq 1$: Evaluate the Chebyshev approximation $C\left[K_{\frac{1}{3}}(x)x^{\frac{1}{3}}\right]x^{-\frac{1}{3}}$. Here, we apporximate $K_{\frac{1}{3}}(x)x^{\frac{1}{3}}$ (as indicated by Eq. (C.1)) to reduce the number of Chebyshev coefficients required. This technique is also applied in the high-x region.

- for $1 < x \leq 7$: Use the Clenshaw recurrence formula to evaluate the Chebyshev approximation $C\left[K_{\frac{1}{3}}(x)\right]$.

- for $7 < x \leq 30$: Compute the approximation $C\left[K_{\frac{1}{3}}(x)e^{x}x^{\frac{1}{2}}\right]e^{-x}x^{-\frac{1}{2}}$. This transformation removes the dominant behavior of $K_{\frac{1}{3}}(x)$ for large x, where it asymptotically expands as

$$K_{\frac{1}{3}}(x) \xrightarrow{x\to\infty} e^{-x}\sqrt{\frac{\pi}{2}}\left(x^{-\frac{1}{2}} - \frac{5}{72}x^{-\frac{3}{2}}\right). \tag{C.2}$$

- for $x \geq 30$: Use the asymptotic expression from Eq. (C.2) directly.

This multi-branched approach ensures efficient and accurate computation of $K_{\frac{1}{3}}(x)$ over its entire domain.

[1] In terms of the computational time and memory required to compute these functions.

For $K_{\frac{2}{3}}(x)$, we adopt a similar strategy to that described above for $K_{\frac{1}{3}}(x)$:

- for $0 < x \leq 0.1$: We use the asymptotic expansion

$$K_{\frac{2}{3}}(x) \xrightarrow{x\to 0} \frac{\Gamma(\frac{2}{3})}{2^{\frac{1}{3}}x^{\frac{2}{3}}} + \frac{\Gamma(-\frac{2}{3})x^{\frac{2}{3}}}{2^{\frac{5}{3}}} + \frac{3\Gamma(\frac{1}{3})x^{\frac{4}{3}}}{2^{\frac{7}{3}}}. \tag{C.3}$$

- for $0.1 < x \leq 1$: The function is approximated by $C\left[K_{\frac{2}{3}}(x)x^{\frac{2}{3}}\right]x^{-\frac{2}{3}}$.

- for $1 < x \leq 7$: We approximate $K_{\frac{2}{3}}(x)$ using $C\left[K_{\frac{2}{3}}(x)\right]$.

- for $7 < x \leq 30$: We employ the approximation $C\left[K_{\frac{2}{3}}(x)e^{x}x^{\frac{1}{2}}\right]e^{-x}x^{-\frac{1}{2}}$.

- for $x \geq 30$: The asymptotic expression

$$K_{\frac{2}{3}}(x) \xrightarrow{x\to\infty} e^{-x}\sqrt{\frac{\pi}{2}}\left(x^{-\frac{1}{2}} + \frac{7}{72}x^{-\frac{3}{2}}\right) \tag{C.4}$$

  is used directly.

This multi-tiered approach ensures efficient and accurate computation of $K_{\frac{2}{3}}(x)$ across its entire domain.

The integral $\int_x^{30} K_{\frac{1}{3}}(y)dy$, primarily used for the computations in Section 5.5, is approximated as follows:

- for $0 < x \leq 0.1$: We use the identity

$$\int_x^{30} K_{\frac{1}{3}}(y)dy = \int_0^{30} K_{\frac{1}{3}}(y)dy - \int_0^{x} K_{\frac{1}{3}}(y)dy.$$

  The first term, $\int_0^{30} K_{\frac{1}{3}}(y)dy \equiv a$, is a constant, while for the second term we substitute (into the integral) the asymptotic expansion from Eq. (C.1). Keeping only the leading terms after integration, we obtain

$$\int_x^{30} K_{\frac{1}{3}}(y)dy \xrightarrow{x\to 0} a - \left(\frac{3\Gamma(\frac{1}{3})}{2^{\frac{5}{3}}}x^{\frac{2}{3}} + \frac{3\Gamma(-\frac{1}{3})}{2^{\frac{10}{3}}}x^{\frac{4}{3}}\right). \tag{C.5}$$

- for $0.1 < x \leq 2.5$: `SFQEDtoolkit` uses the approximation $C\left[\int_x^{\infty} K_{\frac{1}{3}}(y)dy\right] - \int_{30}^{\infty} K_{\frac{1}{3}}(y)dy$. This formulation is preferred because the Chebyshev coefficients for $C\left[\int_x^{\infty} K_{\frac{1}{3}}(y)dy\right]$ are slightly fewer than those needed for $C\left[\int_x^{30} K_{\frac{1}{3}}(y)dy\right]$, and

$$b = \int_{30}^{\infty} K_{\frac{1}{3}}(y)dy$$

  is a constant.

- for $2.5 < x \leq 29.95$ and $29.95 < x < 30$: The same Chebyshev approximation is applied in both ranges

$$C\left[e^x \int_x^{30} K_{\frac{1}{3}}(y)dy\right]e^{-x},$$

with different sets of Chebyshev coefficients computed over the respective intervals. The exponential factor is introduced because, as shown in Eq. (C.2), $K_{\frac{1}{3}}$ decays as e^{-x}. Without this factor, the function to be approximated would be nearly zero, necessitating an impractically large number of coefficients. Since the integral of an exponential remains exponential, multiplying by e^x solves the issue.

- for $x = 30$: the function is forced to be zero.

For the integral $\int_x^{\infty} K_{\frac{1}{3}}(y)dy$, a similar procedure is followed with slight modifications:

- In the first range, the constant becomes $\int_0^{\infty} K_{\frac{1}{3}}(y)dy \equiv a'$, instead of a.
- In the second range, we no longer subtract the constant $b = \int_{30}^{\infty} K_{\frac{1}{3}}(y)dy$; instead, b is added to the approximations in the subsequent intervals (i.e., $2.5 < x \leq 29.95$ and *iv*) $29.95 < x < 30$).
- for $x = 30$: The function evaluates to b.
- for $x > 30$: We integrate the asymptotic expansion from Eq. (C.2):

$$\int_x^{\infty} e^{-y}\sqrt{\frac{\pi}{2}}\left(y^{-\frac{1}{2}} - \frac{5}{72}y^{-\frac{3}{2}}\right)dy = -\frac{5}{36}\sqrt{\frac{\pi}{2}}e^{-y}y^{-\frac{1}{2}} + \frac{41}{36}\frac{\pi}{\sqrt{2}}erfc(\sqrt{y}), \tag{C.6}$$

where $erfc(y) = 1 - erf(y) = \frac{2}{\sqrt{\pi}}\int_y^{\infty} e^{-t^2}dt$ is the complementary error function. Taking the asymptotic expansion of this result (with assistance from Wolfram Mathematica) yields the expression used by the toolkit:

$$\int_x^{\infty} K_{\frac{1}{3}}(y)dy \xrightarrow{x\to\infty} e^{-y}\sqrt{\frac{\pi}{2}}\left(y^{-\frac{1}{2}} - \frac{41}{72}y^{-\frac{3}{2}}\right). \tag{C.7}$$

Finally, it is important to note that each of these approximations has been rigorously tested against the corresponding functions as implemented in the GSL. Our evaluation of both accuracy and performance shows that the percentage error never exceeds 0.1% (see Fig. C.1), and our implementations significantly outperform the Gnu Scientific Libreries (GSL) [115] in terms of speed.

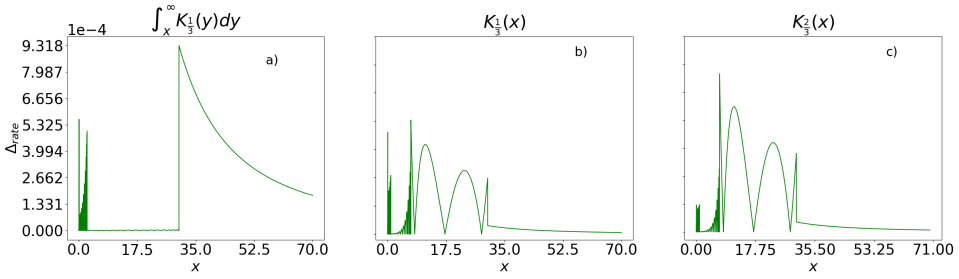

Figure C.1: Relative error between the GSL and `SFQEDtoolkit` implementations of the modified Bessel functions $K_{\frac{1}{3}}(x)$, $K_{\frac{2}{3}}(x)$, and the integral $\int_x^\infty K_{\frac{1}{3}}(y)dy$.

Bibliography

[1] T. H. Maiman, Nature **187**, 493 (1960).

[2] D. Strickland and G. Mourou, Optics Communications **56**, 219 (1985).

[3] Center for relativistic laser science, https://www.ibs.re.kr/eng/sub02_03_05.do.

[4] J. W. Yoon, Y. G. Kim, I. W. Choi, J. H. Sung, H. W. Lee, S. K. Lee, and C. H. Nam, Optica **8**, 630 (2021).

[5] Apollon, https://apollonlaserfacility.cnrs.fr.

[6] Extreme light infrastructure, https://eli-laser.eu.

[7] National ignition facility, https://lasers.llnl.gov/.

[8] Zettawatt-equivalent ultrashort pulse laser system at the university of michigan, https://zeus.engin.umich.edu/.

[9] The international committee on ultra-high intensity lasers, https://www.icuil.org/downloadss/laser-labs.html.

[10] F. Sauter, Zeitschrift für Physik **69**, 742 (1931).

[11] J. Schwinger, Phys. Rev. **82**, 664 (1951).

[12] L. D. Landau and E. M. Lifshitz, The classical theory of fields (Pergamon Press, Oxford, 1971) Chap. 76, 78, 3rd ed.

[13] C. Bula, K. T. McDonald, E. J. Prebys, C. Bamber, S. Boege, T. Kotseroglou, A. C. Melissinos, D. D. Meyerhofer, W. Ragg, D. L. Burke, R. C. Field, G. Horton-Smith, A. C. Odian, J. E. Spencer, D. Walz, S. C. Berridge, W. M. Bugg, K. Shmakov, and A. W. Weidemann, Phys. Rev. Lett. **76**, 3116 (1996).

[14] G. Breit and J. A. Wheeler, Phys. Rev. **46**, 1087 (1934).

[15] D. L. Burke, R. C. Field, G. Horton-Smith, J. E. Spencer, D. Walz, S. C. Berridge, W. M. Bugg, K. Shmakov, A. W. Weidemann, C. Bula, K. T. McDonald, E. J. Prebys, C. Bamber, S. J. Boege, T. Koffas, T. Kotseroglou, A. C. Melissinos, D. D. Meyerhofer, D. A. Reis, and W. Ragg, Phys. Rev. Lett. **79**, 1626 (1997).

[16] G. Sarri, W. Schumaker, A. Di Piazza, M. Vargas, B. Dromey, M. E. Dieckmann, V. Chvykov, A. Maksimchuk, V. Yanovsky, Z. H. He, B. X. Hou, J. A. Nees, A. G. R. Thomas, C. H. Keitel, M. Zepf, and K. Krushelnick, Phys. Rev. Lett. **110**, 255002 (2013).

[17] G. Sarri, K. Poder, J. M. Cole, W. Schumaker, A. Di Piazza, B. Reville, T. Dzelzainis, D. Doria, L. A. Gizzi, G. Grittani, S. Kar, C. H. Keitel, K. Krushelnick, S. Kuschel, S. P. D. Mangles, Z. Najmudin, N. Shukla, L. O. Silva, D. Symes, A. G. R. Thomas, M. Vargas, J. Vieira, and M. Zepf, Nature Communications **6**, 6747 (2015).

[18] R. Ruffini, G. Vereshchagin, and S.-S. Xue, Physics Reports **487**, 1 (2010).

[19] D. A. Uzdensky and S. Rightley, Reports on Progress in Physics **77**, 036902 (2014).

[20] B. Cerutti, A. A. Philippov, and A. Spitkovsky, Monthly Notices of the Royal Astronomical Society **457**, 2401 (2016).

[21] A. Philippov, A. Timokhin, and A. Spitkovsky, Phys. Rev. Lett. **124**, 245101 (2020).

[22] A. R. Bell and J. G. Kirk, Phys. Rev. Lett. **101**, 200403 (2008).

[23] A. M. Fedotov, N. B. Narozhny, G. Mourou, and G. Korn, Phys. Rev. Lett. **105**, 080402 (2010).

[24] N. V. Elkina, A. M. Fedotov, I. Y. Kostyukov, M. V. Legkov, N. B. Narozhny, E. N. Nerush, and H. Ruhl, Phys. Rev. ST Accel. Beams **14**, 054401 (2011).

[25] E. N. Nerush, V. F. Bashmakov, and I. Y. Kostyukov, Phys. Plasmas **18**, 083107 (2011).

[26] E. N. Nerush, I. Y. Kostyukov, A. M. Fedotov, N. B. Narozhny, N. V. Elkina, and H. Ruhl, Phys. Rev. Lett. **106**, 035001 (2011).

[27] C. P. Ridgers, C. S. Brady, R. Duclous, J. G. Kirk, K. Bennett, T. D. Arber, A. P. L. Robinson, and A. R. Bell, Phys. Rev. Lett. **108**, 165006 (2012).

[28] V. F. Bashmakov, E. N. Nerush, I. Y. Kostyukov, A. M. Fedotov, and N. B. Narozhny, Phys. Plasmas **21**, 013105 (2014).

[29] E. G. Gelfer, A. A. Mironov, A. M. Fedotov, V. F. Bashmakov, E. N. Nerush, I. Y. Kostyukov, and N. B. Narozhny, Phys. Rev. A **92**, 022113 (2015).

[30] T. Grismayer, M. Vranic, J. L. Martins, R. A. Fonseca, and L. O. Silva, Phys. Plasmas **23**, 056706 (2016).

[31] T. Grismayer, M. Vranic, J. L. Martins, R. A. Fonseca, and L. O. Silva, Phys. Rev. E **95**, 023210 (2017).

[32] M. Tamburini, A. Di Piazza, and C. H. Keitel, Sci. Rep. **7**, 5694 (2017).

[33] M. Jirka, O. Klimo, M. Vranic, S. Weber, and G. Korn, Scientific Reports **7**, 15302 (2017).

[34] A. Sampath and M. Tamburini, Phys. Plasmas **25**, 083104 (2018).

[35] C. K. Birdsall and A. B. Langdon, *Plasma Physics Via Computer Simulation* (Institute of Physics, Bristol, 1991).

[36] C. Ridgers, J. Kirk, R. Duclous, T. Blackburn, C. Brady, K. Bennett, T. Arber, and A. Bell, J. Comput. Phys. **260**, 273 (2014).

[37] T. D. Arber, K. Bennett, C. S. Brady, A. Lawrence-Douglas, M. G. Ramsay, N. J. Sircombe, P. Gillies, R. G. Evans, H. Schmitz, A. R. Bell, and C. P. Ridgers, Plasma Phys. Control. Fusion **57**, 113001 (2015).

[38] A. Gonoskov, S. Bastrakov, E. Efimenko, A. Ilderton, M. Marklund, I. Meyerov, A. Muraviev, A. Sergeev, I. Surmin, and E. Wallin, Phys. Rev. E **92**, 023305 (2015).

[39] M. Lobet, E. d'Humières, M. Grech, C. Ruyer, X. Davoine, and L. Gremillet, Journal of Physics: Conference Series **688**, 012058 (2016).

[40] F. Niel, C. Riconda, F. Amiranoff, M. Lobet, J. Derouillat, F. Pérez, T. Vinci, and M. Grech, Plasma Physics and Controlled Fusion **60**, 094002 (2018).

[41] L. Fedeli, N. Zaïm, A. Sainte-Marie, M. Thévenet, A. Huebl, A. Myers, J.-L. Vay, and H. Vincenti, New Journal of Physics **24**, 025009 (2022).

[42] Y. Guo, X. Geng, L. Ji, B. Shen, and R. Li, Phys. Rev. E **105**, 025309 (2022).

[43] E. Lefebvre, N. Cochet, S. Fritzler, V. Malka, M.-M. Aléonard, J.-F. Chemin, S. Darbon, L. Disdier, J. Faure, A. Fedotoff, O. Landoas, G. Malka, V. Méot, P. Morel, M. R. L. Gloahec, A. Rouyer, C. Rubbelynck, V. Tikhonchuk, R. Wrobel, P. Audebert, and C. Rousseaux, Nuclear Fusion **43**, 629 (2003).

[44] V. N. Baier, V. M. Katkov, and V. M. Strakhovenko, *Electromagnetic Processes at High Energies in Oriented Single Crystals* (World Scientific, Singapore, 1998).

[45] J.-L. Vay, A. Almgren, J. Bell, L. Ge, D. Grote, M. Hogan, O. Kononenko, R. Lehe, A. Myers, C. Ng, J. Park, R. Ryne, O. Shapoval, M. Thévenet, and W. Zhang, Nuclear Instruments and Methods in Physics Research Section A: Accelerators, Spectrometers, Detectors and Associated Equipment **909**, 476 (2018), 3rd European Advanced Accelerator Concepts workshop (EAAC2017).

[46] U. M. Ascher and L. R. Petzold, *Computer Methods for Ordinary Differential Equations and Differential-Algebraic Equations* (Society for Industrial and Applied Mathematics, Philadelphia, PA, 1998) https://epubs.siam.org/doi/pdf/10.1137/1.9781611971392 .

[47] T. Esirkepov, Computer Physics Communications **135**, 144 (2001).

[48] A. Taflove, S. C. Hagness, and M. Piket-May, in *The Electrical Engineering Handbook*, edited by W.-K. CHEN (Academic Press, Burlington, 2005) pp. 629–670.

[49] Chebyshev polynomials, dymore user's manual.

[50] W. Press, S. Teukolsky, W. Vetterling, and B. Flannery, *Numerical Recipes: The Art of Scientific Computing*, 3rd ed. (Cambridge University Press, 2007).

[51] C. W. Clenshaw, Mathematics of Computation **9**, 118 (1955).

[52] S. Montefiori and M. Tamburini, Computer Physics Communications **292**, 108855 (2023).

[53] A. Di Piazza, C. Müller, K. Z. Hatsagortsyan, and C. H. Keitel, Rev. Mod. Phys. **84**, 1177 (2012).

[54] V. I. Ritus, Journal of Soviet Laser Research **6**, 497 (1985).

[55] W. H. Furry, Phys. Rev. **81**, 115 (1951).

[56] D. M. Wolkow, Zeitschrift für Physik **94**, 250 (1935).

[57] V. B. Berestetskii, E. M. Lifshitz, and L. P. Pitaevskii, *Quantum Electrodynamics*, Course of theoretical physics (Elsevier Butterworth-Heinemann, Oxford, 1982).

[58] A. Di Piazza, Physics Letters B **782**, 559 (2018).

[59] V. N. Baier, V. M. Katkov, and V. M. Strakhovenko, Nuclear Physics B **328**, 387 (1989).

[60] V. Dinu, C. Harvey, A. Ilderton, M. Marklund, and G. Torgrimsson, Phys. Rev. Lett. **116**, 044801 (2016).

[61] A. Di Piazza, M. Tamburini, S. Meuren, and C. H. Keitel, Phys. Rev. A **98**, 012134 (2018).

[62] A. Di Piazza, M. Tamburini, S. Meuren, and C. H. Keitel, Phys. Rev. A **99**, 022125 (2019).

[63] J. Derouillat, A. Beck, F. Pérez, T. Vinci, M. Chiaramello, A. Grassi, M. Flé, G. Bouchard, I. Plotnikov, N. Aunai, J. Dargent, C. Riconda, and M. Grech, Computer Physics Communications **222**, 351 (2018).

[64] T. N. Wistisen, A. Di Piazza, C. F. Nielsen, A. H. Sørensen, and U. I. Uggerhøj (CERN NA63), Phys. Rev. Research **1**, 033014 (2019).

[65] T. N. Wistisen and A. Di Piazza, Phys. Rev. D **100**, 116001 (2019).

[66] T. Heinzl, B. King, and A. J. MacLeod, Phys. Rev. A **102**, 063110 (2020).

[67] C. F. Nielsen, R. Holtzapple, and B. King, Phys. Rev. D **106**, 013010 (2022).

[68] A. Fedotov, J. Phys.: Conf. Ser. **826**, 012027 (2017).

[69] T. Podszus and A. Di Piazza, Phys. Rev. D **99**, 076004 (2019).

[70] A. Ilderton, Phys. Rev. D **99**, 085002 (2019).

[71] R. P. Brent, Comput. J. **14**, 422 (1971).

[72] T. Dekker, Finding a zero by means of successive linear interpolation, constructive aspects of the fundamental theorem of algebra (b. dejon and p. henrici, eds.) (1969).

[73] Smilei documentation, `https://smileipic.github.io/Smilei/index.html` (2022).

[74] J. Arons, Space Science Reviews **24**, 437 (1979).

[75] D. A. Uzdensky and S. Rightley, Reports on Progress in Physics **77**, 036902 (2014).

[76] B. Cerutti and A. M. Beloborodov, Space Science Reviews **207**, 111 (2017).

[77] J. F. C. Wardle, D. C. Homan, R. Ojha, and D. H. Roberts, Nature **395**, 457 (1998).

[78] R. Ruffini, G. Vereshchagin, and S.-S. Xue, Physics Reports **487**, 1 (2010).

[79] V. Tsytovich and C. Wharton, Comments Plasma Phys. Controlled Fusion **4** (2024).

[80] M. H. Thoma, The European Physical Journal D **55**, 271 (2009).

[81] M. V. Medvedev, Physics of Plasmas **30**, 092112 (2023), https://pubs.aip.org/aip/pop/article-pdf/doi/10.1063/5.0160628/18139150/092112_1_5.0160628.pdf .

[82] P. San Miguel Claveria, X. Davoine, J. R. Peterson, M. Gilljohann, I. Andriyash, R. Ariniello, C. Clarke, H. Ekerfelt, C. Emma, J. Faure, S. Gessner, M. J. Hogan, C. Joshi, C. H. Keitel, A. Knetsch, O. Kononenko, M. Litos, Y. Mankovska, K. Marsh, A. Matheron, Z. Nie, B. O'Shea, D. Storey, N. Vafaei-Najafabadi, Y. Wu, X. Xu, J. Yan, C. Zhang, M. Tamburini, F. Fiuza, L. Gremillet, and S. Corde, Phys. Rev. Res. **4**, 023085 (2022).

[83] M. R. Stoneking, T. S. Pedersen, P. Helander, H. Chen, U. Hergenhahn, E. V. Stenson, G. Fiksel, J. von der Linden, H. Saitoh, C. M. Surko, and et al., Journal of Plasma Physics **86**, 155860601 (2020).

[84] H. Chen and F. Fiuza, Physics of Plasmas **30**, 020601 (2023), https://pubs.aip.org/aip/pop/article-pdf/doi/10.1063/5.0134819/20004444/020601_1_5.0134819.pdf .

[85] C. D. Arrowsmith, P. Simon, P. J. Bilbao, A. F. A. Bott, S. Burger, H. Chen, F. D. Cruz, T. Davenne, I. Efthymiopoulos, D. H. Froula, A. Goillot, J. T. Gudmundsson, D. Haberberger, J. W. D. Halliday, T. Hodge, B. T. Huffman, S. Iaquinta, F. Miniati, B. Reville, S. Sarkar, A. A. Schekochihin, L. O. Silva, R. Simpson, V. Stergiou, R. M. G. M. Trines, T. Vieu, N. Charitonidis, R. Bingham, and G. Gregori, Nature Communications **15**, 5029 (2024).

[86] H. Song, C. M. Kim, J. Won, J. Song, S. Lee, C.-M. Ryu, W. Bang, and C. H. Nam, Scientific Reports **13**, 310 (2023).

[87] H. Chen, F. Fiuza, A. Link, A. Hazi, M. Hill, D. Hoarty, S. James, S. Kerr, D. D. Meyerhofer, J. Myatt, J. Park, Y. Sentoku, and G. J. Williams, Phys. Rev. Lett. **114**, 215001 (2015).

[88] K. Qu, S. Meuren, and N. J. Fisch, Phys. Rev. Lett. **127**, 095001 (2021).

[89] T. ERBER, Rev. Mod. Phys. **38**, 626 (1966).

[90] A. Sampath, X. Davoine, S. Corde, L. Gremillet, M. Gilljohann, M. Sangal, C. H. Keitel, R. Ariniello, J. Cary, H. Ekerfelt, C. Emma, F. Fiuza, H. Fujii, M. Hogan, C. Joshi, A. Knetsch, O. Kononenko, V. Lee, M. Litos, K. Marsh, Z. Nie, B. O'Shea, J. R. Peterson, P. S. M. Claveria, D. Storey, Y. Wu, X. Xu, C. Zhang, and M. Tamburini, Phys. Rev. Lett. **126**, 064801 (2021).

[91] R. Nuter, L. Gremillet, E. Lefebvre, A. Lévy, T. Ceccotti, and P. Martin, Physics of Plasmas **18**, 033107 (2011), https://pubs.aip.org/aip/pop/article-pdf/doi/10.1063/1.3559494/16021983/033107_1_online.pdf .

[92] F. Pérez, L. Gremillet, A. Decoster, M. Drouin, and E. Lefebvre, Physics of Plasmas **19**, 083104 (2012), https://pubs.aip.org/aip/pop/article-pdf/doi/10.1063/1.4742167/13891570/083104_1_online.pdf .

[93] B. Martinez, M. Lobet, R. Duclous, E. d'Humières, and L. Gremillet, Physics of Plasmas **26**, 103109 (2019), https://pubs.aip.org/aip/pop/article-pdf/doi/10.1063/1.5118339/15614158/103109_1_online.pdf .

[94] N. Barov, M. E. Conde, W. Gai, and J. B. Rosenzweig, Phys. Rev. Lett. **80**, 81 (1998).

[95] C. E. Clayton, B. E. Blue, E. S. Dodd, C. Joshi, K. A. Marsh, W. B. Mori, S. Wang, P. Catravas, S. Chattopadhyay, E. Esarey, W. P. Leemans, R. Assmann, F. J. Decker, M. J. Hogan, R. Iverson, P. Raimondi, R. H. Siemann, D. Walz, T. Katsouleas, S. Lee, and P. Muggli, Phys. Rev. Lett. **88**, 154801 (2002).

[96] M. V. Ammosov, N. B. Delone, and V. P. Krainov, in *High Intensity Laser Processes*, Vol. 0664, edited by J. A. Alcock, International Society for Optics and Photonics (SPIE, 1986) pp. 138 – 141.

[97] R. N. Manchester, G. B. Hobbs, A. Teoh, and M. Hobbs, The Astronomical Journal **129**, 1993 (2005).

[98] V. Yakimenko, L. Alsberg, E. Bong, G. Bouchard, C. Clarke, C. Emma, S. Green, C. Hast, M. J. Hogan, J. Seabury, N. Lipkowitz, B. O'Shea, D. Storey, G. White, and G. Yocky, Phys. Rev. Accel. Beams **22**, 101301 (2019).

[99] Y.-Y. Chen, K. Z. Hatsagortsyan, C. H. Keitel, and R. Shaisultanov, Phys. Rev. D **105**, 116013 (2022).

[100] Y.-N. Dai, J.-J. Jiang, Y.-H. Jiang, R. Shaisultanov, and Y.-Y. Chen, Phys. Rev. D **108**, 056025 (2023).

[101] Y. Tang, Z. Gong, J. Yu, Y. Shou, and X. Yan, Phys. Rev. A **103**, 042807 (2021).

[102] Y.-F. Li, Y.-Y. Chen, W.-M. Wang, and H.-S. Hu, Phys. Rev. Lett. **125**, 044802 (2020).

[103] Y.-F. Li, Y.-Y. Chen, K. Z. Hatsagortsyan, A. Di Piazza, M. Tamburini, and C. H. Keitel, Phys. Rev. D **107**, 116020 (2023).

[104] T. G. Blackburn, D. Seipt, S. S. Bulanov, and M. Marklund, Phys. Rev. A **101**, 012505 (2020).

[105] Y.-F. Li, R. Shaisultanov, K. Z. Hatsagortsyan, F. Wan, C. H. Keitel, and J.-X. Li, Phys. Rev. Lett. **122**, 154801 (2019).

[106] User's manual of cain version 2.44.

[107] H.-H. Song, W.-M. Wang, and Y.-T. Li, Yunic: A multi-dimensional particle-in-cell code for laser-plasma interaction (2021), arXiv:2104.00642 [physics.plasm-ph] .

[108] T. Podszus, V. Dinu, and A. Di Piazza, Phys. Rev. D **106**, 056014 (2022).

[109] J. M. Cole, K. T. Behm, E. Gerstmayr, T. G. Blackburn, J. C. Wood, C. D. Baird, M. J. Duff, C. Harvey, A. Ilderton, A. S. Joglekar, K. Krushelnick, S. Kuschel, M. Marklund, P. McKenna, C. D. Murphy, K. Poder, C. P. Ridgers, G. M. Samarin, G. Sarri, D. R. Symes, A. G. R. Thomas, J. Warwick, M. Zepf, Z. Najmudin, and S. P. D. Mangles, Phys. Rev. X **8**, 011020 (2018).

[110] K. Poder, M. Tamburini, G. Sarri, A. Di Piazza, S. Kuschel, C. D. Baird, K. Behm, S. Bohlen, J. M. Cole, D. J. Corvan, M. Duff, E. Gerstmayr, C. H. Keitel, K. Krushelnick, S. P. D. Mangles, P. McKenna, C. D. Murphy, Z. Najmudin, C. P. Ridgers, G. M. Samarin, D. R. Symes, A. G. R. Thomas, J. Warwick, and M. Zepf, Phys. Rev. X **8**, 031004 (2018).

[111] E. E. Los, E. Gerstmayr, C. Arran, M. J. V. Streeter, C. Colgan, C. C. Cobo, B. Kettle, T. G. Blackburn, N. Bourgeois, L. Calvin, J. Carderelli, N. Cavanagh, S. J. D. D. A. D. Piazza, R. Fitzgarrald, A. Ilderton, C. H. Keitel, M. Marklund, P. McKenna, C. D. Murphy, Z. Najmudin, P. Parsons, P. P. Rajeev, D. R. Symes, M. Tamburini, A. G. R. Thomas, J. C. Wood, M. Zepf, G. Sarri, C. P. Ridgers, and S. P. D. Mangles, Observation of quantum effects on radiation reaction in strong fields (2024), arXiv:2407.12071 [hep-ph] .

[112] R. Jacobs, Luxe: A new experiment to study non-perturbative qed in electron-laser and photon-laser collisions (2022), arXiv:2205.06096 [hep-ex] .

[113] Z. Chen, S. Meuren, E. Gerstmayr, V. Yakimenko, P. H. Bucksbaum, and D. A. R. and, in *Optica High-brightness Sources and Light-driven Interactions Congress 2022* (Optica Publishing Group, 2022) p. HF4B.6.

[114] A. A. Sokolov and I. M. Ternov, Dokl. Akad. Nauk SSSR **153**, 1052 (1963).

[115] B. Gough, *GNU Scientific Library Reference Manual - Third Edition*, 3rd ed. (Network Theory Ltd., 2009).

[116] Openai: Chatgpt, `https://chat.openai.com/chat`.

Acknowledgments

I would like to express my sincere gratitude to Dr. Matteo Tamburini, Prof. Dr. Antonino Di Piazza, and Hon. Prof. Dr. Christoph H. Keitel for their invaluable guidance and everything they've taught me. I'm really grateful for their endless patience and for welcoming me into the PhD program.

I would also like to thank apl. Prof. Dr. Sandra P. Klevansky for serving as my referee, and Prof. Dr. Stephanie Hansmann-Menzemer and Prof. Dr. Joao Seco for participating on my defense committee.

Finally, I wish to extend my heartfelt gratitude to my friends and colleagues—especially Zozo, Audagio, K-Man, Biondetti, Bisa, and Lorenzino. Their stimulating discussions have enriched both my scientific journey and my personal growth.

Thank you!

To address syntax and grammatical errors and enhance clarity of the English language, numerous sections of this thesis were proofread using ChatGPT [116]. However, all content (scientific or not) is entirely original, and was produced solely by me (and my group) throughout my PhD. Proper credit was given to all sources for their respective contributions to this thesis.